



**HAL**  
open science

# Modeling and simulation of composite plasmonic structures based on graphene and metals

Maha Ben Rhouma

► **To cite this version:**

Maha Ben Rhouma. Modeling and simulation of composite plasmonic structures based on graphene and metals. Electronics. Université Clermont Auvergne, 2021. English. NNT : 2021UCFAC016 . tel-03564154

**HAL Id: tel-03564154**

**<https://theses.hal.science/tel-03564154>**

Submitted on 10 Feb 2022

**HAL** is a multi-disciplinary open access archive for the deposit and dissemination of scientific research documents, whether they are published or not. The documents may come from teaching and research institutions in France or abroad, or from public or private research centers.

L'archive ouverte pluridisciplinaire **HAL**, est destinée au dépôt et à la diffusion de documents scientifiques de niveau recherche, publiés ou non, émanant des établissements d'enseignement et de recherche français ou étrangers, des laboratoires publics ou privés.

Université de Clermont Auvergne  
Ecole doctorale des Sciences pour l'ingénieur

# THÈSE

présentée pour obtenir le grade de

**DOCTEUR D'UNIVERSITÉ**

Spécialité doctorale "Electronique et systèmes"

*soutenue publiquement par*

**Maha BEN RHOUMA**

le 24 Février 2021

## Modeling and simulation of composite plasmonic structures based on graphene and metals

Directeur de thèse : **Kofi EDEE**

Co-directeur de thèse : **Mauro ANTEZZA**

### Jury:

<b>M.Dominique BARCHIESI</b>	Professeur	UTT (Troyes)	Rapporteur
<b>M. Fadi BAIDA</b>	Professeur	FEMTO-ST (Besancon)	Rapporteur
<b>Mme Ségolène CALLARD</b>	Professeur	STMS/INL (Lyon)	Examinatrice
<b>M. Brahim GUIZAL</b>	Professeur	L2C( Montpellier)	Président



- *Le jour se lève,*
- *Sais-tu pourquoi le cri du coq se fait entendre?*
- *Le miroir de l'aube te dit qu'une nuit de ton existence s'en est allée.*
- *Le jour se lève,*
- *Tu n'as encore rien appris.*

Omar Al Khayyâm - AL Rubâi'ât (les quatrains)



*À mon père, ma mère, mon frère  
et mes deux sœurs*



This research was financed by the French government IDEX-ISITE initiative  
16-IDEX-0001 (CAP 20-25)





# Acknowledgments

*Je suis reconnaissant à tous  
ceux qui m'ont dit non. C'est  
grâce à eux que je suis moi-  
même*

---

Albert Einstein

Cette thèse a été effectuée en codirection entre l'équipe "Électromagnétisme et Nanophotonique" de l'institut Pascal (Université Clermont Auvergne) et l'Équipe "Rayonnement Matière et Phénomènes Quantiques" du Laboratoire Charles Coulomb (Université de Montpellier). Par ailleurs, le projet dans lequel s'est inscrit ce travail de thèse était réalisé en collaboration avec Jonathan FAN de l'université de Stanford (USA) et Nikolay A. GIPPIUS du Skolkovo Institute of Science and Technology (Russie).

Je voudrais remercier tous les membres du jury d'avoir accepté d'examiner et évaluer ce travail. Je tiens à remercier Messieurs Fadi BAIDA et Dominique BARCHIESI qui m'ont fait l'honneur de rapporter sur mon travail de thèse. J'aimerais également remercier Madame Ségolène CALLARD qui a accepté d'examiner attentivement mon manuscrit de thèse et pour l'intérêt qu'elle a porté à mon travail.

Mes plus sincères remerciements s'adressent à mes deux encadrants: Kofi Edee et Mauro Antezza qui m'ont fait confiance en me confiant ce sujet. Je leur suis très reconnaissante de tous les précieux conseils et leçons scientifiques, leur soutien, leurs encouragements, leurs disponibilités et leurs grandes qualités humaines. Merci Kofi de m'avoir accordé toute ta confiance et m'avoir laissé une grande liberté dans l'orientation de mon travail de thèse. Je voudrais également te remercier Mauro pour ta rigueur scientifique, ton soutien, ton aide, tes encouragements dans les moments difficiles et ta gentillesse.

Je souhaite également remercier Brahim Guizal d'avoir accepté de présider le jury de ma soutenance de thèse. Merci Brahim pour toute l'aide et le soutien morale et scientifique qui tu m'a accordé et apporté depuis le début de ma première thèse en 2013. Tu m'a transmis le goût pour la recherche par ton enthousiasme passionné et communicatif et tu m'a montré que le monde de la recherche pouvait être un univers passionnant. J'ai trop appris de toi non seulement sur le plan scientifique mais aussi le plan personnel.

J'adresse également tous mes remerciements à l'ensemble des membre du Laboratoire Charles Coulomb, notamment les doctorants et les chercheurs de l'équipe "Théorie

du Rayonnement Matière et Phénomènes Quantiques". Tout particulièrement, je tiens à remercier: Youssef, Chahine, Abir, Pierre...

Je tiens à remercier tous les membres de L'institut Pascal et l'équipe Électromagnétisme et Nanophotonique pour leurs aide, conseils et soutien. Tout Particulièrement, je tiens à remercier Gérard Granet pour sa sympathie, sa gentillesse. Un grand merci aussi à Antoine Moreau et Rafik smaali pour leur gentillesse.

Je suis très reconnaissante à ma chère amie, Insaf, pour son soutien moral, son aide et ses encouragements durant ces années.

Je remercie également Madame Dominique Torrisani, Gestionnaire ED Sciences pour l'ingénieur pour son aide, sa gentillesse et sa bonne humeur.

Enfin, mes vifs remerciements vont à ma famille, mais surtout à mon père Ammar qui m'a soutenue durant mes études moralement et financièrement, qu'il trouve ici ma profonde gratitude. J'adresse des remerciements du même ordre à ma mère Najet, qui m'a constamment encouragée et soutenue tout au long de ces années. Je vous remercie vous deux pour tout le soutien et l'amour que vous me portez depuis mon enfance.

# Contents

<b>Acknowledgments</b>	<b>vii</b>
<b>Contents</b>	<b>ix</b>
<b>Abstract</b>	<b>1</b>
<b>Résumé</b>	<b>3</b>
<b>Introduction</b>	<b>5</b>
<b>I Theoretical and numerical tools</b>	<b>13</b>
<b>1 Theoretical Background</b>	<b>15</b>
1.1 Fundamentals of graphene . . . . .	16
1.1.1 Electronic properties . . . . .	16
1.1.2 Graphene doping . . . . .	20
1.1.3 Electromagnetic properties of graphene: Conductivity Model . . . . .	22
1.2 Theory of graphene surface plasmons polaritons (SPPs) . . . . .	28
1.2.1 Surface plasmons polaritons at planar interfaces . . . . .	28
1.2.2 Surface plasmons polaritons on graphene (GSP) . . . . .	32
1.3 Conclusions . . . . .	45
<b>2 Numerical Tools</b>	<b>51</b>
2.1 Generic Physical Structure . . . . .	51
2.2 Numerical Methods . . . . .	52
2.2.1 Standard Fourier Modal Method (FMM) . . . . .	52
2.2.2 Fourier Modal Method with spatial adaptative resolution (FMM-ASR) . . . . .	60
2.2.3 Aperiodic Fourier Modal Method: FMM with PML . . . . .	64
2.3 Numerical Examples involving graphene:	
Graphene-Strip Gratings . . . . .	67
2.3.1 Graphene horizontal strips grating . . . . .	67
2.3.2 Graphene Vertical strips grating . . . . .	69
2.4 Conclusions . . . . .	72

<b>II</b>	<b>Hybrid Plasmonic Structures Based on Graphene</b>	<b>75</b>
<b>3</b>	<b>Metallic slit grating-Graphene composite structure</b>	<b>77</b>
3.1	Extraordinary optical transmission . . . . .	78
3.1.1	Extraordinary transmission : Two resonant mechanisms . . . . .	79
3.2	Coupling between subwavelength nano-slits lattice modes and metal-insulator-graphene cavity modes: A semi-analytical model . . . . .	82
3.2.1	Physical system . . . . .	82
3.2.2	Modal analysis of the system . . . . .	84
3.2.3	Analysis of the Lorentz and Fano resonances of the system . . . . .	89
3.3	Conclusions . . . . .	92
<b>III</b>	<b>Non-reciprocity devices based on graphene and metals</b>	<b>99</b>
<b>4</b>	<b>Basic concepts</b>	<b>101</b>
4.1	Electromagnetic reciprocity and non reciprocity . . . . .	101
4.1.1	Time reversal symmetry of Maxwell's equations . . . . .	102
4.1.2	Reciprocity Theorem in Electromagnetism . . . . .	103
4.1.3	Non reciprocity with magnetic field . . . . .	104
4.2	Graphene under a static magnetic bias . . . . .	115
4.2.1	Landau Levels in monolayer graphene . . . . .	115
4.2.2	Reflection and transmission properties of a magnetized graphene sheet . . . . .	117
4.2.3	Surface magnetoplasmons polaritons on magnetically biased graphene sheet (GSMP) . . . . .	123
4.2.4	Nonreciprocity and gyrotropy of graphene . . . . .	125
4.3	Conclusions . . . . .	129
<b>5</b>	<b>Propagation properties of a magnetically biased array of graphene ribbons</b>	<b>133</b>
5.1	Semi-analytical model for the analysis of a magnetically Biased subwavelength graphene-strip-grating . . . . .	134
5.1.1	Physical system . . . . .	134
5.1.2	Theoretical Method . . . . .	135
5.1.3	Numerical Results and discussion . . . . .	140
5.2	Conclusion . . . . .	145
<b>6</b>	<b>Theoretical analysis of Optical Hall effect in a 2D nano-cross-slits grating</b>	<b>149</b>
6.1	Statement . . . . .	150
6.2	Polarization independent EOT phenomenon through 2D cross-slits array	151
6.3	Magneto-optical perturbation of the gap plasmon modes . . . . .	158
6.4	Conclusion . . . . .	162
	<b>Conclusion and outlook</b>	<b>165</b>

# Abstract

This thesis work concerns the theoretical modeling and numerical simulations in the areas of nanophotonics (light-matter interactions at the nanoscale) in general and plasmonics in particular. This latter field has received considerable attention over the last decades arising from the unique and unusual optical properties of surface plasmons polaritons such as the confinement and control of light at the subwavelength scale. Noble Metals such as gold and silver have usually been used as the building blocks for several plasmonic structures in the visible range. However, in the infrared (IR) and terahertz (THz) frequencies, these materials exhibit very large losses and are hardly tunable which limits their application as performant plasmonic devices in these frequencies ranges. To overcome this problem, graphene, a two dimensional (2D) material made of carbon atoms arranged in a honeycomb lattice, possessing extraordinary electrical, thermal, and optical properties, has emerged in the plasmonics field as a potential alternative plasmonic material working in the mid-infrared and terahertz (THz) frequencies ranges. In this context, the purpose of this thesis is to develop theoretical models for the study of novel graphene based plasmonic structures and construct numerical codes that allow the simulation of their behavior.

The research presented in this work is articulated around two main axes: (i) the first one concerns the study of hybrid plasmonic structures based on graphene and metals in the absence of an external magnetic field (ii) the second is in the investigation of the magneto-optical and non-reciprocal properties of structures based on graphene and metals subjected to an external static magnetic field.

In the framework of this thesis, three plasmonic structures of academic and technological interests have been explored. The study of each of these structures was carried out into two steps. In the first step, the structures in question were studied in an exact manner using rigorous numerical methods. Once the exact calculation was established and to better understand the obtained results, an approximate semi-analytical model was developed for each structure to reproduce in a simple way the exact results. These simple models allowed us to interpret and explain the optical spectra of the studied structures in terms of some remarkable modes and to understand the underlying physics.

The First studied structure is a hybrid tunable plasmonic system consisting of a 1D array of periodic subwavelength metal slits and a graphene sheet separated by a dielectric gap. By splitting the whole system into two coupled sub-systems which involve two kinds of couplings, we have proposed a semi analytical model allowing to fully describe the spectrums of this system and understand the origin of the resonances appearing in them. After that, we have been interested in two different structures. First, we developed a simple and fast semi-analytical method to accurately and efficiently pre-

dict the magneto-optical response of a one-dimensional graphene strip grating in the presence of an external static magnetic field, in which the graphene is modeled as an anisotropic layer with atomic thickness and a frequency dependent complex permittivity tensor. Finally, we have studied the magneto-optical and non-reciprocal properties of a plasmonic structure consisting of a 2D array of nano-slits perforating a gold film. By extending the 1D model developed for the first structure, we succeeded to study and reproduce the magneto-optical spectra of this structure. First, we studied the response of the structure in the absence of a static magnetic field. Then, we added a static magnetic field and filled the slits with an anisotropic gyrotropic material.

# Résumé

Ce travail de thèse concerne la modélisation dans le domaine de la nanophotonique (interaction de la lumière avec des objets de taille nanométrique) et la plasmonique en particulier. Cette dernière est une thématique de recherche qui a connu un grand attrait au niveau international durant les dernières décennies découlant des propriétés optiques uniques et inhabituelles des plasmons polaritons de surface (PPs) telles que le confinement et l'exaltation du champ EM à des échelles sub-longueur d'onde. Les PPS ont été découverts et étudiés dans le visible avec les métaux nobles tels que l'Or et l'Argent dont les fréquences plasma se situent dans cette gamme de fréquences. Cependant, dans le domaine THz, ces matériaux souffrent de pertes très importantes ce qui dégrade leurs performances et limite plusieurs applications dans ce domaine qui est devenu un domaine attrayant au cours des dernières années. Le grand intérêt pour cette gamme de fréquences découle de son importance pour diverses applications technologiques déjà existantes pour les autres gammes de fréquences du spectre électromagnétique et jusque-là non disponibles pour la gamme THz (imagerie médicale et sécuritaire, capteurs d'agents chimiques et/ou biologiques, radars compacts...). Ces limitations ont été surmontées, en partie, avec l'avènement du graphène, un seul feuillet de graphite, qui consiste en un arrangement périodique et bidimensionnel d'atomes de carbone disposés selon un réseau en nid d'abeilles. Ce matériau a suscité un immense intérêt, à la fois de la part de la communauté scientifique et des industriels, en raison de ses propriétés optiques et électrodynamiques particulières. En particulier, il est possible de contrôler et de modifier sa conductivité via un dopage électrostatique ou chimique. Grâce à ces propriétés, le graphène peut supporter des PPS avec des propriétés exceptionnelles telles qu'un confinement beaucoup plus important que celui des métaux et des pertes qui sont relativement faibles dans les domaines THz et Infra-Rouge lointain. Ceci fait du graphène un matériau prometteur pour la réalisation de nouveaux dispositifs commandables/contrôlables dans les domaines THz et Infra-Rouge. C'est dans ce contexte très concurrentiel que se sont inscrits les travaux de cette thèse qui visent à mettre au point des modèles théoriques pour étudier des structures plasmoniques à base de graphène et de construire des codes de calcul permettant la simulation de leur comportement.

Les travaux présentés dans ce travail s'articulent autour de deux axes principaux : (i) le premier concerne l'étude de structures plasmoniques hybrides à base de graphène et de métaux en absence de champ magnétique statique externe (ii) le second porte sur l'investigation des propriétés magnéto-optiques et non-réciproques de structures à base de graphène et de métaux soumises à l'effet d'un champ magnétique.

Dans le cadre de cette thèse, trois structures plasmoniques d'intérêt académique et technologique ont été explorées. L'étude de chacune de ces structures a été réalisée en

deux étapes. Dans la première étape, les structures en question ont été étudiées de manière exacte en utilisant des méthodes numériques rigoureuses. Une fois le calcul exact établi et afin de mieux comprendre les résultats obtenus, un modèle semi-analytique approché a été développé pour chaque structure afin de reproduire de manière simple les résultats exacts trouvés par des calculs plus ou moins compliqués. Ces modèles simples ont permis d'interpréter et d'expliquer les spectres optiques des structures étudiées en termes de certains modes remarquables et de comprendre la physique sous-jacente.

La première structure étudiée est un système plasmonique hybride constitué d'un réseau périodique, 1D sub-longueur d'onde, fait de nano-fentes gravées dans un métal, le tout étant déposé sur une couche diélectrique elle-même déposée sur une feuille de graphène. En divisant l'ensemble du système en deux sous-systèmes couplés qui mettent en jeu deux types de couplages, nous avons proposé un modèle semi-analytique permettant de décrire les spectres de ce système et de comprendre l'origine des résonances qui y apparaissent. Par la suite, nous nous sommes intéressés à deux structures différentes. Tout d'abord, nous avons développé une méthode semi-analytique simple pour prédire la réponse magnéto-optique d'un réseau périodique de nano-rubans de graphène soumis à l'effet d'un champ magnétique statique dans lequel le graphène est modélisé comme une couche anisotrope avec une épaisseur atomique et une permittivité complexe dépendant de la fréquence. Enfin, nous avons étudié les propriétés magnéto-optiques et non-réciproques d'une structure plasmonique constituée d'un réseau 2D de nano-fentes perforant un film d'Or. En étendant le modèle approché 1D développé pour la première structure, nous avons réussi à étudier et reproduire les spectres magnéto-optiques de cette structure. Dans un premier temps, nous avons étudié la réponse de la structure en absence de champ magnétique statique. Dans un deuxième temps, nous avons ajouté un champ magnétique statique et rempli les fentes par un milieu gyrotrope.

# Introduction

*If the facts don't fit the theory  
change the facts*

---

Albert Einstein

Over the last decades, the control of the behaviour of light as well as light-matter interactions at the nanoscale, namely nanophotonics, has attracted intensive attention among the scientific community and became among the most important research subjects of modern physics. Plasmonics, the central topic of this thesis, is an active sub-branch of nanophotonics that focuses on the analysis, study and manipulation of surface plasmons polaritons (SPPs) which are surface electromagnetic waves that propagate at the interfaces between insulating and conducting media as a result of the coupling between an external electromagnetic wave and collective oscillations of free charged carriers [1]. Historically, the first description of (SPPs) dates back to the beginning of the twentieth century by Wood in 1902 [2] who observed the spectra of a continuous light source and diffracted by an optical diffraction grating. He noticed a surprising phenomenon: *"I was astounded to find that under certain conditions, the drop from maximum illumination to minimum, a drop certainly from 10 to 1, occurred within a range of wavelengths not greater than the distance between the sodium lines"*. These phenomena was called *Wood's anomalies*. One century after the Wood's discovery, plasmonics has attracted a growing and considerable interest arising from the unique and important properties of surface plasmons polaritons, including strongly enhanced local fields at the subwavelength scale, tremendous sensitivity to changes in the local environment, and the ability to localize energy to tiny volumes not restricted by the wavelength of the exciting light. This makes them among the most important forms of strong light matter interactions and gave rise to a wide range of potential applications in many fields. For example, ultrasensitive biosensing [3, 4], photonic metamaterials [5], photovoltaic devices [6, 7], integrated optical circuits [8], subwavelength waveguides [9] and optical superlenses [10].

SPPs were first studied in the visible range over noble metals such as gold and silver that were among the first materials used to devise and study plasmonic structures. Recently, the infrared (IR) and specifically the terahertz (THz) domains have become attractive for their benefits in various applications such as medical imaging [11], biological studies, space exploration, communications [12] and security [13]. Therefore, extending plasmonic properties to the THz and IR spectra can enable many new applications. However, in these frequencies ranges, the traditional plasmonic materials suffer from very large losses and are hardly tunable which limits their applications and affects the performances of the corresponding plasmonic devices. Hence, finding novel

and alternative plasmonic materials able to manipulate and generate SPPs in the THz and IR ranges constitutes a great challenge.

In this context, doped graphene, has emerged in the plasmonics field as a potential and promising plasmonic material working in the mid-infrared and terahertz (THz) spectral windows. Graphene is a two dimensional 2D material made of carbon atoms arranged in a honeycomb lattice. Since its discovery in 2004 by Geim and Novoselov [14], this 2D material which, for decades, was predicted to be experimentally unviable, has generated great interest in scientific studies and technological developments due to its unusual and fascinating, electronic, optical, mechanical and thermal properties which originate from its linear electronic dispersion around the so-called *Dirac points* and to the massless nature of its charge carriers (Dirac fermions). Indeed, graphene displays a high theoretical electron mobility that can reach up to  $200000\text{cm}^2\text{V}^{-1}\text{s}^{-1}$  [15], high thermal conductivity [16] and it also shows a good flexibility. Furthermore, graphene is well known as a transparent material in the visible range where it absorbs only around 2.3% of the incident electromagnetic wave [17]. This property makes graphene suitable for various optical devices such as touch-screens and light emitting diodes (LED)[18]. In addition to the aforementioned properties, graphene exhibits a wide range of electromagnetic properties stemming from its unusual optical conductivity which can be dynamically tuned by electrostatic bias or chemical doping [19, 20, 21].

When graphene is doped via chemical or electrostatic doping, it behaves as an ultra thin metal and can support surface plasmons polaritons similar to those guided by noble metals. However, the graphene surface plasmons polaritons (GSPs) exhibit many advantages compared to their counterparts in metals. In addition to the transverse magnetic (TM) surface plasmons polaritons usually supported by noble metals, graphene can support a new plasmonic mode in the transverse electric (TE) polarization [22, 23]. This last mode is specific for graphene and cannot exist in noble metals since the imaginary part of the conductivity is always positive. For graphene, this mode can take place when the imaginary part of its optical conductivity becomes negative i.e for frequencies above the interband threshold, the region of spectrum governed by the interband transitions. However, due to the Landau damping occurring at the interband threshold, (TE-GSP) can only exist in a very narrow frequency window ( $1.667 < \hbar\omega/\mu_c < 2$ ,  $\mu_c$  is the chemical potential of graphene). Moreover, these modes are weakly bound to the graphene surface and their experimental excitation has not been demonstrated. Furthermore, graphene TM- SPPs are reported to have a high confinement and relatively low losses [24]. Another crucial advantage of SPPs in graphene, over those in noble metals, is their tunability stemming from the simplicity to control of the chemical potential by electrical gating and doping. These extraordinary features of SPPs in graphene have been exploited for devising a variety of tunable plasmonic graphene-based devices in the mid-infrared and terahertz regions of the spectrum such as optical switches [25], antennas [26], absorbers [27], modulators [28] and sensors [29].

On another hand, it is well known that the conductivity of graphene can be also tuned by a magnetic bias. Indeed, when a static magnetic field is applied perpendicular to the graphene sheet, a finite optical Hall conductivity appears and graphene becomes anisotropic with an asymmetric conductivity tensor. It is also shown that a magnetically biased graphene sheet can exhibit gyrotropic properties which leads to many magneto-optical (MO) phenomena such as Giant Faraday rotation [30] and Kerr effect [31]. These phenomena are shown to exhibit non reciprocal properties which may be

useful and crucial for the development of ultra-thin non reciprocal devices operating at the microwave and terahertz frequency ranges [32, 33]. Furthermore, in the presence of the static magnetic field, plasmons and cyclotron excitations hybridise and lead to the appearance of graphene surface magnetoplasmons polaritons (GSMPPs). These modes display various important properties and have a great potential in a lot of plasmonic non reciprocal applications thanks to the combination of the plasmonic properties of graphene with the magneto-optics effects.

The purpose of this thesis is to explore light matter interactions in graphene in the framework of plasmonics. The research presented throughout this manuscript focuses on the theoretical and numerical study of graphene based plasmonic structures working in the infrared and terahertz ranges. This thesis is articulated around two main axes. The first axis concerns the study of the behaviour of hybrid plasmonic structures containing graphene while in the second we investigate the magneto-optical and non-reciprocal properties of structures based on graphene and metals subjected to an external static magnetic field.

## Dissertation outline

The present thesis is structured into three parts, the first part can be viewed as an introduction that gives the Theoretical and numerical tools, the second part is devoted to the investigation of hybrid plasmonic structures based on graphene and finally the last one is dedicated to the study of magneto-optical and non-reciprocity properties of structures based on graphene and metals. Below, we provide a brief description of the content of each chapter.

### chapter 1 | Theoretical Background

In this first chapter, we provide the theoretical background necessary for understanding this thesis. We begin with an overview of the electronic properties of graphene. Then, we describe the magneto-optical conductivity model of graphene characterizing its optical response. After a brief introduction on the foundations of plasmonics, we discuss the different plasmonic modes that can propagate along a graphene sheet and their existence conditions. Finally, we review the basic properties of these modes

### chapter 2 | Numerical Tools

This chapter is dedicated to the description of the numerical tools that will be used in the analysis of the structures studied in this thesis. After presenting the generic multigrating structure, we describe and explain the different numerical methods used for modelling it. In the last section of this chapter, a comparative study will be made between these methods in terms of convergence and stability to identify the most suitable one for each structure.

### chapter 3 | Metallic slit grating-Graphene composite structure

In this chapter we present a semi-analytical model of the resonance phenomena occurring in a hybrid system made of a 1D array of periodic sub-wavelength slits deposited on an insulator/graphene layer. We show that the spectral response of this hybrid system can be fully explained by a simple semi-analytical model based on a weak and a strong couplings between two elementary sub-systems. The first elementary sub-system consists of a 1D array of periodic sub-wavelength slits

viewed as a homogeneous medium. In this medium lives a metal-insulator-metal lattice mode interacting with surface and cavity plasmon modes. A weak coupling with surface plasmon modes on both faces of the perforated metal film leads to a broadband spectrum while a strong coupling between this first sub-system and a second one made of a graphene-insulator-metal gap leads to a narrow band spectrum. We provide a semi-analytical model based on these two interactions allowing to efficiently access the full spectrum of the hybrid system.

#### **chapter 4 | Basic concepts**

This chapter reviews the theory and the basic concepts of the third part of this thesis, we will present the notions of reciprocity and non reciprocity in general and in particular, we will focus on the non reciprocity caused by a static magnetic field. In the next part of this chapter, we will investigate graphene under the presence of an external static magnetic field with focus on its gyrotropic and non reciprocal properties.

#### **chapter 5 | Propagation properties of a magnetically biased array of graphene ribbons**

This chapter is devoted to the theoretical study of the magneto-optical properties of a magnetically-biased sub-wavelength graphene strip grating. For this purpose, we propose a simple and fast semi analytical model that allows to successfully compute its transmittance and reflectance. It is based on the effective medium approach where the graphene is modelled as an anisotropic layer with atomic thickness and a frequency dependent and complex permittivity tensor. The accuracy of the proposed model will be validated by comparing it on the one hand with The PMM method and on the other hand with the effective medium approach proposed in [34].

#### **chapter 6 | Theoretical analysis of Optical Hall effect in a 2D nano-cross-slits grating**

In this last chapter, We theoretically demonstrate the nonreciprocal behaviour, for circularly polarized electromagnetic waves, of a 2D crossed-grating made of nano-slits filled with a gyrotropic material. We provide closed-form expressions for the reflection and transmission of the system, allowing one to fully describe and understand the extraordinary optical transmission (EOT) mechanism occurring in the system. When the slits are filled with a gyrotropic material, the structure exhibits non-reciprocal unidirectional light transmission in the frequency range where the EOT occurs. This will be fully explained through the proposed modal analytic analysis.

# Bibliography

- [1] Barchiesi. D Salvi. J. Measurement of thicknesses and optical properties of thin films from surface plasmon resonance (spr). *Appl. Phys. A*, (245-255), 2014. 5
- [2] R.W. Wood. Xlii. on a remarkable case of uneven distribution of light in a diffraction grating spectrum. *The London, Edinburgh, and Dublin Philosophical Magazine and Journal of Science*, 4(21):396–402, 1902. 5
- [3] O. Lyandres N. C. Shah J. Zhao J. N. Anker, W. P. Hall and R. P. Van Duyne. Biosensing with plasmonic nanosensors. *Nat. Mater*, 7(6):442–453, 2008. 5
- [4] Dominique Barchiesi. *Surface Plasmon Resonance Biosensors: Model and Optimization*. Pan Stanford Series on the High-Tech of Biotechnology. Pan Stanford Publishing, 2013. 5
- [5] Nikolay I. Zheludev. A roadmap for metamaterials. *Opt. Photon. News*, 22(3):30–35, Mar 2011. 5
- [6] H. A. Atwater and A. Polman. Plasmonics for improved photovoltaic devices,. *Nat. Mater*, 9(3):205, 2010. 5
- [7] E. Stassen S. Xiao and N. A. Mortensen. Ultrathin silicon solar cells with enhanced photocurrents assisted by plasmonic nanostructures. *Journal of Nanophotonics*, 6(1):0661503, 2012. 5
- [8] E. Devaux J. Y. Laluet S. I. Bozhevolnyi, V. S. Volkov and T. W. Ebbesen. Channel plasmon subwavelength waveguide components including interferometers and ring resonators,. *Nature*, 440(7083):508, 2006. 5
- [9] J. A. Dionne, L. A. Sweatlock, H. A. Atwater, and A. Polman. Planar metal plasmon waveguides: frequency-dependent dispersion, propagation, localization, and loss beyond the free electron model. *Phys. Rev. B*, 72:075405, Aug 2005. 5
- [10] J. B. Pendry. Negative refraction makes a perfect lens. *Phys. Rev. Lett.*, 85:3966–3969, Oct 2000. 5
- [11] KG Kudrin IV Reshetov KI Zaitsev, NV Chernomyrdin and SO Yurchenko. Terahertz spectroscopy of pigmentary skin nevi in vivo. *Optics and Spectroscopy*, 119(3):404–410, 2015. 5
- [12] H. Sariaeddeen, N. Saeed, T. Y. Al-Naffouri, and M. Alouini. Next generation terahertz communications: A rendezvous of sensing, imaging, and localization. *IEEE Communications Magazine*, 58(5):69–75, 2020. 5

- 
- [13] John F Federici, Brian Schulkin, Feng Huang, Dale Gary, Robert Barat, Filipe Oliveira, and David Zimdars. THz imaging and sensing for security applications—explosives, weapons and drugs. *Semiconductor Science and Technology*, 20(7):S266–S280, jun 2005. 5
- [14] K. S. Novoselov, A. K. Geim, S. V. Morozov, D. Jiang, Y. Zhang, S. V. Dubonos, I. V. Grigorieva, and A. A. Firsov. Electric field effect in atomically thin carbon films. *Science*, 306(5696):666–669, 2004. 6
- [15] K.I. Bolotin, K.J. Sikes, Z. Jiang, M. Klima, G. Fudenberg, J. Hone, P. Kim, and H.L. Stormer. Ultrahigh electron mobility in suspended graphene. *Solid State Communications*, 146(9):351 – 355, 2008. 6
- [16] Wenzhong Bao Irene Calizo Desalegne Teweldebrhan Feng Miao Alexander A. Balandin, Suchismita Ghosh and Chun Ning Lau. Superior thermal conductivity of single-layer graphene. *Nano Lett*, 8(3):902–907, 2008. 6, 20
- [17] R. R. Nair, P. Blake, A. N. Grigorenko, K. S. Novoselov, T. J. Booth, T. Stauber, N. M. R. Peres, and A. K. Geim. Fine structure constant defines visual transparency of graphene. *Science*, 320(5881):1308–1308, 2008. 6
- [18] T Hasan Francesco Bonaccorso, Z Sun and AC Ferrari. Graphene photonics and optoelectronics. *Nature photonics*, 4(9):611–622, 2010. 6
- [19] L. A. Falkovsky. Optical properties of graphene. *J.Phys.Conf.Ser.*, 129(1):2004, 2008. 6, 26
- [20] L. A. Falkovsky and A. A. Varlamov. Space-timedispersion of graphene conductivity. *Eur.Phys.J.B*, 56(4):281, 2007. 6, 26
- [21] S. G. Sharapov V. P. Gusynin and J. p. Carbotte. Magneto-optical conductivity in graphene. *J.Phys.Condens.Matter.*, 19(2):6222, 2007. 6, 26
- [22] W. Hanson. Quasi transverse electromagnetic modes supported by a graphene parallel-plate waveguide. *J.App.Phys.Lett*, 104:084314, 2008. 6, 33, 40
- [23] S. A. Mikhailov and K. Ziegler. New electromagnetic mode in graphene. *PRL*, 99(01):6803, 2007. 6, 33, 40, 41
- [24] M. Kafesaki P. Tassin, T. Koschny and C. M. Soukoulis. A comparison of graphene , superconductors and metals as conductors for metamaterials and plasmonics. *Nat .Photonics*, 6:259–264, 2012. 6, 43, 44
- [25] J. S. Gómez-Díaz and J. Perruisseau-Carrier. Graphene-based plasmonic switches at near infrared frequencies. *Opt. Express*, 21(13):15490–15504, Jul 2013. 6
- [26] Patrice Genevet Nanfang Yu Yi Song Jing Kong Yu Yao, Mikhail A. Kats and Federico Capasso. Broad electrical tuning of graphene-loaded plasmonic antennas. *Opt. Express*, 13(3):15490–15504, 2013. 6
- [27] M. Grande, M. A. Vincenti, T. Stomeo, G. V. Bianco, D. de Ceglia, N. Aközbe, V. Petruzzelli, G. Bruno, M. De Vittorio, M. Scalora, and A. D’Orazio. Graphene-based absorber exploiting guided mode resonances in one-dimensional gratings. *Opt. Express*, 22(25):31511–31519, Dec 2014. 6

- [28] Berardi Sensale-Rodriguez, Tian Fang, Rusen Yan, Michelle M. Kelly, Debdeep Jena, Lei Liu, and Huili (Grace) Xing. Unique prospects for graphene-based terahertz modulators. *Applied Physics Letters*, 99(11):113104, 2011. [6](#)
- [29] Daniel Rodrigo, Odeta Limaj, Davide Janner, Dordaneh Etezadi, F. Javier García de Abajo, Valerio Pruneri, and Hatice Altug. Mid-infrared plasmonic biosensing with graphene. *349(6244):165–168*, 2015. [6](#)
- [30] Andrew L. Walter Markus Ostler Aaron Bostwick Eli Rotenberg Thomas Seyller Dirk van der Marel Alexey B. Kuzmenko Iris Crassee, Julien Levallois. Giant faraday rotation in single- and multilayer graphene. *Nature Phys*, (7):48–51, 2011. [6](#), [133](#)
- [31] Toshihiko Yoshino. Theory for oblique-incidence magneto-optical faraday and kerr effects in interfaced monolayer graphene and their characteristic features. *J. Opt. Soc. Am. B*, 30(5):1085–1091, May 2013. [6](#), [133](#)
- [32] Jean-Marie Pomirol Alexey B. Kuzmenko Adrian M. Ionescu Juan R. Mosig Michele Tamagnone, Clara Moldovan and Julien Perruisseau-Carrier. Near optimal graphene terahertz non-reciprocal isolator. *Nature Communications*, 7(11216), 2016. [7](#)
- [33] Fei Gao Baile Zhang Hongsheng Chen Xiao Lin, Zuojia Wang. Atomically thin nonreciprocal optical isolation. *Scientific Reports*, 4(4190), 2014. [7](#)
- [34] J. S. Gomez-Diaz and A. Alù. Magnetically-biased graphene-based hyperbolic metasurfaces. In *2016 IEEE International Symposium on Antennas and Propagation (APSURSI)*, pages 359–360, June 2016. [8](#), [134](#), [140](#), [141](#), [142](#)



# Part I

## Theoretical and numerical tools



# Chapter 1

## Theoretical Background

*If learning the truth is the scientist's goal, then he must make himself the enemy of all that he reads.*

Ibn Al-Haytham

### Contents

---

<b>1.1</b>	<b>Fundamentals of graphene</b>	<b>16</b>
1.1.1	Electronic properties	16
1.1.2	Graphene doping	20
1.1.3	Electromagnetic properties of graphene: Conductivity Model	22
<b>1.2</b>	<b>Theory of graphene surface plasmons polaritons (SPPs)</b>	<b>28</b>
1.2.1	Surface plasmons polaritons at planar interfaces	28
1.2.2	Surface plasmons polaritons on graphene (GSP)	32
<b>1.3</b>	<b>Conclusions</b>	<b>45</b>

---

In this chapter some fundamentals on graphene physics will be given. First, we will present a brief overview of the electronic properties of graphene including the lattice and the electronic configuration resulting from that lattice. After that, we will review the basic properties of the optical conductivity of graphene and introduce the fundamental concepts of plasmonics. These concepts will be used to investigate the electromagnetic behavior of the surface plasmons polaritons guided by the graphene and outline their properties

## 1.1 Fundamentals of graphene

### 1.1.1 Electronic properties

In this section, The electronic properties of graphene will be presented. First, we describe the crystal structure of graphene and the graphene carbon bonding. We then apply these concepts to derive the electronic band structure of graphene by using the tight binding model and explain the relativistic behavior of the charge carriers near the Dirac point.

## Crystal structure

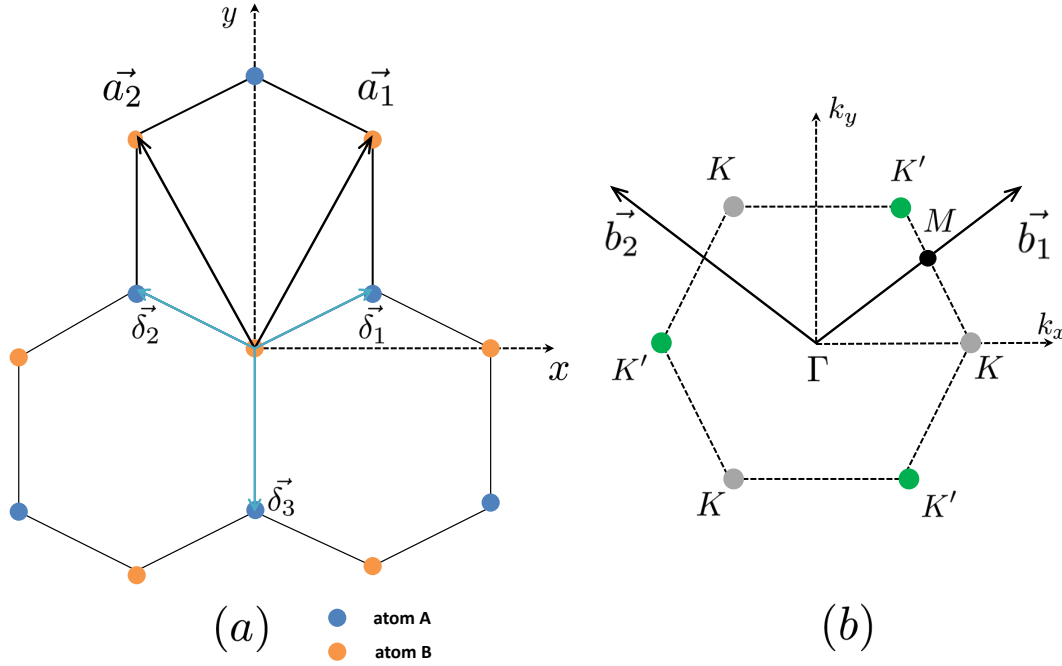


Figure 1.1: (a) Graphene honeycomb lattice, made out of hexagonal primitive cells.  $\vec{a}_1$  and  $\vec{a}_2$  are lattice unit vectors and  $\vec{\delta}_1, \vec{\delta}_2$  and  $\vec{\delta}_3$ , are the closest neighbours vectors (b) Brillouin zone: reciprocal lattice of graphene with reciprocal lattice vectors  $\vec{b}_1$  and  $\vec{b}_2$ .  $\Gamma$ ,  $M$ ,  $K$  and  $K'$  are the high symmetry points in the reciprocal space

Graphene is a single two dimensional sheet made up of carbon atoms arranged on a honeycomb lattice. This structure can be thought of as a hexagonal Bravais lattice with two carbon atoms per unit cell represented as A and B in figure 1.1. The direct lattice vectors of the hexagonal Bravais lattice are given as:

$$\vec{a}_1 = \frac{a}{2} (\sqrt{3}, 3) \quad \vec{a}_2 = \frac{a}{2} (-\sqrt{3}, 3) \quad (1.1)$$

With  $a = 1.42\text{\AA}$  is the interatomic distance and the nearest neighboring atoms are represented by the vectors :

$$\vec{\delta}_1 = \frac{a}{2} (\sqrt{3}, 1), \quad \vec{\delta}_2 = \frac{a}{2} (-\sqrt{3}, 1) \quad \text{and} \quad \vec{\delta}_3 = \frac{a}{2} (0, -1) \quad (1.2)$$

The reciprocal lattice of graphene has also a hexagonal lattice but rotated  $90^\circ$  with respect to the direct lattice (see figure 1.1). The reciprocal basis vectors can be expressed as :

$$\vec{b}_1 = \frac{2\pi}{3a} (\sqrt{3}, 1) \quad \vec{b}_2 = \frac{2\pi}{3a} (-\sqrt{3}, 1) \quad (1.3)$$

As shown in Figure 1.1 (b) the first Brillouin zone (BZ) of the reciprocal lattice has a hexagonal shape. The six points of the corners of this zone are called the Dirac points. Every second corner is equivalent, because they differ only by the addition or subtraction of a basic vector. Only two points  $K = (2\pi/3a, 2\pi/3\sqrt{3}a)$  and  $K' = (2\pi/3a, -2\pi/3\sqrt{3}a)$  of these points are inequivalent.

The high symmetry points are also presented in figure 1.1 (b). These points are  $\Gamma$  at the center,  $M$  the center of an edge and inequivalent hexagonal corners  $K$  et  $K'$  of the Brillouin zone. The position of the  $M$  and  $K$  can be given by:

$$\Gamma\vec{M} = \frac{2\pi}{a} (\sqrt{3}, 0) \quad \Gamma\vec{K} = \frac{2\pi}{a} (1/\sqrt{3}, 3) \quad (1.4)$$

### Carbon bonds in graphene

The carbon atom, the unique and principal constituent of graphene, has four valence electrons with an atomic configuration  $2s^2 2p^2$ . In the crystalline phase, these four valence electrons give rise to four valence orbitals ( $2s, 2p_x, 2p_y, 2p_z$ ), which can be mixed in many different ways in  $sp^n, n = 1, 2, 3$  hybridizations to form a variety of carbon materials with different bonding configurations. In graphene, the valence orbitals ( $2s, 2p_x, 2p_y$ ) mix to produce three identical  $sp^2$  hybrid orbitals, which form  $120^\circ$  angles in the plane of graphene (see Figure 1.2). These  $sp^2$  orbitals form three strong, covalent  $\sigma$  bonds in the  $xy$  plane as shown in Figure 1.3. These bonds are responsible for the rigidity and the mechanical stability of graphene. However, since the  $\sigma$  band in graphene is completely filled, its electrons do not contribute to the electronic properties of graphene. Around the Fermi energy, the remaining  $p_z$ -orbitals, which have a small overlap, give rise to weak delocalized covalent  $\pi$  bonds. It is this bonding that are responsible for the electronic transport and optical properties of graphene. That is why, in the next section, in order to calculate the electronic band structure of graphene, we will adopt the tight binding method to model only the  $\pi$  band.

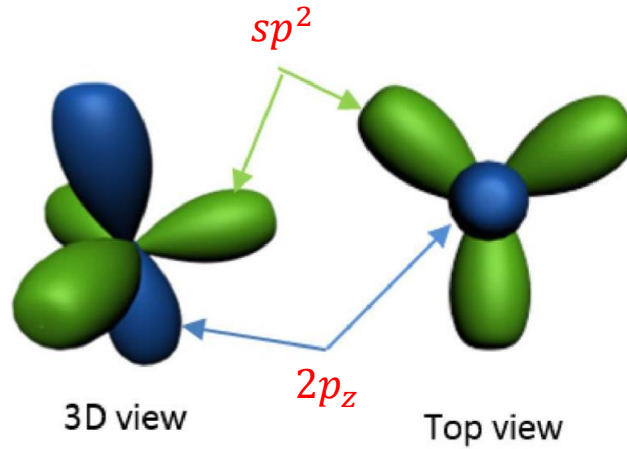


Figure 1.2: Graphical representation of the  $sp^2$  and  $sp_z$  orbitals in graphene. Adapted from [1]

### The electronic Band Structure: Tight binding model

In the present section, we will use the tight-binding approximation to derive the electronic dispersion relation of graphene. According to work done by Wallace [2], this method provides a good description of the band structure of graphene, where the overlap of the  $2p_z$  orbitals is small. In this model and using the Bloch theorem, the wave function of the electron in graphene is described as a linear combination of the  $2p_z$  orbitals and can be written as the superposition of the orbitals of the carbon atoms A and B:

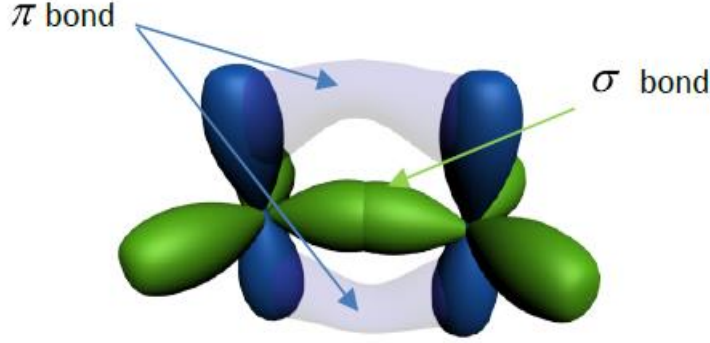


Figure 1.3:  $\sigma$  and  $\pi$  bonds in graphene. For forming the graphene's honeycomb lattice, each  $sp^2$  orbital overlaps with an  $sp^2$  orbital of a neighboring atom to create a  $\sigma$  bond, while the remaining  $p_z$  orbitals give rise to a  $\pi$  bond. Adapted from [1]

$$\Psi(\vec{k}, \vec{r}) = C_A(\vec{k})\Phi_A(\vec{k}, \vec{r}) + C_B(\vec{k})\Phi_B(\vec{k}, \vec{r}) \quad (1.5)$$

where  $\Phi_A(\vec{k}, \vec{r})$  and  $\Phi_B(\vec{k}, \vec{r})$  are the Bloch wave functions given by:

$$\Phi_j(\vec{k}, \vec{r}) = \frac{1}{\sqrt{N}} \sum_{\vec{R}_j} e^{i\vec{k}\vec{R}_j} \phi(\vec{r} - \vec{R}_j) \quad (j = A \text{ or } B) \quad (1.6)$$

$\vec{R}_A$  and  $\vec{R}_B$  are the vectors position of  $A$  and  $B$  sites, respectively and  $\phi(\vec{r})$  is the wave function of the  $2p_z$  orbital. The energy states are determined by solving the shrodinger equation:

$$\widehat{H}\Psi = E(\vec{k})\Psi \quad (1.7)$$

with  $\widehat{H}$  being the Hamiltonian of the crystal. By inserting electron wave function to Eq 1.7 and integrating over the entire lattice, we obtain the following two equations:

$$\begin{aligned} H_{AA}C_A + H_{AB}C_B &= ESC_A \\ H_{BA}C_A + H_{BB}C_B &= ESC_B \end{aligned} \quad (1.8)$$

Here  $H_{jj'} = \langle \Phi | H | \Psi \rangle$  ( $j, j' = A, B$ ) and  $S = \langle \Phi | \Psi \rangle$  are the transfer integral and the overlap integral matrices, respectively. The entire problem can be reduced to a eigenvalue problem and equation 1.8 can be written as:

$$\begin{pmatrix} H_{AA}(\vec{k}) & H_{AB}(\vec{k}) \\ H_{BA}(\vec{k}) & H_{BB}(\vec{k}) \end{pmatrix} \begin{pmatrix} C_A(\vec{k}) \\ C_B(\vec{k}) \end{pmatrix} = E(\vec{k})S \begin{pmatrix} 1 & 0 \\ 0 & 1 \end{pmatrix} \begin{pmatrix} C_A(\vec{k}) \\ C_B(\vec{k}) \end{pmatrix} \quad (1.9)$$

the energy eigenvalues are therefore obtained by solving :

$$\det(H - ES) = 0 \quad (1.10)$$

which gives the electron band structure of graphene as:

$$E \pm(k_x, k_y) = \pm\gamma\sqrt{3 + f(k_x, k_y)} \quad (1.11)$$

$$f(k_x, k_y) = 2\cos(\sqrt{3}ak_y) + 4\cos\left(\frac{\sqrt{3}}{2}ak_y\right)\cos\left(\frac{3}{2}ak_x\right) \quad (1.12)$$

where  $\gamma = 2.8eV$  refers to the nearest neighbor hopping energy [3]. A (+) sign corresponds to the conduction ( $\pi$ ) band and a (-) sign to the valence ( $\pi^*$ ) band. The electronic dispersion relation of Eq 1.12 is shown in Figure 1.4. We can see two symmetrical energy bands around energy 0. The upper one is the conduction band and the lower is the valence band. These two bands meet at six distinct points in the Brillouin zone and create the zero band gap. As pointed out above, due to the symmetry, only two points ( $K, K'$ ) are inequivalent and are called Dirac points. Since there are two  $\pi$  electron per unit cell (for intrinsic graphene) and taking into account spin degeneracy, the valence band is completely filled and the conduction band is completely empty. This means that graphene can be seen as a zero gap semiconductor (the density of electronic states (DOS) is zero at Fermi level) or even as a semi metal.

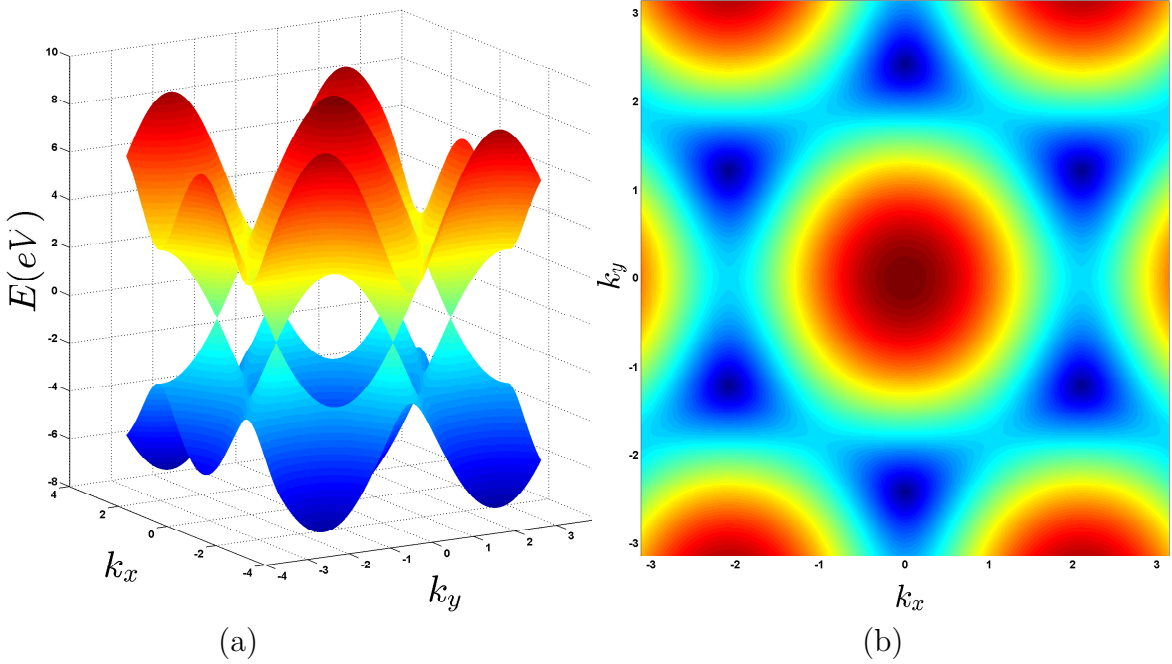


Figure 1.4: Electronic band structure of graphene calculated by using the tight binding model for the whole first Brillouin zone. (a) The electronic energy dispersion of graphene: Valence and conduction band are symmetrical around  $E = 0$  and touch each other in six points in the Brillouin zone, which are called Dirac points. (b) Projected color plot of the conduction band

### Band structure close to the $K$ and $K'$ points

As mentioned above, the two bands touch at Dirac points  $K$  and  $K'$ . Near these points and with a simple Taylor development, the electronic relation dispersion is approximated by the linear symmetric Dirac cone equation:

$$E(\vec{k}) = \pm\hbar v_f |\delta\vec{k}| \quad (1.13)$$

where  $\vec{k} = \vec{K} + \delta\vec{k}$  with  $|\delta\vec{k}| \ll |\vec{K}|$  and  $\delta\vec{k}$  is the 2D wave vector measured from Dirac point.  $v_f$  denotes the Fermi velocity defined by  $v_f = \frac{3a\gamma}{2\hbar} \simeq 10^6 \text{ms}^{-1}$ .

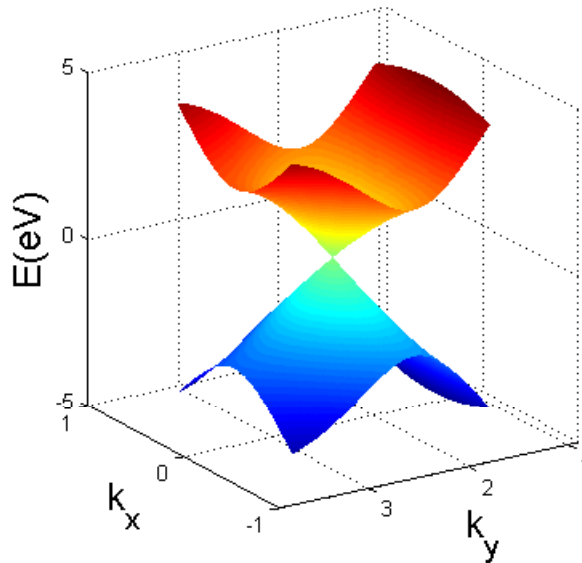


Figure 1.5: Dirac cones at K point

Unlike conventional 2D materials, which have a quadratic dispersion relation, the electron dispersion relation in graphene shows linear behavior and is independent of the electron mass and energy. This relation is similar to the dispersion of relativistic particles with vanishing mass like photons in free space. In other words, electrons in graphene near the Dirac points behave like ultra-relativistic massless Dirac Fermions and follow the 2D Dirac equation. This unique band structure in graphene leads to important properties such as high electron mobility that can reach up to  $200000 \text{cm}^2 \text{V}^{-1} \text{s}^{-1}$  [4], high thermal conductivity [5] and broadband transparency. One of the most important consequences of this unique energy spectrum is the tunability of its properties stemming from the dependence of its optical conductivity on the chemical potential which can be varied by applying a backgate voltage on the graphene. Another interesting consequence of this band structure is the ability to provide unusual conductivity with negative imaginary part induced by the dominance of the interband transitions. This leads as we will investigate below to exotic effects such as the appearance of a new plasmon mode in TE polarization.

### 1.1.2 Graphene doping

We have pointed out in the previous section that, one of the important consequences of the unusual electronic band structure of graphene is the tunability. Indeed, the chemical potential (Fermi Level) that defines the density of charge carriers and thus the conductivity of graphene can be controlled by doping. For pristine graphene, the Fermi Level is located at the Dirac point. This means that the conduction band is completely filled while the valence band is fully empty. When a doping is applied, the Fermi level can be moved up or down and then some holes (electrons) can be created in the valence (conduction) band (see figure 1.6). The common methods used to modify the Fermi level on graphene are namely chemical doping and electrostatic doping (electric field effect). The chemical doping consists of adding other atoms,

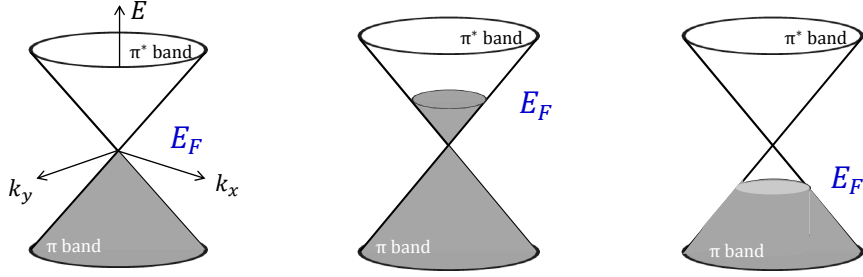


Figure 1.6: Variation of Fermi level in graphene as a function of doping: Band structure of pristine graphene ( $E_F = 0$  eV), n-doping ( $E_F > 0$ ) and p-doping ( $E_F < 0$ ), respectively.

known as adatoms, which will become either donor dopant or acceptor dopant. The created carriers are then free to move and will participate in the conduction. For graphene, many molecules and adsorbant atoms have been used to modify the doping concentration such as *Bi, Sb, Au, H<sub>2</sub>O, NH<sub>3</sub>, NO<sub>2</sub>, F4 – TCNQ*.... [6].

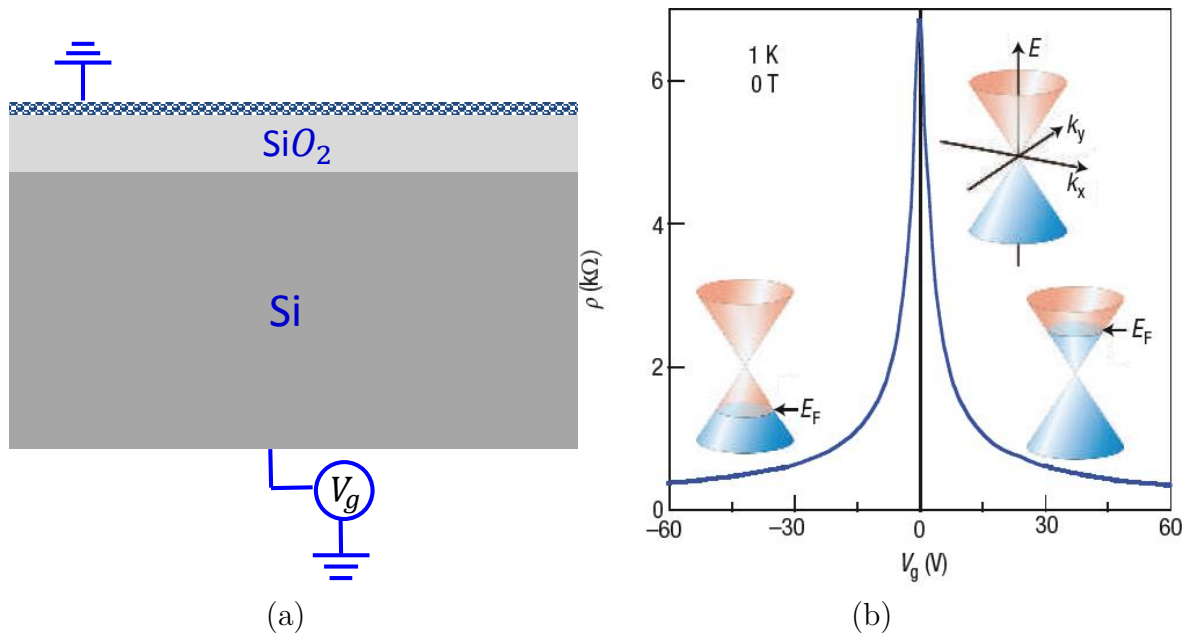


Figure 1.7: (a) Electrostatic doping device. (b) Variation of resistivity plotted as a function of gate voltage  $V_g$  (Adapted from [7]).

The second method: the electrostatic doping has usually been explored to control the electronic and magnetic properties of graphene. This method allows to modify the charge density and consequently the chemical potential without increasing the level of disorders and defects in graphene [8, 9]. It is based essentially on applying of a potential difference between two terminals to induce capacitance in a device (which usually behave as a parallel-plate capacitor). The basic device used to achieve electrostatic doping in graphene is shown in figure 1.7 (a). It consists of a graphene sheet deposited on an insulating layer of silicon dioxide ( $SiO_2$ ) that act as a dielectric spacer. The whole structure is deposited on a heavily doped silicon substrate serving as back gate. Applying a gate voltage  $V_g$  between the graphene and the back gate induces a surface charge density which can be given as follows:

$$n = \frac{\varepsilon_0 \varepsilon_r}{te} V_g = \alpha V_g \quad (1.14)$$

Such that  $\varepsilon_r$  is the permittivity of the  $SiO_2$  layer that is set here to be equal to 3.9,  $t$  is its thickness and  $e$  being the electron charge. One can clearly see from this equation that changing the gate voltage leads to directly modify the charge carrier density in graphene and then its Fermi level which can be calculated through the relation  $\mu_c = \hbar v_f \sqrt{\pi n}$ . Figure 1.7 (b) displays the behaviour of graphene resistivity as a function of gate voltage for a graphene device on Si/290nm. For pristine graphene, The Fermi level is located at the Dirac point where the density of states vanishes. This point corresponds to a peak of resistivity for  $V_g = 0$  V. When, the Fermi level is shifted away from the Dirac point by varying the back gate voltage, the resistivity decreases with the increase of gate voltage.

### 1.1.3 Electromagnetic properties of graphene: Conductivity Model

In this section, we are going to describe the Magneto-optical Conductivity Model of graphene in its most general form, which we will use to study interactions of electromagnetic waves with graphene. The graphene Conductivity will also be used in the next section to derive the dispersion relation of the surface plasmons polariton on graphene and in chapter 5, to study the surface magnetoplasmons under the presence of a static magnetic field.

Due to its gapless electronic band structure and its monoatomic thickness, the electromagnetic properties of graphene can be characterized by its surface conductivity. In the general case and when a uniform static magnetic field is applied perpendicularly to the graphene sheet, graphene becomes anisotropic with an asymmetric  $2 \times 2$  conductivity tensor of the form:

$$\sigma = \begin{pmatrix} \sigma_{xx} & \sigma_{xy} \\ \sigma_{yx} & \sigma_{yy} \end{pmatrix} = \begin{pmatrix} \sigma_L & \sigma_H \\ -\sigma_H & \sigma_L \end{pmatrix} \quad (1.15)$$

Where  $\sigma_L$  and  $\sigma_H$  are the longitudinal and Hall conductivities of the graphene, respectively. For typical magnetic fields  $B \leq 15$ T when the Zeeman effect is negligible, these conductivities can be obtained through a quantum mechanical analysis using the equation of motion approach (EOM) [10]:

$$\sigma_{L(H)}(\omega) = \frac{e^2}{h} \sum_{n \neq m} \frac{\Lambda_{nm}^{L(H)}}{iE_{nm}} \frac{n_F(E_n) - n_F(E_m)}{\hbar\omega + E_{nm} + i\Gamma} \quad (1.16)$$

with  $e$  being the charge of the electron,  $h$  is the Planck constant,  $\Gamma$  is a phenomenological scattering rate which represents the loss mechanisms in graphene,  $n_F(E_n) = 1/(1 + \exp((E_n - \mu_c)/k_B T))$  is the Fermi-Dirac distribution where  $\mu_c$  is the chemical potential,  $k_B$  is the Boltzmann constant and  $T$  is the temperature.  $E_{nm} = E_n - E_m$  stands for the Landau Level (LL) energy transition with  $E_n = \text{sign}(n)(\hbar v_f/l_B)\sqrt{2|n|}$  is the energy of the  $n$ -th LL,  $n = 0, \pm 1, \pm 2, \dots$ ,  $l_B = \sqrt{\hbar/(eB)}$  denoting the magnetic length and  $v_f = 10^6 \text{ms}^{-1}$  is the Fermi velocity. By using the selection rule of LLs transition, the longitudinal and Hall transition matrix elements can be respectively given by:

$$\Lambda_{nm}^L = \frac{\hbar^2 v_f^2}{l_B^2} (1 + \delta_{m,0} + \delta_{n,0}) \delta_{|m|-|n|,\pm 1} \quad (1.17)$$

$$\Lambda_{nm}^H = i\Lambda_{nm}^L (\delta_{|m|,|n|-1} - \delta_{|m|-1,|n|}) \quad (1.18)$$

It is of fundamental importance to notice that, in graphene, light/ matter interaction

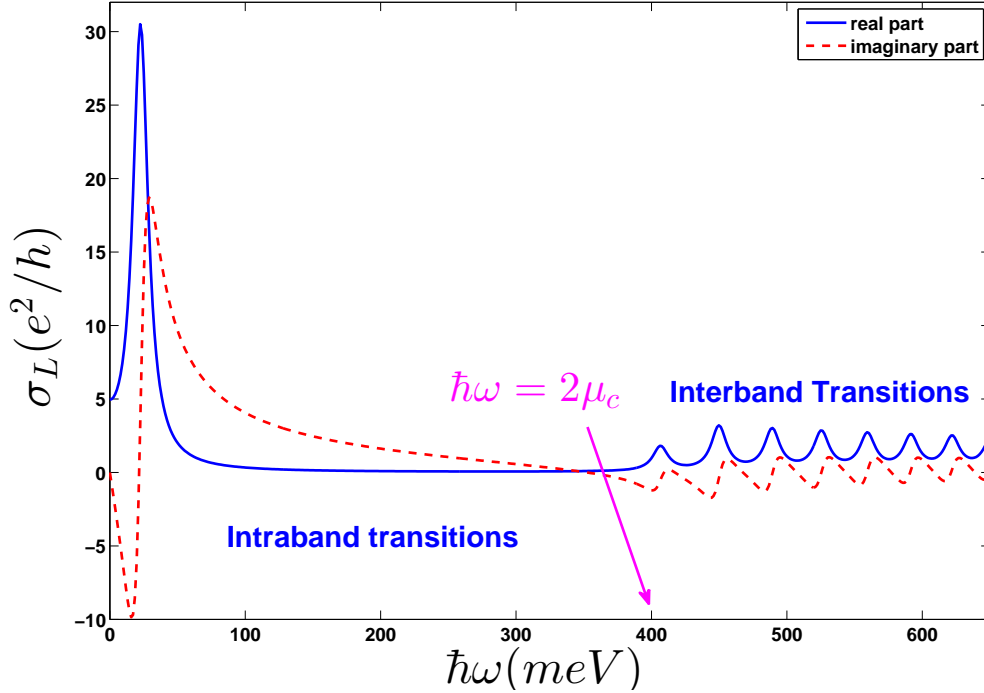


Figure 1.8: Real and imaginary parts of the longitudinal magneto-optical conductivity  $\sigma_L$  as a function of photon energy computed using the full quantum model for  $B = 7T$ ,  $\mu_c = 0.2$  eV,  $T = 17K$  and  $\Gamma = 6.8\text{meV}$

involves two main transition mechanisms which explain its magneto-optical response: the first being the interband contribution and the second is the intraband contribution. For doped graphene, the intraband transitions occur within the same band and dominate at low photon frequencies i.e for photon energies below the interband threshold. While, the interband transitions, connecting LLs in the valence and conduction bands, arise at frequencies close or above the interband threshold. Hence, the graphene magneto-optical conductivity can be written as the sum of these two contributions Figure 1.8 shows the real (blue) and imaginary (red) parts of the longitudinal component of the magneto optical conductivity of graphene computed from equation 1.16 for  $B = 7$  T,  $\mu_c = 0.2$  eV,  $T = 17$  K and  $\Gamma = 6.8\text{meV}$ . One can see that the conductivity of graphene presents a set of absorption peaks. At low frequencies, we can observe a peak which is called intraband peak and as its name indicates is due to the intraband transition. While, the remaining absorption peaks occurring at high frequencies specifically above the intraband threshold ( $\omega = 2\mu_c/\hbar$ ) correspond to the different allowed LLs interband transitions.

It can be seen from equation 1.16, that the components of the conductivity tensor depend significantly on the frequency, magnetic field and chemical potential. Based to the strength of the applied magnetic field and the doping of the graphene in question,

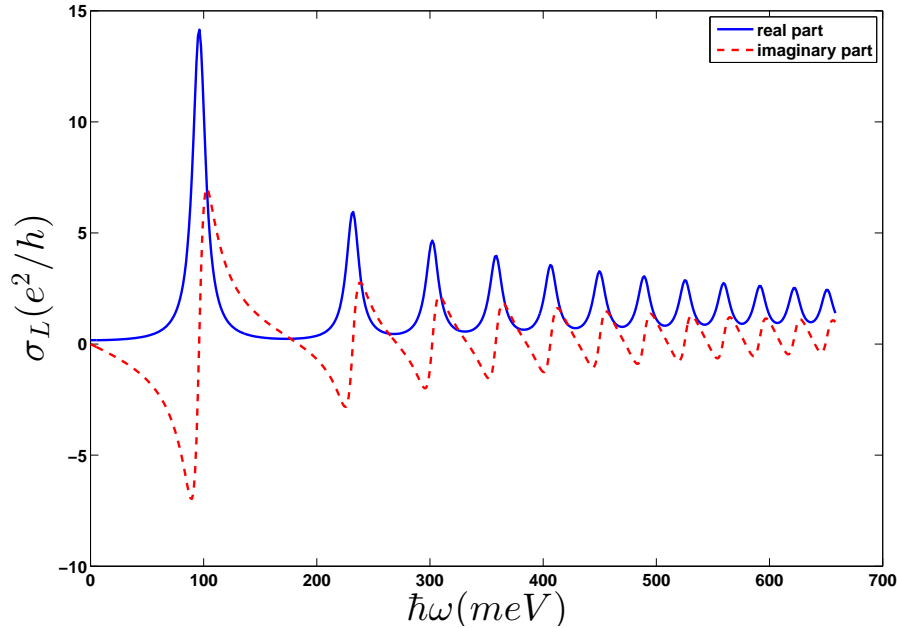


Figure 1.9: Real and imaginary part of the longitudinal magneto-optical conductivity  $\sigma_L$  in units of  $e^2/h$  as a function of photon energy computed using the full quantum model for  $\mu_c = 0\text{eV}$ . The Other parameters are the same as in figure 1.8 (Quantum Hall regime)

we can explore two different regimes that characterize the magneto-optical response of graphene:(i) the semiclassical regime, given by low fields and/or high electronic density and (ii) the quantum hall regime of strong fields and /or low electronic density.

For lowly doped graphene where no intraband transitions can take place, the magneto-optical conductivity is fully described by interband transitions and graphene is in the quantum Hall regime. Whereas, in the limit of no interband transition and for high doping i.e  $\mu_c \gg \hbar\omega$  and  $\mu_c \gg k_B T$ , graphene is in the semiclassical regime and its conductivity is dominated by the intraband contributions. In this case, the general quantum mechanical conductivity reduces to the semiclassical Drude model form [10]:

$$\sigma_L = \frac{e^2 \tau \mu_c}{\hbar^2 \pi} \frac{1 - i\omega\tau}{(1 - i\omega\tau)^2 + (\tau\omega_c)^2} \quad (1.19)$$

$$\sigma_H = -\frac{e^2 \tau \mu_c}{\hbar^2 \pi} \frac{\tau\omega_c}{(1 - i\omega\tau)^2 + (\tau\omega_c)^2} \quad (1.20)$$

Such that  $\tau = 1/\Gamma$  being the relaxation time and  $\omega_c = eBv_f^2/\mu_c$  is the graphene's cyclotron frequency.

Figure 1.9 depicts the longitudinal conductivity of graphene in units of  $e^2/h$  versus the photon energy in the absence of gate voltage when the chemical potential is equal to zero ( $\mu_c = 0\text{eV}$ ). Similar to figure 1.8, a sequence of absorption peaks are observed. However, in this case, there is no intraband contribution and only interband transitions are allowed. it can be also seen that the conductivity never vanishes even for very low chemical potential  $\mu_c = 0\text{eV}$ .

An example of the longitudinal conductivity of graphene in the semiclassical regime using equation 1.20 is shown in figure 1.10 where the semi classical result is plotted with solid line and the full quantum solution with the dashed line. We can clearly observe an excellent agreement between the two Models.

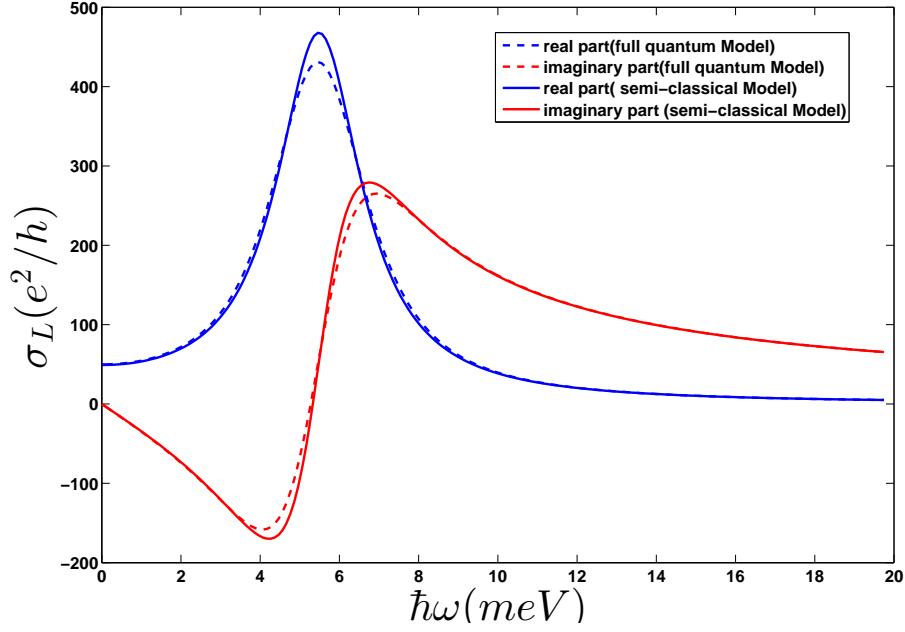


Figure 1.10: Real and imaginary parts of the longitudinal magneto-optical conductivity  $\sigma_L$  in units of  $e^2/h$  as a function of photon energy for  $B = 5$  T,  $\mu_c = 0.6$  eV,  $T = 17$  K and  $\Gamma = 1.3$  meV. The solid lines represent the semiclassical model and the dashed lines represent the full quantum results.

Let us now consider the limiting case when the magnetic field is low ( $B \rightarrow 0$ ). In this limit, the Landau levels become dense and very close to each other. Therefore, these discrete levels turn out to a continuum and then the series shown in equation 1.16 converge into integrals, which yields:

$$\sigma_L(\omega, \mu_c, \Gamma) = \frac{-i\sigma_0(\omega + 2i\Gamma)}{\pi} \times \left( \frac{1}{(\omega + 2i\Gamma)^2} \int_0^\infty \varepsilon \left( \frac{\partial n_F(\varepsilon)}{\partial \varepsilon} - \frac{\partial n_F(-\varepsilon)}{\partial \varepsilon} \right) d\varepsilon - \int_0^\infty \frac{n_F(-\varepsilon) - n_F(\varepsilon)}{(\omega + 2i\Gamma)^2 - 4(\varepsilon/\hbar)^2} d\varepsilon \right) \quad (1.21)$$

and

$$\sigma_H(\omega, \mu_c, B_0, \Gamma) = \frac{-\sigma_0 v_f^2 e B_0}{\pi} \left( \frac{1}{(\omega + 2i\Gamma)^2} \int_0^\infty \left( \frac{\partial n_F(\varepsilon)}{\partial \varepsilon} + \frac{\partial n_F(-\varepsilon)}{\partial \varepsilon} \right) d\varepsilon + \int_0^\infty \frac{1}{(\omega - 2i\Gamma)^2 + 4(\varepsilon/\hbar)^2} d\varepsilon \right) \quad (1.22)$$

where  $\sigma_0 = e^2/(4\hbar)$  is called the universal conductivity of graphene [11].

At zero magnetic field ( $B = 0$ ) (which is the case of our studies in the second part of the thesis), the Hall conductivity vanishes and graphene can be considered to be isotropic. In this situation, the conductivity is given by its longitudinal component and as shown in equation 1.21 is independent on the magnetic field [12, 13, 14].

The first term in 1.21 corresponds to the intraband contributions and it can be analytically evaluated as:

$$\sigma_{intra} = \frac{i8\sigma_0 k_B T}{\pi(\hbar\omega + i\hbar\gamma)} \ln \left( 2 \cosh\left(\frac{\mu_c}{2k_B T}\right) \right) \quad (1.23)$$

In general, the second term which is due to the interband contributions cannot be evaluated analytically. However, it can be put into a more appropriate form for numerical calculations as follows:

$$\sigma_{inter} = \sigma_0 \left( \mathcal{G}\left(\frac{\hbar\omega}{2}\right) + \frac{i4\hbar\omega}{\pi} \int_0^\infty \frac{\mathcal{G}(\varepsilon) - \mathcal{G}\left(\frac{\hbar\omega}{2}\right)}{(\hbar\omega)^2 - 4\varepsilon^2} d\varepsilon \right) \quad (1.24)$$

With  $\mathcal{G}(x) = \frac{\sinh(x/k_B T)}{\cosh(\mu_c/k_B T) + \cosh(x/k_B T)}$ .

At low temperatures when the conditions ( $k_B T \ll |\mu_c|, \hbar\omega$ ) are fulfilled, the intraband conductivity follows the usual Drude form that describes the collective behavior of free electron :

$$\sigma_{intra} = \sigma_D = \frac{i4\sigma_0 \mu_c}{\pi(\hbar\omega + i\hbar\gamma)} \quad (1.25)$$

In this limit, the interband term can be approximated as [12]

$$\sigma_{inter} = \sigma_0 \left( \theta(\omega - 2\mu_c) - \frac{i}{\pi} \ln \left| \frac{\omega + 2\mu_c}{\omega - 2\mu_c} \right| \right) \quad (1.26)$$

where  $\theta$  denotes the Heaviside step function presenting the condition necessary for interband electron transitions at low temperatures.

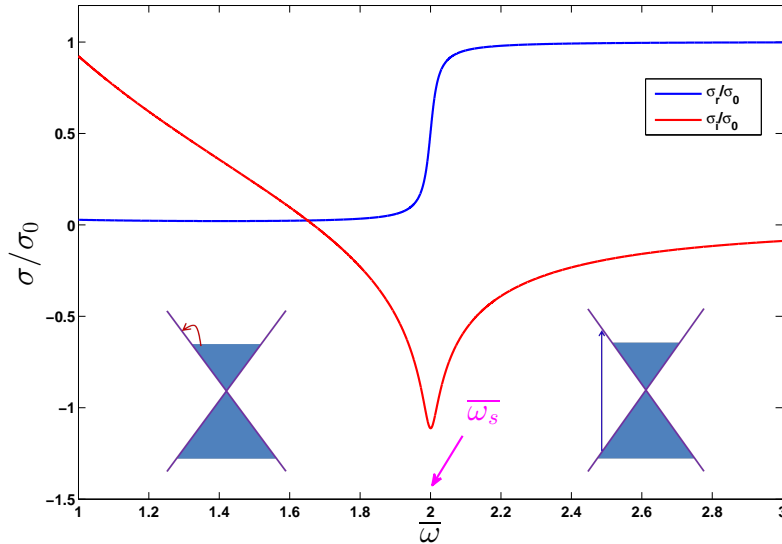


Figure 1.11: the real (blue line) and the imaginary (red line) part of the graphene conductivity in units of  $\sigma_0$  versus dimensionless frequency  $\bar{\omega} = \hbar\omega/\mu_c$  for  $B = 0T$   $T = 10K$ ,  $\mu_c = 0.2eV$  et  $\gamma = 3.3$  meV

The isotropic total, intraband and interband conductivities, when the magnetic field vanishes, are respectively represented in figures 1.11 and 1.12. The conductivity is normalized to the universal conductivity  $\sigma_0$ , while the frequency is normalized to

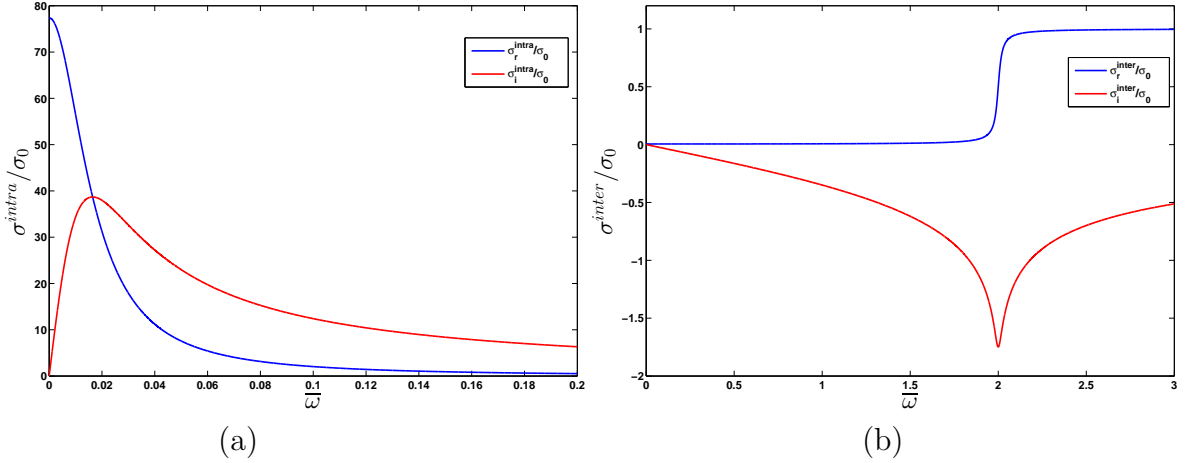


Figure 1.12: Real and imaginary parts of (a) the intraband conductivity and (b) the interband conductivity calculated at zero magnetic field.

$\omega_n = \mu_c/\hbar$ . As the anisotropic case, one can see that the total conductivity as well as the interband part show a threshold frequency in  $\bar{\omega}_s = \hbar\omega/\mu_c = 2$ , it is the threshold for interband transitions which marks the limit between two transitions regions: (i) Drude (intraband transitions) region and (ii) interband transitions region) which corresponds to the onset of the interband transitions in graphene. Indeed, at low frequencies i.e. for frequencies below  $\bar{\omega}_s$  the conductivity is governed by its intraband contributions described by the Drude conductivity. Within this region of the spectrum, typically from the Terahertz to the far infrared region, the imaginary part of the conductivity is positive. In the vicinity of the threshold frequency, the real part which determines the optical loss in graphene, shows a step and it increases drastically towards the universal value, while the imaginary part changes sign to become minimal and negative. For photon frequencies above the threshold frequency  $\bar{\omega} \gg \bar{\omega}_s$ , where the interband transitions are dominant, the real part remains equal to  $\sigma_0$  and the imaginary part is still negative but it is almost equal to zero. It is for this reason that, within the near infrared and visible region, the graphene monolayer is considered to be a transparent material. It transmits almost all visible light and absorbs only  $\pi\alpha = 2.3\%$  of the incident light ( $\alpha$  being the fine-structure constant) [11, 15]. The imaginary part, as we will see in the next section, plays a crucial role for describing the characteristics of surface plasmons on graphene as well as their conditions of existence. It is also important to notice that throughout this thesis we are interested in structures in the range of frequencies lying in the far-infrared and terahertz bands where the conductivity is well represented by the Drude conductivity. Having presented the general electronic properties of graphene and described the magneto-optical conductivity model, we now turn to study the surface plasmons on graphene.

## 1.2 Theory of graphene surface plasmons polaritons (SPPs)

In the previous section of this chapter, we have shown that the optical response of graphene under the influence of external electromagnetic fields is characterized by its optical surface conductivity described within a quantum approach based on the EOM method. In the isotropic case when  $B = 0$ , this model will be used in this section to

study the surface plasmons polaritons propagating along a single graphene monolayer and to explain some of their properties. Specifically we are interested in deriving their dispersion relation which relates the frequency of (SPPs) to its wave vector. However, before going into the details of graphene (SPPs), we need to provide a brief review on the fundamentals of plasmonics. In particular, we focus on the properties of the (SPPs) propagating at metal-dielectric interfaces .

## 1.2.1 Surface plasmons polaritons at planar interfaces

### Drude Model of a Metal: Plasmons and Surface Plasmons

Noble metals play an important role in the field of plasmonics and they can be considered as the building blocks for several plasmonic structures. Their optical response characterized by their electric permittivity can be well described by the Drude Model (proposed by Paul Drude in 1900 [16]). In this Model, the metal is considered to be as a gas made up of free conduction electrons moving against a fixed background of positively charged ions: a dense gas of charged particles called plasma. Collective oscillations of this plasma can propagate in the volume of the metal forming the so called plasma oscillation (see figure 1.13(a)). The quantum of plasma oscillations is called *plasmon* and its energy is given by  $\hbar\omega_p$  where  $\omega_p$  is the plasma frequency:

$$\omega_p = \sqrt{\frac{N_e e^2}{\varepsilon_0 m_e}} \quad (1.27)$$

$N_e$  is the electron density,  $e$  the elementary charge,  $\varepsilon_0$  the permittivity of the vacuum and  $m_e$  the electron free mass.

This model is based on the kinetic theory of electrons in a metal which assumes that the microscopic behaviour of electrons may be treated within a classical approach and only simple collisions of electrons with the ionic lattice are allowed. As a consequence, the dielectric permittivity can be written as:

$$\varepsilon_{Drude}(\omega) = 1 - \frac{\omega_p^2}{\omega(\omega + i\gamma)} \quad (1.28)$$

where  $\gamma$  is a damping constant that takes into account the electrons scattering inside the metal.

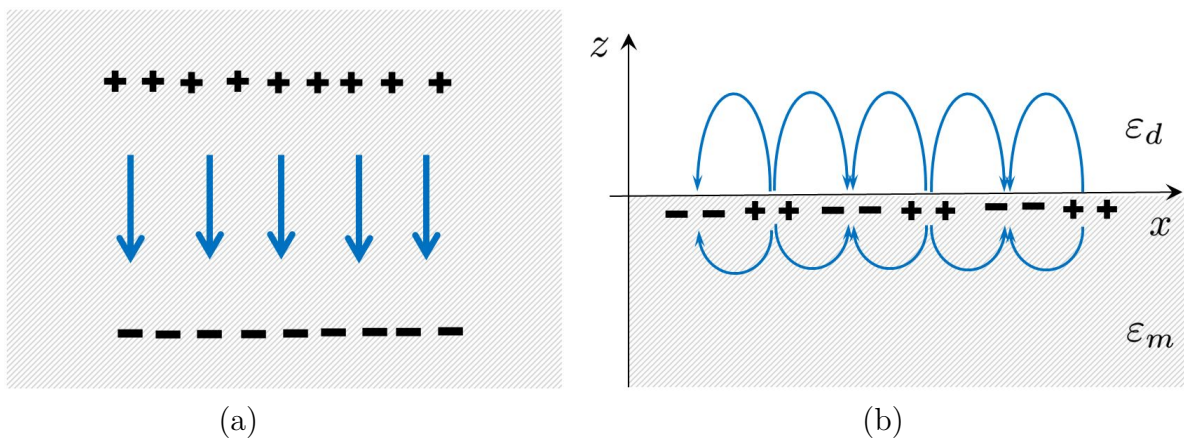


Figure 1.13: Schematic illustration of electronic charge density oscillations of (a) a bulk plasmon in a Metal (b) a surface plasmon at the interface between a dielectric and a metal

There are two kinds of plasmons: the first one is *the bulk or volume plasmon* which corresponds to the oscillation of three-dimensional (3D) electron gas occurring inside the metal. When the Metal is not infinite but limited by a surface, a second kind of plasmons is allowed: *surface plasmons*: the surface waves propagating at the interface between a metal and a dielectric. These collective oscillations can couple to light, creating hybrid modes which are referred to as *Surface Plasmons Polaritons (SPPs)*. The illustration of both bulk plasmons and surface plasmons are shown on Figure 1.13. Let us underline that, for the work presented within this thesis, we are only interested in the SPP modes.

### Existence conditions and dispersion relation

SPPs are surface modes that arise as special solutions of Maxwell's equations. In order to understand their physical properties and discuss their existence conditions, we have to apply these equations to the flat interface between a metal and a dielectric and obtain the field profile and the dispersion relation. Let us consider a planar interface separating two semi infinite, homogeneous and isotropic media. One medium is a metal characterized by its permittivity  $\varepsilon(\omega)$  given by the Drude Model stated above ( $z < 0$ ). The other medium is a dielectric with dielectric constant  $\varepsilon_d$  at  $z > 0$ . Figure 1.14 depicts a schematic representation of the structure under study. The interface between the two media is located in the  $xoy$  plane (infinite along  $y$ ) and the  $z$  axis is assumed to be perpendicular to it. In this geometry, we assume that the SPP wave propagates along the  $x$  direction with a wavevector  $k_{sp}$  and there is no variation in the  $y$  direction ( $\partial_y = 0$ ).

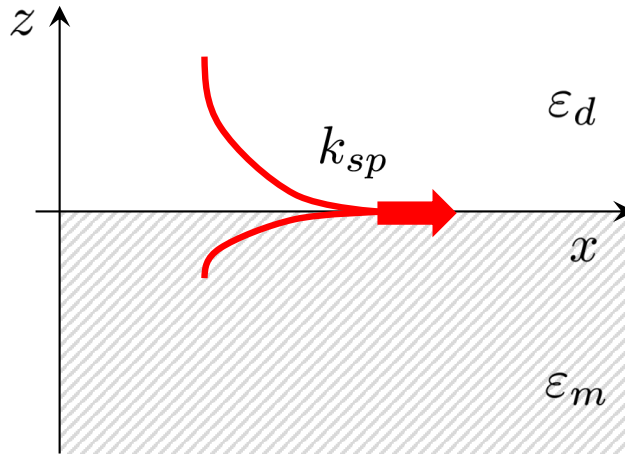


Figure 1.14: Schematic description of a SPP propagating along a metal dielectric interface.

Assuming a harmonic form of Maxwell's equations and adopting the temporal convention  $e^{-i\omega t}$ , the  $y$  component of the electric (TE) and magnetic (TM) fields can take the form:  $u(x, z) = U(z)e^{i\alpha x}$ . In each medium, the field  $u(x, z)$  satisfies the following Helmholtz equation:

$$\Delta u + k_0^2 \varepsilon_p u = 0 \quad (1.29)$$

Here  $\varepsilon_p$  is the permittivity in each medium ( $p = d, m$ ) and  $k_0 = \omega/c$  is the wave vector of the propagating wave in vacuum. We will now distinguish the two sets of

polarization modes of the electromagnetic field, The TM (transverse magnetic or p-polarized) mode corresponding to a magnetic field perpendicular to the incidence plane and TE(transverse electric or s-polarized) mode corresponding to a magnetic field lying in the plane of incidence. In the case of TM polarization, only the  $E_x, E_z$  and  $H_y$  will be non-zero,  $u(x, z) = H_y(x, z)$  and the equation 1.29 becomes:

$$\frac{\partial^2 H_y}{\partial z^2} + (k_0^2 \varepsilon_p - \alpha^2) H_y = 0 \quad (1.30)$$

We are looking for bound solutions that propagate along the interface and decay away from it. Thus, they can be expressed as :

$$\begin{cases} H_{my} = A e^{i\alpha x} e^{\gamma_m z} & z < 0 \\ H_{dy} = B e^{i\alpha x} e^{-\gamma_d z} & z > 0 \end{cases} \quad (1.31)$$

where  $\alpha$  indicates the parallel component of the wave vector corresponding to the propagation of the wave along the  $x$  direction.  $\gamma_{d/m} = \sqrt{\alpha^2 - k_0^2 \varepsilon_{d/m}}$  are the components of the wave vector perpendicular to the interface and since the field evanescently decays in this direction, they must have positive real part. A and B represent the amplitudes of the field in each of the two media. Applying the following boundary conditions at the interface  $z = 0$ :

$$\begin{aligned} H_{my}(z = 0) &= H_{dy}(z = 0) \\ \frac{1}{\varepsilon_m} \frac{\partial H_{my}}{\partial z}(z = 0) &= \frac{1}{\varepsilon_d} \frac{\partial H_{dy}}{\partial z}(z = 0) \end{aligned} \quad (1.32)$$

Yields:

$$\begin{cases} A = B \\ \gamma'_m A = -\gamma'_d B \end{cases} \quad (1.33)$$

with  $\gamma'_{d(m)} = \frac{\gamma_{d(m)}}{\varepsilon_{d(m)}}$ , which gives :

$$\gamma'_m + \gamma'_d = 0 \quad (1.34)$$

Let us analyze equation 1.34 to obtain the conditions which have to be fulfilled for surface plasmons under TM polarization. One can see that since  $\gamma_d$  et  $\gamma_m$  have positive real parts, this equation requires that  $\varepsilon_m$  et  $\varepsilon_d$  must have opposite signs. That means the permittivity of metal must be negative ( $\varepsilon_m < 0$ ). This requirement is largely fulfilled by many metals in the visible and near infrared ranges.

By following, a similar approach for TE polarization, the boundary conditions at the interface lead to  $\gamma_m + \gamma_d = 0$ , which cannot be satisfied and consequently TE SPP modes cannot exist and this set of solutions is thus discarded.

Replacing  $\gamma_d$  et  $\gamma_m$  by their expressions in equation 1.34, we obtain the SPP dispersion relation:

$$k_{sp} = \alpha = k_0 \sqrt{\frac{\varepsilon_d \varepsilon_m}{\varepsilon_d + \varepsilon_m}} \quad (1.35)$$

It is worth noting that in addition to the condition stated above, this relation imposes a second condition on the permittivities of both media. Indeed, to have a propagative wave,  $k_{sp}$  must have a real part. Since the product of the dielectric functions

is negative ( $\varepsilon_d \varepsilon_m < 0$ ), the sum in the denominator of equation 1.35 should be also negative. This condition implies that:

$$\omega < \omega_{sp} = \frac{\omega_p}{\sqrt{1 + \varepsilon_d}} \quad (1.36)$$

From this, we conclude that The SPP exists when  $\varepsilon_m$  is negative and larger in magnitude than the dielectric permittivity  $\varepsilon_d$  and only for frequencies below the surface plasmon resonant frequency  $\omega_{sp}$ .

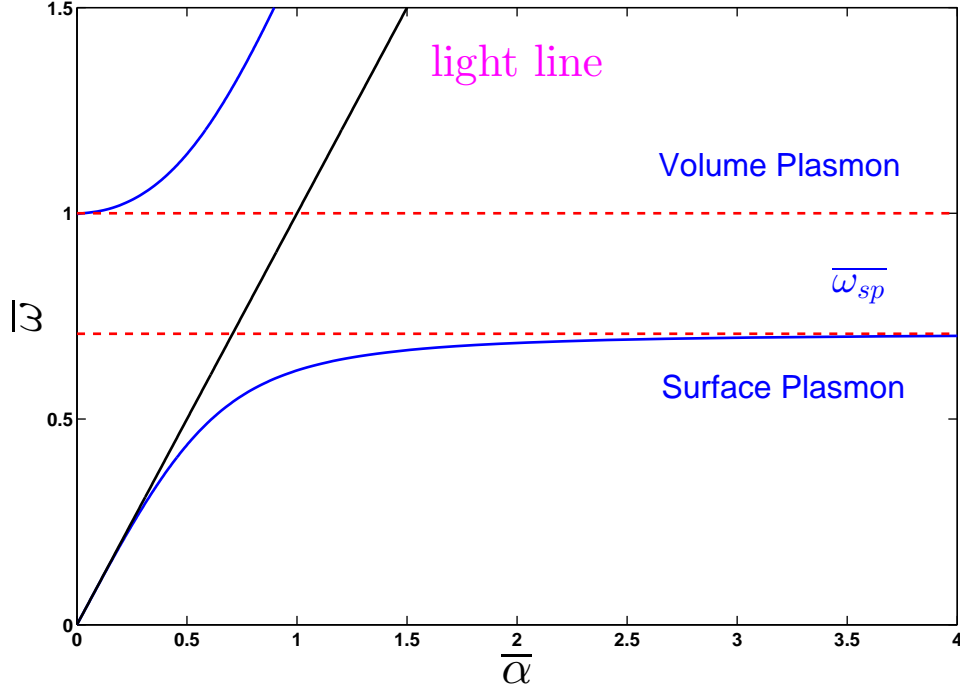


Figure 1.15: Dispersion relation of a surface plasmon polariton (SPP) at an air-gold interface . The gold dispersion is described by the Drude Model when the damping constant is assumed to be equal to zero ( $\omega_p = 9$  eV and  $\gamma = 0$ ). The light line is shown in solid black line. The horizontal red dashed lines correspond , respectively, to the normalized surface plasmon frequency  $\bar{\omega}_{sp}$  and the volume plasmon frequency. The frequency and the propagation constant are normalized to the plasma frequency of gold

Note that the above calculations are carried under the assumption that the losses are negligible in the metal. In the case of a real metal (with losses), where the dielectric function of the metal is complex  $\varepsilon_m(\omega) = \varepsilon'_m(\omega) + i\varepsilon''_m(\omega)$ . The surface wave associated to the SPP will be attenuated by the presence of losses in the metal, which lead to a complex  $k_{sp} = k'_{sp} + ik''_{sp}$  constant propagation. Assuming that  $|\varepsilon'_m| \gg \varepsilon''_m$  , the real and imaginary parts of  $k_{sp}$  will be given by :

$$k'_{sp} = k_0 \left( \frac{\varepsilon'_m \varepsilon_d}{\varepsilon'_m + \varepsilon_d} \right)^{1/2} \quad (1.37)$$

$$k''_{sp} = k_0 \left( \frac{\varepsilon'_m \varepsilon_d}{\varepsilon'_m + \varepsilon_d} \right)^{3/2} \frac{\varepsilon''_m}{2\varepsilon'^2_m} \quad (1.38)$$

Let us now examine the properties of (SPP) by considering the dispersion relation given by equation 1.35. At this point, it is instructive to introduce dimensionless

parameters. For that, we normalize the frequency and the wave vector according to gold's plasma frequency:  $\bar{\omega} = \omega/\omega_{pAu}$  and  $\bar{\alpha} = \alpha c/\omega_{pAu}$ . Figure 1.15 shows the dispersion relation for a surface plasmon polariton in the interface between vacuum ( $\varepsilon_d = 1$ ) and a metal, where, we use the Drude Model without loss ( $\omega_p = 9$  eV corresponding to  $f_{pAu} = 2.176 \times 10^{15}$  Hz and  $\gamma = 0$ ) to calculate the gold permittivity. The free space dispersion relation of equation  $\bar{\omega} = \bar{\alpha}$  is also presented.

We can distinguish two energy branches in the dispersion relation curve. The first branch for which  $\bar{\omega} < \bar{\omega}_{sp}$ , ( $\bar{\omega}_{sp} = 1/\sqrt{1+\varepsilon_d} = 1/\sqrt{2}$ ) corresponds to a surface plasmon polariton (SPP), while the second one for which  $\bar{\omega} > 1$  represents the propagation of bulk modes inside the metallic plasma. In this latter case, the metal is transparent (i.e.  $\varepsilon_m > 0$ ) and thus  $\gamma_d$  et  $\gamma_m$  become imaginary allowing then the propagation of unbound radiation. For  $\bar{\omega} < \bar{\omega}_{sp} < 1$ , the dispersion relation curve shows a gap for which no propagative mode can exist, since  $\bar{\alpha}$  is imaginary in this frequency region. At low frequencies, the dispersion relation follows closely the light line, so in this region the SPP possesses a photon like nature. When  $\bar{\omega}$  approaches gradually  $\bar{\omega}_{sp}$ , the dispersion curve starts to depart from the light line. In the limit where  $\bar{\omega} \rightarrow \bar{\omega}_{sp}$ , the group velocity  $v_g = \partial\bar{\omega}/\partial\bar{\alpha}$  vanishes and the surface plasmon resonance can occur at this frequency. In this case, *the surface plasmon polariton* (that is a hybrid mode) becomes a pure *surface plasmon*.

As can be observed from figure 1.15, the SPP dispersion curve is always below that of light and they do not cross at any point. In other words, for a given frequency the wavevector of the SPP is always higher than that of light. As a result of this wavevector mismatch, a direct excitation of SPPs with an electromagnetic wave is not possible and we say that the SPP is a non radiative mode. To overcome this limitation, various special excitation techniques have been proposed to deal with the wavevector mismatch allowing then the coupling between light and SPPs. Having understood the properties of SPPs guided by a metallic interface, we are now ready to study the properties of the surface plasmons polariton supported by a graphene sheet.

## 1.2.2 Surface plasmons polaritons on graphene (GSP)

Owing to its semi-metallic nature, graphene can support electronic collective oscillations similar to that guided by the conventional 2D electron gases and noble Metals (see figure 1.16). These modes are called graphene surface plasmons which hereafter will be named simply GSP. In this section, we review the basic properties of graphene surface plasmons including their dispersion relation, localization and propagation.

### Electrodynamic models of graphene

Before delving into calculations details of the dispersion relation of the GSPs modes, it is useful to present the different methods for electromagnetic modeling of graphene. In this section we present the two popular models encountered in the literature [17] and we perform a comparison between them by calculating the transmittance, reflectance and absorbance through a single graphene layer surrounded by two dielectric media.

**First approach:** This approach, called *Single Sheet Approach* or *Zero Thickness Model* (ZTM), has been employed in several works [18, 19, 20]. Within this model, graphene is considered as a (2D) conductive sheet characterized by its surface conductivity  $\sigma_g$  (see figure 1.19a).

**Second approach:** In this second model, graphene is treated as an extremely thin film with a very small finite thickness  $a_g$ , which later we will tend it towards zeros

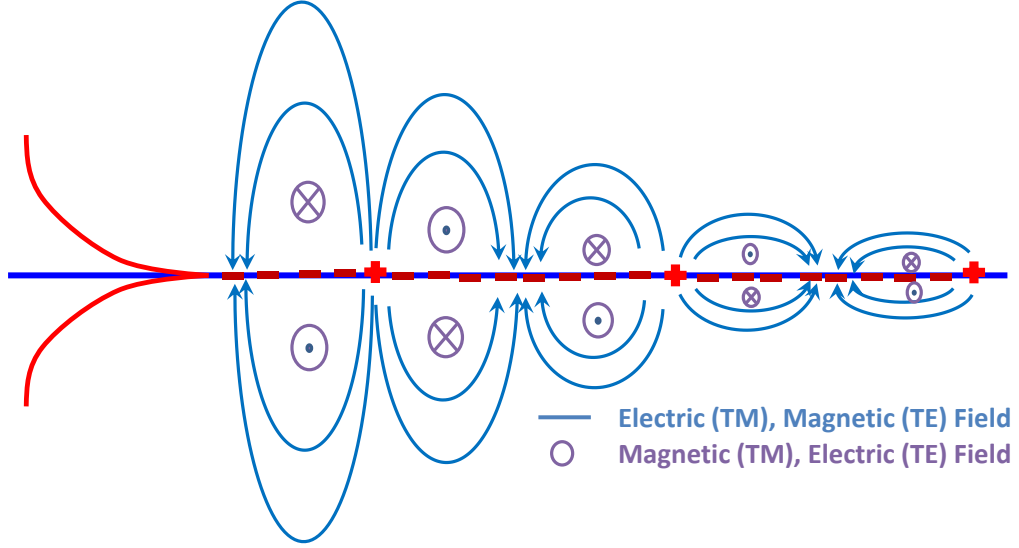


Figure 1.16: Schematic representation of the plasmon polariton mode on a graphene sheet: The charge density oscillations for TM(TE) waves can be represented in terms of electric (magnetic) dipole waves.

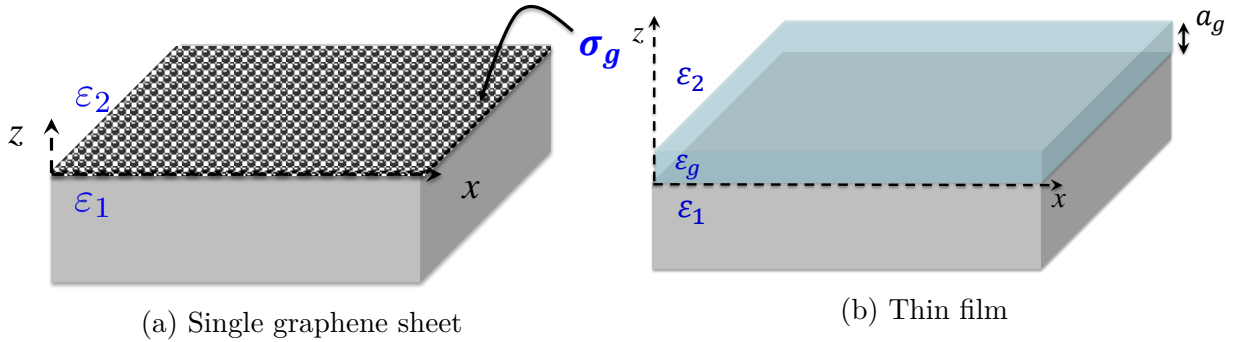


Figure 1.17: Schematic representation of the two configurations considered for modeling of graphene.

( $a_g \rightarrow 0$ ). For this thick layer, we define a volume conductivity that can be deduced from its surface conductivity:

$$\sigma_{g,v} = \frac{\sigma_g}{a_g} \quad (1.39)$$

Thus, the volume current density in graphene can be given by:

$$\vec{J}_v = \sigma_{g,v} \vec{E} \quad (1.40)$$

The Ampere-Maxwell equation states that:

$$\vec{\nabla} \times \vec{H} = \vec{J}_v + \frac{\partial \vec{D}}{\partial t} = \sigma_{g,v} \vec{E} - i\omega \epsilon_0 \epsilon_r \vec{E} \quad (1.41)$$

where  $\vec{D} = \epsilon_0 \epsilon_r \vec{E}$  is the electric displacement field of graphene. Using this equation, we can obtain the effective dielectric permittivity of graphene as:

$$\epsilon_g(\omega) = 1 + \frac{i\sigma_g(\omega)}{\omega \epsilon_0 a_g} \quad (1.42)$$

So, by assuming a small (sub-nanometer) thickness  $a_g$ , graphene can be considered as a bulk material layer with an equivalent permittivity  $\varepsilon_g$  (see figure 1.19b). This model can be named as *Thin film's effective thickness approach* or *bulk Model* [21].

Now, in order to test the validity and efficiency of each model, we make a comparison between the two approaches by applying them to study the optical properties of a single graphene layer embedded by two dielectric media with permittivities  $\varepsilon_1$  and  $\varepsilon_2$ . Let us start by deriving the expressions of the reflectance, transmittance and the absorbance using the single sheet Model. We Consider the structure depicted in Figure 1.18a where a single graphene sheet is located on the  $xy$  plane and a plane wave falls onto it from the lower region ( $z < 0$ ).

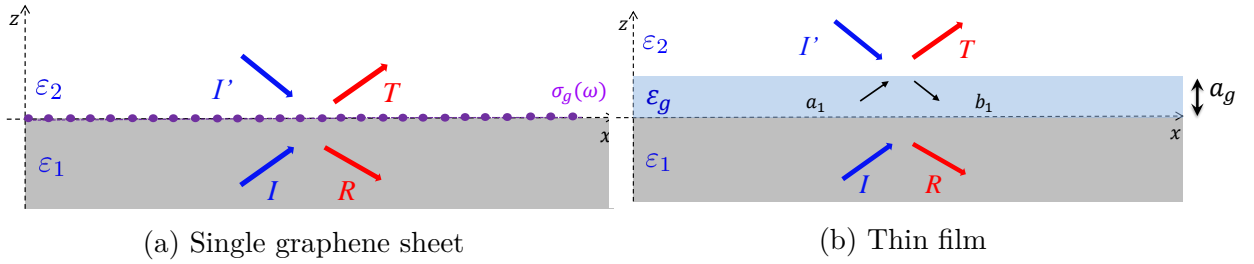


Figure 1.18: Light propagation through a system composed of a single graphene layer which is surrounded by two dielectric media. The graphene layer is considered as 2D conductive sheet characterized by its conductivity in (a) and as a thin film with a thickness  $a_g$  and an effective permittivity  $\varepsilon_g$  in (b).  $R$  and  $T$  are the outgoing amplitudes and  $I$  and  $I'$  are the incoming ones.  $a_1$  and  $b_1$  are the amplitudes in the graphene layer for the case of the film model.

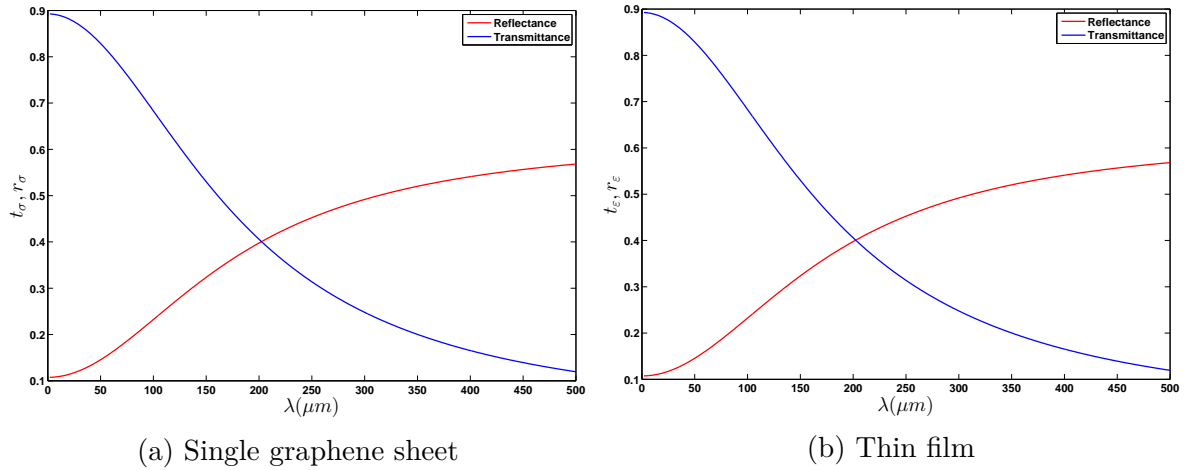


Figure 1.19: Transmittance and reflectance versus wavelength of a single layer of graphene for TM polarization at normal incidence. The results calculated using the ZTM Model are shown in the right panel and those obtained within the bulk Model are given in the left panel. The permittivities of the dielectric media are  $\varepsilon_1 = 3.9$  ( $SiO_2$ ) and  $\varepsilon_2 = 1$ . The parameters of graphene are  $\mu_c = 0.6\text{eV}$ ,  $\gamma = 1.1\text{meV}$ ,  $a_g = 0.34\text{nm}$ .

The first thing to do for finding the transmittance and the reflectance of this structure is to write the electromagnetic fields in the two dielectric media for both TM and TE polarizations and then apply the right boundary conditions that include the surface conductivity of graphene at  $z = 0$ . For the TM polarization, the reflection and

the transmission coefficients can be obtained as:

$$R_{TM} = \frac{k_0\gamma'_1 + \gamma'_1\gamma'_2 Z_0\sigma_g - k_0\gamma'_2}{k_0\gamma'_1 + \gamma'_1\gamma'_2 Z_0\sigma_g + k_0\gamma'_2} \quad (1.43)$$

$$T_{TM} = \frac{2k_0\gamma'_1}{k_0\gamma'_1 + \gamma'_1\gamma'_2 Z_0\sigma_g + k_0\gamma'_2} \quad (1.44)$$

And for the TE polarization case, we find:

$$R_{TE} = \frac{\gamma_1 - \gamma_2 - k_0 Z_0 \sigma_g}{\gamma_1 + \gamma_2 + k_0 Z_0 \sigma_g} \quad (1.45)$$

$$T_{TE} = \frac{2\gamma_1}{\gamma_1 + \gamma_2 + k_0 Z_0 \sigma_g} \quad (1.46)$$

The reflectance and the transmittance are then calculated as :

$$r_{TM} = |R_{TM}|^2 \quad \text{and} \quad r_{TE} = |R_{TE}|^2 \quad (1.47)$$

$$t_{TM} = \frac{\gamma'_2}{\gamma'_1} |T_{TM}|^2 \quad \text{and} \quad t_{TE} = \frac{\gamma_2}{\gamma_1} |T_{TE}|^2 \quad (1.48)$$

Finally, the absorbance can be readily deduced from:

$$A = 1 - r - t \quad (1.49)$$

We turn now our attention to the second approach where the graphene layer can

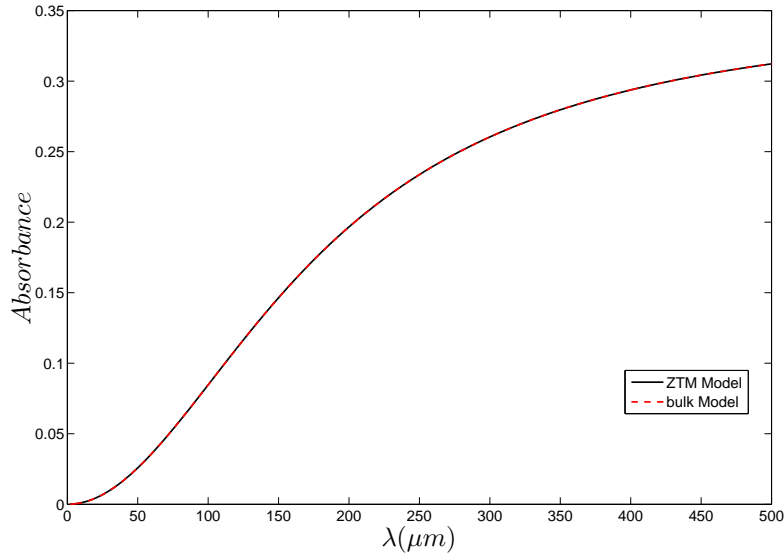


Figure 1.20: Absorbance as a function of the wavelength obtained using the Bulk Model (Red dashed line) and the ZTM Model (Black solid line). The parameters are the same as in figure 1.19.

be seen as a slab with equivalent permittivity  $\epsilon_g$  and thickness  $a_g$ . In this case, the transmission and reflection coefficients can be given by the following Fresnel coefficients:

$$R = \frac{r_1 + \phi_1 r_2 \phi_2}{1 + r_1 r_2 \phi_1 \phi_2} \quad (1.50)$$

$$T = \frac{t_1 t_2 \phi_2}{1 + r_1 r_2 \phi_1 \phi_2} \quad (1.51)$$

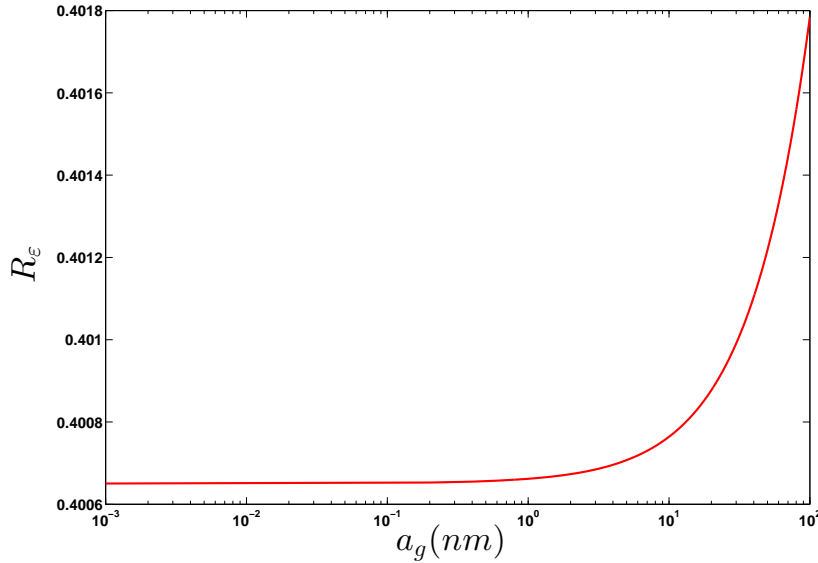


Figure 1.21: Reflectance versus the thickness of graphene  $a_g$  obtained for  $\lambda = 202.3694\mu\text{m}$  and  $\theta = 0^\circ$ . The Others parameters are the same as in figure 1.19.

Where  $\phi_1 = \phi_2 = e^{i\gamma_g a_g}$ ,  $\gamma_g = \sqrt{k_0^2 \varepsilon_g - \alpha^2}$ ,  $r_{1/2}$  and  $t_{1/2}$  are the Fresnel coefficients at the two interfaces.

Let us now compare the results of the two approaches. We consider a graphene surrounded by the fused silica ( $SiO_2$ ) of permittivity  $\varepsilon_1 = 3.9$  and the vacuum ( $\varepsilon_2 = 1$ ). The parameters of the graphene layer are  $\mu_c = 0.6\text{eV}$ ,  $\gamma = 1.1\text{meV}$  and for the Bulk Model the thickness of graphene is taken to be  $0.34\text{nm}$ . Figures 1.19a, 1.19b and 1.20 display the transmittance, reflectance, absorbance, respectively, as a function of wavelengths calculated at normal incidence. The results are computed with the single sheet Model from eqs 1.47, 1.48 and 1.49 (fig 1.19a and black solid line in fig 1.20) and with the Bulk Model from eq 1.51 (fig 1.19b and red dashed line in fig 1.20). We can clearly see that the results obtained from the two approaches are in very good agreement.

In order to test the validity of the Thin film's effective thickness approach and identify the range of the thickness of graphene in which this model still valid, we present in Figure 1.21 the reflectance computed for  $\lambda = 202.3694\mu\text{m}$  as a function of thickness of graphene. It can be seen from this figure that for  $a_g \lesssim 1\text{nm}$ , the reflectance is almost a constant and it converges towards the reflectance value calculated with the ZTM Model  $r_\varepsilon^s \rightarrow r_\sigma \simeq 0.4007$ . Then for  $a_g \simeq 1\text{nm}$ , it begins to increase rapidly as the thickness increases and moves away from  $r_\sigma$ . As a consequence, this Model is only valid for thicknesses  $a_g$  less than  $1\text{nm}$ .

Note that, in this section, we have only shown the isotropic case. A more detailed explanation on the two approaches and the validity of each model in the anisotropic case can be found in [17].

### Existence conditions and dispersion relation

Let's now begin by deriving the dispersion relation of GSPs. We consider the structure depicted in figure 1.22, where a graphene layer is placed in the  $xoy$  plane at an interface between two dielectric media with dielectric constants  $\varepsilon_1$  for  $z < 0$  and  $\varepsilon_2$  for  $z > 0$ . The graphene sheet is treated as a conducting surface characterized by its surface conductivity  $\sigma(\omega)$  and we assume that the electromagnetic wave propagates in

the  $x$  direction and confined to the  $xoy$  plane. The whole structure is invariant in the  $y$  direction ( $\partial_y = 0$ ) and a time dependence of the form  $e^{-i\omega t}$  is assumed. To obtain

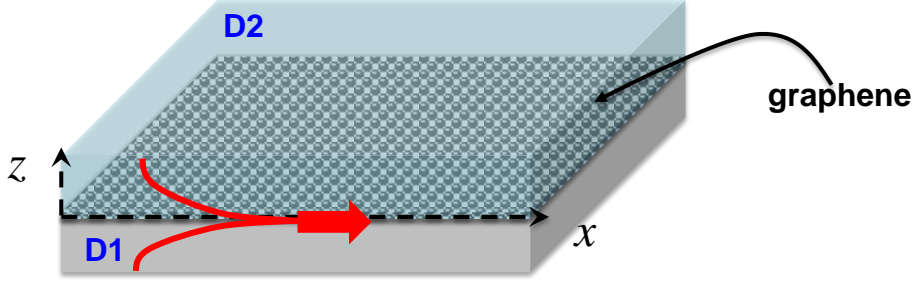


Figure 1.22: Sketch of the studied structure: a graphene sheet is surrounded by two semi-infinite dielectric media D1 and D2. The surface plasmon mode (red) is propagating along the graphene surface in the  $x$  direction

the dispersion relation of graphene surface plasmons that relates the frequency to the wavevector ( $\omega(\alpha)$ ) as well as their existence conditions, we will follow an approach similar to that described in section 1.2.1 by solving the Maxwell's equations and matching the appropriate boundary conditions taking into account the surface conductivity of graphene. Since the structure is invariant along the  $y$  direction, Maxwell's equations can be decomposed into two separate sets with different polarizations: TE and TM polarizations. We treat first the case of TM polarization, then in a second step that of TE polarization.

### - Transverse magnetic graphene SPPs (TM-GSP)

Consider first the case of TM polarisation where the magnetic field of the electromagnetic wave is polarized along the  $y$  direction. Using the wave equation given by equation 1.29, the magnetic field in each medium can be expressed as follows:

$$\begin{cases} H_{1y} = Ae^{i\alpha x} e^{\gamma_1 z} & z < 0 \\ H_{2y} = Be^{i\alpha x} e^{-\gamma_2 z} & z > 0 \end{cases} \quad \gamma_{1/2} > 0 \quad (1.52)$$

The tangential component of the electric field  $E_x$  is deduced from Maxwell's equations :

$$E_x(x, z) = \frac{-iZ_0}{k_0 \varepsilon_p} \partial_z H_y(x, z) \quad (1.53)$$

where  $Z_0 = \sqrt{\mu_0/\varepsilon_0}$  indicates the impedance of free space. This allows us to write:

$$\begin{cases} E_{1x} = \frac{-iZ_0 \gamma'_1}{k_0} Ae^{i\alpha x} e^{\gamma_1 z} & z < 0 \\ E_{2x} = \frac{-iZ_0 \gamma'_2}{k_0} Be^{i\alpha x} e^{-\gamma_2 z} & z > 0 \end{cases} \quad (1.54)$$

with  $\gamma'_{1/2} = \gamma_{1/2}/\varepsilon_{1/2}$ . The continuity of the  $x$ -component of the electric field at  $z = 0$  gives:

$$\gamma'_1 A = \gamma'_2 B \Rightarrow B = \frac{\gamma'_2}{\gamma'_1} A \quad (1.55)$$

Due to the surface current density  $J_x = \sigma E_x$  that flows along the graphene layer, the magnetic field becomes discontinuous at  $z = 0$ :

$$H_{1y} - H_{2y} = \sigma E_{1x} \quad (1.56)$$

which leads to:

$$B = \left(1 + \frac{-iZ_0\gamma'_1}{k_0}\right)A \quad (1.57)$$

Combining Eqs 4.11 and 4.12, we get the dispersion relation of graphene surface plasmons for TM modes:

$$\frac{1}{\gamma'_1} + \frac{1}{\gamma'_2} + \frac{i\sigma(\omega)Z_0}{k_0} = 0 \quad (1.58)$$

As mentioned above, the optical conductivity of graphene is a complex quantity that can be written  $\sigma(\omega) = \sigma_r(\omega) + i\sigma_i(\omega)$ , this leads to:

$$\frac{1}{\gamma'_1} + \frac{1}{\gamma'_2} = -\frac{i\sigma_r(\omega)Z_0}{k_0} + \frac{\sigma_i(\omega)Z_0}{k_0} \quad (1.59)$$

Since  $\gamma'_{1/2}$  are real and positive, we must have:

$$\begin{cases} \sigma_r(\omega) = 0 \\ \sigma_i(\omega) > 0 \end{cases} \quad (1.60)$$

The conditions for the existence of graphene surface plasmons under TM polarisation are given by 1.60. In order to obtain a bound waves that are exponentially decaying in both directions away from the graphene sheet, we require that the normal wave vectors ( $\gamma_p$ ,  $p = 1, 2$ ) are positive in both media. This can only be achieved if the imaginary part of the graphene conductivity is positive and its real part is equal to zero. These conditions are fulfilled in the Drude regime (i.e  $\bar{\omega} \ll \bar{\omega}_s = 2$ ), when the intraband conductivity is dominant (see Figure 1.23 )

Figure 1.24 displays the dispersion curve of the surface plasmon on graphene for TM polarisation calculated for  $\varepsilon_1 = 1$  and  $\varepsilon_2 = 2$ . One can clearly see that this curve is largely below the light line. In other words, for a given frequency, the wave vector of the GSP is much larger than that of the incoming light i.e  $k_{GSP} \gg k_0$ . Therefore, the excitation of those modes is not possible by direct illumination due to a huge mismatch between the parallel wave vectors components.

Let us now analyse the influence of the different parameters acting on the dispersion relation of the GSP which are mainly the optical contrast between the two semi infinite dielectric media surrounding the graphene and the chemical potential of graphene. We begin first by the influence of the optical contrast which is depicted in figure 1.25 (a), we observe that increasing the contrast between the dielectrics in contact with graphene brings the dispersion curve downwards. Now, in order to understand how the dispersion relation curve is affected by the variation of the doping, we keep  $\varepsilon_1 = \varepsilon_2 = 1$  and calculate the dispersion curve for different chemical potential  $\mu_c = 100, 200, 300$  and 400 meV. The corresponding results are shown in figure 1.25(b). When the chemical potential increases from 100 to 400 meV, the dispersion relation curve moves upwards.

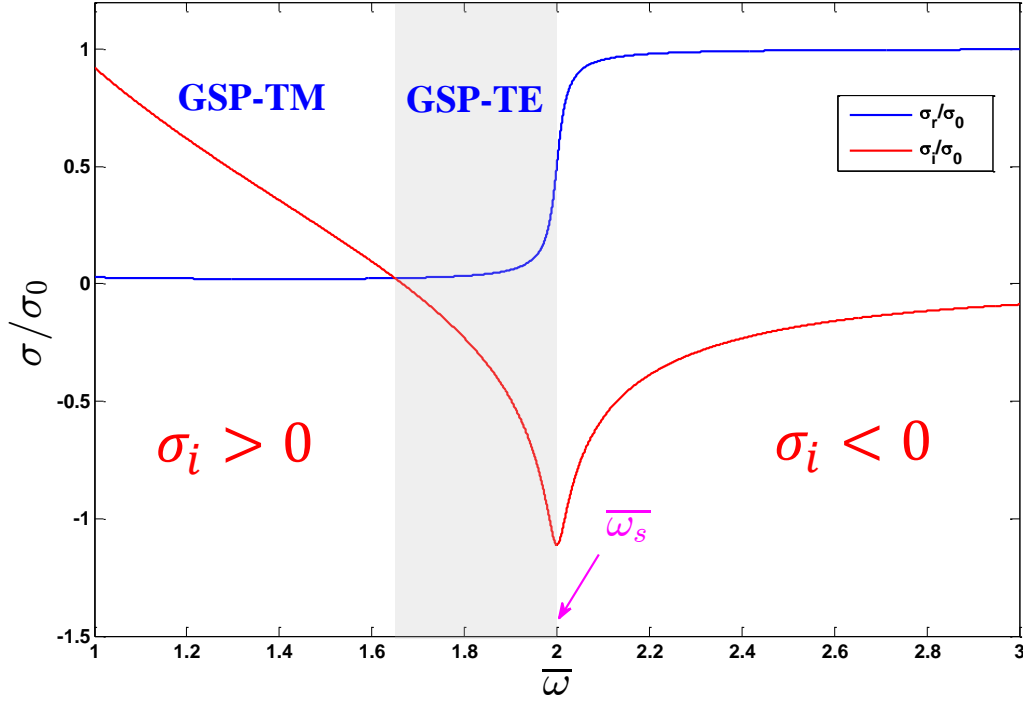


Figure 1.23: illustration of the existence zones of the graphene surface plasmon for both TE and TM modes. When  $\bar{\omega} < 1.667$ , the imaginary part of the graphene conductivity is positive and graphene can support TM electromagnetic SPP surface wave(TM GSP). While, TE surface plasmons can only exist when  $1.667 < \bar{\omega} < 2$  where the imaginary part of the conductivity becomes negative.

As a results, changing the optical contrast or the doping can be used to manipulate the surface plasmons polaritons in graphene.

### - Transverse electric graphene SPPs (TE-GSP)

Let us now find the form of the surface wave propagating on graphene under TE polarization. For this case, the electric field has the form:

$$\begin{cases} E_{1y} = Ae^{i\alpha x}e^{\gamma_1 z} & z < 0 \\ E_{2y} = Be^{i\alpha x}e^{-\gamma_2 z} & z > 0 \end{cases} \quad (1.61)$$

The tangential magnetic field  $H_x$  is determined from Maxwell's equations:

$$H_x = iZ_0k_0\partial_z E_y \quad (1.62)$$

The Boundary conditions at  $z = 0$  read:

$$\begin{cases} E_{1y}(z = 0) = E_{2y}(z = 0) \\ H_{2x}(z = 0) - H_{1x}(z = 0) = \sigma(\omega)E_{1y}(z = 0) \end{cases} \quad (1.63)$$

which leads to:

$$\begin{cases} A = B \\ (\gamma_1 + \gamma_2)A = \frac{i\sigma(\omega)}{k_0Z_0} \end{cases} \quad (1.64)$$

The dispersion relation is then given by:

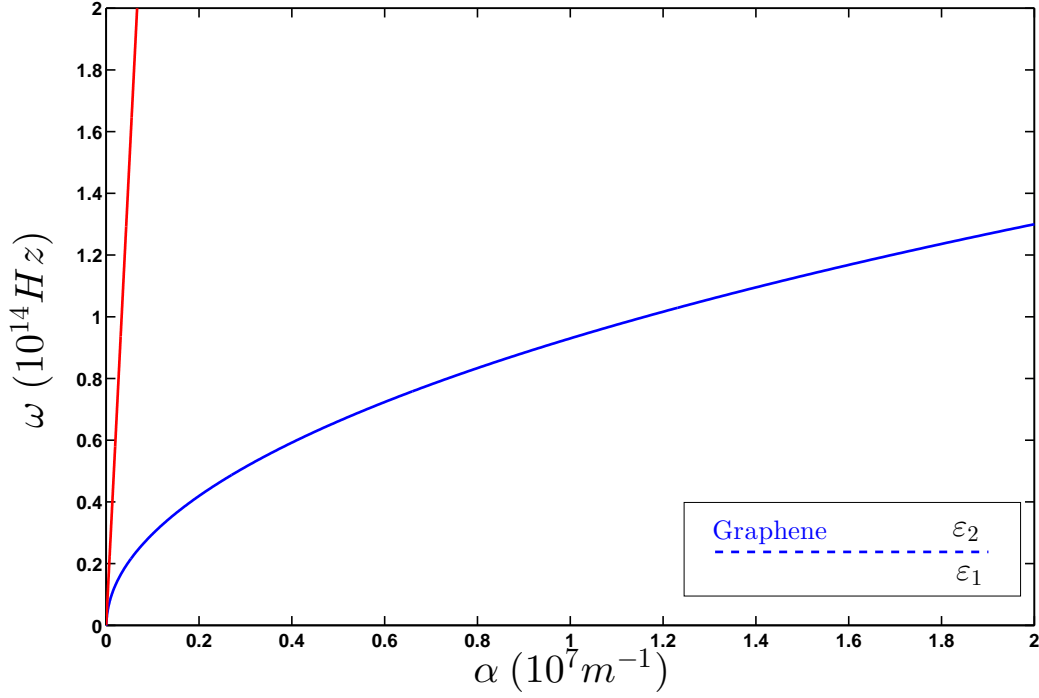


Figure 1.24: Dispersion relation curve of the TM-GSP of graphene surrounded by two dielectric media with dielectric constants  $\varepsilon_1 = 1$  and  $\varepsilon_2 = 2$  respectively. The parameters of graphene are  $\mu_c = 200$  meV and  $\gamma = 0$  eV.

$$\gamma_1 + \gamma_2 - \frac{i\sigma(\omega)}{k_0 Z_0} = 0 \quad (1.65)$$

The term  $\gamma_1 + \gamma_2$  is always positive, which means that we must have:

$$\begin{cases} \sigma_r(\omega) = 0 \\ \sigma_i(\omega) < 0 \end{cases} \quad (1.66)$$

Consequently, graphene can support a TE GSP only if the imaginary part of the conductivity is negative and its real part is zero [19, 18]. Note that, this mode cannot exist in the traditional plasmonic materials since the imaginary part of the conductivity is always positive. We have shown in section 1.1.3, that, unlike Drude materials, the conductivity of graphene can take a negative imaginary part for frequencies above the interband threshold, the region of spectrum governed by the interband transitions. However, due to the Landau damping that occurs at  $\bar{\omega} = 2$  (for  $T=0K$  and  $T=300K$ ) with  $\bar{\omega} = \frac{\hbar\omega}{\mu_c}$ , TE SPPs can only exist in a very narrow frequency range, defined by  $1.667 < \bar{\omega} < 2$  (see Figure 1.23).

In the general case of different dielectric media, the analytical resolution of equation 1.65 is quite difficult. However, in the simple case, when the two media above and below the graphene sheet are the same ( $\varepsilon_1 = \varepsilon_2 = \varepsilon$ ), the TE dispersion relation can be reduced to  $k_{GSPT E} \simeq \omega\sqrt{\varepsilon}/c$  (Note that, in this case, we can neglect the third term in equation 1.65 because in this frequency range the real part of the conductivity is equal to its universal value). Then, in the case of free standing graphene where  $\varepsilon_1 = \varepsilon_2 = \varepsilon = 1$ , the spectrum of TE waves almost coincides with that of free wave in vacuum  $k_{GSPT E} \cong k_0$ . That is why, as we can see from figure 1.26, the dispersion relation of TE GSP is very close to the light line. As a consequence, TE modes are weakly

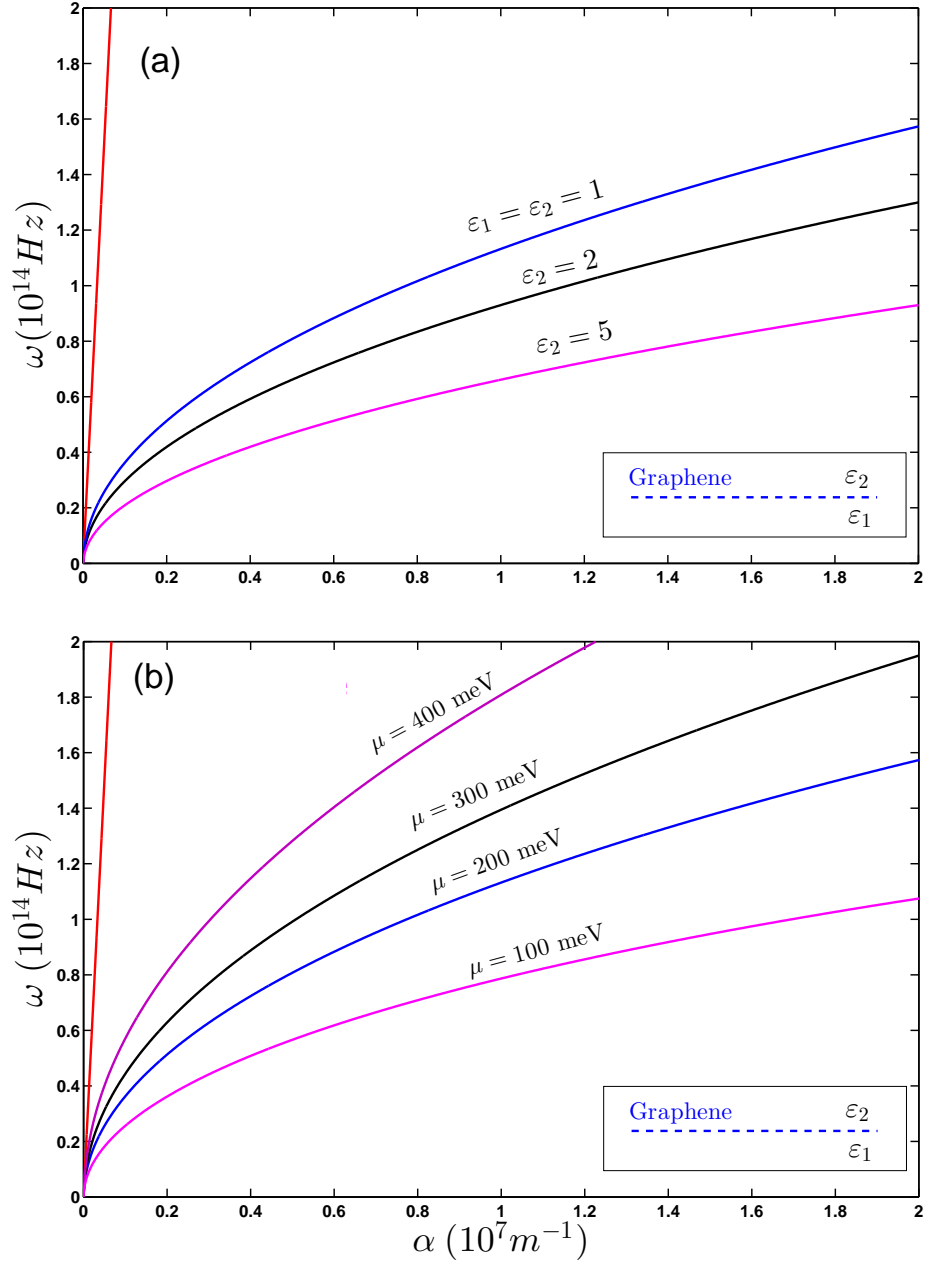


Figure 1.25: Influence of (a) the contrast  $\varepsilon_2 - \varepsilon_1$  and (b) the chemical potential when ( $\varepsilon_1 = \varepsilon_2 = 1$ ), on the dispersion curve of the TM-GSP.

bound to the graphene surface[19]. Nevertheless, it has been predicted that, they exhibit very low propagation loss and have ultrahigh sensitivity to the optical contrast between the two dielectric media surrounding the graphene layer [19, 22]. This new surface electromagnetic (TE GSP) mode guided by graphene and characterized by its plasmonic response has been theoretically predicted in several works. A TE-plasmonic gas-sensor was proposed theoretically in ref [22] to achieve a high refractive index sensitivity that surpasses the sensitivity of traditional SPR (Surface Plasmon Resonance) sensors. Moreover, it was suggested numerically in [23, 24], that the Attenuated Total Reflection technique (ATR) in the Otto geometry could be used for the excitation of this kind of mode. However, these modes remain purely theoretical objects because so far, their experimental excitation has not been demonstrated. For that reason, our

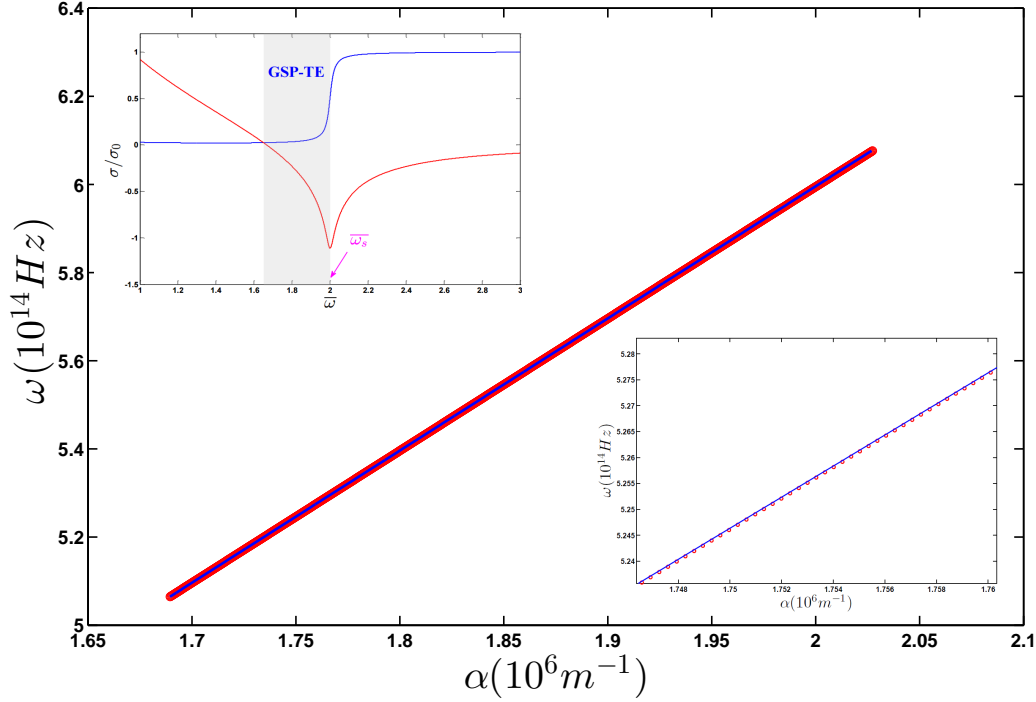


Figure 1.26: Dispersion relation of surface plasmons for TE polarized waves (TE GSP for a free standing graphene layer (red circles). The blue solid line corresponds to the light line in vacuum. The parameters of graphene are  $\mu_c = 200$  meV et  $\gamma = 0$ .

interest in the following chapters, will focus on the case of TM-GSP.

### Properties of Graphene surface plasmons

Let us now pass to the discussion of the main physical properties of SPPs in graphene. But before that, we need first to provide some of the length scales that are important for characterizing SPPs. For that, we shall consider the case of a real conducting medium with a complex dielectric function  $\varepsilon_m(\omega) = \varepsilon'_m(\omega) + i\varepsilon''_m(\omega)$  which leads to a complex parallel wavevector  $k_{sp} = k'_{sp} + ik''_{sp}$ .

#### SPPs length scales

- **Surface plasmon polariton wavelength  $\lambda_{sp}$ :** Surface plasmons are characterized by several parameters. The first one is their wavelength  $\lambda_{sp}$ , which corresponds to the spatial period of the surface charge density oscillation. This parameter can be derived from the complex dispersion relation by taking the real part of the parallel wavevector. Under the assumption  $|\varepsilon'_m| \gg \varepsilon''_m$ , it can be expressed as:

$$\lambda_{sp} = \frac{2\pi}{k'_{sp}} \quad (1.67)$$

It should be noted that  $\lambda_{sp}$  is always much smaller than the free space wavelength  $\lambda_0$  which is obviously a consequence of the bound nature of the SPP modes.

- **SPPs propagation length  $L_{sp}$ :** Due the dissipation in the metal, the SPP is attenuated during its propagation. As the decay is linked to the term  $\exp(-2k''_{sp}x)$ ,

the propagation distance  $L_{sp}$  can be defined as the distance over which the intensity of the mode reduces to  $1/e$  of its initial value:

$$L_{sp} = \frac{1}{2k''_{sp}} \quad (1.68)$$

- **SPP penetration depth  $\delta$ :** Another important parameter of SPPs is the penetration depth that characterizes the degree of confinement of the mode into its supporting material. In each medium, it can be given by

$$\delta_p = \frac{1}{2|k''_z|} \quad p = m, d \quad (1.69)$$

where  $m(d)$  stands for metal(dielectric). This parameter is directly related to the imaginary part of the transverse component of the wave vector  $k''_z$  and is defined as the distance where the exponentially decreasing evanescent field drops to  $1/e$  of its maximum amplitude.

For doped graphene and within the Drude regime (where the conductivity is well described by the drude conductivity), the later parameters can be expressed as:

$$\lambda_{sp} = \frac{2\pi}{k'_{sp}} = \lambda_0 \frac{4\alpha\mu_c}{\hbar\omega(\varepsilon_1 + \varepsilon_2)} \quad (1.70)$$

$$L_{sp} = \frac{1}{2k''_{sp}} = \lambda_0 \frac{\tau\alpha\mu_c}{\pi\hbar(\varepsilon_1 + \varepsilon_2)} \quad (1.71)$$

and

$$\delta_{sp} = \frac{1}{2|k''_z|} = \frac{\lambda_{sp}}{2\pi} \quad (1.72)$$

It should be mentioned that in order to minimize losses and avoid those caused by the interband transitions, we will work in the frequency window just below the threshold of interband transition i.e for graphene with high doping.

### Relatively low loss for GSPs

Noble metals such as gold and silver have usually been used in traditional plasmonic structures as plasmonic materials in the visible and near IR frequencies. However, in the terahertz frequencies, these materials suffer from very large losses which limits their applications and performances in this frequencies range. To circumvent this drawback, graphene, has been proposed as a potential alternative plasmonic material. A comparison of the plasmonic properties between metals and graphene has been made in Ref [25]. It was shown that for frequencies above 20 THz (visible and infrared spectrum), graphene has a SPP propagation length smaller than that of a 30-nm thin Au film. This makes graphene less attractive in this frequency range. However at lower frequencies (THz region), the loss as well as the penetration depth in metals increase dramatically as the frequency decreases. In this frequency range, graphene exhibits less losses [26]. It was also demonstrated that in the case of highly doped graphene, Landau damping becomes weak and does not contribute to the losses processes. As a result, the effective mode index  $\delta_{sp}/\lambda_{sp}$  will increase as the frequency decreases in the THz region and can achieve 2000 when  $f = 1$  THz for a free-standing graphene sheet [27].

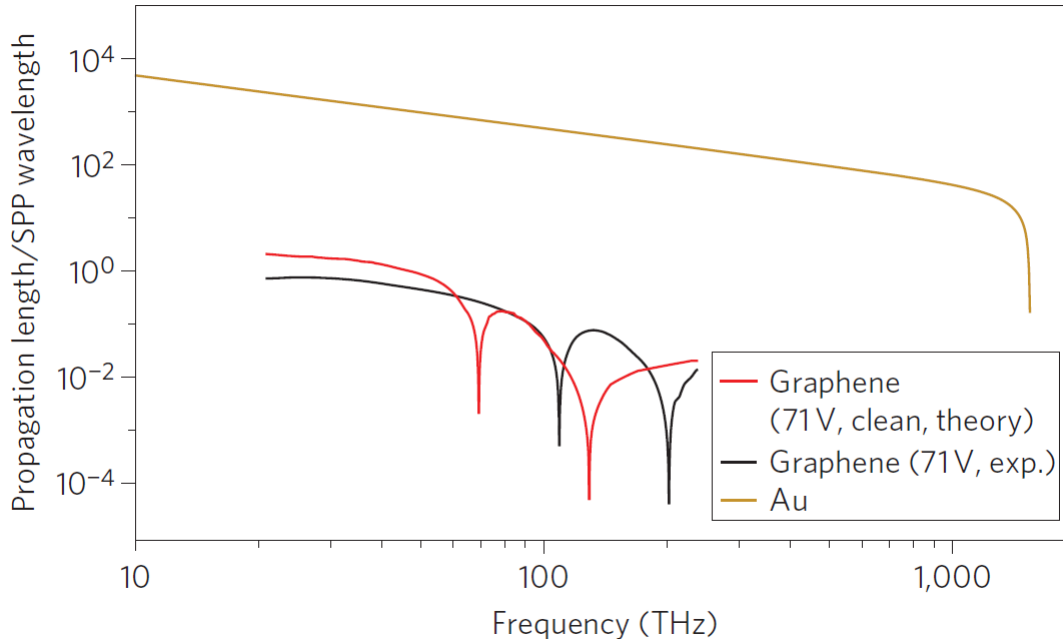


Figure 1.27: Comparison of plasmonic properties of graphene and gold:  $L_{sp}/\lambda_{spp}$  as a function of the frequency of the incident light [25]. The results for Au are for a 30-nm thick film at room temperature while the results for graphene are for a highly doping case and are calculated from the experimental data in Ref [28] and from theoretical data in Ref [29].

### High confinement of GSPs

As stated above, the confinement of SPPs into plasmonic materials is characterized by its penetration depth. The comparison between graphene and silver (which is considered as the best metallic plasmonic material) has shown that the penetration depth in graphene is a few orders smaller than that in silver [27]. In the other hand, the effective SPP index  $\lambda_0/\lambda_{sp}$  in metals is only slightly larger than  $\sqrt{\epsilon_d}$  and since  $\epsilon_d$  of common dielectric does not exceed 10, the SPP index for metals are relatively small. For graphene, this index which is given by  $\hbar\omega(\epsilon_1 + \epsilon_2)/4\alpha\mu_c$  is largely greater than 1. Therefore, GSPs are excellently confined to the surface of graphene with a SPP wavelength  $\lambda_{sp}$  much smaller than in free space. To summarize, the comparison between highly doped graphene and metals gives that metals are potential plasmonic materials in the visible and near infrared region while highly doped graphene is more suitable for the far infrared and the THz region.

### The tunability of GSPs

One of the great advantages of SPPs in graphene over those in noble metals is their tunability. We have shown in previous sections that the conductivity of graphene as well as the GSP dispersion relation are highly sensitive to some parameters such as the chemical potential. We have also shown that the Fermi level in graphene can be easily tuned by changing the carrier charge density by electrostatic gating or chemical doping. This is not possible with SPPs in noble metals. In the same way, the threshold of interband transitions which defines the working frequency of graphene plasmons strongly depends on doping which makes it highly tunable by varying the graphene chemical potential [28, 30]. Although the working frequency of GSPs is in the THz region because of the Landau damping at higher frequencies, it can be extended to the

mid infrared range by increased doping. For example, the working frequency can reach up 80 THz for  $\mu_c = 0.246$  eV and increase to achieve 250 THz for  $\mu_c = 0.8$ eV [26].

### 1.3 Conclusions

In this first chapter, we have presented the basic concepts that are important for understanding this thesis. We have presented the direct and reciprocal lattice of graphene and described its electronic band structure using the Tight binding model. Next, according to a quantum approach based on the EOM method, we have also determined and explained the magneto-optical conductivity model of graphene characterizing its optical response. Using this model, we have then investigated the different plasmonic modes that can propagate along a graphene sheet and their existence conditions. Finally, we have reviewed the basic properties of these modes.



# Bibliography

- [1] N. chamanara and C. Caloz. Fundamentals of graphene magnetoplasmons: principales, structures and devices. *Forum for Electromagnetic reseach methods and Application Technologies (FERMAT)*, 10:1–15, 2015. [18](#), [19](#)
- [2] P. R. Wallace. Electric field effect in atomically thin carbon. *Phys.Rev*, 71(9):622, 1947. [17](#)
- [3] N. M. R. Peres K. S. Novoselov A. H. Castro Neto, F. Guinea and A. K. Geim. The electronic properties of graphene. *Rev.Mod.Phys*, 81(1):109–162, 2009. [18](#)
- [4] Z. Jiang M. Klima G. Fudenberg J. Hone P. Kim K. I. Bolotin, K. J. Sikes and H. L. Stormer. Ultrahigh electron mobility in suspended graphene. *Solid State Comm*, 146(9-10):351–355, 2008. [20](#)
- [5] W. bao I. Calizo D. Teweldebhan F. Miao A. A. balandin, S. Ghosh and C. N. lau. Superior thermal conductivity of single layer graphene. *Nano Lett*, 8(3):902–907, 2008. [6](#), [20](#)
- [6] C. Coletti, C. Riedl, D. S. Lee, B. Krauss, L. Patthey, K. von Klitzing, J. H. Smet, and U. Starke. Charge neutrality and band-gap tuning of epitaxial graphene on sic by molecular doping. *Phys. Rev. B*, 81:235401, Jun 2010. [21](#)
- [7] A. K. Geim and K. S. Novoselov. The rise of graphene. *Nature Materials*, 6(3):183–191, 2007. [21](#)
- [8] M. D. ventra J. N. Echestein C. D. Frisbie M. E. Gershenson A. M. Goldman I. H. Inoue J. Mannhart A. J. Millis A. Forpurgo D. Natelson C. H. Ahn, A. Bhattacharya and J. M. Triscone. Electrostatic modification of novel materials. *Rev.Mod.Phys*, 78(4):1185, 2006. [22](#)
- [9] C. Casiraghi. Doping dependance of the raman peaks intensity of graphene close to dirac point. *Phys.Rev.B*, 80(23):233407, 2009. [22](#)
- [10] Aires Ferreira, J. Viana-Gomes, Yu. V. Bludov, V. Pereira, N. M. R. Peres, and A. H. Castro Neto. Faraday effect in graphene enclosed in an optical cavity and the equation of motion method for the study of magneto-optical transport in solids. *Phys. Rev. B*, 84:235410, Dec 2011. [22](#), [24](#), [115](#)
- [11] A. N. Grigorenko K. S. Novoslov T. J. Booth T. stauber N .M. R. Peres R. R. .Nair, P. Blake and A. K. Geim. Fine structure constatnt defines visual transparency of graphene. *Sciences*, 320(5881):1308, 2008. [25](#), [27](#)

- 
- [12] L. A. Falkovsky. Optical properties of graphene. *J.Phys.Conf.Ser*, 129(1):2004, 2008. [6](#), [26](#)
- [13] L. A. Falkovsky and A. A. Varlamov. Space-timedispersion of graphene conductivity. *Eur.Phys.J.B*, 56(4):281, 2007. [6](#), [26](#)
- [14] S. G. Sharapov V. P. Gusynin and J. p. Carbotte. Magneto-optical conductivity in graphene. *J.Phys.Condens.Matter.*, 19(2):6222, 2007. [6](#), [26](#)
- [15] T. Hasan F. Bonaccorso, Z. Sun and A. C. Ferrari. Graphene photonics and optoelectronics. *Nature photonics*, 9(4):611–622, 2010. [27](#)
- [16] P. Drude. Zur electronen theorie der metalle. *Annalen der physik*, 306(3):566–613, 1900. [28](#)
- [17] Bruno Majérus, Evdokia Dremetsika, Michaël Lobet, Luc Henrard, and Pascal Kockaert. Electrodynamics of two-dimensional materials: Role of anisotropy. *Phys. Rev. B*, 98:125419, Sep 2018. [33](#), [36](#)
- [18] W. Hanson. Quasi transverse electromagnetic modes supported by a graphene parallel-plate waveguide. *J.App.Phys.Lett*, 104:084314, 2008. [6](#), [33](#), [40](#)
- [19] S. A. Mikhailov and K. Ziegler. New electromagnetic mode in graphene. *PRL*, 99(01):6803, 2007. [6](#), [33](#), [40](#), [41](#)
- [20] H. Buljan M. Jablan and M. Soljacis. Plasmonics in graphene at infrared frequencies. *Phys.Rev. B*, 80:245435, 2009. [33](#)
- [21] A.Vakil and N. Engheta. Transformation optics using graphene. *Science*, 332(6035):1291–1294, 2011. [34](#)
- [22] M. A. Kol’chenko O. V. Kotov and Yu. E. Lozovik. Ultrahigh refractive index sensitivity of te-polarized electromagnetic waves in graphene at the inetrface between two dielectric media. *Opt.Express*, 21(11):13533–13546, 2013. [41](#), [42](#)
- [23] S. G. Menabde D. R. Mason and N. Park. Unusual otto exctations dynamics and enchanced coupling of light to te plasmons in graphene. *Opt.Express*, 22(1):847–858, 2014. [42](#)
- [24] F. Ramos-Mendieta. Mid-indrared excitation of transverse electric modes in doped graphene. *J.Appl.phys*, 117(13):133101, 2015. [42](#)
- [25] M. Kafesaki P. Tassin, T. Koschny and C. M. Soukoulis. A comparaisn of graphene , superconductors and metals as conductors for metamaterials and plasmonics. *Nat .Photonics*, 6:259–264, 2012. [6](#), [43](#), [44](#)
- [26] H. J. u Z. G. Dong T. J. Cui W. B. Lu, W. Zhu. Flexible transformation plasmonics using graphene. *Opt.Express*, 21(9):10475, 2013. [44](#), [45](#)
- [27] F. Garcia-Vidal A. Y. Nikitin, F. Guinea and L. Martin-Moreno. Field radiated a nanoemitter in graphene sheet. *Phys.Rev.B*, 84(19):195446, 2011. [44](#)
- [28] Z. Jiang Z. Hao M. C. Martin P. Kim H. L. Stormer Z. Q. Li, E. A. Henriksen and D. N .Basov. Dirac charge dynamics in graphene by infrared spectroscopy. *Nat.Phys*, 4:532–535, 2008. [44](#), [45](#)

- [29] R. M. Ribeiro N. M. Peres and A. H. Castro Neto. Excitonic effects in the optical conductivity of gated graphene. *Phys Rev Lett*, 105(5), 2010. [44](#)
- [30] S. Ryu L. E. Brus K. S. Kim Y-J. You, Y. Zhao and P. Kim. Tuning the graphene work function by electric field effect. *Nano Lett*, 9(10):3430–3434, 2009. [45](#)



# Chapter 2

## Numerical Tools

*In every branch of knowledge  
the progress is proportional to  
the amount of facts on which to  
build*

James Clerk Maxwell

### Contents

<b>2.1</b>	<b>Generic Physical Structure</b>	<b>51</b>
<b>2.2</b>	<b>Numerical Methods</b>	<b>52</b>
2.2.1	Standard Fourier Modal Method (FMM)	52
2.2.2	Fourier Modal Method with spatial adaptative resolution (FMM-ASR)	60
2.2.3	Aperiodic Fourier Modal Method: FMM with PML	64
<b>2.3</b>	<b>Numerical Examples involving graphene: Graphene-Strip Gratings</b>	<b>67</b>
2.3.1	Graphene horizontal strips grating	67
2.3.2	Graphene Vertical strips grating	69
<b>2.4</b>	<b>Conclusions</b>	<b>72</b>

This chapter is devoted to the introduction of the numerical tools that will be used in the analysis of the structures studied in this thesis. Since all these structures have the common property of being either periodic or aperiodic diffractive structures, their dynamics will be studied in the framework of the Fourier Model Method (FMM). In the first section, we will present the generic multigrating structure that can contain graphene gratings. Then in the next section, we will describe in detail the different standard numerical methods used for modelling the diffraction preproperties of electromagnetic waves on this structure. After that, we will introduce the concept of perfectly matched layers (PML) and combine it with the FMM Method to solve the problem of the aperiodic structures. Finally, we conclude with the last section by applying these methods that take into account graphene for solving the problem of light diffraction by two types of graphene grating systems. A comparative study will be made between these methods in terms of convergence and stability to identify the most suitable one for each structures.

## 2.1 Generic Physical Structure

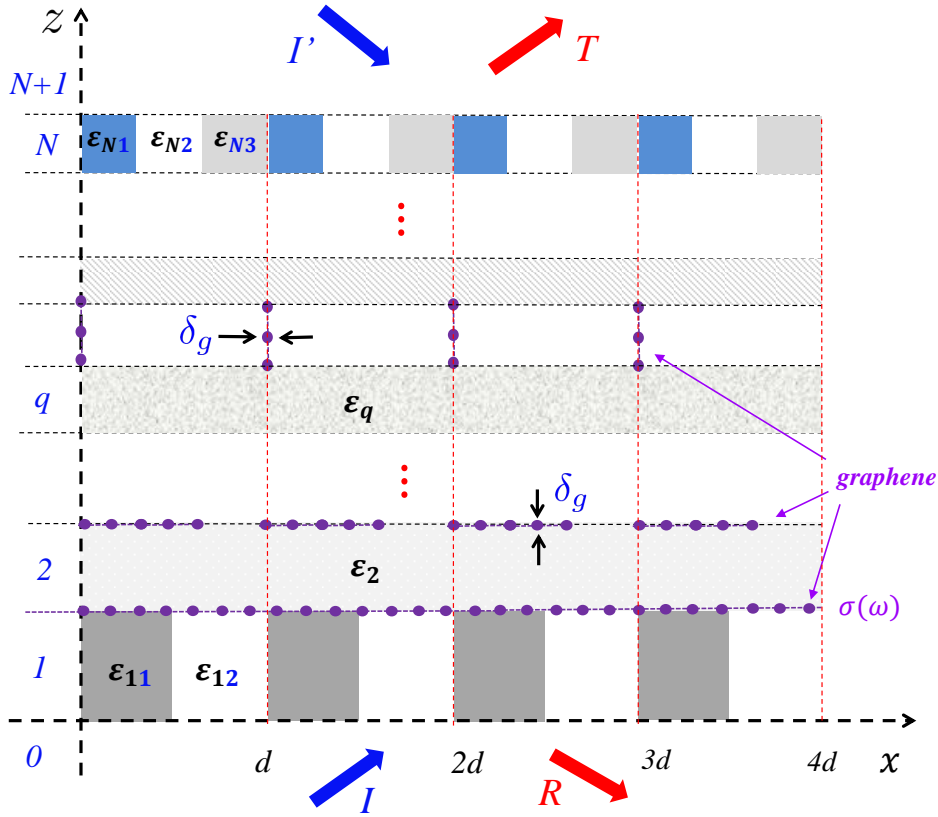


Figure 2.1: Geometry of the diffraction problem: A graphene based multilayers structure in which each layer can be either a homogeneous medium or a grating with the period  $d$

Before we start to develop and explain the different numerical methods, we first present the system which is investigated. The general graphene based multilayered grating structure under study is schematically depicted in figure 2.1. It consists of a stack of  $N$  layers where each of which can be either a periodic lamellar grating or a homogeneous layer or vertical strip grating. This structure is embedded between two homogeneous dielectric media with permittivities  $\varepsilon_{in}$  and  $\varepsilon_{out}$ . All gratings share the same period  $d$  and the graphene can be inlaid in this structure under three configurations: either continuous graphene layers or horizontal or vertical graphene strip gratings. The whole structure is assumed to be invariant in the  $y$  direction and is illuminated from below by a monochromatic plane wave under the angle of incidence  $\theta$ . The corresponding wavenumber is denoted  $k_0 = 2\pi/\lambda$ ,  $\lambda$  being the vacuum wavelength and the time dependence will be assumed to be  $e^{-i\omega t}$ . Here, we adopt the *Thin film's effective thickness approach* explained in the previous chapter for modelling graphene in which the graphene layer is taken into account by its equivalent relative permittivity.

## 2.2 Numerical Methods

### 2.2.1 Standard Fourier Modal Method (FMM)

The Fourier Modal (FMM) Method, also known as the rigorous coupled analysis (RCWA), is one of the most popular methods used for modeling diffraction from grat-

ings and in particular is considered as a simple and efficient tool for one-dimensional (1D) gratings analysis [1, 2, 3]. In this section, we provide a step by step presentation of this method. The departing point will be the use of curl Maxwell's equations in cartesian coordinates which can be expressed as follows:

$$\begin{cases} \partial_y E_z - \partial_z E_y = i\omega\mu_0 H_x \\ \partial_z E_x - \partial_x E_z = i\omega\mu_0 H_y \\ \partial_x E_y - \partial_y E_x = i\omega\mu_0 H_z \end{cases} \quad \begin{cases} \partial_y H_z - \partial_z H_y = -i\omega\varepsilon_0\varepsilon_r E_x \\ \partial_z H_x - \partial_x H_z = -i\omega\varepsilon_0\varepsilon_r E_y \\ \partial_x H_y - \partial_y H_x = -i\omega\varepsilon_0\varepsilon_r E_z \end{cases} \quad (2.1)$$

Since the structure is completely invariant in the  $y$  direction and since we are in the classical diffraction case (the plane of incidence corresponds to the plane of invariance of the structure), all the partial  $y$  derivatives vanish and thus the latter system decouples into two independent sub-systems one of which corresponds to the so called TE-polarization:

$$\begin{cases} \partial_z E_y = -i\omega\mu_0 H_x \\ \partial_x E_y = i\omega\mu_0 H_z \\ \partial_z H_x - \partial_x H_z = -i\omega\varepsilon_0\varepsilon_r E_y \end{cases} \quad (2.2)$$

and the other one to the TM-polarization:

$$\begin{cases} \partial_z H_y = i\omega\varepsilon_0\varepsilon_r E_x \\ \partial_x H_y = -i\omega\varepsilon_0\varepsilon_r E_z \\ \partial_z E_x - \partial_x E_z = i\omega\mu_0 H_y \end{cases} \quad (2.3)$$

The First step in the FMM is to split the computational domain into layers. For our diffraction problem, as shown in Figure 2.1, the physical space is divided into  $N + 2$  regions : the two media in the regions 0 and  $N + 1$  that are assumed to be homogeneous and the  $N$  different layers which constitute the so called modulated region. After that, the second step is to solve the wave equations everywhere and find the general expressions of the different fields before applying the boundary conditions. We consider first the TE polarization and treat afterwards the TM polarization problem.

## TE polarization

Under TE polarization, the electromagnetic field is such that  $\vec{E} = (0, E_y, 0)$  and  $\vec{H} = (H_x, 0, H_z)$ . In this case, the Electric field is expressed through its non null  $y$  component and in each layer  $q$ , it satisfies the following wave equation:

$$\frac{\partial^2 E_{qy}}{\partial x^2} + \frac{\partial^2 E_{qy}}{\partial z^2} + k_0^2 \varepsilon_q(x) E_{qy} = 0 \quad (2.4)$$

In the lower and upper homogeneous regions labeled by 0 and  $N + 1$ , the permittivity  $\varepsilon_q$  is constant and thus, the field can be written as Rayleigh expansions:

$$E_{0y}(x, z) = \sum_n \left( I_n e^{i\gamma_{in,n}z} + R_n e^{-i\gamma_{in,n}z} \right) e^{i\alpha_n x} \quad z < 0 \quad (2.5)$$

$$E_{(N+1)y}(x, z) = \sum_n \left( T_n e^{i\gamma_{out,n}(z-z_N)} + I'_n e^{-i\gamma_{out,n}(z-z_N)} \right) e^{i\alpha_n x} \quad z > z_N \quad (2.6)$$

where  $\alpha_n = \alpha_0 + Kn$  with  $\alpha_0 = k_0 \sqrt{\varepsilon_{in}} \sin\theta$  and  $K = 2\pi/d$  denotes the spatial wave vector .  $I_n = \delta_{0n}$  and  $I'_n = 0$  where  $\delta_{0n}$  stands for the Kronecker symbol. The normal components of the wave vectors  $\gamma_{in,n/out,n}$  are deduced from  $\alpha_n^2 + \gamma_{in,n/out,n}^2 = k_0^2 \varepsilon_{in/out}$  and  $R_n$  and  $T_n$  are the complex amplitudes of the  $n$ 'th reflected or transmitted diffraction order.

Let us now continue by considering the fields inside the modulated region  $0 < z < z_N$ . Using the Floquet-Bloch theorem, the electric field  $E_{qy}$  can be expanded in generalized Fourier series under the form:

$$E_{qy}(x, z) = \sum_n E_{qn}(z) e^{i\alpha_n x} \quad \forall q \in [1, \dots, N] \quad (2.7)$$

where  $E_n^q$  are the Fourier coefficients in the  $q^{\text{th}}$  layer. Moreover, since the permittivity  $\varepsilon_q(x)$  is periodic, it can be expanded in Fourier series as follows:

$$\varepsilon_q(x) = \sum_p \varepsilon_{qp} e^{iK_p x} \quad \forall q \in [1, \dots, N] \quad (2.8)$$

Substituting (2.7) and (2.8) into equation 2.4, one can find:

$$\sum_n \left( \frac{d^2 E_{qn}}{dz^2} - \alpha_n^2 E_{qn} + k_0^2 \sum_p \varepsilon_{qn-p} E_{qp} \right) e^{i\alpha_n x} = 0 \quad \forall q \in [1, \dots, N] \quad (2.9)$$

Projecting on the  $(e^{i\alpha_n x})_{n \in \mathbb{Z}}$  basis, we get:

$$\frac{d^2 E_{qn}}{dz^2} - \alpha_n^2 E_{qn} + k_0^2 \sum_p \varepsilon_{qn-p} E_{qp} = 0 \quad \forall n \in \mathbb{Z} \quad \forall q \in [1, \dots, N] \quad (2.10)$$

### Eigenvalue problem

So far, the Fourier series used in the above equations to describe the electric field and the permittivity are assumed to be infinite. At this stage and for the numerical implementation, it is necessary to work with Fourier series truncated between  $-M$  and  $+M$  where  $M$  will be called *the truncation order*. Thus, in this case, equation 2.10 can be written in Fourier space as:

$$\frac{d^2 \mathcal{E}_q(z)}{dz^2} = \left( \alpha^2 - k_0^2 \|\varepsilon_q\| \right) \mathcal{E}_q(z) \quad (2.11)$$

which can be put in the following form:

$$\mathcal{E}_q''(z) = A_q^{TE} \mathcal{E}_q(z) \quad (2.12)$$

where  $A_q^{TE} = \alpha^2 - k_0^2 \|\varepsilon_q\|$ ,  $\alpha^2 = \text{diag}(\alpha_n^2)$  and  $\mathcal{E}_q = [\dots, E_{q,-1}, E_{q,0}, E_{q,1}, \dots]^t$  is a column vector of size  $(2M + 1) \times 1$  that contains the Fourier components of the electric field.  $\|\varepsilon_q\|$  denotes the Toeplitz matrix of the permittivity in the  $q^{\text{th}}$  layer whose elements are given by  $\|\varepsilon_q\|_{ij} = \varepsilon_{q,(i-j)}$ . This equation has the standard form of a matrix eigenvalue problem and can be considered as the master equation of the Fourier modal method for the case of TE polarization. We seek solutions of the form:

$$\mathcal{E}_q(z) = e^{X_q z} \mathcal{E}_{0q} \quad (2.13)$$

Inserting this solution into equation 2.12 leads to:

$$\mathcal{E}_q(z) = e^{X_q z} \mathcal{E}_{0q} \Rightarrow X_q^2 = A_q^{TE} \quad (2.14)$$

Then, by diagonalizing the matrix  $A_{TE}^q$  for each layer, one can obtain:

$$A_q^{TE} = P_q D_q^2 P_q^{-1} \Rightarrow X_q = \pm \sqrt{P_q D_q^2 P_q^{-1}} = \pm P_q D_q P_q^{-1} \quad (2.15)$$

Where  $D_q$  is a diagonal matrix containing the complex square roots of the eigenvalues of  $A_q^{TE}$  and  $P_q$  is the matrix of the corresponding eigenvectors. According to this result, two solutions are possible:

$$\mathcal{E}_q^{1,2}(z) = P_q e^{\pm D_q z} P_q^{-1} \mathcal{E}_{0q} = P_q e^{\pm D_q z} \mathcal{E}'_{0q} \quad (2.16)$$

The first solution represents a mode that propagates and decays in the forward direction while the second solution represents a mode in the backward direction. The total field in the  $q^{th}$  layer can then be written as a linear combination of these two latter solutions:

$$\mathcal{E}^q(z) = P_q \left( e^{D_q(z-z_{q-1})} a_q + e^{-D_q(z-z_q)} b_q \right) \quad (2.17)$$

where  $a_q = [\dots, a_{q,-1}, a_{q,0}, a_{q,1}, \dots]^t$  and  $b_q = [\dots, b_{q,-1}, b_{q,0}, b_{q,1}, \dots]^t$  are the amplitudes of forward and backward propagating modes, respectively. Finally, by combining equations (2.7) and (2.17), one gets the general expression of the total field in each layer:

$$E_y^q = \sum_n \left[ \sum_p P_{q,np} \left( e^{D_{qp}(z-z_{q-1})} a_{q,p} + e^{-D_{qp}(z-z_q)} b_{q,p} \right) \right] e^{i\alpha_n x} \quad (2.18)$$

It worth mentioning here that the eigenvalues  $D_{qp}$  are chosen in such a way that  $Re(D_{qp}) + Im(D_{qp}) < 0$ .

### TM polarization

Let us now pass to the formulation of the FMM in the TM polarization case. For that, we follow a methodology similar to that laid out above. In this case, the  $y$  component of the magnetic field in each layer  $q$  fulfil the following wave equation:

$$\vec{\nabla} \cdot \left[ \frac{1}{\varepsilon_q(x)} \vec{\nabla} H_{yy}(x, z) \right] + k_0^2 H_{yy}(x, z) = 0 \quad (2.19)$$

Since  $\varepsilon_q$  is a function of  $x$  only, one can readily find:

$$\partial_x \left( \frac{1}{\varepsilon_q(x)} \partial_x H_{yy} \right) + \frac{1}{\varepsilon_q(x)} \frac{\partial^2 H_{yy}}{\partial z^2} + k_0^2 H_{yy} = 0 \quad (2.20)$$

Similarly to the TE polarization case, the magnetic fields for the homogeneous regions 0 and  $N + 1$  can be given by:

$$H_{0y}(x, z) = \sum_n \left( I_n e^{i\gamma_{in,n} z} + R_n e^{-i\gamma_{in,n} z} \right) e^{i\alpha_n x} \quad z < 0 \quad (2.21)$$

$$H_{(N+1)y}(x, z) = \sum_n \left( T_n e^{i\gamma_{out,n}(z-z_N)} + I'_n e^{-i\gamma_{out,n}(z-z_N)} \right) e^{i\alpha_n x} \quad z > z_N \quad (2.22)$$

After having written the magnetic field as well as the permittivity for each layer inside the modulated region as a pseudo-Fourier series and a Fourier series respectively and projecting into Fourier space, we get the following matrix equation:

$$\frac{d^2 \mathcal{H}_q(z)}{dz^2} = \|\varepsilon_q(x)\| \left( \alpha \left\| \frac{1}{\varepsilon_q(x)} \right\| \alpha - k_0^2 I_d \right) \mathcal{H}_q \quad (2.23)$$

$$\mathcal{H}_q''(z) = A_q^{TM} \mathcal{H}_q(z) \quad (2.24)$$

Where  $\alpha$  is a diagonal matrix whose elements are  $\alpha_n$ ,  $I_d$  is the identity matrix and  $\|\varepsilon_q(x)\|$  and  $\|\frac{1}{\varepsilon_q(x)}\|$  are The Toeplitz matrices associated with  $\varepsilon_q$  and its inverse. Unfortunately, the numerical results obtained from this formulation have shown very slow convergence and severe numerical instabilities problems, especially in the case of metallic gratings [4]. This problem owed its origin to the inadequate formulation of the eigenvalue problem and was related to the truncation process of the Fourier series which is as mentioned above inevitable for the numerical implementation of the method. In fact, this process does not preserve the continuity of certain components of the electromagnetic field at the points of discontinuity of the permittivity. Furthermore in 1996, it was found that the convergence has been improved by taking the inverse of the Toeplitz matrix of the permittivity function [5, 6]. In the same year, based on this finding, Lifeng Li investigated this problem and established a theory called Fourier factorization[7, 8].

### Fourier Factorization Rules

Let us now briefly discuss the factorization rules of Li. Consider first two periodic piecewise continuous functions  $f(x)$  and  $g(x)$  such that their product is  $h(x) = f(x)g(x)$ . In the Fourier space, their truncated Fourier coefficients are related by the so called Laurent's rule as:

$$h_n = \sum_{p=-M}^{p=M} f_{n-p}g_p \quad (2.25)$$

In order to rewrite equation 2.25 in a simple manner, let us introduce the following matrix notations. We denote by  $[g]$  the vector composed of the fourier coefficients of  $g(x)$  and by  $\|f\|$  the Toeplitz matrix whose element are given by the  $(m-n)^{th}$  Fourier coefficient of function  $f$ . Using these notations the latter equation becomes:

$$[h] = \|f\|[g] \quad (2.26)$$

The present rule has been applied without precautions for years and as pointed out above it was the main cause of the slow convergence in the TM case. The problem is that in some cases, the usual truncated Laurent Fourier series induce errors on the reconstruction of the product function  $h$ . For these special cases, Li has described three theorems of considerable importance:

- if  $f(x)$  is discontinuous and  $g(x)$  is continuous in others words if  $f$  and  $g$  have no concurrent discontinuities then the Fourier coefficient of the product  $h$  can be derived using the above Laurent's rule.
- if both  $f(x)$  and  $g(x)$  are discontinuous but  $h(x)$  is continuous, in this case, the product  $h$  should be constructed in Fourier space by the inverse rule

$$[h] = \|1/f\|^{-1}[g] \quad (2.27)$$

- if the three functions are discontinued at the same point, neither laurent's rule nor its inverse can be used.

Let us now return to the TM case and apply the correct rules in order to reformulate the eigenvalue problem. For that, taking into account the inverse rule and the continuity of the fields, the matrix  $A_{TM}^q$  can be written in a slightly different form as:

$$A_q^{TM} = \|\frac{1}{\varepsilon_q(x)}\|^{-1} (\alpha\|\varepsilon_q(x)\|^{-1}\alpha - k_0^2 I_d) \quad (2.28)$$

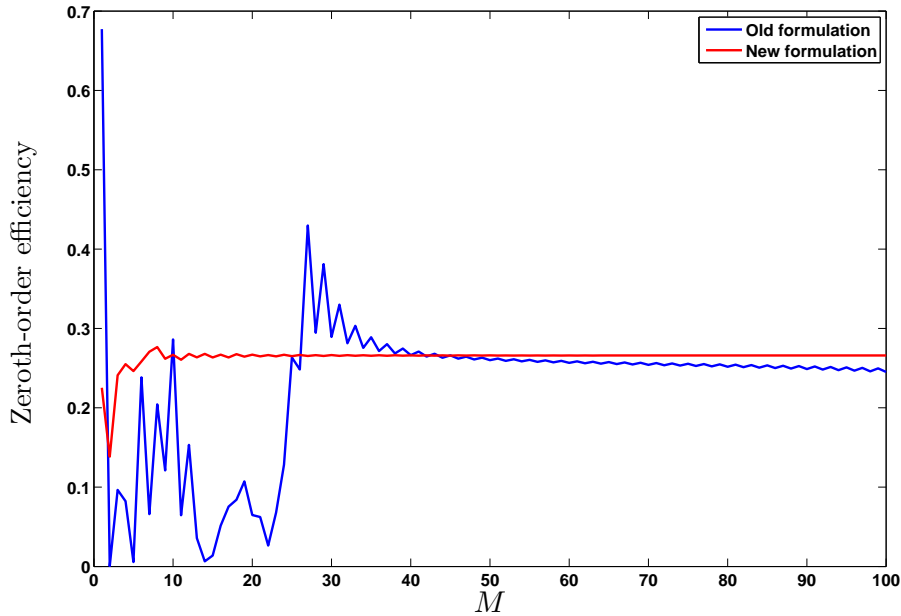


Figure 2.2: Convergence of the zeroth order diffraction efficiency of a metallic lamellar grating for TM polarized wave. the parameter are  $\theta = 30^\circ$ ,  $d = h = \lambda$ , filling factor  $f = 1/2$  and  $\varepsilon_m = (0.22 + 6.71i)^2, \varepsilon_{in} = \varepsilon_{out} = 1$

This is the empirical expression previously established by [5, 6] as a numerical solution to achieve a fast convergence rate in the analysis of lamellar gratings with the Fourier modal method. It is interesting to notice that in an infinite Fourier space, expressions 2.23 and 2.28 are equivalent. Whereas, in the case where the Fourier series are truncated, the new formulation ensures better convergence. To show the efficiency of this new formulation, we plot in Figure 2.2 the convergence behavior of the zeroth order diffraction efficiency using both the old formulation and the new one. It can be clearly seen that this new formulation allows to improve considerably the convergence of the FMM method.

### Amplitudes of the diffracted fields

After solving the eigenvalue problem and deriving the general expression of the total field in each layer, the next step is to determine the unknown amplitudes of the modes that appear in the fields expressions. We start first by applying the boundary conditions at the interfaces between the different regions. This leads to a linear system of algebraic equations linking the unknown coefficients that are then determined by solving this system by using the so called S-matrix algorithm.

### Boundary conditions

In the Fourier modal method enforcing the boundary conditions consists of imposing the continuity of the tangential components of the fields at each interface. First of all, we need to recall the expressions of the fields in each region for both TE and TM

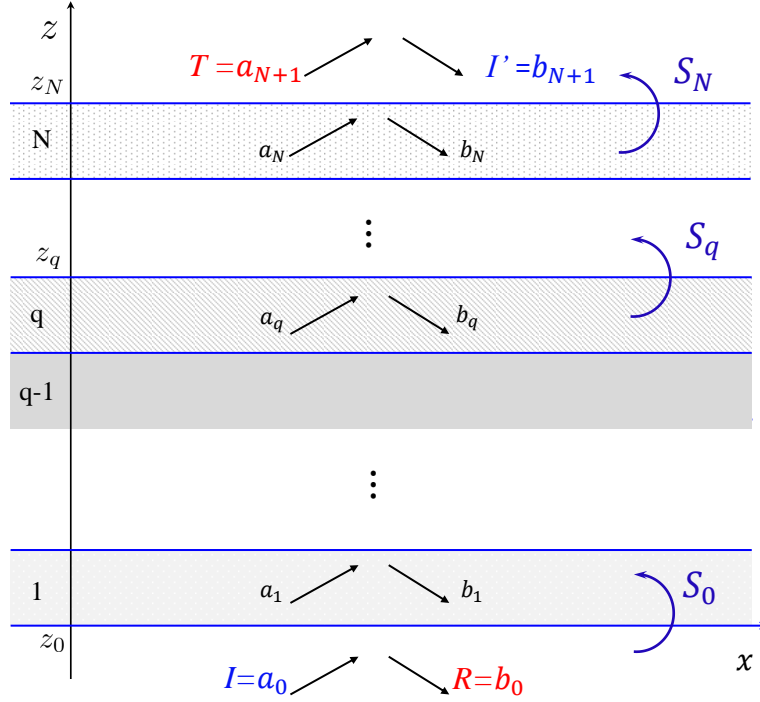


Figure 2.3: Schematic representation of the modes and the scattering matrices in a stratified medium

polarisation:

$$U_0(x, z) = \sum_n \left( I_n e^{i\gamma_{in,n}z} + R_n e^{-i\gamma_{in,n}z} \right) e^{i\alpha_n x} \quad z < 0 \quad (2.29)$$

$$U_{N+1}(x, z) = \sum_n \left( T_n e^{i\gamma_{out,n}(z-z_N)} + I'_n e^{-i\gamma_{out,n}(z-z_N)} \right) e^{i\alpha_n x} \quad z > z_N \quad (2.30)$$

$$U_q = \sum_n \left[ \sum_p P_{q,np} \left( e^{D_{qp}(z-z_{q-1})} a_{q,p} + e^{-D_{qp}(z-z_q)} b_{q,p} \right) \right] e^{i\alpha_n x} \quad 0 < z_q < z_N \quad (2.31)$$

where  $U_q(x, z)$  stands for  $E_{qy}(x, y)(H_{qy}(x, y))$  in the TE (TM) polarization case. The other tangential component, the  $x$  component of the field, needed for the above boundary conditions, is deduced from Maxwell's equations :

TE	TM
$H_x = (i/k_0 Z_0 \mu) \partial_z E_y$	$E_x = -i Z_0 / (k_0 \varepsilon) \partial_z H_y$

(2.32)

For  $z = 0$ :

$$\text{TE} \begin{cases} E_{0y}(x, 0) = E_{1y}(x, 0) \\ H_{0x}(x, 0) = H_{1x}(x, 0) \end{cases} \quad \text{TM} \begin{cases} E_{0x}(x, 0) = E_{1x}(x, 0) \\ H_{0y}(x, 0) = H_{1y}(x, 0) \end{cases} \quad (2.33)$$

Replacing with the field expressions stated above, we obtain in matrix notation:

$$\begin{cases} (I + R) = P_1(a_1 + b_1 \phi_1) \\ i\gamma_{in}(I - R) = P'_1(a_1 - b_1 \phi_1) \end{cases} \quad (2.34)$$

with  $\phi_1 = e^{D_1 z_1}$  and  $P'_1 = P_1 D_1$  for TE polarisation and  $P'_1 = \left\| \frac{1}{\varepsilon_1(x)} \right\| P_1 D_1$  for TM Polarization. For  $z = z_q$ , we get:

$$\begin{cases} P_q(\phi_q a_q + b_q) = P_{q+1}(a_{q+1} + \phi_{q+1} b_{q+1}) \\ P'_q(\phi_q a_q - b_q) = P'_{q+1}(a_{q+1} - \phi_{q+1} b_{q+1}) \end{cases} \quad (2.35)$$

where  $\phi_q = e^{D_q(z_q - z_{q-1})}$  and  $\phi_{q+1} = e^{D_{q+1}(z_q - z_{q+1})}$ .  $P'_q = P_q D_q$  for TE polarization and  $P'_q = \frac{1}{\varepsilon_q(x)} P_q D_q$  for TM Polarization .

And for  $z = z_N$ :

$$\begin{cases} P_N(\phi_N a_N + b_N) = (T + I') \\ P'_N(\phi_N a_N - b_N) = i\gamma_{out}(T - I') \end{cases} \quad (2.36)$$

With  $\phi_N = e^{D_N(z_N - z_{N-1})}$ .

Note that here  $R = [\dots, R_{-1}, R_0, R_1 \dots]^t$  and  $T = [\dots, T_{-1}, T_0, T_1 \dots]^t$  are the vectors composed of amplitudes of the reflected and transmitted diffraction orders. While  $I = [\dots, 0, 1, 0 \dots]$  and  $I' = [\dots, 0, 0, 0 \dots]$  are the vectors composed of the amplitudes of incident waves. Thus, we end up with a set of  $2N + 2$  algebraic equations linking  $2N + 2$  unknown coefficients  $a_q$  and  $b_q$ . Many algorithms can be used to solve this system. Among these, the most efficient and stable one is the S-matrix algorithm that will be described in detail hereafter.

### Scattering matrix Formalism

In this section, we will adopt the S-matrix formalism for our general multilayered grating problem in order to calculate the amplitudes of the diffracted field and show how to construct the global scattering matrix of the whole structure from the combination of the transition matrices obtained for each interface  $z = z_q$  by the use of a cascading process (see figure 2.3). By definition, the scattering matrix provide a relation between the outgoing amplitudes and the incoming ones and is given as follows:

$$\begin{pmatrix} b_q \\ a_{q+1} \end{pmatrix} = S_q \begin{pmatrix} a_q \\ b_{q+1} \end{pmatrix} \quad (2.37)$$

From equation (2.34), one can deduce the scattering matrix corresponding to the interface  $z = z_0$ :

$$\begin{pmatrix} b_0 \\ a_1 \end{pmatrix} = \begin{pmatrix} -P_0 & P_1 \\ P'_0 & P'_1 \end{pmatrix}^{-1} \begin{pmatrix} P_0 & -P_1 \\ P'_0 & P'_1 \end{pmatrix} \begin{pmatrix} I_d & 0 \\ 0 & \phi_1 \end{pmatrix} \begin{pmatrix} a_0 \\ b_1 \end{pmatrix} \quad (2.38)$$

$$\begin{pmatrix} b_0 \\ a_1 \end{pmatrix} = S_0 \begin{pmatrix} a_0 \\ b_1 \end{pmatrix} \quad (2.39)$$

$$S_0 = \begin{pmatrix} -P_0 & P_1 \\ P'_0 & P'_1 \end{pmatrix}^{-1} \begin{pmatrix} P_0 & -P_1 \\ P'_0 & P'_1 \end{pmatrix} \begin{pmatrix} I_d & 0 \\ 0 & \phi_1 \end{pmatrix} \quad (2.40)$$

In the same way, from (2.35), we can get:

$$\begin{pmatrix} b_q \\ a_{q+1} \end{pmatrix} = \begin{pmatrix} -P_q & P_{q+1} \\ P'_q & P'_{q+1} \end{pmatrix}^{-1} \begin{pmatrix} P_q & -P_{q+1} \\ P'_q & P'_{q+1} \end{pmatrix} \begin{pmatrix} \phi_q & 0 \\ 0 & \phi_{q+1} \end{pmatrix} \begin{pmatrix} a_q \\ b_{q+1} \end{pmatrix} \quad (2.41)$$

$$\begin{pmatrix} b_q \\ a_{q+1} \end{pmatrix} = S_q \begin{pmatrix} a_q \\ b_{q+1} \end{pmatrix} \quad (2.42)$$

$$S_q = \begin{pmatrix} -P_q & P_{q+1} \\ P'_q & P'_{q+1} \end{pmatrix}^{-1} \begin{pmatrix} P_q & -P_{q+1} \\ P'_q & P'_{q+1} \end{pmatrix} \begin{pmatrix} \phi_q & 0 \\ 0 & \phi_{q+1} \end{pmatrix} \quad (2.43)$$

For  $z = z_N$ , we find:

$$\begin{pmatrix} b_N \\ a_{N+1} \end{pmatrix} = \begin{pmatrix} -P_N & P_{N+1} \\ P'_N & P'_{N+1} \end{pmatrix}^{-1} \begin{pmatrix} P_N & -P_{N+1} \\ P'_N & P'_{N+1} \end{pmatrix} \begin{pmatrix} \phi_N & 0 \\ 0 & I_d \end{pmatrix} \begin{pmatrix} a_N \\ b_{N+1} \end{pmatrix} \quad (2.44)$$

$$\begin{pmatrix} b_N \\ a_{N+1} \end{pmatrix} = S_N \begin{pmatrix} a_N \\ b_{N+1} \end{pmatrix} \quad (2.45)$$

$$S_N = \begin{pmatrix} -P_N & P_{N+1} \\ P'_N & P'_{N+1} \end{pmatrix}^{-1} \begin{pmatrix} P_N & -P_{N+1} \\ P'_N & P'_{N+1} \end{pmatrix} \begin{pmatrix} \phi_N & 0 \\ 0 & I_d \end{pmatrix} \quad (2.46)$$

Therefore, the global S-matrix connecting the reflection and transmission coefficients can be expressed as:

$$\begin{pmatrix} R \\ T \end{pmatrix} = S \begin{pmatrix} I \\ I' \end{pmatrix} \quad (2.47)$$

$$S = S_0 \star S_1 \star \dots \star S_N \quad (2.48)$$

where the  $\star$  product  $S = S^a \star S^b$  between two matrices  $S^a$  and  $S^b$  is given by:

$$\begin{cases} S_{11} = S_{11}^a + S_{12}^a (1 - S_{11}^b S_{22}^a)^{-1} S_{11}^b S_{21}^a \\ S_{12} = S_{12}^a (1 - S_{11}^b S_{22}^a)^{-1} S_{12}^b \\ S_{21} = S_{21}^b (1 - S_{22}^a S_{11}^b)^{-1} S_{21}^a \\ S_{22} = S_{22}^b + S_{21}^b (1 - S_{22}^a S_{11}^b)^{-1} S_{22}^a S_{12}^b \end{cases} \quad (2.49)$$

Finally, once this calculation is achieved and thereby the amplitudes of the diffracted fields are obtained, one can readily have access to the quantities of interests such as the diffraction efficiency and fields distributions

## 2.2.2 Fourier Modal Method with spatial adaptative resolution (FMM-ASR)

In the previous section, we have shown that the Fourier Modal method suffers from a slow convergence problems in the case of TM polarisation. This has been overcome by applying the correct Fourier factorisation rules for discontinuous functions. Although this implementation has tremendously improved the convergence of the FMM method, there remained the problem of so called Gibbs phenomenon at the discontinuity points which inhibit the convergence of the Fourier series yielding to a slow convergence, especially in the case of metallic gratings. To tackle this latter limitation and accelerate the convergence, Granet suggested in 1999 [9] to employ a new coordinate system that increases the spatial resolution in the neighborhood of the discontinuities of the permittivity profile by stretching the coordinate around them. This concept is known as *Adaptative Spatial resolution* (ASR). In 2001, the original approach proposed by Granet, was extended and reformulated for treating multilayered gratings with different transitions [10]. This latter modified approach involved two main steps, the first one is to solve the eigenvalue problem for each layer with its own transformed coordinate system and the second step is to bring all the fields back to the original space for solving the boundary conditions. Despite the effectiveness of this modified formulation, it had a major drawback : the computation of transformation matrices for each layer destroys the stability of the S-matrix and it requires a nonnegligible additional computation time. Later, in [11, 12], a numerical improvement of the FMM ASR was obtained by introducing a much more stable formulation of the eigenvalue problem. They proposed an elegant and smart way consisting of solving merely the eigenvalue problem for only one homogeneous region and deducing then the solution of all the eigenvalue problems corresponding to remaining homogeneous regions from this one. This allowed to avoid to solving the eigenvalue problem in all the homogeneous regions leading to drastic reduction of the computational load. In this section, we are going to describe

the mathematical foundations of the FMM ASR Method following the derivation of [11, 12] but we will slightly reformulate the eigenvalue problem and apply a few minor modifications to achieve a more stable formulation for modelling multigrating systems.

### Foundations of the Method

Let us begin by the description of the general concepts and the Foundations of the FMM ASR method. We have mentioned above that the classical formulation of the FMM method is known to be slowly converging. The main reason of this slow convergence is that this latter is directly related to the permittivity contrast in the grating region. To solve this problem, we introduce the parametric representation by choosing a new coordinate system in such a way that the mapping space corresponds to the variations of the periodic function of the dielectric permittivity. For that, we need first to define a function  $x = x(u)$  which here is chosen to be in accordance with what is proposed in [10]:

$$x(u) = F(u) = a_1 + a_2u + \frac{a_3}{2\pi} \sin 2\pi \left( \frac{u - u_{l-1}}{u_l - u_{l-1}} \right) \quad u_{l-1} \leq u \leq u_l \quad (2.50)$$

such that:

$$a_1 = \frac{u_l x_{l-1} - u_{l-1} x_l}{u_l - u_{l-1}} \quad (2.51)$$

$$a_2 = \frac{x_l - x_{l-1}}{u_l - u_{l-1}} \quad (2.52)$$

$$a_3 = G(u_l - u_{l-1}) - (x_l - x_{l-1}) \quad (2.53)$$

Where  $G = f(u_{l-1}) = f(u_l)$  with  $f(u)$  denoting the resolution function and is determined by the dependance between  $x$  and  $u$  as  $f(u) = \partial x / \partial u$ . ( $G$  is an almost zero constant and is generally taken equal to  $10^{-4}$  or  $10^{-5}$ ). The  $x_l$  are the transition points in the  $x$  space and  $u_l$  are their counterparts in  $u$  space. Figure 2.4 represents the above

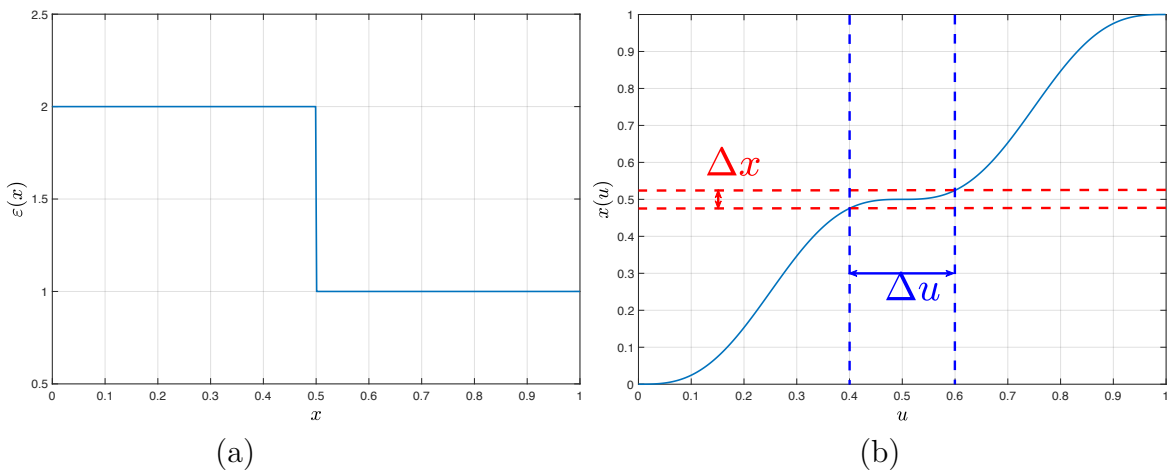


Figure 2.4: Dependence between  $x$  and  $u$  (a) Profile of the grating dielectric permittivity. (b) change of variable  $x = x(u)$

coordinate transformation function. One can clearly see that around the transition points a given variation  $\Delta u$  of  $u$  result in a smaller variation  $\Delta x$  of  $x$ . We can also notice that this change of variable does not keep the same discontinuity positions. Indeed,

the discontinuities in the new basis can differ from the old basis and their positions are given by dividing the period  $d$  into equal parts according to the number of transitions. Furthermore, the new function is a periodic function with the same period as the dielectric permittivity of the grating and its derivative is minimal at the discontinuities points.

### Eigenvalue problem

We apply now the above variable change, then we get :

$$\frac{\partial}{\partial x} \rightarrow \frac{\partial u}{\partial x} \frac{\partial}{\partial u} = \frac{1}{f} \frac{\partial}{\partial u} \quad (2.54)$$

Using this notation equations 2.4 and 2.20 become:

$$\frac{1}{f} \frac{\partial}{\partial u} \left( \frac{1}{f} \frac{\partial E_{qy}}{\partial u} \right) + \frac{\partial^2 E_{qy}}{\partial z^2} + k_0^2 \varepsilon_q(u) E_{qy} = 0 \quad (TE) \quad (2.55)$$

$$\frac{1}{f} \frac{\partial}{\partial u} \left( \frac{1}{\varepsilon_q(u)} \frac{1}{f} \frac{\partial H_{qy}}{\partial u} \right) + \frac{1}{\varepsilon_q(u)} \frac{\partial^2 H_{qy}}{\partial z^2} + k_0^2 H_{qy} = 0 \quad (TM) \quad (2.56)$$

In the  $u$  space the fields  $E_y$  and  $H_y$  are also pseudoperiodic with period  $d$  and thus they can be expressed as a pseudo-Fourier series:

$$U_q(u, z) = \sum_n U_{qn}(z) e^{i\alpha_n u} \quad (2.57)$$

Where  $U^q$  represents either the transverse electric field for the TE polarization or transverse magnetic field for the TM polarization. Now, inserting the expansion (2.57) into (2.55) and (2.56), written in Fourier space and using the correct rules of Fourier factorization and the matrix notations, we obtain the desired eigenvalue problem:

$$\frac{d^2 \mathcal{E}_q(z)}{dz^2} = \left( \left\| \frac{1}{f} \right\| \alpha \left\| \frac{1}{f} \right\| \alpha - k_0^2 \varepsilon_q \right) \mathcal{E}_q(z) = A_q^{TE} \mathcal{E}_q(z) \quad (TE) \quad (2.58)$$

$$\frac{d^2 \mathcal{H}_q(z)}{dz^2} = \left\| \frac{1}{\varepsilon_q(x)} \right\|^{-1} \left( \left\| \frac{1}{f} \right\| \alpha \left\| \varepsilon_q(x) \right\|^{-1} \left\| \frac{1}{f} \right\| \alpha - k_0^2 I_d \right) \mathcal{H}_q = A_q^{TM} \mathcal{H}_q \quad (TM) \quad (2.59)$$

With  $\left\| \frac{1}{f} \right\|$  being the Toeplitz matrix formed from the fourier coefficients of  $1/f$ . Having chosen a fitting coordinate  $u$  and solving the corresponding eigenvalue problem, the fields in each region  $q$  can be written in the same way as for the FMM method as:

$$U_q = \sum_n \left[ \sum_p P_{q,np} \left( e^{D_{qp}(z-z_{q-1})} a_{q,p} + e^{-D_{qp}(z-z_q)} b_{q,p} \right) \right] e^{i\alpha_n u} \quad q \in [0 \dots N + 1] \quad (2.60)$$

where  $a_{q,p}$  and  $b_{q,p}$  are the unknown amplitudes that are to be determined by matching boundary conditions. It is important at this stage to emphasize that the exact eigenvalues do not depend on the chosen coordinates. While, the eigenvectors depend on the choice of the coordinate system and should therefore be projected on the same basis for applying the boundary conditions.

Now, To find the unknown coefficients and afterwards the total fields expressions in all the regions, we proceed as follows: First, we still work completly in the transformed

space  $u$  using only one coordinate system  $x(u)$  for all the regions of the structure. In this situation, it is necessary to solve the eigenvalue problem in each layer and even in the incident and transmission regions. Let us begin with the incident region. The eigenvalue equation corresponding to this region can be given for both TE and TM polarisation by the following equation:

$$\frac{d^2\mathcal{U}_0(z)}{dz^2} = \left( \left\| \frac{1}{f} \right\| \alpha \left\| \frac{1}{f} \right\| \alpha - k_0^2 \varepsilon_{in} I_d \right) \mathcal{U}_0(z) = A_0 \mathcal{U}_0(z) \quad (2.61)$$

$$A_0 = \left\| \frac{1}{f} \right\| \alpha \left\| \frac{1}{f} \right\| \alpha - k_0^2 \varepsilon_{in} I_d \quad (2.62)$$

Then, After solving this eigenvalue problem, we can get  $U^0$  in terms of the eigenvalue matrix  $D_0$  and the corresponding eigenvector matrix  $P_0$  as follows:

$$U_0 = P_0 (e^{D_0 z} a_0 + e^{-D_0 z} b_0) \quad (2.63)$$

Consider now another homogeneous layer labeled by  $q$  and characterized by its permittivity  $\varepsilon_q$ . The  $A^q$  matrix that corresponds to this medium can be written as:

$$A_q = \left\| \frac{1}{f} \right\| \alpha \left\| \frac{1}{f} \right\| \alpha - k_0^2 \varepsilon_q I_d \quad (2.64)$$

Subtracting (2.64) and (2.62), One gets :

$$A_q = A_0 + k_0^2 (\varepsilon_{in} - \varepsilon_q) I_d \quad (2.65)$$

Left multiplying by  $P_0$  and right multiplying by its inverse gives:

$$P_0 A_q P_0^{-1} = D_0^2 + k_0^2 (\varepsilon_0 - \varepsilon_q) I_d \quad (2.66)$$

From this equation, one can clearly see that  $P_0$  can be also an eigenvector of  $A_q$  associated to the eigenvalues  $D_0^2 + k_0^2 (\varepsilon_0 - \varepsilon_q) I_d$ . As a result, all the homogeneous regions are equivalent to the incident one since they share the same eigenvectors. Once the eigenvalues for all layers are solved and all field expressions are determined in space  $u$ , by following the same way as we did in the classical FMM such that applying the boundary conditions and using the S-matrix algorithm, one can easily find the distribution of the fields and then all diffraction efficiencies. The final step in our strategy is to transformed back the fields to the original space  $x$ . To this end, it is necessary to projet the term  $e^{i\alpha_n u}$  on the Fourier basis in  $x$  space. This can be achieved by the help of the transformation matrix  $[K]$ , whose elements  $(p, m)$  are given by:

$$[K]_{pm} = \frac{1}{d} \int_0^d f(u) \exp(-i\alpha_p x(u) + i\alpha_m u) du \quad (2.67)$$

Hence, all vectors  $U^u$  defined in the new coordinate system  $(u, y, z)$  can be straightforwardly transformed in the originate cartesian system  $(x, y, z)$  as follows:

$$U^x = [K] U^u \quad (2.68)$$

In the end, it should be pointed out that this way of proceeding has the great advantage of using the same Fourier basis for all layers. This allows to write the continuity equations of the electromagnetic field through the interfaces without projecting this one on the common basis of the original  $x$  space leading to a significant reduction of the computational cost. Another advantage for this strategy is that it allows to avoid the instability problems coming from the transformation matrix  $[K]$ .

### 2.2.3 Aperiodic Fourier Modal Method: FMM with PML

So far, we have shown that the FMM method is a versatile and powerful tool for modelling periodic structures. However, several systems in nanophotonics are non-periodic structures such that optical resonators [13], photonic crystal fibers [14], individual metallic nano-particles [15] and photonic crystal waveguides [16]. Hence, it is of great importance to investigate the optical properties of non-periodic structures. One simple and efficient way to simulate a general aperiodic structure by the use of the FMM method, is to insert artificial absorbing layers in the boundaries between adjacent periods in order to truncate the infinite periodic system volume to a finite volume. These absorbing layers should completely inhibit the interactions between neighboring periods by minimizing backward parasitic reflections of light into the structure. In fact, the scattered light in a period is absorbed by these layers without reflection and the fields at the period boundary should decrease to zero. In this way, the single periods can be considered as isolated systems (see Figure 2.5). Such layer is called perfectly matched

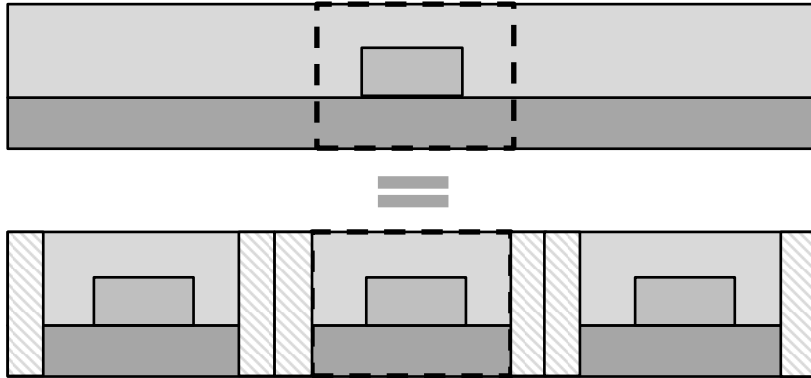


Figure 2.5: Schematic illustration of a aperiodic structure (a single rectangular groove) and its equivalent artificially periodized system

layer (PML) and was first proposed by Berenger [17] in 1994 for the finite-difference time domain (FDTD) method. Later, the original approach was extended to three dimensions by Katz and al [18] and to anisotropic media by Sacks and al [19]. Another interesting formulation of The (PML) technique was introduced by Chew and al [20] through the complex coordinate stretching concept which is essentially the analytical extension of the electromagnetic field in the complex space. It is on this last approach that we will focus in the following.

In practical computations, the PML can be introduced in the computational domain using a coordinate transformation. By this coordinate transformation, the boundaries exist in a complex space providing absorbing boundary conditions without reflection. Furthermore, the new absorbing coordinate system does not change Maxwell's equations as well as the wave propagation equation into the PML layer. An example of a complex coordinate transformation can be given by:

$$S(x) = \begin{cases} 1 - i\eta & \text{if } x \in [0, e_{PML}] \cup [d - e_{PML}, d] \\ 1 & \text{otherwise} \end{cases} \quad (2.69)$$

Inside the PML, the complex variable change  $\tilde{x}$  is expressed as:

$$\tilde{x} = \int_0^x S(x) dx \quad (2.70)$$

Where  $e_{PML}$  is the thickness of the PML layer and  $\eta$  the attenuation factor of the PML. By Applying the above variable change, the partial derivative in the complex coordinates reads:

$$\frac{\partial}{\partial \tilde{x}} = \frac{\partial x}{\partial \tilde{x}} \frac{\partial}{\partial x} = \frac{1}{S(x)} \frac{\partial}{\partial x} \quad (2.71)$$

Now, to combine the FMM with the PML, we will follow the same reasoning as the one used in the case of The FMM-ASR. First, we begin by solving the eigenvalue problem in the new coordinate  $\tilde{x}$ , then second we bring back all to the original coordinate  $x$ . Using this transformation, written in Fourier space and using the correct rules of Fourier factorization, the matrices  $A_{TE}$  and  $A_{TM}$  resulting from the eigenvalue problems for the TE and TM polarisations are written as:

$$A_{TE} = \left( \left\| \frac{1}{S} \right\| \alpha \left\| \frac{1}{S} \right\| \alpha - k_0^2 \varepsilon_q \right) \quad (TE) \quad (2.72)$$

$$A_{TM} = \left\| \frac{1}{\varepsilon_q(x)} \right\|^{-1} \left( \left\| \frac{1}{S} \right\| \alpha \left\| \varepsilon_q(x) \right\|^{-1} \left\| \frac{1}{S} \right\| \alpha - k_0^2 I_d \right) \quad (TM) \quad (2.73)$$

Finally, once the eigenvalues and their corresponding eigenvectors are calculated, we can determine the total fields expressions by following a procedure similar to that described above for the FMM-ASR case *i.e* by using the S-matrix algorithm after matching the boundary conditions.

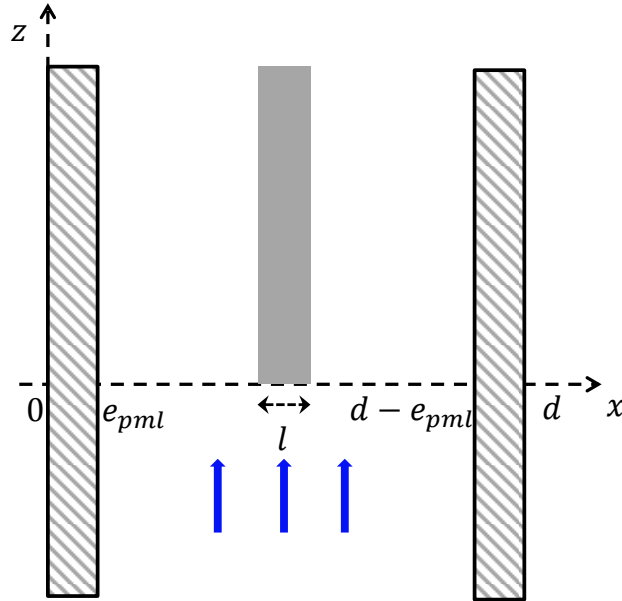


Figure 2.6: the diffraction problem of an electromagnetic plane wave by a perfectly conducting infinite rectangular bar.

We illustrate the efficiency of the PML technique by considering the example of the diffraction of an electromagnetic plane wave by a perfectly conducting infinite rectangular bar. As shown in Figure 2.6, a monochromatic plane wave falls on a bar of width  $L = \lambda$  from the vacuum ( $z < 0$ ) under normal incidence. Figure 2.7 plotted the maps of the diffracted field obtained for  $d = \lambda$ ,  $e_{PML} = 4\lambda$ ,  $\eta = 2$ . The upper panel in this Figure shows the results with PMLs layers while the lower one shows those without PMLs. It can be, clearly, seen that there are interferences in the absence of PMLs stemming from interactions between the different fields scattered from each

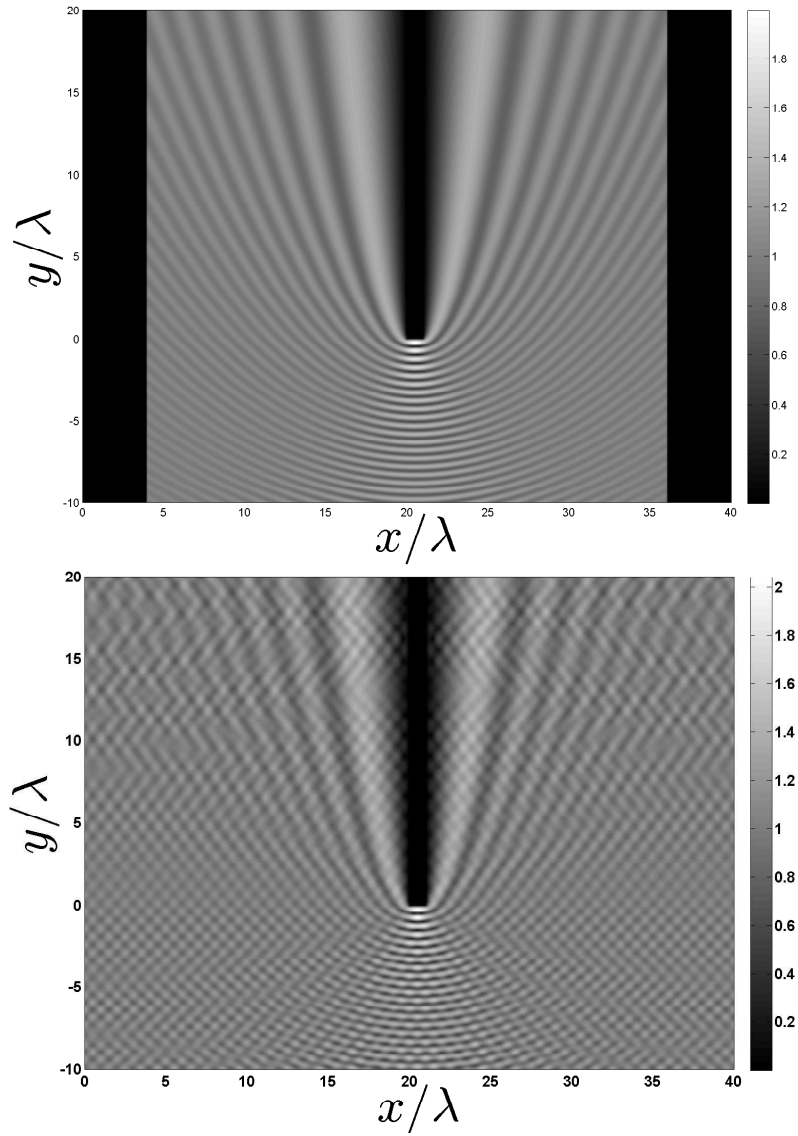


Figure 2.7: Maps of a diffracted field by a perfectly conductive infinite rectangular bar computed by the use of FMM with PMLs (the upper panel) and without PMLs layers (the lower panel). The parameters are  $d = \lambda, L = \lambda, e_{PML} = 4\lambda$  and  $\eta = 2$ .

elementary period. These spurious fields are completely absent when the PML technique is used.

## 2.3 Numerical Examples involving graphene: Graphene-Strip Gratings

This section attempts to answer the question of the suitability of the above described numerical methods for the modelling of diffraction properties of graphene based periodic structures. For doing so, we apply these methods to two different structures. The first structure consisting of a periodic arrangement of horizontal graphene strips and the second structure is an infinite periodic array of graphene vertical strips. Numerical tests of all methods with respect to convergence and stability is also provided in order to test the validity and efficiency of each one.

### 2.3.1 Graphene horizontal strips grating

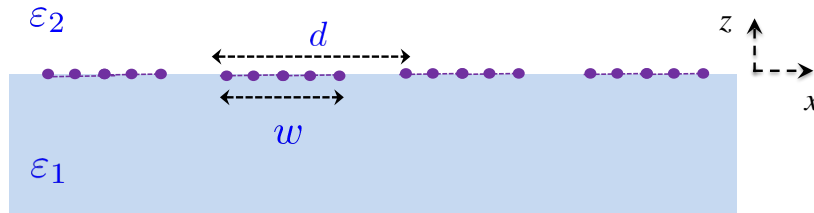


Figure 2.8: sketch of the studied structure: a periodic grating of graphene ribbons of width  $w$  and period  $d$ . The grating is inlayed between two dielectric media with permittivities  $\varepsilon_1$  and  $\varepsilon_2$

Let us start by illustrating the first structure which is depicted in Figure 2.8. It consists of a 1D graphene ribbons array with width  $w$  and period  $d$  surrounded by two dielectric media with permittivities  $\varepsilon_1$  and  $\varepsilon_2$ . The graphene array is located on the  $xy$  plane and the whole structure is invariant in the  $y$  direction. Note that here, we are only interested to treat the TM polarization case. In order to test and verify the validity of each method, we consider the example of an array of graphene with the following parameters:  $d = 8\mu\text{m}$ ,  $w = d/2$ ,  $\varepsilon_1 = 3, \varepsilon_2 = 4$ ,  $\tau = 1/\Gamma = 0.25\text{ps}$  and  $\mu_c = 0.6\text{eV}$ . Figure 2.9 shows the absorption of the given structure as a function of wavelength calculated at normal incidence. The results are obtained using the FMM method (blue solid line) and the FMM equipped with the concept of adaptative spatial resolution(ASR)(circles) for a fixed truncation order  $M = 100$ . We observe a resonance peak around  $\lambda = 78\mu\text{m}$  and we can clearly see a good agreement between the two methods.

To show the convergence behavior of each method, we plot the absorption of the structure at the resonance wavelength ( $\lambda = 78\mu\text{m}$ ) for different truncation orders as shown in Figure 2.10. The results obtained using the technique of adaptative spatial resolution are compared against those computed by the use of the conventional FMM with the correct Fourier factorization method. Red solid line shows the convergence rate of the FMM method and the results of the FMM-ASR are shown by the blue solid line. One can observe a very good convergence rate with the FMM-ASR method. Indeed, the curve corresponding to this latter method converges rapidly and for a rather small truncation order  $M \simeq 10$ . Whereas, the FMM curve tends towards that of the FMM-ASR, but converges rather slowly from a truncation order  $M \simeq 50$ . This comparison shows that both methods can deal with this kind of diffraction problems

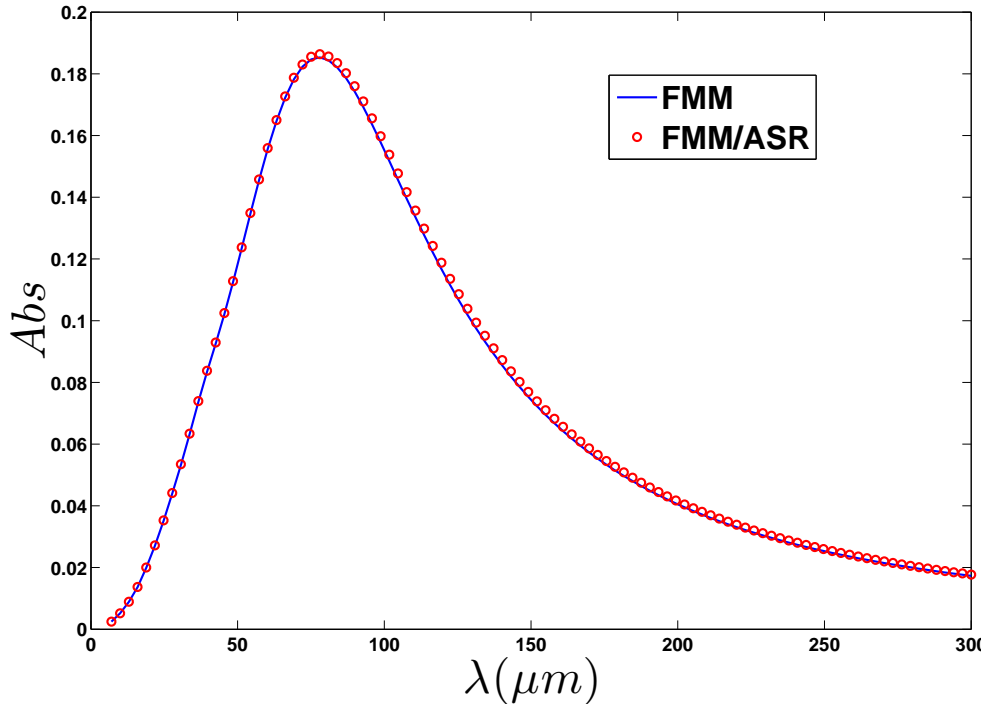


Figure 2.9: Absorption versus wavelength for a periodic array of graphene ribbons in TM polarisation with normal incidence. The parameters are  $\varepsilon_1 = 3, \varepsilon_2 = 4, \mu_c = 0.6eV$  and  $\tau = 1/\Gamma = 0.25ps$ . The results are obtained by using The FMM method (blue solid line) and the FMM-ASR Method (circles).

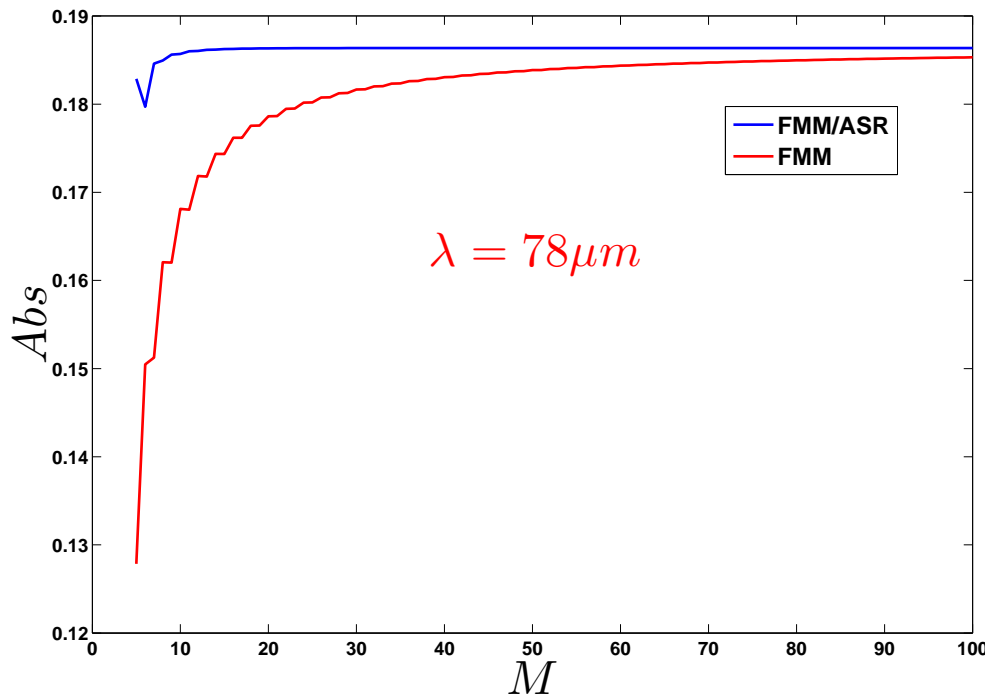


Figure 2.10: Convergence curves versus the truncation order obtained for  $\lambda = 78\mu m$ . Red solid line shows the FMM method and the blue line shows the FMM-ASR results. The parameters are the same as figure 2.9

but the FMM-ASR is more suitable since it brings an improvement and enhancement of the computational efficacy in this case.

### 2.3.2 Graphene Vertical strips grating

Let us pass now to the second diffraction problem. We consider the structure shown in Figure 2.11 in which the space is divided into three regions. Region 1 ( $z \leq 0$ ) and Region 3 ( $z \geq h$ ) are assumed to be dielectric and homogenous with relative dielectric permittivities  $\varepsilon_1$  and  $\varepsilon_3$ . Region 2 is the grating region. It consists of identical vertical strips periodically inlaid in a homogeneous dielectric medium of relative dielectric permittivity  $\varepsilon_2$ . The period and the height of the grating are  $d$  and  $h$ , respectively. A TM-polarized monochromatic plane wave is obliquely incident on the structure from the lower medium and the graphene grating is assumed to be invariant along the  $y$  direction. Similarly to the first case, we consider a numerical example with the parameters  $d = 8\mu\text{m}$ ,  $h = 1\mu\text{m}$ ,  $\mu_c = 0.6eV$  and  $\theta = 50^\circ$ .

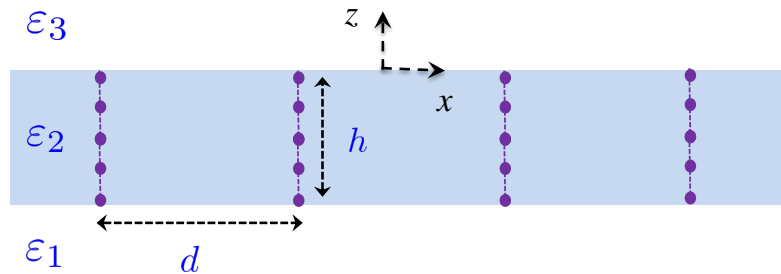


Figure 2.11: Structure geometry: a periodic grating of vertical strips of graphene

It should be noted that this configuration, could constitute a pathological case because of its extremely small filling ratios  $f$  which is given by  $f = \delta_g/d = 0.34 \times 10^{-9}/d \propto 10^{-3}$ . This would lead to use a high truncation number  $M$  and thus large computational times.

This is why in such a situation, we choose to use the FMM-ASR. Figure 2.12 shows the absorption versus the wavelength. As in the previous case a resonance peak is observed around  $\lambda = 19.82\mu\text{m}$  which probably corresponds to the excitation of surface plasmons polaritons over graphene strips. Let us now study the convergence of this method for the structure. The convergence of the absorption computed by the help of the FMM-ASR as the truncation order increases is plotted in the Figure 2.13. It can be seen that the absorption converges remarkably fast with truncation order as low as 20. We can also clearly see that it remains stable even for large truncation orders. As a result, we can conclude that the FMM with the ASR concept can provide accurate and stable results which makes it promising and suitable for studying these kind of pathological structures. After checking the rapidity of the convergence of the FMM-ASR and being ensured of its stability. We use it now to plot the spatial distribution of the electromagnetic field for a better understanding of the nature of the mode. Figure 2.14 shows the spatial distribution of the mode corresponding to the resonance peak where the real part of the  $y$  component of the magnetic field is drawn and where the different interfaces  $z = 0$  and  $z = h$  are indicated by dashed white lines. From this figure, one can see that the field is mostly localized at the graphene vertical strips which confirms our above assumption that the mode corresponds to a GSP mode.

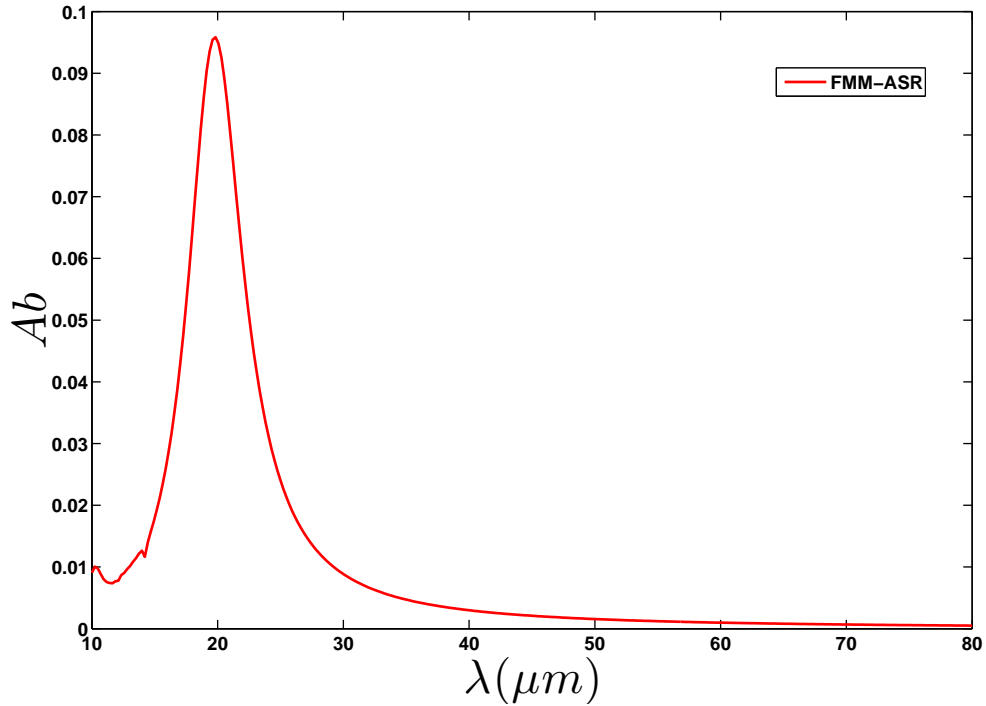


Figure 2.12: Absorption versus wavelength for a free standing graphene periodic vertical strips grating in TM polarization whose parameters are  $d = 8\mu\text{m}$ ,  $h = 1\mu\text{m}$ ,  $\varepsilon_1 = \varepsilon_2 = \varepsilon_3 = 1$ ,  $\mu_c = 0.6\text{eV}$  and  $\theta = 50^\circ$ . The results are obtained using the FMM-ASR method for truncation order  $M = 100$

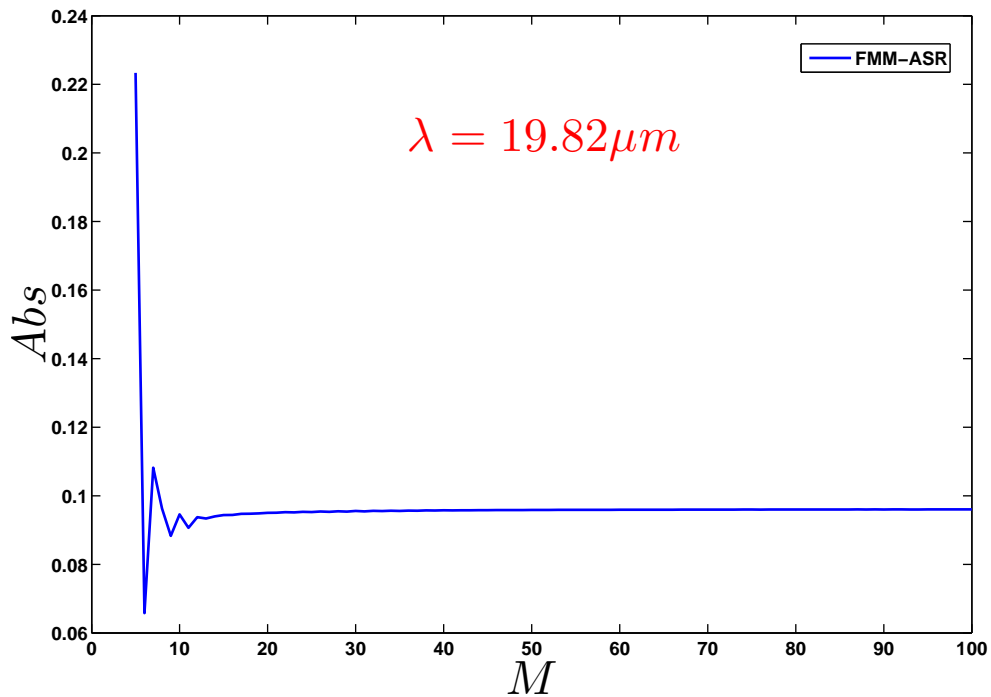


Figure 2.13: Convergence behavior of the absorption in terms of truncation order at  $\lambda = 19.82\mu\text{m}$ . The structure is the same in Figure 2.12

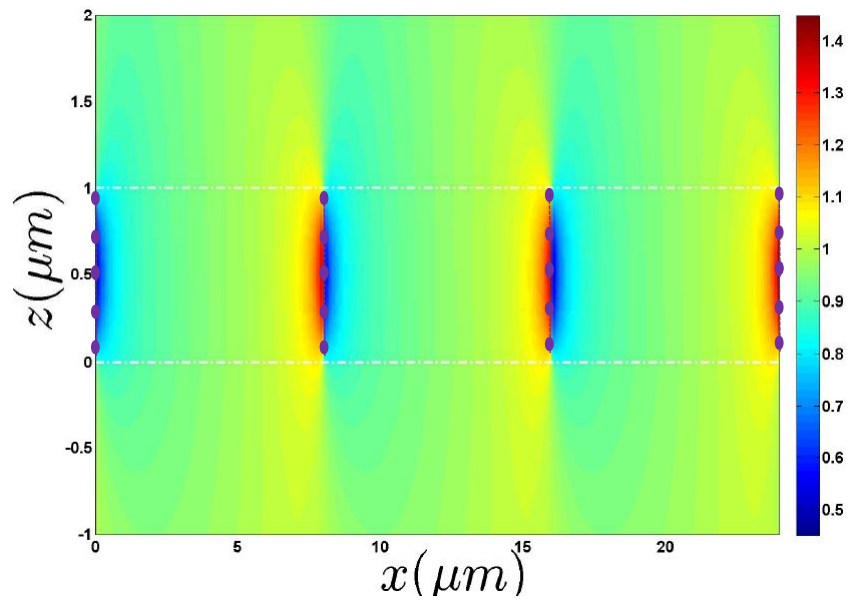


Figure 2.14: Map of the  $y$  component of the magnetic field for the mode corresponding to the resonance peak seen in Figure 2.12

## 2.4 Conclusions

In conclusion, we have presented the Fourier modal method (FMM) under its classical form as well as the Fourier modal method equipped with the concept of adaptive spatial resolution (FMM-ASR) in order to adapt them for investigating general multilayered gratings structures comprising graphene gratings. The FMM method is demonstrated to be a powerful tool that enables to calculate the reflectance and transmittance spectra for periodic structures as well as the fields distributions in these structures. However, it is shown that when the permittivity function is discontinuous, the latter method is known to converge slowly in the case of TM polarization, especially for metallic gratings. This problem was attributed to the use of wrong Fourier factorization rules. We have shown also that even the correct rules of Fourier factorization are applied, there remained a problem which is originated from the uniform spatial resolution of the Fourier expansion around the discontinuities points of the permittivity that does not take into account the genuine profile of the permittivity. This problem has been overcome by the help of the concept of adaptive spatial resolution that allows to increase the spatial resolution at the level of the discontinuities points using a new coordinate system. We have seen that the implementation of this technique led to a drastic and significant improvement in the performance of the FMM method in terms of convergence and stability. We have then extended the FMM method to aperiodic structures by placing perfectly matched layers at the lateral sides of the computational domain. Finally, in the last section, in order to test the reliability of these methods for treating graphene gratings, we have applied them to two different configurations: the first structure was a 1D graphene ribbon array and the second one a periodic grating of vertical strips of graphene. The comparison between the results obtained using the classical FMM with the correct Fourier factorization method and those computed by the FMM-ASR have shown that a better convergence rate has been achieved with the FMM-ASR method for both configurations. This point makes it best suited for modeling these kind of structures.

# Bibliography

- [1] K. Knop. Rigorous diffraction theory for transmission phase gratings with deep rectangular grooves. *J. Opt. Soc. Am.*, 68(9):1206–1210, Sep 1978. [52](#)
- [2] M. G. Moharam and T. K. Gaylord. Rigorous coupled-wave analysis of planar-grating diffraction. *J. Opt. Soc. Am.*, 71(7):811–818, Jul 1981. [52](#)
- [3] M. G. Moharam and T. K. Gaylord. Diffraction analysis of dielectric surface-relief gratings. *J. Opt. Soc. Am.*, 72(10):1385–1392, Oct 1982. [52](#)
- [4] Lifeng Li and Charles W. Haggans. Convergence of the coupled-wave method for metallic lamellar diffraction gratings. *J. Opt. Soc. Am. A*, 10(6):1184–1189, Jun 1993. [55](#)
- [5] G. Granet and B. Guizal. Efficient implementation of the coupled-wave method for metallic lamellar gratings in tm polarization. *J. Opt. Soc. Am. A*, 13(5):1019–1023, May 1996. [56](#)
- [6] Philippe Lalanne and G. Michael Morris. Highly improved convergence of the coupled-wave method for tm polarization. *J. Opt. Soc. Am. A*, 13(4):779–784, Apr 1996. [56](#)
- [7] Lifeng Li. Use of fourier series in the analysis of discontinuous periodic structures. *J. Opt. Soc. Am. A*, 13(9):1870–1876, Sep 1996. [56](#)
- [8] Lifeng Li. Formulation and comparison of two recursive matrix algorithms for modeling layered diffraction gratings. *J. Opt. Soc. Am. A*, 13(5):1024–1035, May 1996. [56](#)
- [9] Gérard Granet. Reformulation of the lamellar grating problem through the concept of adaptive spatial resolution. *J. Opt. Soc. Am. A*, 16(10):2510–2516, Oct 1999. [60](#)
- [10] T. Vallius and M. Honkanen. Reformulation of the fourier modal method with adaptive spatial resolution: application to multilevel profiles. *Opt. Express*, 10(1):24–34, Jan 2002. [60](#), [61](#)
- [11] B. Guizal, H. Yala, and D. Felbacq. Reformulation of the eigenvalue problem in the fourier modal method with spatial adaptive resolution. *Opt. Lett.*, 34(18):2790–2792, Sep 2009. [60](#), [61](#)

- [12] Hakim Yala, Brahim Guizal, and Didier Felbacq. Fourier modal method with spatial adaptive resolution for structures comprising homogeneous layers. *J. Opt. Soc. Am. A*, 26(12):2567–2570, Dec 2009. [60](#), [61](#)
- [13] S. Spillane D. Armani, T. Kippenberg and K. Vahala. Ultra-high-q toroid micro-cavity on a chip. *Nature.*, 421:925–928, 2003. [64](#)
- [14] Knight JC. Photonic crystal fibres. *Nature.*, 424:847–851, 2003. [64](#)
- [15] N. Feth M. Konig M. Husnik, M. Klein. Absolute extinction cross-section of individual magnetic split-ring resonators. *Nat. Photon.*, 2:614, 2008. [64](#)
- [16] Hamann HF McNab SJ Vlasov YA, O’Boyle M. Active control of slow light on a chip with photonic crystal waveguides. *Nature.*, 438:65, 2005. [64](#)
- [17] Jean-Pierre Berenger. A perfectly matched layer for the absorption of electromagnetic waves. *Journal of Computational Physics*, 114(2):185 – 200, 1994. [64](#)
- [18] D. S. Katz, E. T. Thiele, and A. Taflove. Validation and extension to three dimensions of the berenger pml absorbing boundary condition for fd-td meshes. *IEEE Microwave and Guided Wave Letters*, 4(8):268–270, 1994. [64](#)
- [19] Z. S. Sacks, D. M. Kingsland, R. Lee, and Jin-Fa Lee. A perfectly matched anisotropic absorber for use as an absorbing boundary condition. *IEEE Transactions on Antennas and Propagation*, 43(12):1460–1463, 1995. [64](#)
- [20] Weng Cho Chew and William H. Weedon. A 3d perfectly matched medium from modified maxwell’s equations with stretched coordinates. *Microwave and Optical Technology Letters*, 7(13):599–604, 1994. [64](#)

## **Part II**

# **Hybrid Plasmonic Structures Based on Graphene**



# Metallic slit grating-Graphene composite structure

*The knowledge of anything,  
since all things have causes, is  
not acquired or complete unless  
it is known by its causes.*

Avicenna

## Contents

<b>3.1</b>	<b>Extraordinary optical transmission . . . . .</b>	<b>78</b>
3.1.1	Extraordinary transmission : Two resonant mechanisms . . .	79
<b>3.2</b>	<b>Coupling between subwavelength nano-slits lattice modes and metal-insulator-graphene cavity modes: A semi-analytical model . . . . .</b>	<b>82</b>
3.2.1	Physical system . . . . .	82
3.2.2	Modal analysis of the system . . . . .	84
3.2.3	Analysis of the Lorentz and Fano resonances of the system .	89
<b>3.3</b>	<b>Conclusions . . . . .</b>	<b>92</b>

Extraordinary optical transmission (EOT) [1, 2, 3] through an opaque metallic film perforated with subwavelength slits has received great interest over the past two decades because of its numerous applications in optoelectronics such as mid-infrared spatial light modulators, linear signal processing or biosensing. Many theoretical and experimental works were carried out in order to understand and predict EOT and, especially, to highlight the role of surface waves [4, 5, 6, 7]. More recently K.Edee provided, in [8], a simple and versatile model, for this phenomenon, involving only a specific mode living in an equivalent homogeneous medium and a phase correction to account for surface waves. The proposed semi-analytical model is valid from the visible to the infrared frequencies ranges. On the other hand, significant efforts have been made to create active or tunable plasmonic devices operating from THz to mid-infrared frequencies. Thanks to its extraordinary electronic and optical properties, graphene, a single layer of arranged carbon atoms has attracted much attention in the last years. This material can support both TE and TM SPPs and can exhibit some remarkable properties

such as flexible wideband tunability that can be exploited to build new plasmonic devices. The main challenge when designing a graphene-plasmon-based device is how to efficiently excite GSPs with a free space electromagnetic wave since there is a huge momentum mismatch between the two electromagnetic modes. Generally two strategies are used. The first one consists in patterning the graphene sheet into nano-resonators [9, 10, 11, 12, 13, 14, 15, 16, 17, 18, 19, 20, 21]. In this case a surface plasmon of the obtained structure which is very similar to the GSP is excited and an absorption rate close to 100% can be reached. In particular, in [15], the authors presented an electrically tunable hybrid graphene-gold Fano resonator which consists of a square graphene patch and a square gold frame. They showed that the destructive interference between the narrow- and broadband dipolar surface plasmons, which are induced respectively on the surfaces of the graphene patch and the gold frame, leads to the plasmonic equivalent of electromagnetically induced transparency (EIT). However patterning a graphene sheet requires sophisticated processing techniques and deteriorates its extraordinary mobility. The second strategy consists in using a continuous graphene sheet instead of undesirable patterned graphene structures [22, 23, 24, 25, 26, 27]. In this approach, the graphene sheet is coupled with nano-scatterers such as nano-particles, or nano-gratings. Gao *et al.* proposed [22] to use diffractive gratings to create a guided-wave resonance in the graphene film that can be directly observed from the normal incidence transmission spectra. In [27] Zhao *et al.* studied a tunable plasmon-induced-transparency effect in a grating-coupled double-layer graphene hybrid system at far-infrared frequencies. They used a diffractive grating to couple a normally incident wave and plasmonic modes living in a system of two graphene-films separated by a spacer. Zhang *et al.* [24] investigated optical field enhancements, in a wide mid-infrared band, originating from the excitation of GSPs, by introducing a dielectric grating underneath a graphene monolayer. Usually, the optical response of all grating-graphene based structures listed above is performed thanks to the finite difference time domain method (FDTD) or to the finite element method (FEM). However the features of these hybrid graphene-resonators devices are often linked to a plasmon resonance phenomenon. Therefore a modal method allowing for a full modal analysis of the couplings occurring in these plasmonic systems seems more suitable. In this chapter, we investigate an optical tunable plasmonic system involving two fundamental phenomena: an EOT phenomenon and a metal-insulator-graphene (M-I-G) cavity plasmon mode excitation. We propose a semi-analytical model allowing to fully describe the spectrum behaviour of an hybrid plasmonic structure, made of a 1D periodic subwavelength slits array deposited on an insulator/graphene layers. The spectrum of the proposed hybrid system exhibits Lorentz and Fano-like resonances and also other broadband and narrow band resonances that are efficiently captured by our simplified model. In order to explain the origin of this particular behaviour, we first split the hybrid system into a couple of sub-systems. Second, thanks to a modal analysis through the polynomial modal method (PMM: one of the most efficient methods for modeling the electromagnetic properties of periodic structures and available in our laboratory) [28, 29, 30, 31] and the FMM-ASR presented in chapter 2, we demonstrate that the scattering parameters of each sub-system can be computed through a concept of weak and strong couplings. Finally we provide analytical expressions of the reflection and transmission coefficients of the structure and describe the mechanisms leading to Lorentz and Fano resonances occurring in it.

### 3.1 Extraordinary optical transmission

For decades, it has been known in classical electromagnetics theory that when an electromagnetic wave is impinging on an aperture whose dimension is larger than the wavelength of the light, it will be transmitted through it. Whereas a subwavelength aperture diffracts light in all direction leading to a very low transmission [32]. In 1998, Ebbesens et al [1] found that a 2D subwavelength metal aperture array exhibits unusual high transmission at a certain frequency. This phenomenon has been called *extraordinary optical transmission* (EOT). One year later, Porto et al [33] theoretically investigated the transmission through one dimensional subwavelength metallic gratings with very narrow slits. In this case, they proved that the EOT phenomenon find its physical origin in the surface plasmons polaritons resonances. In particular, they distinguished two different mechanisms of SPP resonances which are responsible for this enhancement of the transmission. The first mechanism is the excitation of a cavity resonant mode located in the slit (Vertical surface resonance) and the second one is related to the resonant coupling between horizontal plasmons on both sides. The goal of this section is to explain and present the basic physical mechanisms behind the EOT phenomenon taking place in a one dimensional metallic slit grating.

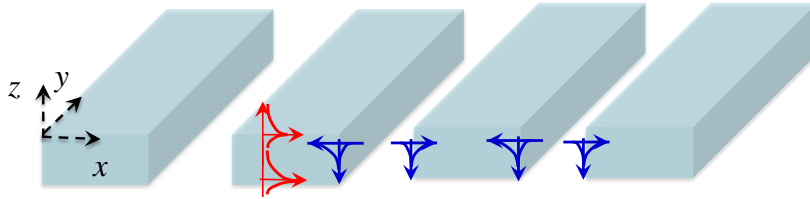


Figure 3.1: Schematic of EOT through a subwavelength metal slit array: The horizontal surface plasmons on the upper and lower surfaces of the metallic film (red) can be excited by the waves diffracted by the grating. The vertical surface plasmons (blue) couple to form the fundamental TM mode guided in the slits. When the thickness of the slit grating is sufficient, vertical resonances can occur which correspond to Fabry-Perot-like resonances of this guided mode.

In order to highlight the(EOT) and understand the different mechanisms contributing to this phenomenon, we consider the structure depicted in Figure 3.1 which is similar to the one presented by Porto et al [33]. It consists of a subwavelength 1D metallic slit grating made of gold and surrounded with air. The period of the grating is  $d = 3.5\mu m$ , the width of the slit is set to be  $w = 0.5\mu m$  and the thickness  $h$  takes the values  $0.2 - 1.2 - 3\mu m$ .

#### 3.1.1 Extraordinary transmission : Two resonant mechanisms

The Figure 3.1 plotted the transmission spectra of a TM wave incident onto the structure shown in Figure 3.1. One can clearly see two transmissions peaks for sufficiently large thickness ( $h = 3\mu m$ ). In ref [33], Porto and al suggest the existence of two different mechanisms responsible for the appearance of these peaks in the transmission spectra: the Horizontal and Vertical SPPs resonances. Hereafter, we will explain these two resonances mechanisms.

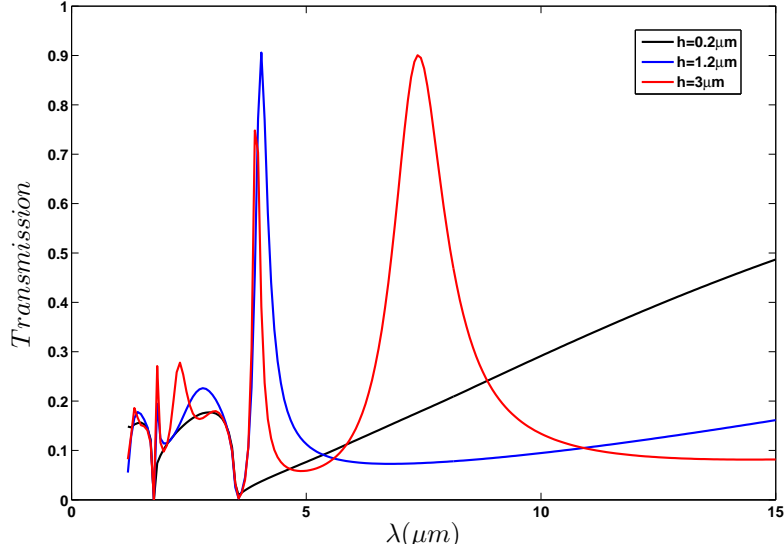


Figure 3.2: Transmission spectra for a 1D gold slit array at normal incidence. The period of the grating is  $d = 3.5\mu\text{m}$  and the width of the slit is  $w = 0.5\mu\text{m}$ . The results are calculated for three values of the thickness of the grating  $h$  :  $h = 0.2\mu\text{m}$  (black line),  $h = 1.2\mu\text{m}$  (blue line) and  $h = 3\mu\text{m}$  (red line)

### Horizontal SPP resonance (Periodic structure resonance)

As we can see from Figure 3.2, the grating can support horizontal SPPs (in red) which can propagate on its upper and lower sides. When a TM polarized wave is incident into the grating, the latter will generate different diffraction orders and one of those diffracted waves can couple to the horizontal SPPs. This is achieved when the following condition is fulfilled:

$$k_{sp} = k_{xn} = k_{x0} + \frac{2\pi n}{d} \quad (3.1)$$

Where  $k_{xn}$  is the parallel wavevector of the  $n^{\text{th}}$  diffracted wave and  $k_x^0$  is the incident parallel wavevector. We can see from this equation that the horizontal surface resonances depend strongly on the period  $d$  of the grating and on the incident parallel wavevector.

### Vertical surface plasmon resonance (Fabry -Perot like resonance)

The slits that constitute the grating can be considered as independent planar 1D waveguides. In the case where the width of the slit is very narrow, only the fundamental mode can propagate in the waveguide. In ref [34], it has been predicted that this mode is composed of two coupled surface plasmons polaritons propagating along both the metallic walls of the slit (see Figure 3.3). Surface waves are then reflected at the upper and lower ends of the slit and consequently the obtained vertical resonances can be seen as Fabry perot like resonances of the TM fundamental mode inside the slit.

### Transmission mechanism through the structure

To summarize, the mechanism of extraordinary transmission through a metallic sub-wavelength grating is as follows: the incident wave couples to the fundamental guided mode inside the slit partly directly and partly via the horizontal surface plasmons on the top metal surface (upper surface). On the lower surface, the waveguide mode

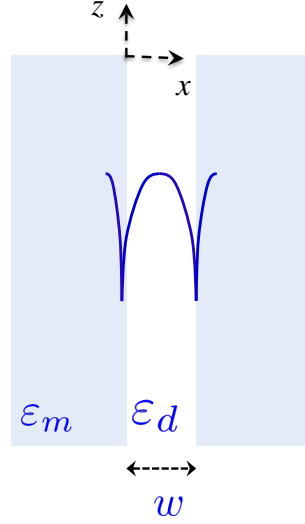


Figure 3.3: Schematic representation of a 1D planar metallic waveguide with very narrow width. Inside the waveguide only the fundamental TM mode is propagative and is composed of two surface plasmons waves

couples with a propagative wave partly directly and partly via the horizontal surface plasmons on the bottom metal surface. As a result, the coupling between the upper and lower surface plasmons is achieved by the guided mode in the slit. This coupling is more effective in the case of symmetrical structure i.e when the permittivities of the surrounding media are equal.

## 3.2 Coupling between subwavelength nano-slits lattice modes and metal-insulator-graphene cavity modes: A semi-analytical model

### 3.2.1 Physical system

The hybrid structure under study is presented in Fig. (3.4). It consists of two sub-systems. The first sub-system earlier studied in [8] is a sub-wavelength periodic array of nano-slits with height  $h_1 = 800nm$ , period  $d = 165nm \ll \lambda$  and slits-width  $s = 15nm$ . The relative permittivity of the material filling the slits is denoted by  $\varepsilon^{(s)}$  while the dispersive relative permittivity of the metal (gold) is denoted by  $\varepsilon^{(m)}$  and described by the Drude-Lorentz model [35, 8, 36]. This first sub-structure is deposited on a dielectric spacer (with relative permittivity  $\varepsilon^{(2)} = 1.54^2$  and height  $h_2 = 10nm$ ) itself deposited on a continuous graphene sheet. Here, the monolayer graphene is modeled as a thin film within the *Thin film's effective thickness approach* described previously in chapter 1. This hybrid structure is excited, from the upper medium (having relative permittivity  $\varepsilon^{(0)}$ ) by a TM polarized plane wave (the magnetic field is parallel to the  $y$  axis). The wave vector of the incident wave is denoted by  $\vec{K}_0 = k_0(\alpha_0\vec{e}_x + \beta_0\vec{e}_y + \gamma_0\vec{e}_z)$ , where  $k_0 = 2\pi/\lambda = \omega/c$  denotes the wavenumber,  $\lambda$  being the wavelength and  $c$  the light velocity in vacuum. The relative permittivity of the lower region is denoted by  $\varepsilon^{(3)}$ .

As mentioned above in the introduction, the spectrum behaviour of the studied hybrid plasmonic structure is performed through the FMM-ASR and PMM methods.

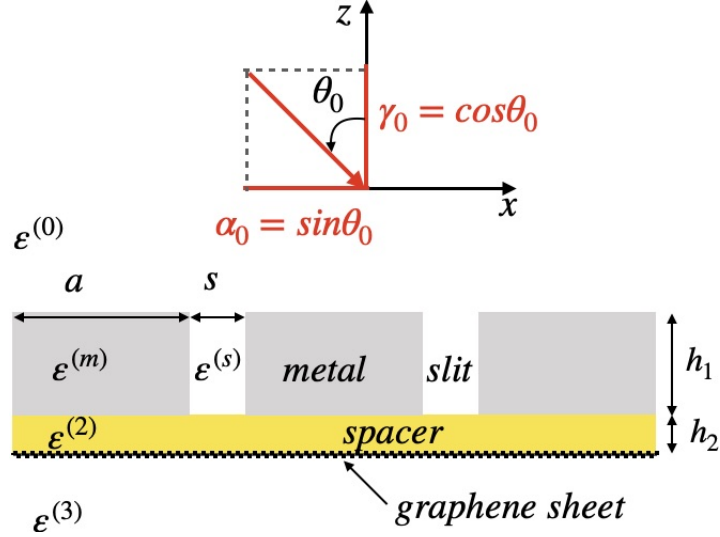


Figure 3.4: Sketch of hybrid structure made of a dispersive metal film perforated with a subwavelength periodic array of 1D nano-slits deposited on a dielectric spacer ended by a continuous graphene sheet.

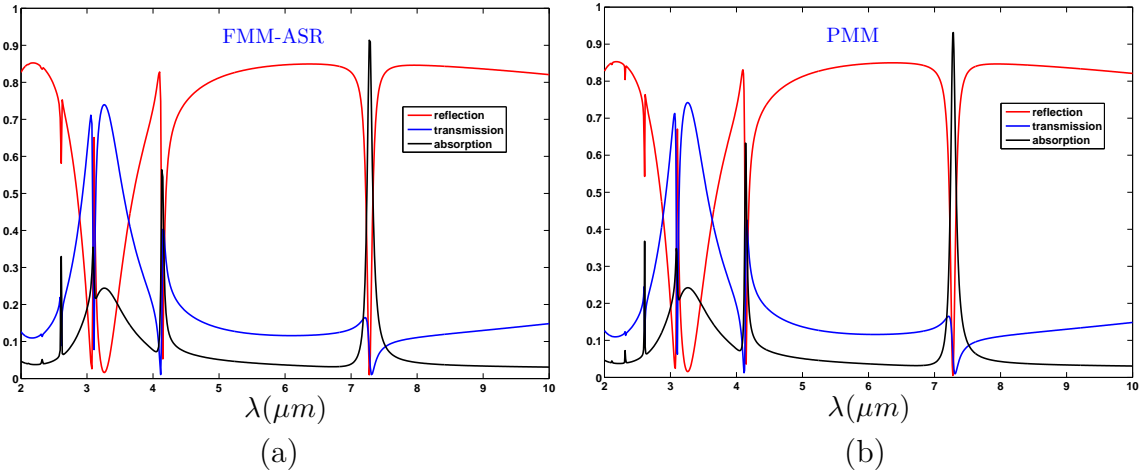


Figure 3.5: Reflection, transmission and absorption spectra of the hybrid system for computed with (a) FMM-ASR (b) PMM. Parameters:  $\varepsilon^1 = \varepsilon^3 = \varepsilon^{slit} = 1$ ,  $\varepsilon^{(2)} = 2.3716$ ,  $\mu_c = 1eV$  incidence angle =  $0^\circ$ ,  $h = 800nm$ ,  $d = 165nm$ ,  $s = 15nm$ .

Figure 3.5 shows the transmission (blue solid line), reflection (red solid line) and absorption (black solid line) spectra computed using the FMM-ASR and the PMM methods for a normally incident plane wave. The chemical potential of the graphene layer is set to  $\mu_c = 1eV$ . From this figure, we can clearly see that both methods can efficiently and successfully predict the electromagnetic and plasmonic response of the structure. We can also observe an excellent agreement between the results obtained with the FMM-ASR method and those computed using the PMM method. In the following, we choose to use only the PMM method for computing the optical spectra and as a method to validate and test our proposed semi analytical approach.

We report in Figure 3.6, the spectra of the hybrid structure for two values of the chemical potential:  $\mu_c = 1eV$  and  $\mu_c = 1.5eV$ . These curves display both broadband and narrow bands resonance phenomena. It has been shown in [8] that a Lorentz-like resonance corresponding to an EOT phenomenon can occur in the first sub-system

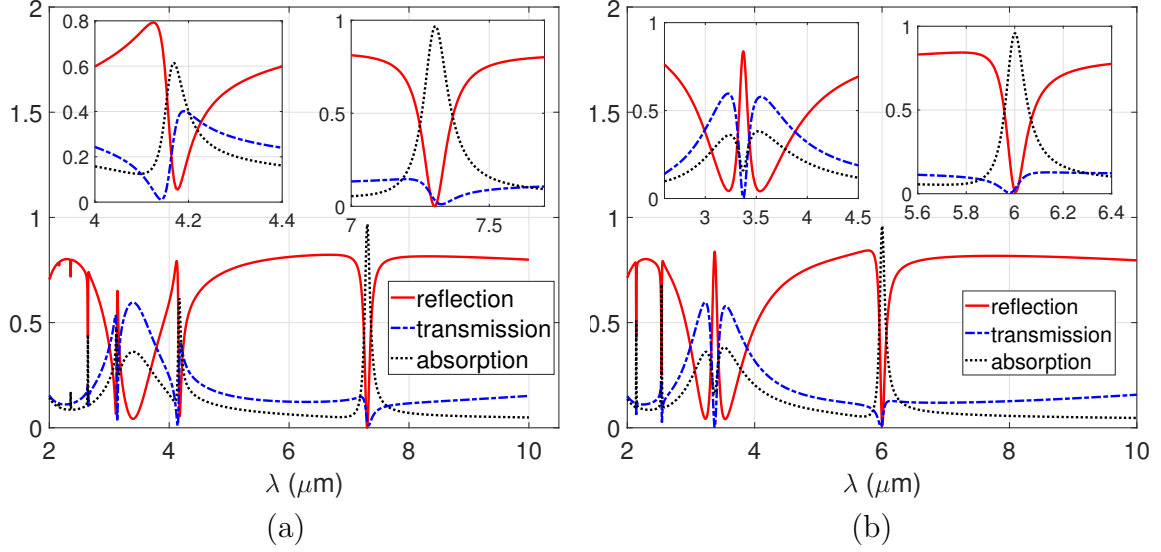


Figure 3.6: Reflection, transmission and absorption spectra of the hybrid system for (a)  $\mu_c = 1eV$  and (b)  $\mu_c = 1.5eV$ . The hybrid structure exhibits both broadband and tunable narrow band resonances with respect to the chemical potential. Parameters:  $\varepsilon^1 = \varepsilon^3 = \varepsilon^{slit} = 1$ , incidence angle =  $0^\circ$ ,  $h = 800nm$ ,  $d = 165nm$ ,  $a = 15nm$ .

i.e. the dispersive metal film perforated with a subwavelength periodic array of 1D nano-slits excited by a plane. In the current case, this EOT occurs around  $\lambda = 3.37\mu m$  and as pointed out in [8] it is related to the excitation of a particular eigenmode of the slit grating structure : the so-called lattice mode. The broadband resonance is related to the EOT phenomenon outlined later, while the narrow band resonance phenomena are due to Fabry-Perrot-like resonances of a cavity mode living in the metal/spacer/graphene gap. For example, for  $\mu_c = 1eV$ , a first two narrow resonances are observed around  $\lambda = 4.17\mu m$  and  $\lambda = 7.3\mu m$  as shown in the insets.

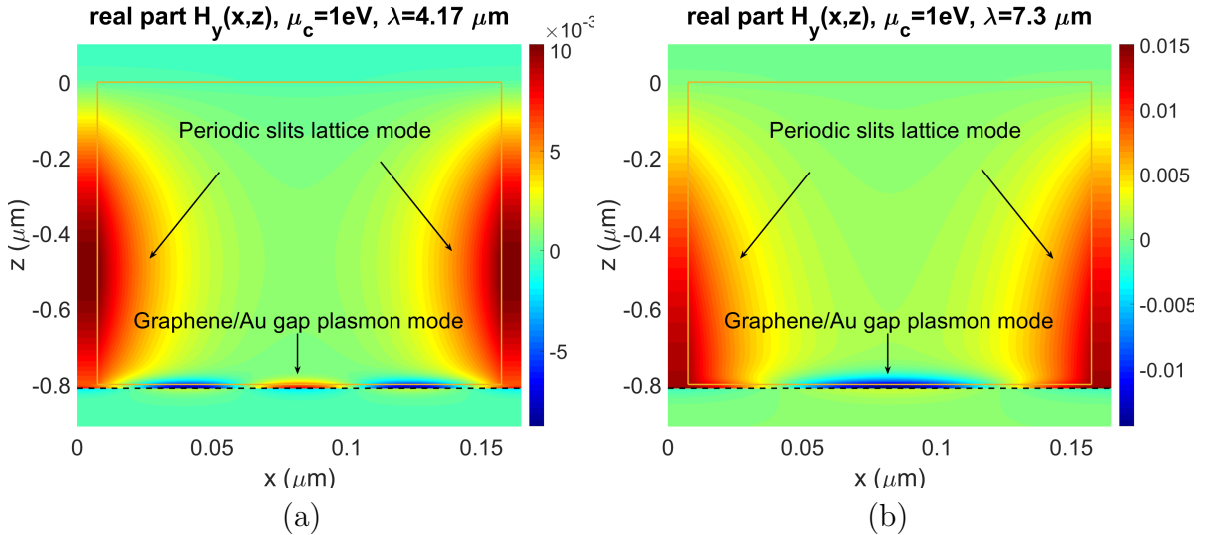


Figure 3.7: Real part of the magnetic field  $H_x(x, z)$  at (a)  $\lambda = 4.17\mu m$  and at (b)  $\lambda = 7.30\mu m$ . Parameters:  $\varepsilon^1 = \varepsilon^3 = \varepsilon^{slit} = 1$ , incidence angle =  $0^\circ$ ,  $h = 800nm$ ,  $d = 165nm$ ,  $a = 15nm$ .

The real parts of the magnetic field plotted in Figure 3.7(a) at  $\lambda = 4.17\mu m$  and in Figure 3.7(b) at  $\lambda = 7.30\mu m$ , for  $\mu_c = 1eV$ , support the fact that the narrow band resonances are linked to the resonance of a cavity mode of the horizontal

metal/insulator/graphene sub-system. As the effective index of this mode strongly depends on the chemical potential  $\mu_c$ , the resonance frequencies of this hybrid cavity mode shift with increasing  $\mu_c$ . Comparing the reflection spectrum of the first sub-system with that of the hybrid structure, we can interpret the latter spectral response as a weak or strong coupling between the lattice mode of the former sub-system with the cavity mode of the metal/insulator/graphene gap. We propose in the following, a simple single mode model allowing to efficiently describe, and understand the mechanism of this vertical-to-horizontal cavity modes coupling.

### 3.2.2 Modal analysis of the system

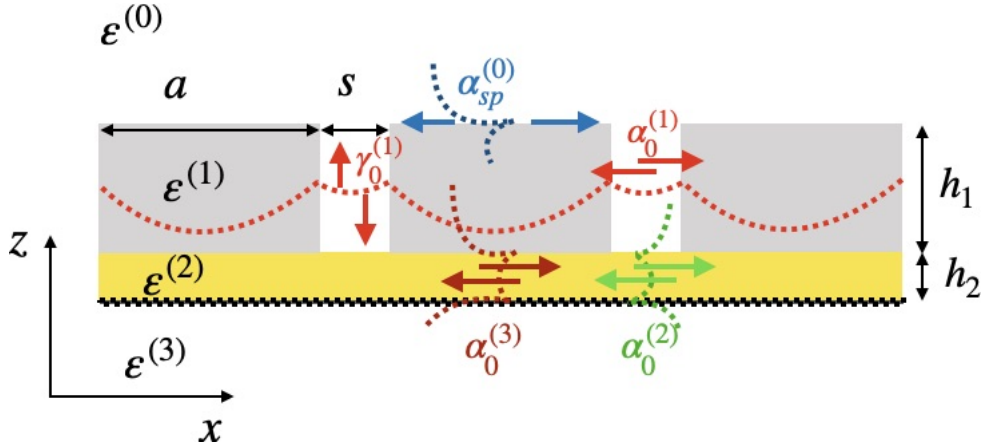


Figure 3.8: Sketch of the mechanism of the coupling between cavity lattice modes of the periodic array of nano-slits and the metal/insulator/graphene gap plasmon modes. Strong and weak couplings between three modes are responsible of the resonance phenomena of the hybrid structure.

The sketch of vertical-to-horizontal cavity modes coupling outlined in the previous section is presented in Fig. (3.8), where  $\gamma_0^{(1)}$  denotes effective index of the periodic slits array lattice mode in the  $z$ -direction while  $\alpha_0^{(3)}$  denotes that of the metal/insulator/graphene cavity mode in the  $x$ -direction. The effective indices  $\alpha_0^{(1)}$  and  $\alpha_0^{(2)}$  will be introduced later. Modal methods are very suitable to deal with the current problem since it is related to mode resonances. Thus, all required effective indices are computed as eigenvalues of the generic operator  $\mathcal{L}^{(k)}$ :

$$\mathcal{L}^{(k)}(\omega)|H_q^{(k)}(\omega)\rangle = (\gamma_q^{(k)}(\omega))^2|H_q^{(k)}(\omega)\rangle \quad (3.2)$$

with

$$\mathcal{L}^{(k)}(x, \omega) = \left(\frac{c}{\omega}\right)^2 \varepsilon^{(k)}(x, \omega) \partial_x \frac{1}{\varepsilon^{(k)}(x, \omega)} \partial_x + \varepsilon^{(k)}(x, \omega).$$

Figure 3.9 illustrates the different configurations used for the computation of the required effective indices. Recall that these effective indices are computed as eigenvalues of equation (3.2). The first configuration (*config.1*) is used for the computation of the modes of periodic arrays of nano-slits in general and particularly for the computation of the cavity lattice mode effective index  $\gamma_0^{(1)}$ . The second configuration (*config.2*) is used for the computation of the plasmon mode effective index  $\alpha_0^{(2)}$  while the cavity plasmon mode effective index  $\alpha_0^{(3)}$  is computed thanks to the third configuration

(*config.3*). Practically, the PMM is used to solve numerically the eigenvalue equation Eq. (3.2). For that purpose, the structure is divided into sub-intervals  $I_x^{(k)}$ , in the  $x$ -direction:  $k \in \{1, 2\}$  for *config.1* while  $k \in \{1, 6\}$  for *config.2* and *config.3*. At this

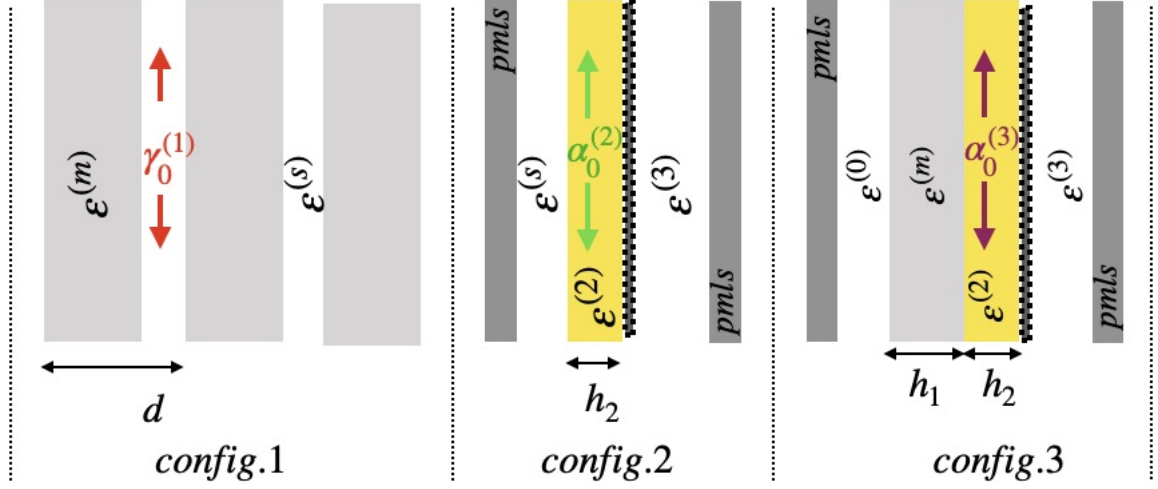


Figure 3.9: Configurations used for the computation of the required effective indices (eigenvalues of equations 3.2). *config.1* is used for the computation of the modes of periodic arrays of nano-slits in general and in particular for the computation of the cavity lattice mode effective index  $\gamma_0^{(1)}$ . *config.2* is used for the computation of the effective index  $\alpha_0^{(2)}$  of the plasmon mode. The gap plasmon mode effective index  $\alpha_0^{(3)}$  is computed thanks to *config.3*.

stage, we split the hybrid system into two coupled sub-systems:

- a weakly coupled sub-system sketched in figures 3.10 and 3.11 which leads to the broadband resonances.
- a strongly coupled sub-system sketched in figures 3.13 and 3.14 leading to a narrow bands dispersion curves.

Let us now analyse each coupled sub-system and provide semi-analytical models allowing to describe them.

### Weakly coupled sub-system

A semi-analytical model for the weakly coupled system has been already described in [8]. This system consists of a periodic array of subwavelength nano-slits encapsulated between media with relative permittivities  $\epsilon^{(0)}$  and  $\epsilon^{(3)}$ . As pointed out in [8], the electromagnetic response of the system to an incident plane wave excitation, in the static limit ( $d \ll \lambda$ ), is equivalent to that of a slab with equivalent permittivity  $\epsilon^{(1)} = \langle 1/\epsilon^{(m,s)}(x) \rangle^{-1}$  and height  $h_1$ .

Its reflection and transmission coefficients  $R_{12}$  and  $T_{12}$  are then given by :

$$R_{12} = \frac{r_1 + \phi_1 r_2 \phi_2}{1 + r_1 \phi_1 r_2 \phi_2} \quad (3.3)$$

and

$$T_{12} = \frac{t_1 t_2 \phi_2}{1 + r_1 \phi_1 r_2 \phi_2} \quad (3.4)$$

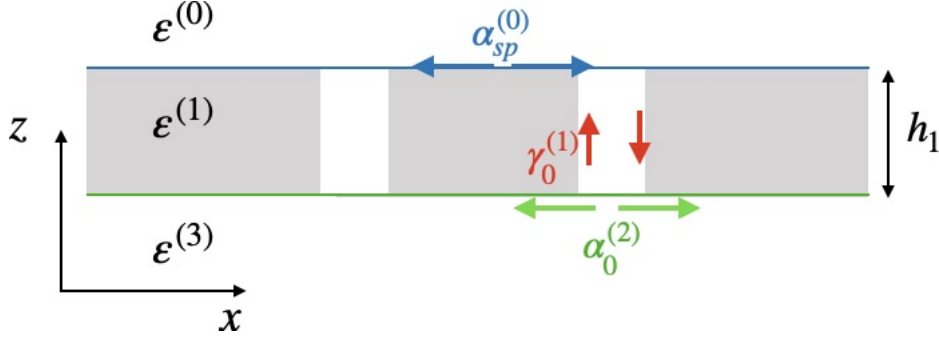


Figure 3.10: Sketch of the weak coupling sub-system consisting of a periodic array of nano-slits encapsulated between  $\varepsilon^{(0)}$  and  $\varepsilon^{(3)}$  media. The lattice mode  $\gamma_0^{(1)}$  is assumed to live in an  $\sqrt{\varepsilon^{(1)}}$  effective homogeneous medium. Two plasmon modes  $\alpha_{sp}^{(0)}$  and  $\alpha_0^{(2)}$  ensure the phase matching with the plane waves in media  $\varepsilon^{(0)}$  and  $\varepsilon^{(3)}$

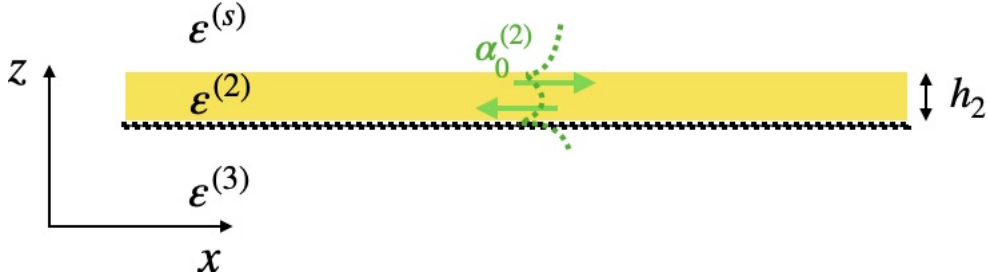


Figure 3.11: The sketch of  $\alpha_0^{(2)}$  plasmon mode computation.

where  $r_1, t_1$  and  $r_2, t_2$  are the Fresnel coefficients at the interfaces  $\varepsilon^{(0)}/\varepsilon^{(1)}$  and  $\varepsilon^{(1)}/\varepsilon^{(3)}$  under TM polarization:

$$r_1 = \frac{1 - n_{01}(\omega)}{1 + n_{01}(\omega)}, \quad r_2 = \frac{1 - n_{13}(\omega)}{1 + n_{13}(\omega)}, \quad (3.5)$$

$$t_1 = \frac{2}{1 + n_{01}(\omega)}, \quad t_2 = \frac{2}{1 + n_{13}(\omega)}. \quad (3.6)$$

where

$$n_{01}(\omega) = \frac{\gamma_0^{(1)}(\omega)/\varepsilon^{(1)}(\omega)}{\gamma_0^{(0)}(\omega)/\varepsilon^{(0)}(\omega)}, \quad \text{and} \quad n_{13}(\omega) = \frac{\gamma_0^{(3)}(\omega)/\varepsilon^{(3)}(\omega)}{\gamma_0^{(1)}(\omega)/\varepsilon^{(1)}(\omega)}, \quad (3.7)$$

and

$$\phi_1 = e^{-ik_0\gamma_0^{(1)}h_1}\phi_c^{(0)}, \quad \phi_2 = e^{-ik_0\gamma_0^{(1)}h_1}\phi_c^{(2)} \quad (3.8)$$

with

$$\phi_c^{(0)} = e^{-ik_0\alpha_{sp}^{(0)}a^{(0)}}, \quad \phi_c^{(2)} = e^{-ik_0\alpha_0^{(2)}a^{(2)}}. \quad (3.9)$$

Phase correction terms are introduced in order to take into account the phase matching between the lattice mode with effective index  $\gamma_0^{(1)}$  and the incident plane wave (see [8]). In equation Eq. (3.9),  $\alpha_{sp}^{(0)} = \sqrt{\frac{\varepsilon^{(0)}\varepsilon^{(m)}}{\varepsilon^{(0)} + \varepsilon^{(m)}}$  is the effective index of the surface plasmon propagating along the upper interface,  $a^{(0)} = \frac{a}{4}\sqrt{\frac{\varepsilon^{(0)}}{\varepsilon^{(s)}}}$  and  $a^{(2)} = \frac{a}{4}\sqrt{\frac{\varepsilon^{(3)}}{\varepsilon^{(s)}}}$ . We

compare in Fig (3.12) (a) the spectrum of the reflectivity  $|R_{12}|^2$ , with the reflectivity of the hybrid system. As expected, the  $|R_{12}|^2$  curve perfectly matches the broadband resonance of the hybrid structure. The impact of the phase correction terms  $\phi_c^{(0),(2)}$  on the results is not significant since the omission of these terms only induces a little shift of the  $|R_{12}|^2$  curve. This is why we consider the coupling between the  $\gamma_0^{(1)}$ -effective index-slit-mode and the  $\alpha_0^{(2)}$ -effective index-plasmon-mode as a weak coupling.

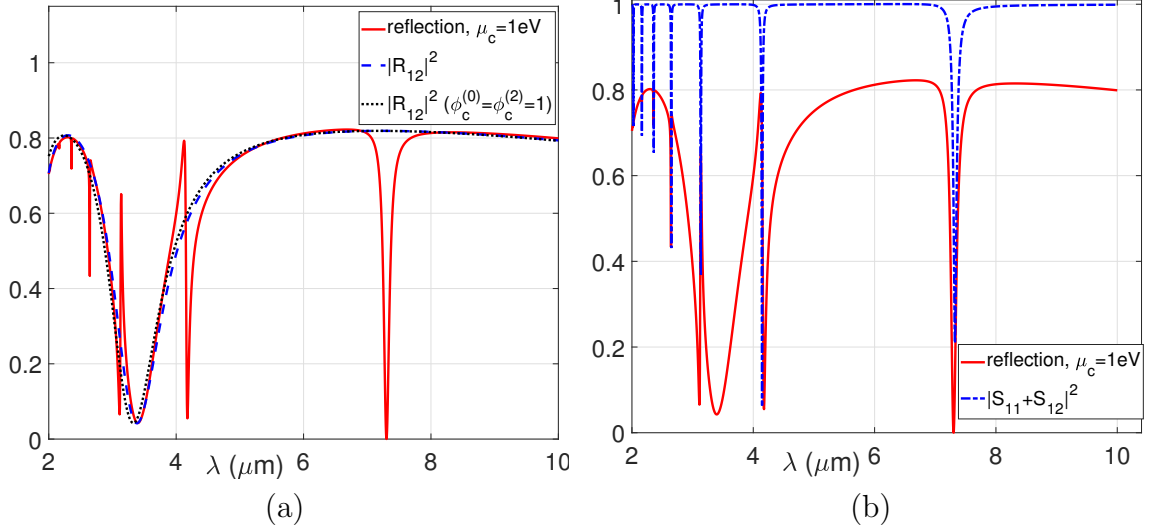


Figure 3.12: Comparison between the reflection spectrum of the hybrid structure and the responses of the weakly coupled sub-system (a) and the strongly coupled sub-system (b). As expected, the weakly coupled sub-system reflection spectrum  $|R_{12}(\lambda)|^2$  perfectly matches the broadband resonances of the hybrid structure. On the other hand, the strongly coupled sub-system spectrum characteristic function  $|S_{11}(\lambda) + S_{12}(\lambda)|^2$  perfectly matches the narrow band resonances of the hybrid structure. Parameters:  $\lambda \in [2, 10] \mu\text{m}$ ,  $\varepsilon^{(1)} = \varepsilon^{(3)} = \varepsilon^{(s)} = 1$ ,  $\varepsilon^{(2)} = 1.54^2$ , incidence angle =  $0^\circ$ ,  $\mu_c = 1\text{eV}$ .

### Strongly coupled sub-system

Consider now the strongly coupled sub-system sketched in Figs. (3.13) and (3.14). Since the transverse geometrical parameters of the grating are smaller than the incident field wavelength  $\lambda$  ( $d \ll \lambda$ ), we can introduce for the lattice mode an effective index  $\alpha_0^{(1)}$  along the  $x$ -axis as follows:

$$\alpha_0^{(1)} = \sqrt{\varepsilon^{(1)} - \gamma_0^{(1)2}}, \quad (3.10)$$

where  $\alpha_0^{(1)}$  has a positive real part and a negative imaginary part. The  $S$ -parameters of the equivalent two ports network of Fig. (3.13) are then given by :

$$\begin{bmatrix} S_{11} & S_{12} \\ S_{21} & S_{22} \end{bmatrix} \begin{bmatrix} a_1 \\ a_2 \end{bmatrix} = \begin{bmatrix} b_1 \\ b_2 \end{bmatrix} \quad (3.11)$$

where

$$\begin{cases} S_{11}(\omega) = S_{22}(\omega) = \frac{[1 - n^2(\omega)][1 - \phi^2(\omega)]}{[1 + n(\omega)]^2 - [1 - n(\omega)]^2 \phi^2(\omega)} \\ S_{12}(\omega) = S_{21}(\omega) = \frac{4n(\omega)\phi(\omega)}{[1 + n(\omega)]^2 - [1 - n(\omega)]^2 \phi^2(\omega)} \end{cases}, \quad (3.12)$$

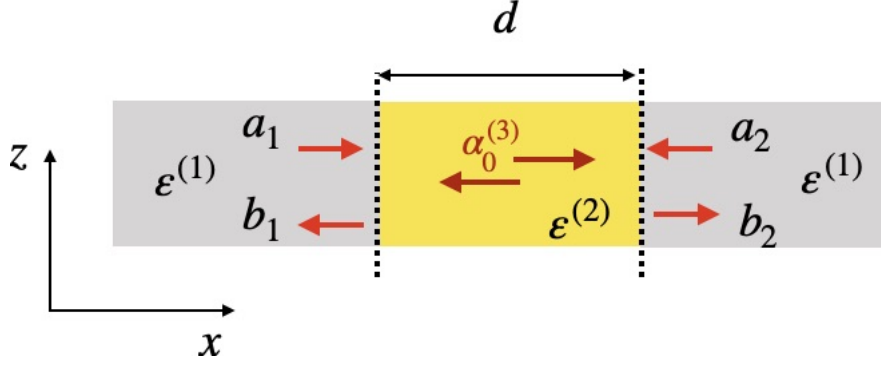


Figure 3.13: Sketch showing the strong coupling between the gap plasmon mode  $\alpha_0^{(3)}$  living in an  $\sqrt{\epsilon^{(2)}}$  homogeneous medium and  $\alpha_0^{(1)}$  lattice mode in an  $\sqrt{\epsilon^{(1)}}$  effective homogeneous medium.

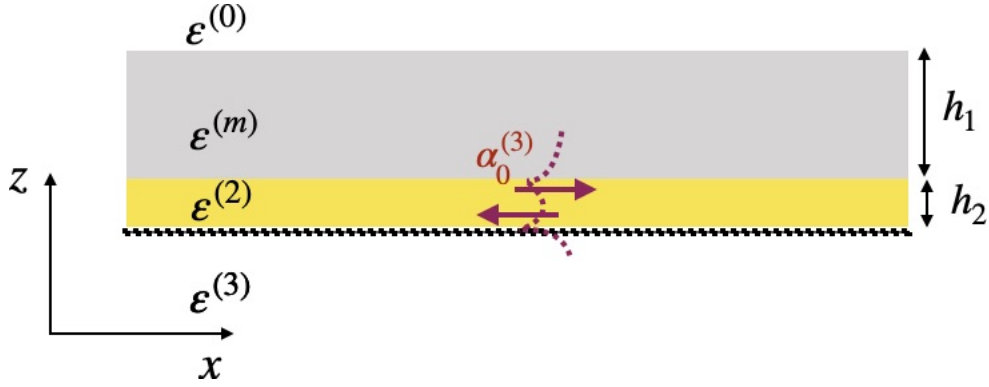


Figure 3.14: The sketch of  $\alpha_0^{(3)}$  plasmon mode computation.

with

$$\begin{cases} n(\omega) = \frac{\alpha_0^{(3)}(\omega)/\epsilon^{(3)}(\omega)}{\alpha_0^{(1)}(\omega)/\epsilon^{(1)}(\omega)} , \\ \phi = e^{-ik_0\alpha_0^{(3)}d} . \end{cases} \quad (3.13)$$

The resonances of this system are obtained by finding the zeros of the determinant  $\Delta(\omega)$  of the matrix  $S(\omega)$  of equation Eq. (6.5) :

$$\Delta(\omega) = S_{11}(\omega)S_{22}(\omega) - S_{12}(\omega)S_{21}(\omega) = [S_{11}(\omega) - S_{12}(\omega)] [S_{11}(\omega) + S_{12}(\omega)] = 0. \quad (3.14)$$

Then we have two classes of solutions:

$$\begin{cases} S_{11}(\omega) - S_{12}(\omega) = 0 \\ \text{or} \\ S_{11}(\omega) + S_{12}(\omega) = 0 \end{cases} . \quad (3.15)$$

As shown Figure 3.12(b) the resonance frequencies defined by the class of solutions satisfying to  $S_{11}(\omega) + S_{12}(\omega) = 0$  match with the narrow band resonances of the hybrid structure. Let us set

$$r_{13}(\omega) = -(S_{11}(\omega) + S_{12}(\omega)). \quad (3.16)$$

Coefficient  $r_{13}$  corresponds to the reflection coefficient of the strongly coupled system where the output and input ports are excited by two fields of equal amplitudes  $a_1 = a_2$ .

Therefore the reflection spectrum of the whole system can take the following form :

$$R = \frac{r_1 + \phi_1 r_{13} r_2 \phi_2}{1 + r_1 \phi_1 r_{13} r_2 \phi_2} \quad (3.17)$$

and

$$T = \frac{t_1 r_{13} t_2 \phi_2}{1 + r_1 \phi_1 r_{13} r_2 \phi_2}. \quad (3.18)$$

By using the approximate model of Eqs. (3.17) and (3.18), we provide some numerical simulations (In Figs. (3.15a), (3.15b), (3.15c) and (3.15d)) for different values of  $\mu_c$ . In these figures, we compare the spectra of the hybrid-structure with the reflection and transmission curves obtained from rigorous PMM computations. The chemical potential is set to  $\mu_c = 1eV$ , in Figs. (3.15a) and (3.15b), while  $\mu_c = 1.5eV$ , in Figs. (3.15c) and (3.15d). All these results fit very well the rigorous numerical simulations obtained with the PMM. Our model captures very well all resonances occurring in the hybrid system namely Lorentz and Fano resonances and thus confirms that couplings between some fundamental modes of elementary sub-structures are of fundamental importance in these phenomena. Armed with this model, we are now ready to deepen the explanation of the curves of Figure 3.6.

### 3.2.3 Analysis of the Lorentz and Fano resonances of the system

Analysing the reflection  $|R|^2$ , transmission  $|T|^2$  from Eqs. (3.17), (3.18), it is possible to provide justifications for the curves shapes in Figure 3.6. From these figures, we remark that:

1. In the frequency range close to the resonance frequencies of the weak sub-system, the reflection and transmission spectra generally exhibit asymmetric Fano-like shapes while the absorption presents Lorentz-like shapes (left inserts of Figure 3.6).
2. When the resonance frequency of both strongly and weakly coupled systems match each other, it results in an exaltation of the reflection and annihilation of both transmission and absorption. This can be seen as a sort of induced reflection.
3. In the frequency range far from the resonance frequencies of the weakly coupled sub-system, a Lorentz-like absorption enhancement can be observed (right inserts of Figure 3.6). The scattering efficiency vanishes and the absorption takes its maximum value close to unity.

Before commenting on the first point raised above, let us recall that, in general, the Fano resonance occurs when a narrow band resonance sub-system interferes with a continuum or a broadband resonance sub-system. The signature of this resonance in the spectrum is the presence of two closed critical points corresponding to a vanishing value of the amplitude followed or preceded by an enhancement. In the current case, the zeros of the transmission  $T$ , in Eq. (3.18), are the zeros of the coefficient  $r_{13}$  and these frequency values are always followed or preceded by great or little transmission enhancements. Therefore the Fano resonance shape becomes obvious.

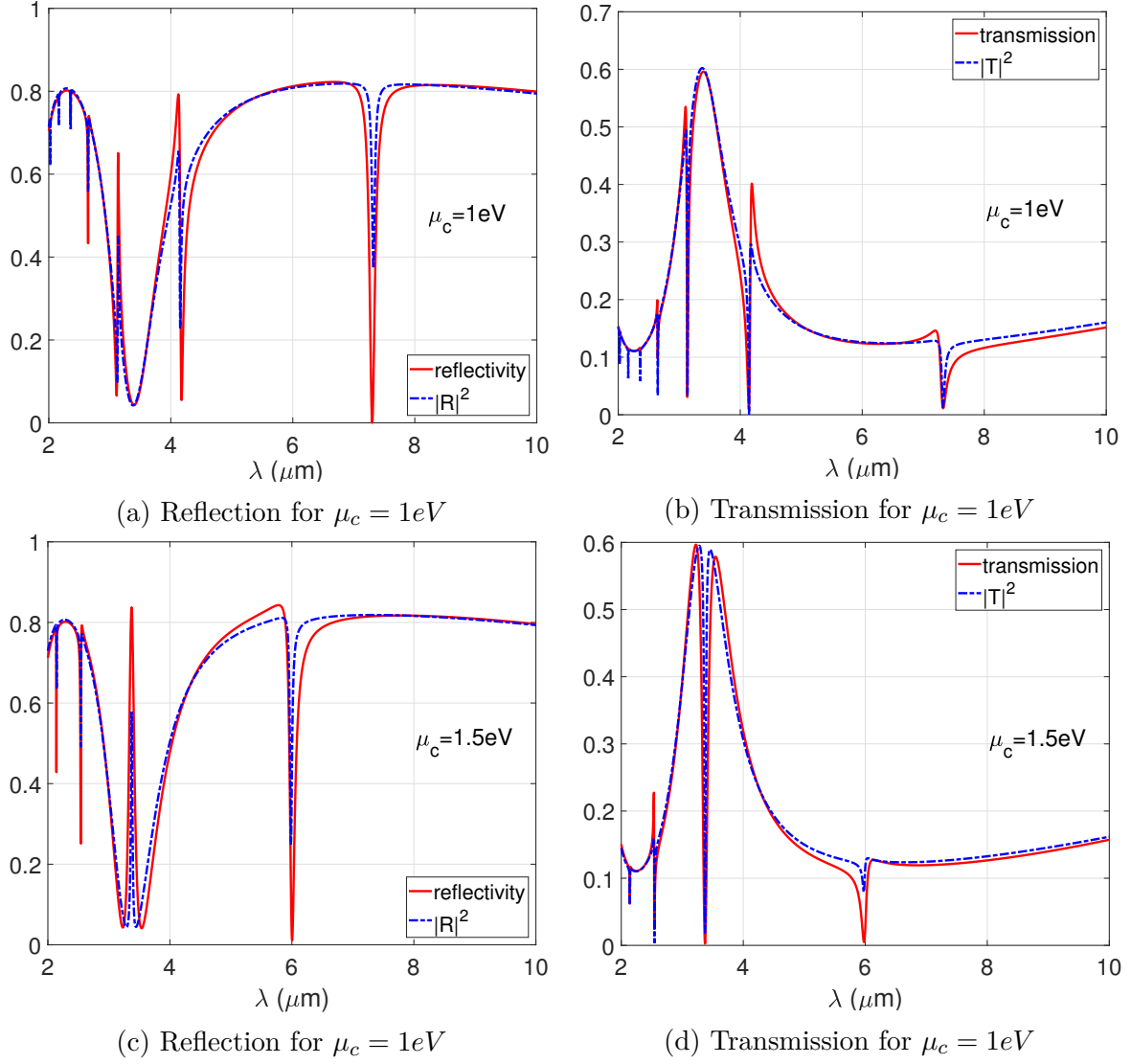


Figure 3.15: Comparison between the spectra of the hybrid-structure with the reflection and transmission curves obtained from the PMM for two values of the chemical potential  $\mu_c$ . The chemical potential is set to  $\mu_c = 1eV$ , in Figs. (3.15a) and (3.15b), while  $\mu_c = 1.5eV$ , in Figs. (3.15c) and (3.15d). All these results fit very well with the rigorous numerical simulations obtained with the PMM. Our model captures very well all resonances occurring in the hybrid system namely Lorentz and Fano ones. Parameters:  $\lambda \in [2, 10]\mu m$ ,  $\epsilon^{(1)} = \epsilon^{(3)} = \epsilon^{(s)} = 1$ ,  $\epsilon^{(2)} = 1.54^2$ , incidence angle =  $0^\circ$

For the second point, let us recall the resonance condition of the first sub-system. It is obtained from the zeros of the reflection coefficient  $R_{12}$ , in Eq. 6.8, as soon as:

$$\phi_1 r_2 \phi_3 \simeq -r_1 \text{ and } 1 + r_1 \phi_1 r_2 \phi_2 \neq 0, \quad (3.19)$$

There is an extinction of the reflection without any annihilation of the transmission. Knowing that the resonance condition of the strongly coupled system is given by

$$r_{13}(\omega) \simeq 0, \quad (3.20)$$

when the latter resonance condition Eq. (3.20) meets the former Eq. (3.19), it results

$$r_{13} \phi_1 r_2 \phi_3 \simeq 0 \quad (3.21)$$

which leads to an exaltation of reflection, and an annihilation of the transmission ( see Eq. 3.18) and the absorption. The spectral responses of the structure are shown to be highly tunable by changing a gate voltage applied to the graphene sheet. The height  $h_2$  of the horizontal cavity influences the system through the effective index  $\alpha_0^{(3)}$ . The dispersion curves of the effective index  $\alpha_0^{(3)}$  are plotted in Fig. 3.16a for different values of  $h_2$  while  $\mu_c$  is kept constant and equal to  $1\text{eV}$ . It can be seen that increasing  $h_2$  leads to a decrease of the real part of  $\alpha_0^{(3)}$ . Since the  $x$  dependance of the electromagnetic field in the cavity may be approximated by  $H_y(x) = A^+ \exp(ik\alpha_0^{(3)}x) + A^- \exp(-ik\alpha_0^{(3)}x)$ , ( $k = 2\pi/\lambda$ ), for a given  $d$ -length cavity, the resonance wavelengths can be approximately obtained through a phase condition on the term  $A^\pm \sin(2\pi d\alpha_0^{(3)}/\lambda_r)$ . When  $\alpha_0^{(3)}$  decreases, the resonance wavelength  $\lambda_r$  brought by the strongly coupled sub-system also decreases. Consequently increasing spacer height pushes the resonance wavelengths resulting from the strongly coupling sub-system towards the visible wavelengths range. The same behavior can be observed when the height  $h_2$  is kept constant while increasing the chemical potential  $\mu_c$  (see figure 3.16b). This time it is  $\mu_c$  that influences the system through the effective index of the horizontal cavity. Increasing  $\mu_c$  decreases  $\alpha_0^{(3)}$  and thereby leads to a decrease of the resonance wavelengths.

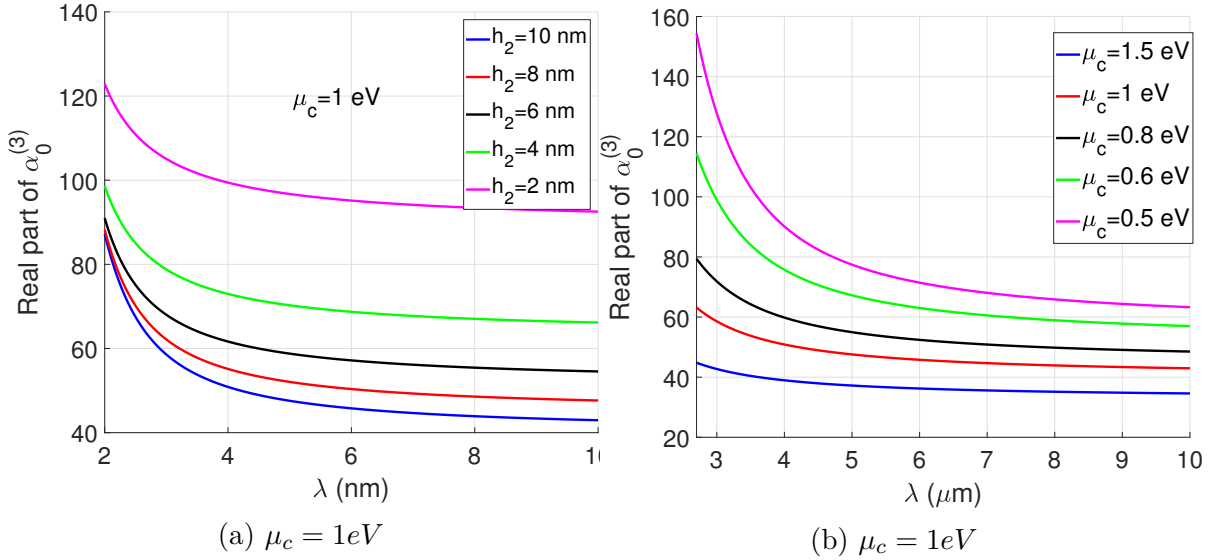


Figure 3.16: Dispersion curves of the effective index  $\alpha_0^{(3)}$  for different values of  $h_2$ , ( $\mu_c = 1\text{eV}$ ) (Fig. (3.16a)) and for different values of  $\mu_c$  ( $h_2 = 10\text{nm}$ ) (Fig. (3.16b)). Increasing the chemical potential  $\mu_c$  or the spacer width  $h_2$ , the real part of  $\alpha_0^{(3)}$  decreases. Parameters:  $\varepsilon^2 = 1.54^2$ .

By tuning the potential  $\mu_c$ , one can realize the condition of Eq. (3.21) leading to an induced reflection phenomenon. For the last raised point, the Lorentz resonance shape of the absorption is provided by the poles of the scattering parameters of the system *i.e.* when  $1 + r_1\phi_1r_{13}r_2\phi_2 \simeq 0$  leading to weak values of both reflection and transmission. Besides, the exaltation of the absorption always occurs around frequencies where both reflection and transmission are weak and equal and these frequencies are different from the zeros of the coefficient  $r_{13}$ . Therefore in the frequency range far from the resonance frequency of the EOT sub-system, the hybrid structure behaves as a tunable perfect absorber.

Finally, it is worth noticing that the present model works very well for normal incidence and reasonably well for angles of incidence up to twenty degrees. For large

angles of incidence, some new resonances appear in the spectra and are not captured by our model

### 3.3 Conclusions

In conclusion, we have proposed a simple model, allowing to deepen the comprehension of the resonance phenomena involving the EOT phenomenon and a (M-I-G) gap plasmon excitation. We consider a hybrid structure that consists of a 1D array of periodic subwavelength slits ended by a gap.

For our analysis, this hybrid structure is split into two sub-systems. Each sub-system is driven by eigenmodes operating in an appropriate coupling regime. The study of the first sub-system, characterised by modes operating in a weak coupling regime, allows to understand the broadband resonance of the hybrid system. We provided an analytical expression of the reflection and transmission coefficients of this first sub-system. The behavior of the second sub-system, characterized by modes acting in a regime of strong coupling allows to understand the narrow-band nature of the hybrid system. Here, the resonance frequencies directly depend on the metal-insulator-graphene horizontal Perot Fabry cavity effective index. Since the real part of this effective index decreases by increasing the graphene sheet chemical potential, the resonance wavelengths of the system become perfectly tunable ; better yet an induced reflection phenomenon or perfect absorption can be achieved with suited values of the graphene sheet Fermi level. We proposed a spectral function allowing not only to characterize the resonance frequencies of this second sub-system, but also showed that introducing this spectral function into the reflection and transmission coefficients of the first sub-system, we obtain an analytical expression of the reflection and transmission coefficients of the global hybrid system which are successfully compared with those obtained with rigorous numerical simulations (through the PMM approach). Finally, armed with these analytical expressions, we provided a full description of the resonance phenomena occurring in the system.

Our analysis in terms of simple modes couplings can be extended to study the coupling of the lattice modes with a substrate made by a non-reciprocal photonic topological materials, of particular interest for energy management and transport [37] and for atomic manipulation [38]. The analysis of such complex hybrid configurations involving diffraction gratings coupled to hybrid graphene multilayer structures could also be applied to study and to estimate more complicated phenomena, like the Casimir effect [39] and the radiative heat transfer [40].

# Bibliography

- [1] H.F. Ghaemi T. Thio T.W. Ebbesen, H.J. Lezec and P.A. Wolff. Extraordinary optical transmission through sub-wavelength hole arrays,”. *Nature*, (391):667–669, 1998. [77](#), [79](#), [149](#)
- [2] F.I. Baida, Y. Poujet, B. Guizal, and D. Van Labeke. New design for enhanced transmission and polarization control through near-field optical microscopy probes. *Optics Communications*, 256(1):190–195, 2005. [77](#), [149](#)
- [3] Fadi I. Baida, Yannick Poujet, Jérôme Salvi, Daniel Van Labeke, and Brahim Guizal. Extraordinary transmission beyond the cut-off through sub-annular aperture arrays. *Optics Communications*, 282(7):1463–1466, 2009. [77](#), [149](#)
- [4] L. Aigouy, P. Lalanne, J. P. Hugonin, G. Julié, V. Mathet, and M. Mortier. Near-field analysis of surface waves launched at nanoslit apertures. *Phys. Rev. Lett.*, 98:153902, Apr 2007. [77](#)
- [5] H. T. Liu and P. Lalanne. Microscopic theory of the extraordinary optical transmission. *Nature*, 452:728–731, 2008. [77](#), [149](#)
- [6] L. Martín-Moreno, F. J. García-Vidal, H. J. Lezec, K. M. Pellerin, T. Thio, J. B. Pendry, and T. W. Ebbesen. Theory of extraordinary optical transmission through subwavelength hole arrays. *Phys. Rev. Lett.*, 86:1114–1117, Feb 2001. [77](#), [149](#)
- [7] A Yu Nikitin, Sergio G Rodrigo, F J García-Vidal, and L Martín-Moreno. In the diffraction shadow: Norton waves versus surface plasmon polaritons in the optical region. *New Journal of Physics*, 11(12):123020, dec 2009. [77](#)
- [8] Kofi Edee. Single mode approach with versatile surface wave phase correction for the extraordinary optical transmission comprehension of 1d period nano-slits arrays. *OSA Continuum*, 1(2):613–624, Oct 2018. [77](#), [82](#), [83](#), [86](#), [87](#)
- [9] Sherrott M Lopez JJ Atwater HA Brar VW, Jang MS. Highly confined tunable mid-infrared plasmonics in graphene nanoresonators. *Nano Lett*, (6):2541–2547, 2013. [78](#)
- [10] O. Limaj F. J. GarcÃa de Abajo V. Pruneri D. Rodrigo, A. Tittl and H. Altug. Damping pathways of mid-infrared plasmons in graphene nanostructures. *Light Sci Appl*, (6):16277, 2013. [78](#)
- [11] Arya Fallahi and Julien Perruisseau-Carrier. Design of tunable biperiodic graphene metasurfaces. *Phys. Rev. B*, 86:195408, Nov 2012. [78](#)

- 
- [12] Zheyu Fang, Yumin Wang, Andrea E. Schlather, Zheng Liu, Pulickel M. Ajayan, F. Javier García de Abajo, Peter Nordlander, Xing Zhu, and Naomi J. Halas. Active tunable absorption enhancement with graphene nanodisk arrays. *Nano Letters*, 14(1):299–304, 2014. PMID: 24320874. [78](#)
- [13] Wenjuan Zhu Yanqing Wu Marcus Freitag Xuesong Li Phaedon Avouris Fengnian Xia Hugen Yan, Tony Low. Damping pathways of mid-infrared plasmons in graphene nanostructures. *Nature Photon*, (7):394–399, 2013. [78](#)
- [14] Frank H. L. Koppens, Darrick E. Chang, and F. Javier García de Abajo. Graphene plasmonics: A platform for strong light–matter interactions. *Nano Letters*, 11(8):3370–3377, 2011. PMID: 21766812. [78](#)
- [15] M. Farhat M. Amin and H. Bagci. A dynamically reconfigurable fano metamaterial through graphene tuning for switching and sensing applications”. *Sci Rep*, (3):2105, 2013. [78](#)
- [16] A. Yu. Nikitin, F. Guinea, F. J. Garcia-Vidal, and L. Martin-Moreno. Surface plasmon enhanced absorption and suppressed transmission in periodic arrays of graphene ribbons. *Phys. Rev. B*, 85:081405, Feb 2012. [78](#)
- [17] Jared H. Strait, Parinita Nene, Wei-Min Chan, Christina Manolatou, Sandip Tiwari, Farhan Rana, Joshua W. Kevek, and Paul L. McEuen. Confined plasmons in graphene microstructures: Experiments and theory. *Phys. Rev. B*, 87:241410, Jun 2013. [78](#)
- [18] Hugen Yan, Xuesong Li, Bhupesh Chandra, George Tulevski, Yanqing Wu, Marcus Freitag, Wenjuan Zhu, Phaedon Avouris, and Fengnian Xia. Tunable infrared plasmonic devices using graphene/insulator stacks. *Nature Nanotechnology*, 7(5):330–334, May 2012. [78](#)
- [19] Sukosin Thongrattanasiri and F. Javier García de Abajo. Optical field enhancement by strong plasmon interaction in graphene nanostructures. *Phys. Rev. Lett.*, 110:187401, Apr 2013. [78](#)
- [20] Soongyu Yi, Ming Zhou, Xi Shi, Qiaoqiang Gan, Jian Zi, and Zongfu Yu. A multiple-resonator approach for broadband light absorption in a single layer of nanostructured graphene. *Opt. Express*, 23(8):10081–10090, Apr 2015. [78](#)
- [21] Bo Zhao and Zhuomin M. Zhang. Strong plasmonic coupling between graphene ribbon array and metal gratings. *ACS Photonics*, 2(11):1611–1618, 2015. [78](#)
- [22] Weilu Gao, Jie Shu, Ciyuan Qiu, and Qianfan Xu. Excitation of plasmonic waves in graphene by guided-mode resonances. *ACS Nano*, 6(9):7806–7813, 2012. PMID: 22862147. [78](#)
- [23] Zizhuo Liu and Koray Aydin. Enhanced infrared transmission through gold nanoslit arrays via surface plasmons in continuous graphene. *Opt. Express*, 24(24):27882–27889, Nov 2016. [78](#)
- [24] B. Wang T. Zhang, L Chen and X. Li. Tunable broadband plasmonic field enhancement on a graphene surface using a normal-incidence plane wave at mid-infrared frequencies. *Sci Rep*, (5):11195, 2015. [78](#)

- [25] Linlong Tang, Haofei Shi, Jun Yang, Chunlei Du, Fuhua Gao, Jianhua Zhu, and Jinglei Du. Complete optical absorption in graphene by using nano-gratings to excite graphene surface plasmons. *Microelectronic Engineering*, 145:58 – 61, 2015. Micro/Nano Devices and Systems 2014 An open focused special thematic issue of Microelectronic Engineering. [78](#)
- [26] Sheng-Xuan Xia, Xiang Zhai, Ling-Ling Wang, Bin Sun, Jian-Qiang Liu, and Shuang-Chun Wen. Dynamically tunable plasmonically induced transparency in sinusoidally curved and planar graphene layers. *Optics express*, 24(16):17886—17899, August 2016. [78](#)
- [27] Xiaolei Zhao, Lin Zhu, Cai Yuan, and Jianquan Yao. Tunable plasmon-induced transparency in a grating-coupled double-layer graphene hybrid system at far-infrared frequencies. *Opt. Lett.*, 41(23):5470–5473, Dec 2016. [78](#)
- [28] K. Edee and J. P. Plumey. Numerical scheme for the modal method based on subsectional gegenbauer polynomial expansion: application to biperiodic binary grating. *J. Opt. Soc. Am. A*, 32(3):402–410, Mar ts , url = <http://josaa.osa.org/abstract.cfm?URI=josaa-32-3-402>, doi = 10.1364/JOSAA.32.000402,. [78](#), [152](#)
- [29] K. Edee, J.-P. Plumey, A. Moreau, and B. Guizal. Matched coordinates in the framework of polynomial modal methods for complex metasurface modeling. *J. Opt. Soc. Am. A*, 35(4):608–615, Apr 2018 ,. [78](#)
- [30] Kofi Edee. Modal method based on subsectional gegenbauer polynomial expansion for lamellar gratings. *J. Opt. Soc. Am. A*, 28(10):2006–2013, Oct 2011. [78](#), [150](#), [151](#)
- [31] G. Granet K. Edee, I. Fenniche and B. Guizal. Modal method based on subsectional gegenbauer polynomial expansion for lamellar gratings: weighting function, convergence and stability. *PIER*, (133):17–35, 2013. [78](#)
- [32] H. A. Bethe. Theory of diffraction by small holes. *Phys. Rev.*, 66:163–182, Oct 1944. [78](#)
- [33] J. A. Porto, F. J. García-Vidal, and J. B. Pendry. Transmission resonances on metallic gratings with very narrow slits. *Phys. Rev. Lett.*, 83:2845–2848, Oct 1999. [79](#)
- [34] S. Collin, F. Pardo, R. Teissier, and J.-L. Pelouard. Strong discontinuities in the complex photonic band structure of transmission metallic gratings. *Phys. Rev. B*, 63:033107, Jan 2001. [80](#)
- [35] R. Brendel and D. Bormann. An infrared dielectric function model for amorphous solids. *Journal of Applied Physics*, 71(1):1–6, 1992. [82](#), [150](#)
- [36] Aleksandar D. Rakić, Aleksandra B. Djurišić, Jovan M. Elazar, and Marian L. Majewski. Optical properties of metallic films for vertical-cavity optoelectronic devices. *Appl. Opt.*, 37(22):5271–5283, Aug 1998. [82](#), [150](#)
- [37] Pierre Doyeux, S. Ali Hassani Gangaraj, George W. Hanson, and Mauro Antezza. Giant interatomic energy-transport amplification with nonreciprocal photonic topological insulators. *Phys. Rev. Lett.*, 119:173901, Oct 2017. [93](#)

- [38] Mário G. Silveirinha, S. Ali Hassani Gangaraj, George W. Hanson, and Mauro Antezza. Fluctuation-induced forces on an atom near a photonic topological material. *Phys. Rev. A*, 97:022509, Feb 2018. [93](#)
- [39] Riccardo Messina, Paulo A. Maia Neto, Brahim Guizal, and Mauro Antezza. Casimir interaction between a sphere and a grating. *Phys. Rev. A*, 92:062504, Dec 2015. [93](#)
- [40] Bo Zhao, Brahim Guizal, Zhuomin M. Zhang, Shanhui Fan, and Mauro Antezza. Near-field heat transfer between graphene/hbn multilayers. *Phys. Rev. B*, 95:245437, Jun 2017. [93](#)

## Part III

# Non-reciprocity devices based on graphene and metals



# Chapter 4

## Basic concepts

*Symmetry is what we see at a glance.*

Blaise Pascal

### Contents

<b>4.1</b>	<b>Electromagnetic reciprocity and non reciprocity</b>	<b>101</b>
4.1.1	Time reversal symmetry of Maxwell's equations	102
4.1.2	Reciprocity Theorem in Electromagnetism	103
4.1.3	Non reciprocity with magnetic field	104
<b>4.2</b>	<b>Graphene under a static magnetic bias</b>	<b>115</b>
4.2.1	Landau Levels in monolayer graphene	115
4.2.2	Reflection and transmission properties of a magnetized graphene sheet	117
4.2.3	Surface magnetoplasmons polaritons on magnetically biased graphene sheet (GSMP)	123
4.2.4	Nonreciprocity and gyrotropy of graphene	125
<b>4.3</b>	<b>Conclusions</b>	<b>129</b>

This chapter is intended to provide the theoretical background that forms the basis for the following chapters of this part. In the first place, we introduce the reciprocity and non reciprocity notions with focus on the concept of non reciprocity with magnetic fields. In particular, we explain the optical Hall effect in the general case and give a detailed analysis of wave propagation and dispersion characteristics of gyrotropic media. These concepts are applied in the next part of this chapter to investigate graphene under the presence of a static external magnetic field.

### 4.1 Electromagnetic reciprocity and non reciprocity

The notion of reciprocity and non reciprocity is a fundamental and crucial scientific concept that occurs in many different branches of physics such as condensed-matter physics, classical mechanics, optics, thermodynamics, quantum mechanics, electromagnetism and particle and nuclear physics. From an etymological point of view,

reciprocity stems from the adjective *reciprocal* which comes from the Latin word *reciprocus*, build on the phrase *recus-procus* ("re"(backward)) and (" pro" (forward)). As a consequence, the term *reciprocal* means "going the same way backward as forward". Reciprocity is a fundamental symmetry in electromagnetism, which implies that the amplitude of a wave created by a source and scattered from an object does not change when the source and the detector are interchanged [1] (see Figure 4.1). Historically, the first study of reciprocity in electromagnetism was given by Stokes [2] in 1849 in which he derived the equation that related the reflection and transmission of light through an interface between lossless optical media. This concept was later extended to describe more complex systems in the field of electromagnetic waves in 1866 by Helmholtz [3] and in 1905 by Lorentz [4] which leads to the so called Stokes-Helmholtz-Lorentz reciprocity principle. Recently, electromagnetic reciprocity becomes an important technological

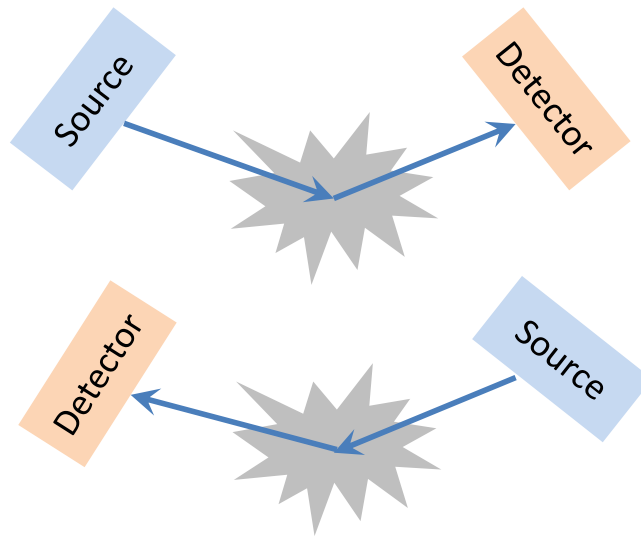


Figure 4.1: Schematic illustration of the reciprocity principle

concept and it is extensively used for analyzing antenna systems. In fact, if an antenna is an excellent transmitter, then based on the reciprocity principle, it will also serve as an excellent receiver.

#### 4.1.1 Time reversal symmetry of Maxwell's equations

Now, in order to understand the electromagnetic reciprocity in a simple and easy way, let's consider the concept of the time reversal symmetry of Maxwell's equation which is closely related to the reciprocity. Time reversal inversion of the Maxwell equations such that  $\vec{\nabla}' = \vec{\nabla}$  are:

$$\vec{\nabla} \times \vec{E} = -\frac{\partial \vec{B}'}{\partial t'} \quad (4.1)$$

$$\vec{\nabla} \times \vec{H} = -\frac{\partial \vec{D}'}{\partial t'} + \vec{j}' \quad (4.2)$$

Assuming that under time reversal, the electric charge  $q$ , charge density  $\rho$  and coordinate  $\vec{r}$  do not change. Hence, the speed  $\vec{v}$ , electric current  $\vec{j}$  and magnetic field  $\vec{B}$  are

odd with respect to time reversal. While, the electric field  $\vec{E}$  and displacement  $\vec{D}$  are time reversal even(see table 4.1). Under these assumptions, we get:

$$\vec{\nabla} \times \vec{E} = -\frac{\partial(-\vec{B})}{\partial(-t)} \quad (4.3)$$

$$\vec{\nabla} \times (-\vec{H}) = -\frac{\partial(\vec{D})}{\partial(-t)} + (-\vec{j}) \quad (4.4)$$

or by simplifying:

$$\vec{\nabla} \times \vec{E} = -\frac{\partial\vec{B}}{\partial t} \quad (4.5)$$

$$\vec{\nabla} \times \vec{H} = \frac{\partial\vec{D}}{\partial t} + \vec{j} \quad (4.6)$$

These equations are identical to the original Maxwell equations. Thus, we can conclude that the Maxwell equations are invariant under time reversal transformation. We pass now to introduce the Lorentz reciprocity theorem which plays a very central role in the electromagnetic reciprocity .

Physical Quantity	Time Reversal	Parity
Charge density	$\rho(t) \rightarrow +\rho(-t)$	even
Current density	$\vec{j}(t) \rightarrow -\vec{j}(-t)$	odd
Displacement	$\vec{D}(t) \rightarrow +\vec{D}(-t)$	even
Electric field	$\vec{E}(t) \rightarrow +\vec{E}(-t)$	even
Magnetic field	$\vec{H}(t) \rightarrow -\vec{H}(-t)$	odd
Magnetic induction	$\vec{B}(t) \rightarrow -\vec{B}(-t)$	odd
Magnetization	$\vec{M}(t) \rightarrow -\vec{M}(-t)$	odd
Polarization density	$\vec{P}(t) \rightarrow +\vec{P}(-t)$	even
Poynting vector	$\vec{S}(t) \rightarrow -\vec{S}(-t)$	odd

Table 4.1: Transformation properties of the main electromagnetic quantities under time reversal [5].

### 4.1.2 Reciprocity Theorem in Electromagnetism

In this section, we shall derive the Lorentz reciprocity theorem for electromagnetic fields. Let us Consider a volume  $V$  containing a current distribution  $j_1$  which gives rise to an electric fields  $E_1$  and a magnetic field  $H_1$ , where all three have time dependance  $e^{i\omega t}$ . Using the time harmonic Maxwell's equations form, we get:

$$\vec{\nabla} \times \vec{E}_1 = -i\omega\mu\vec{H}_1 \quad (4.7)$$

$$\vec{\nabla} \times \vec{H}_1 = i\omega\varepsilon\vec{E}_1 + \vec{j}_1 \quad (4.8)$$

Similary, consider a second current distribution  $j_2$  which is completely contained within the same volume  $V$ . This new current distribution produces fields  $E_2$  and  $H_2$  that are related by the following equations:

$$\vec{\nabla} \times \vec{E}_2 = -i\omega\mu\vec{H}_2 \quad (4.9)$$

$$\vec{\nabla} \times \vec{H}_2 = i\omega\varepsilon\vec{E}_2 + \vec{j}_2 \quad (4.10)$$

Now, let us take the dot product of  $H_2$  with each side of equation 4.7:

$$\vec{H}_2 \cdot (\vec{\nabla} \times \vec{E}_1) = -i\omega\mu\vec{H}_1 \cdot \vec{H}_2 \quad (4.11)$$

Similarly, let us take the dot product of  $E_1$  with each side of equation 4.10:

$$\vec{E}_1 \cdot (\vec{\nabla} \times \vec{H}_2) = i\omega\varepsilon\vec{E}_1 \cdot \vec{E}_2 + \vec{E}_1 \cdot \vec{j}_2 \quad (4.12)$$

By subtracting Equation 4.11 from equation 4.12, we obtain:

$$\vec{E}_1 \cdot (\vec{\nabla} \times \vec{H}_2) - \vec{H}_2 \cdot (\vec{\nabla} \times \vec{E}_1) = \vec{E}_1 \cdot \vec{j}_2 + i\omega\varepsilon\vec{E}_1 \cdot \vec{E}_2 + i\omega\mu\vec{H}_1 \cdot \vec{H}_2 \quad (4.13)$$

Using the vector identity, the left side of this equation is written as:

$$\vec{E}_1 \cdot (\vec{\nabla} \times \vec{H}_2) - \vec{H}_2 \cdot (\vec{\nabla} \times \vec{E}_1) = \vec{\nabla} \cdot (\vec{H}_2 \times \vec{E}_1) \quad (4.14)$$

So, equation 4.13 becomes:

$$\vec{\nabla} \cdot (\vec{H}_2 \times \vec{E}_1) = \vec{E}_1 \cdot \vec{j}_2 + i\omega\varepsilon\vec{E}_1 \cdot \vec{E}_2 + i\omega\mu\vec{H}_1 \cdot \vec{H}_2 \quad (4.15)$$

Next, by following the same process, we find:

$$\vec{\nabla} \cdot (\vec{H}_1 \times \vec{E}_2) = \vec{E}_2 \cdot \vec{j}_1 + i\omega\varepsilon\vec{E}_1 \cdot \vec{E}_2 + i\omega\mu\vec{H}_1 \cdot \vec{H}_2 \quad (4.16)$$

Finally, subtracting equation 4.33 from equation 4.15, we obtain:

$$\vec{\nabla} \cdot (\vec{H}_2 \times \vec{H}_1 - \vec{H}_1 \times \vec{E}_2) = \vec{E}_1 \cdot \vec{j}_2 - \vec{E}_2 \cdot \vec{j}_1 \quad (4.17)$$

This equation is commonly known as the differential form of the Lorentz reciprocity theorem. To obtain the associated form of this theorem which is applied to contiguous regions of space, we should integrate both sides of equation 4.17 over the volume  $V$ , thus we get:

$$\int \int \int_V \vec{\nabla} \cdot (\vec{H}_2 \times \vec{H}_1 - \vec{H}_1 \times \vec{E}_2) dv = \int \int \int_V (\vec{E}_1 \cdot \vec{j}_2 - \vec{E}_2 \cdot \vec{j}_1) dv \quad (4.18)$$

Using the divergence theorem to transform the left side, this equation can be expressed as:

$$\int \int_S (\vec{H}_2 \times \vec{H}_1 - \vec{H}_1 \times \vec{E}_2) \cdot d\vec{s} = \int \int \int_V (\vec{E}_1 \cdot \vec{j}_2 - \vec{E}_2 \cdot \vec{j}_1) dv \quad (4.19)$$

where  $S$  is the closed mathematical surface which bounds  $V$ . If we now confine the sources to finite region of space, while allowing  $V$  to grow infinitely large, expanding to include all space. In this situation, the closest distance between any point containing non-zero source current and  $S$  is infinite. Since field magnitude diminishes with distance from the source, all the fields are zeros on  $S$ . Thus the left side of (4.19) is zero and we obtain:

$$\int \int \int_V (\vec{E}_1 \cdot \vec{j}_2 - \vec{E}_2 \cdot \vec{j}_1) dv = 0 \quad (4.20)$$

which can be written as follows:

$$\int \int \int_V \vec{E}_1 \cdot \vec{j}_2 dv = \int \int \int_V \vec{E}_2 \cdot \vec{j}_1 dv \quad (4.21)$$

This equation provides the intergral form of the lorentz reciprocity theorem which relates fields on the bounding surface to sources within the volume. The question now

is why do we refer to this relationship as reciprocity? the answer is simply because the expression remains the same by interchanging the subscripts "1" and "2". In other words, a reaction of a reciprocal system is insensitive of the interchange of source and measurement locations.

The notion of non reciprocity refers to the absence of reciprocity and it requires to break and violate the Lorentz theorem. In general, nonreciprocity in a system is based on breaking the time reversal symmetry of light-matter interaction (time reversal becomes asymmetric). This time reversal symmetry breaking can be achieved by an external bias for linear systems or by a combination of self-biasing and structural asymmetry for nonlinear systems [5].

### 4.1.3 Non reciprocity with magnetic field

We have shown above that one way to achieve non reciprocity is by introducing an external bias, for example by applying a static magnetic field. This applied magnetic field breaks the time reversal symmetry of Maxwell equations as well as the reciprocity theorem leading to the creation of an anisotropy and gyrotropic behavior in the medium. The interaction of a polarized light with such a medium, also called gyrotropic media, affects its polarisation state yielding various magneto-optical effects. In the following, we first make a description of the Optical Hall effect to explain the occurrence of the anisotropy in materials subjected to an external magnetic field. Then, we focus our attention to the investigation of characteristics of electromagnetic waves propagation in gyrotropic medium. Lastly, we introduce and define magneto-optical effects.

#### Optical Hall effect (OHE)

In this section the Optical Hall effect (OHE), an essential tool that we use throughout this part of the thesis, is discussed. First, we begin by giving a brief description of the static electric Hall effect. Next, we present the theoretical model that can able to explain these phenomena.

The Optical Hall effect, developed by Mathias Schubert [6, 7], is a physical phenomenon that describes the external magnetic field induced optical anisotropy in conductive materials caused by the non-time-reciprocal response of electric charge carriers. This induced magneto optic anisotropy results from the motion of the free charge carriers (FCCs) under the influence of the Lorentz force. The OHE is the equivalent of the classical static electric Hall effect at the optical frequencies, hence the name "optical". So, for a deeper understanding of this phenomenon, let us start by describing and explaining its electrical analogous.

The static electric Hall effect, discovered by the American physicist Edwin Hall in 1879 [8], is a phenomenon resulting from the interaction between the electric and magnetic fields and moving charge carriers in a conducting medium. This effect is considered as an important and useful tool for the characterization of materials especially semi conductors and metals and it permits easy and direct determination of the density and sign of the charge carriers in these materials. Hall found that when an electrical current passes through a conductor material placed in a transverse magnetic field, a potential difference is appeared across the material in a direction perpendicular to both the current and to the magnetic field. This voltage is called *Hall voltage* and is proportional to the product between the current and the magnetic field. A schematic representation of this effect in a thin conducting material is depicted in Figure 4.2. It shows a strip of conducting material placed in  $xoy$  plane where a magnetic field is

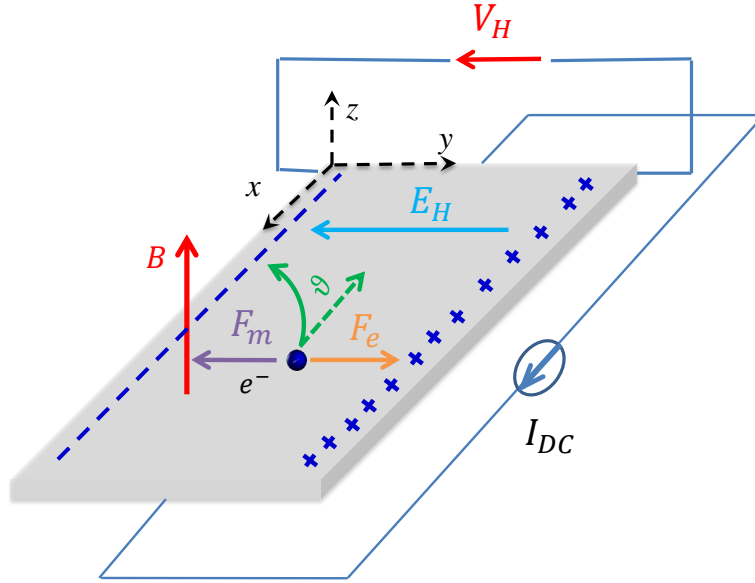


Figure 4.2: Schematic representation of the electrical Hall effect in a thin conducting material.

applied perpendicular to its surface along  $z$  direction. A constant electric current  $I_x$  flows through the conductor in the  $x$  direction caused by the application of an electric field  $E_x$ . Assume that the conductor has charge carrier  $q$  which can be either positive or negative or both (in the following we take ( $q = -e$ )), charge carrier number density  $n$  (number of carriers per unit volume) and charge carrier drift velocity  $\vec{v}$  (average velocity of the charge carriers over the volume of the conductor). Under the influence of the electric and magnetic fields, the charge carrier ( $-e$ ) will experience a Lorentz force which is given by:

$$\vec{F}_L = -e(\vec{E} + \vec{v} \times \vec{B}) \quad (4.22)$$

As seen in Figure 4.2, this force acts on the moving charge carriers (electrons) by deflecting them toward one side of the strip. This deflection leads to an accumulation of charges along one side of the strip which produces a transverse electric field  $E_y$  that tends to counteract the force of Lorentz and opposes the migration of further charge. This process continues until a steady-state situation is reached and then a steady potential difference  $V_H$  is established between the two faces in the  $y$  direction.

After having described the principle of the Hall effect, we will now give a model for electric currents under electric and magnetic fields in order to provide physical explanation of this effect. Generally, the most commonly used models are: the classical Model and the quantum mechanics approach. Here, Our discussion will be limited to the classical approach.

### Extended Drude Model

The equation of motion of an electron subjected to an electric and magnetic fields reads:

$$m \frac{d\vec{v}}{dt} = -e(\vec{E} + \vec{v} \times \vec{B}) - \frac{m}{\tau} \vec{v} \quad (4.23)$$

where  $\tau$  is the scattering time,  $e$  and  $m$  are respectively the charge and the mass of the electron. The First term on the right hand side of this equation is the above described force of Lorentz and the second term is a retarding force resulting from scattering of

electrons with impurities. At steady-state, the time derivative of  $v$  vanishes which leads to:

$$v_x = \frac{-e\tau}{m}(E_x + v_y B_z) \quad (4.24)$$

$$v_y = \frac{-e\tau}{m}(E_y - v_x B_z) \quad (4.25)$$

$$v_z = \frac{-e\tau}{m}E_z = 0 \quad (4.26)$$

The current densities  $J_x$  and  $J_y$  are given by:

$$J_x = -nev_x \quad (4.27)$$

$$J_y = -nev_y \quad (4.28)$$

$$J_z = 0 \quad (4.29)$$

Using the definition of the cyclotron frequency  $\omega_c = \frac{eB}{m}$ , we can write:

$$\begin{pmatrix} 1 & \omega_c\tau \\ -\omega_c\tau & 1 \end{pmatrix} \begin{pmatrix} J_x \\ J_y \end{pmatrix} = \frac{e^2 n\tau}{m} \begin{pmatrix} E_x \\ E_y \end{pmatrix} \quad (4.30)$$

Ohm's Law that relates the current density with the electric field is :

$$J = \sigma E \quad (4.31)$$

with  $\sigma$  is the conductivity. Thus Eq 4.30 can be written as the following form:

$$\begin{pmatrix} J_x \\ J_y \end{pmatrix} = \begin{pmatrix} \sigma_{xx} & \sigma_{xy} \\ \sigma_{yx} & \sigma_{yy} \end{pmatrix} \begin{pmatrix} E_x \\ E_y \end{pmatrix} \quad (4.32)$$

where

$$\sigma = \begin{pmatrix} \sigma_{xx} & \sigma_{xy} \\ \sigma_{yx} & \sigma_{yy} \end{pmatrix} = \frac{e^2 n\tau}{m} \frac{1}{1 + \omega_c^2 \tau^2} \begin{pmatrix} 1 & \omega_c\tau \\ -\omega_c\tau & 1 \end{pmatrix} \quad (4.33)$$

By comparing with Eq 4.33, it is found that:

$$\sigma = \begin{pmatrix} \sigma_{xx} & \sigma_{xy} \\ -\sigma_{xy} & \sigma_{xx} \end{pmatrix} = \begin{pmatrix} \sigma_L & \sigma_H \\ -\sigma_H & \sigma_L \end{pmatrix} \quad (4.34)$$

It is clearly seen from Eq 4.34 that the presence of the static magnetic field gives rise to a finite optical Hall conductivity  $\sigma_H$  which leads to generate an anisotropy in the material. Note that while the longitudinal optical conductivity is related to the light absorption, the optical Hall conductivity is the basis of the Magneto-optical effects, the subject of our next discussion. Hence studying the optical Hall effect is one of the key tools for exploring magneto optical applications.

### Gyrotropic medium

When passing through a medium in the presence of a static magnetic field, the plane of polarisation of light can be rotated to the left or right. This effect is known as optical gyrotropy and the medium is said to be gyrotropic. The noun 'Gyrotropy' refers to this rotating motion and is composed of the prefix 'gyro' which comes from the Ancient Greek word *gyros* 'a circle' and the suffix 'tropy' coming from Ancient Greek word

*tropía* and meaning 'a turn' or in science 'exhibiting a behavior'. Thus, the etymological meaning of "gyrotropy" is 'exhibiting a rotational behavior'. As pointed out in the previous section, a gyrotropic material is an anisotropic medium whose optical and magneto-optical properties are described within its relative permittivity and permeability tensors  $\varepsilon$  and  $\mu$ . In the presence of a magnetic field, the components of these tensors cease to be symmetric. The generalized symmetry of the kinetic coefficients requires that:

$$\varepsilon_{ik}(\vec{B}) = \varepsilon_{ki}(-\vec{B}) \quad (4.35)$$

For lossless material, the tensor should be hermitian:

$$\varepsilon_{ik} = \varepsilon_{ki}^* \quad (4.36)$$

Equation 4.36 implies that the real and imaginary parts of  $\varepsilon_{ik}$  must be respectively symmetrical and antisymmetrical:

$$\varepsilon'_{ik} = \varepsilon'_{ki} \quad (4.37)$$

$$\varepsilon''_{ik} = -\varepsilon''_{ki} \quad (4.38)$$

Using Eq 4.35, we find that:

$$\varepsilon'_{ik}(\vec{B}) = \varepsilon'_{ki}(\vec{B}) = \varepsilon'_{ki}(-\vec{B}) \quad (4.39)$$

$$\varepsilon''_{ik}(\vec{B}) = -\varepsilon''_{ki}(\vec{B}) = -\varepsilon''_{ki}(-\vec{B}) \quad (4.40)$$

This gives the condition that in a lossless medium, the real and imaginary parts of the permittivity tensor are even and odd functions of the applied field respectively. The inverse tensor  $\varepsilon_{ik}^{-1} = \eta_{ik}$  has the same symmetry properties.

$$\varepsilon_{ik}^{-1} = \eta_{ik} = \eta'_{ik} + i\eta''_{ik} \quad (4.41)$$

Since  $\eta''_{ik}$  is an antisymmetrical tensor of rank two, it should have an equivalent axial vector. Let consider  $\vec{G}$  this vector. The relation between  $\eta''_{ik}$  and  $G_i$  is:

$$\eta''_{ik} = e_{ikl}G_l \quad (4.42)$$

where  $e_{ikl}$  is the antisymmetrical unit tensor. Thus, the relation between the electrical field and electric displacement becomes:

$$E_i = (\eta'_{ik} + ie_{ikl}G_l)D_k = \eta'_{ik}D_k + i(\vec{D} \times \vec{G})_i \quad (4.43)$$

This is the characteristic equation of a gyrotropic medium. The gyrotropic medium is said to be electrically gyrotropic or gyroelectric if the relative permittivity tensor is written as the following form:

$$\varepsilon = \varepsilon_1(I - \vec{b}_0\vec{b}_0) + i\varepsilon_2(\vec{b}_0 \times I) + \varepsilon_3\vec{b}_0\vec{b}_0 \quad (4.44)$$

$$\mu = \mu_0 I \quad (4.45)$$

$\vec{b}_0$  is the direction of the applied magnetic field  $\vec{B}$ . The gyrotropic medium becomes magnetically gyrotropic or gyromagnetic if the relative permeability tensor is:

$$\mu = \mu_1(I - \vec{b}_0\vec{b}_0) + i\mu_2(\vec{b}_0 \times I) + \mu_3\vec{b}_0\vec{b}_0 \quad (4.46)$$

$$\varepsilon = \varepsilon_0\varepsilon_r I \quad (4.47)$$

Assuming that the magnetic field is along  $z$  direction ( $\vec{B} = B\vec{e}_z$ ), the relative permittivity tensor and the relative permeability are given by the following matrix form:

$$\varepsilon = \begin{pmatrix} \varepsilon_1 & -i\varepsilon_2 & 0 \\ i\varepsilon_2 & \varepsilon_1 & 0 \\ 0 & 0 & \varepsilon_3 \end{pmatrix} \quad (4.48)$$

$$\mu = \begin{pmatrix} \mu_1 & -i\mu_2 & 0 \\ i\mu_2 & \mu_1 & 0 \\ 0 & 0 & \mu_3 \end{pmatrix} \quad (4.49)$$

The off diagonal components, which contain the gyration term  $\varepsilon_2$ , are at the origin of the magneto-optical effects.

If the medium is a lossless metal which is a gyroelectric medium, the permittivity tensor components can be expressed as:

$$\varepsilon_1 = 1 - \frac{\omega_p^2}{\omega^2 - \omega_c^2} \quad (4.50)$$

$$\varepsilon_2 = \frac{\omega_c \omega_p^2}{\omega(\omega^2 - \omega_c^2)} \quad (4.51)$$

$$\varepsilon_3 = 1 - \frac{\omega_p^2}{\omega} \quad (4.52)$$

In the following subsections, we will analyze the propagation characteristics of an (EM) wave in a gyrotropic medium. Since all the structures studied in this part are gyroelectric media, we will give a detailed analysis of wave propagation and dispersion characteristics in a gyroelectric medium.

### Dispersion relation for Gyrotropic medium

First, we have to derive the dispersion relation for an electrically gyrotropic medium. Let us Consider the structure depicted in Figure 4.3 where a plane wave is incident on the surface of a gyroelectric medium with a wave vector  $k$  and a static magnetic field is applied along the  $z$  direction ( $\vec{B} = B\vec{e}_z$ ). The gyroelectric medium is characterized by its relative permittivity and permeability tensors given above by the equation 4.47. The angle between  $k$  and  $B$  is  $\theta$  and the incident wave vector is defined as  $\vec{k} = \alpha\vec{e}_x + \beta\vec{e}_y + \gamma\vec{e}_z = \vec{k}_\rho + \gamma\vec{e}_z$  where  $\vec{k}_\rho = \alpha\vec{e}_x + \beta\vec{e}_y$ ,  $\alpha = k \sin \theta \cos \phi$ ,  $\beta = k \sin \theta \sin \phi$  and  $\gamma = k \cos \theta$  such that  $(\alpha^2 + \beta^2 + \gamma^2 = k^2)$ . Since under the influence of the magnetic field, carriers move in cyclotron orbits, all the components of the electric and magnetic fields are present:  $\vec{E} = (E_x, E_y, E_z)$  and  $\vec{H} = (H_x, H_y, H_z)$ . These components satisfy the following time harmonic Maxwell equations (with  $e^{-i\omega t}$  dependence):

$$\vec{\nabla} \times \vec{E} = i\omega\mu_0\vec{H} \quad (4.53)$$

$$\vec{\nabla} \times \vec{H} = -i\omega\varepsilon_0\varepsilon\vec{E} + \vec{j} \quad (4.54)$$

In the source free region ( $\vec{j} = \vec{0}$ ), we find:

$$\begin{cases} \partial_y E_z - \partial_z E_y = i\omega\mu_0 H_x \\ \partial_z E_x - \partial_x E_z = i\omega\mu_0 H_y \\ \partial_x E_y - \partial_y E_x = i\omega\mu_0 H_z \end{cases} \quad (4.55)$$

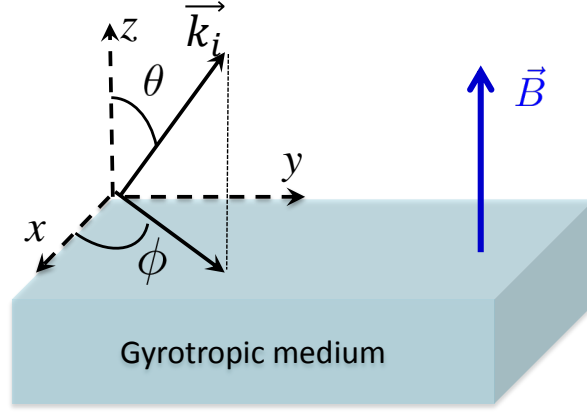


Figure 4.3: Wave propagation in a gyroelectric medium

$$\begin{cases} \partial_y H_z - \partial_z H_y = -i\omega\varepsilon_0(\varepsilon_1 E_x - i\varepsilon_2 E_y) \\ \partial_z H_x - \partial_x H_z = -i\omega\varepsilon_0(i\varepsilon_2 E_x + \varepsilon_1 E_y) \\ \partial_x H_y - \partial_y H_x = -i\omega\varepsilon_0\varepsilon_3 E_z \end{cases} \quad (4.56)$$

We look for the solution of the plane wave of the form:

$$\vec{E} = \vec{E}_0 e^{i(\alpha x + \beta y + \gamma z)} \quad (4.57)$$

$$\vec{H} = \vec{H}_0 e^{i(\alpha x + \beta y + \gamma z)} \quad (4.58)$$

where  $\vec{E}_0 = (E_{0x}, E_{0y}, E_{0z})$  and  $\vec{H}_0 = (H_{0x}, H_{0y}, H_{0z})$ . Inserting (4.58) in (4.55) and (4.56) and performing straightforward calculations, gives:

$$\begin{pmatrix} k_0\varepsilon_1 - \beta^2 - \gamma^2 & \alpha\beta - i\varepsilon_2 k_0^2 & \alpha\beta \\ \alpha\beta + i\varepsilon_2 k_0^2 & k_0^2\varepsilon_1 - \alpha^2 - \gamma^2 & \beta\gamma \\ \alpha\gamma & \beta\gamma & k_0^2\varepsilon_3 - \alpha^2 - \beta^2 \end{pmatrix} \begin{pmatrix} E_{0x} \\ E_{0y} \\ E_{0z} \end{pmatrix} = M_E \begin{pmatrix} E_{0x} \\ E_{0y} \\ E_{0z} \end{pmatrix} = 0 \quad (4.59)$$

With  $M_E$  being the electric wave matrix. This system has non trivial solutions if the determinant of  $M_E$  vanishes:

$$|M_E| = \begin{vmatrix} k_0\varepsilon_1 - \beta^2 - \gamma^2 & \alpha\beta - i\varepsilon_2 k_0^2 & \alpha\beta \\ \alpha\beta + i\varepsilon_2 k_0^2 & k_0^2\varepsilon_1 - \alpha^2 - \gamma^2 & \beta\gamma \\ \alpha\gamma & \beta\gamma & k_0^2\varepsilon_3 - \alpha^2 - \beta^2 \end{vmatrix} = 0 \quad (4.60)$$

which yields:

$$\gamma^4 k_0^2 \varepsilon_3 + \gamma^2 [k_0^2 k_\rho^2 (\varepsilon_1 + \varepsilon_3) - 2k_0^4 \varepsilon_1 \varepsilon_3] + [k_0^6 \varepsilon_3 (\varepsilon_1^2 - \varepsilon_2^2) - k_0^4 k_\rho^2 (\varepsilon_1^2 - \varepsilon_2^2 + \varepsilon_1 \varepsilon_3) + k_0^4 k_\rho^4 \varepsilon_1] = 0 \quad (4.61)$$

This equation provide the dispersion relation of an electrically gyrotropic or gyroelectric medium and has two solutions in  $\gamma^2$  as:

$$\gamma_1^2 = k_0^2 \frac{\left[ 2\varepsilon_1 \varepsilon_3 - \frac{k_\rho^2}{k_0^2} (\varepsilon_1 + \varepsilon_3) \right] + \left[ \frac{k_\rho^4}{k_0^4} (\varepsilon_1 \varepsilon_3)^2 + 4\varepsilon_2^2 \varepsilon_3 \left( \varepsilon_3 - \frac{k_\rho^2}{k_0^2} \right) \right]^{1/2}}{2\varepsilon_3} \quad (4.62)$$

$$\gamma_2^2 = k_0^2 \frac{\left[ 2\varepsilon_1 \varepsilon_3 - \frac{k_\rho^2}{k_0^2} (\varepsilon_1 + \varepsilon_3) \right] - \left[ \frac{k_\rho^4}{k_0^4} (\varepsilon_1 \varepsilon_3)^2 + 4\varepsilon_2^2 \varepsilon_3 \left( \varepsilon_3 - \frac{k_\rho^2}{k_0^2} \right) \right]^{1/2}}{2\varepsilon_3} \quad (4.63)$$

Equations(4.62)and (4.63) represent the wave numbers corresponding to the eigenmodes of wave propagation in gyroelectric medium.

### Propagation in Gyrotropic media

This subsection is dedicated to the investigation of the waves propagation in a gyroelectric medium. First of all, it is important to emphasize that when the angle between the magnetic field and the wave propagation  $\theta$  is equal to 0 or  $\pi/2$ , the waves propagating within the medium will be named as *principle waves*. Hence, we can distinguish two type of propagation: when  $\theta = 0$  i.e the direction of propagation is parallel to the direction of the magnetic field, the wave propagation is called *longitudinal propagation*. When the direction of wave propagation is perpendicular of the direction of the magnetic field  $\theta = \pi/2$ , the wave propagation is called *transverse propagation*.

**Longitudinal Propagation ( $\theta = 0$ )** : Considering now the longitudinal propagation when  $\theta = 0$ , in this case (4.62) and (4.63) reduce to:

$$k_1 = \gamma_1 = k_0 \sqrt{\varepsilon_1 + \varepsilon_2} \quad (4.64)$$

$$k_2 = \gamma_2 = k_0 \sqrt{\varepsilon_1 - \varepsilon_2} \quad (4.65)$$

From Maxwell equations and the helmoltz equation we can deduce that the components of the electric field for  $\theta = 0$  satisfy the following equations:

$$E_{0x} (k_0^2 \varepsilon_1 - k^2) - i\varepsilon_2 E_{0y} = 0 \quad (4.66)$$

$$-i\varepsilon_2 k_0^2 E_{0x} + E_{0y} (k_0^2 \varepsilon_1 - k^2) = 0 \quad (4.67)$$

$$E_{0z} k_0^2 \varepsilon_3 = 0 \quad (4.68)$$

One can clearly see that for a longitudinal propagation there is no electric field component in the  $z$  direction i.e in the direction of propagation. While, the magnetic field  $H$  is transverse to the direction of propagation. Therefore, the two waves that propagate parallel to  $B$  are transverse electromagnetic waves. Substituting (4.64) in (4.68), gives:

$$\frac{E_{0x}}{E_{0y}} = -i \quad (4.69)$$

This equation corresponds to a right handed circularly polarized (RCP) wave. Now when (4.65) is substituted in (4.68), we find:

$$\frac{E_{0x}}{E_{0y}} = i \quad (4.70)$$

Which corresponds to the left handed circularly polarized (LCP) wave. The electric fields associated with the two waves can be expressed as:

$$\vec{E}_1 = (\vec{e}_x + i\vec{e}_y) A e^{i\gamma_1 z} \quad RCP \quad (4.71)$$

$$\vec{E}_2 = (\vec{e}_x - i\vec{e}_y) B e^{i\gamma_2 z} \quad LCP \quad (4.72)$$

Where  $A$  and  $B$  are arbitrary amplitudes. So, we can conclude that when an electromagnetic wave propagates through a gyroelectric medium with a vector wave parallel to the direction of  $B$ , the eigenmodes of propagation are right and left circularly polarized waves. Let us consider now a linearly polarized electric field given by the sum of both circularly waves when  $A = B$ :

$$\vec{E} = \vec{E}_1 + \vec{E}_2 = (e^{i\gamma_1 z} + e^{i\gamma_2 z}) \vec{e}_x + (ie^{i\gamma_1 z} - ie^{i\gamma_2 z}) \vec{e}_y \quad (4.73)$$

The polarisation of this wave can be obtained by:

$$\frac{E_x}{E_y} = -i \frac{1 + e^{i(\gamma_2 - \gamma_1)z}}{1 - e^{i(\gamma_2 - \gamma_1)z}} = -\cot\left(\frac{\gamma_2 - \gamma_1}{2}z\right) \quad (4.74)$$

From equation 4.74, it is found that the polarisation of the polarized wave rotates as the wave propagates along the  $z$  direction by an angle  $\theta_F$ :

$$\theta_F = \cot^{-1}\left(\frac{\gamma_2 - \gamma_1}{2}z\right) = -\left(\frac{\gamma_2 - \gamma_1}{2}z\right) \quad (4.75)$$

The rotation angle per unit of distance has the form:

$$\Theta_F = -\left(\frac{\gamma_2 - \gamma_1}{2}\right) \quad (4.76)$$

This rotation angle is called Faraday rotation.

**Transverse Propagation ( $\theta = 0$ )** : As pointed out earlier, for this kind of propagation, the direction of wave propagation is perpendicular to the direction of the magnetic field i.e ( $\theta = 90^\circ$ ). By assuming a plane wave propagating along  $y$  direction equations (4.62) and (4.63) reduce to:

$$k_1 = \beta_1 = k_0 \sqrt{\frac{\varepsilon_1^2 + \varepsilon_2^2}{\varepsilon_1}} \quad (4.77)$$

$$k_2 = \beta_2 = k_0 \sqrt{\varepsilon_3} \quad (4.78)$$

In this case, from Maxwell equation we can obtain:

$$E_{0x} (k_0^2 \varepsilon_1 - k^2) - i \varepsilon_2 k_0^2 E_{0y} = 0 \quad (4.79)$$

$$-i \varepsilon_2 k_0^2 E_{0x} + E_{0y} (k_0^2 \varepsilon_1) = 0 \quad (4.80)$$

$$E_{0z} (k_0^2 \varepsilon_3 - k^2) = 0 \quad (4.81)$$

By substituting (4.78) into (4.81), it is found that  $E_{ox}$  and  $E_{oy}$  are equal to zeros and the electric field has only one component along the  $z$  direction. Since the propagation constant given in (4.78) is equal to the propagation constant of a wave propagating in a isotropic medium and is independent of the magnetic field, this wave is called as *ordinary wave*. Thus, we can see that the obtained wave is a linearly polarized wave whose electric vector is parallel to  $B$  and is given by:

$$\vec{E}_2 = A e^{i\beta_2 y} \vec{e}_z \quad (4.82)$$

With  $A$  is an arbitrary amplitude. Now, when (4.77) is substituted in (4.81), we obtain:

$$\frac{E_{0x}}{E_{0y}} = i \frac{\varepsilon_1}{\varepsilon_2} \quad (4.83)$$

The electric vector corresponding to this wave, known as *extraordinary wave*, has the following form:

$$\vec{E}_1 = \left( i \frac{\varepsilon_1}{\varepsilon_2} \vec{e}_x + \vec{e}_y \right) C e^{i\beta_1 y} \quad (4.84)$$

Where  $C$  is an arbitrary constant. Finally, to summarize, in both cases  $\theta = 0^\circ$  and  $\theta = 90^\circ$ , which correspond to longitudinal and transverse propagation, there exist two uncoupled waves which are known as principal waves. For the longitudinal propagation, they are the right circularly polarized wave and the left circularly polarized wave. While for the transverse propagation, they are the ordinary wave and extraordinary wave.

### Magneto-optical (MO) effects

Magneto-optical effects are phenomena referring to changes in the polarisation state of light after interacting with a magnetic material. Historically, the first magneto-optical effect was discovered by Michael Faraday in 1846 [9]. He found that the plane of linearly polarized light was rotated after passing through a glass rod subjected to an external magnetic field parallel to the direction of the path of the light. This rotation was known as Faraday rotation. Thirty years later (1877), kerr found the corresponding magneto-optical effect in reflection performed by a magnetized metallic iron mirror [10]. According to the interaction of incident light with matter, the basic magneto-optical can be classified into three categories

- MO effects in reflection
- MO effects in transmission
- MO effects in absorption

For the last two categories of MO effects, we can distinguish two basic geometries according to the orientation between the wave vector of light and the magnetic field.

- Faraday geometry: the light propagates parallel to the magnetic field ( $\vec{k} \parallel \vec{B}$ )
- Voigt or Cotton-Mouton geometry: the light travels perpendicular to the direction of the magnetic field ( $\vec{k} \perp \vec{B}$ )

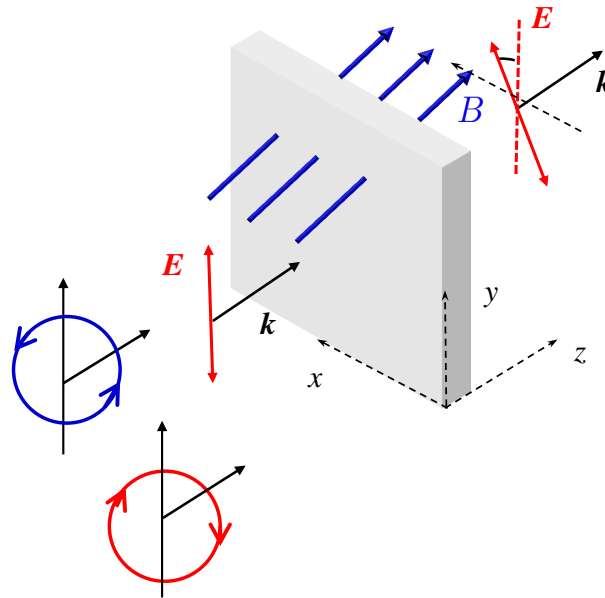


Figure 4.4: Schematic representation of the Faraday effect

As shown in the previous subsection, In Faraday geometry (longitudinal propagation), the eigen modes are left and right circularly polarized light and in Voigt geometry (transverse propagation) the eigenmodes are linearly polarized light. The symmetry is broken and violated by the magneto-optical effects, which leads to induce an asymmetry of the propagation of the eigenmodes. For example, in Faraday geometry, left and right circularly polarized wave propagate differently. The difference between eigenmodes

propagation can be explained by the effects of birefringence and dichroism. Circular Birefringence results from the difference between phase velocities for left and right circularly polarized light. As shown above This difference causes a rotation of the plane of polarisation of the wave by an angle  $\Theta_F$ . A schematic representation of the faraday effect is shown in Figure 4.4 .

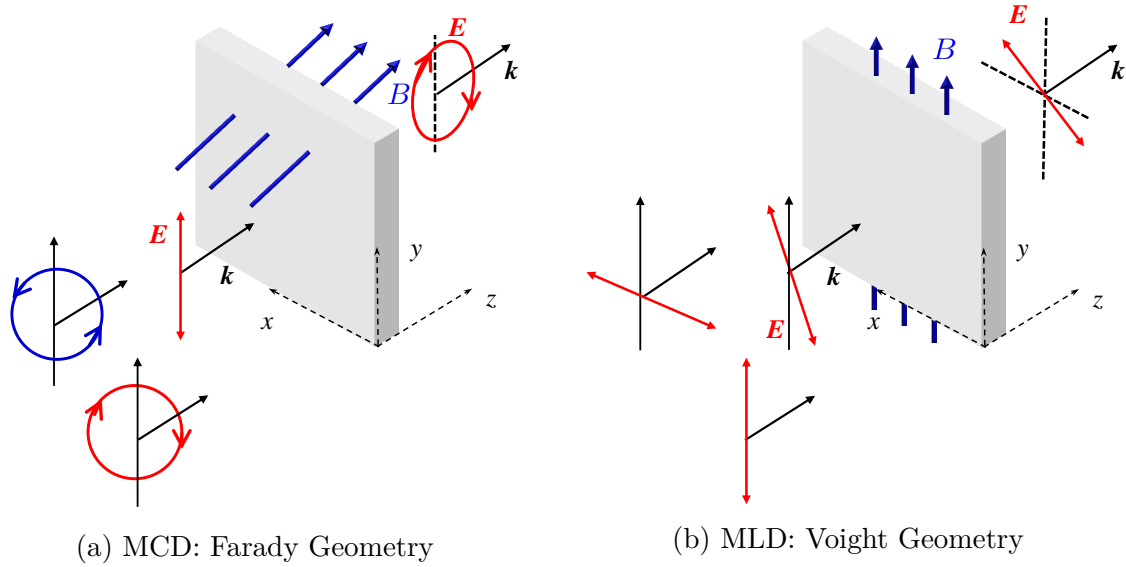


Figure 4.5: Magneto-optical effects in Absorption depending on the geometry:(a) Magnetic circular dichroism (MCD).(b) Magnetic linear dichroism (MLD)

Dichroism arises when the two eigenmodes are absorbed differently by the magnetic medium. In the Fraday geometry, circular magnetic dichroism (MCD) is produced from the difference in absorption coefficients for left and right circularly polarized EM wave. While, in the case of the Voigt geometry, dichroism, known as magnetic linear dichroism (MLD), is related to the difference between the absorption of the components polarized parallel and perpendicular to the magnetic field (see Figure 4.5). MCD changes an incident linearly polarized EM wave into elliptically one and the MLD rotates an elliptically polarized wave by and angle.

We turn now our attention to the magneto-optical effects in reflection often known as *Kerr effects*. These effects occur when an EM wave is reflected from a magnetized medium and are related to the change of the polarisation state of the reflected light. First, it is important to underline that when working in reflection, the polarisation state is defined with respect to the plane of incidence. According to that, we can distinguish two linear polarizations: a linear polarisation "s", where the electric field is perpendicular to the plane of incidence, and a linear polarization "p" where the electric field is parallel to plane of incidence. These two linear polarizations are orthogonal and thus they can form a basis. Let us consider a magnetic medium subjected to a linearly polarized ( $s$  or  $p$ ) wave. After reflection, an orthogonal polarisation appears and we will have both  $s$  and  $p$  components. As a consequence, the reflected wave becomes elliptically polarized which causes the rotation of the polarisation plane. This evolution of the polarisation state of light can be described in the framework of the Jones formalism. The Jone vector  $J$  is defined as:

$$\vec{J} = \begin{pmatrix} E_s \\ E_p \end{pmatrix} \quad (4.85)$$

Where  $E_s$  and  $E_p$  represents the  $s$  and  $p$  polarized components of light. The total intensity of the wave can be expressed as:

$$I = JJ^* = (E_s E_s^* + E_p E_p^*) = (|E_s|^2 + |E_p|^2) \quad (4.86)$$

The change of the polarization state caused by the reflection can be described by the reflection matrix  $R$ :

$$R = \begin{pmatrix} r_{ss} & r_{ps} \\ r_{sp} & r_{pp} \end{pmatrix} \quad (4.87)$$

where the coefficients are defined as the ratio between reflected and incident electromagnetic waves:

$$r_{ss} = \frac{E_s^r}{E_s^i} \quad r_{pp} = \frac{E_p^r}{E_p^i} \quad r_{sp} = \frac{E_s^r}{E_p^i} \quad r_{ps} = \frac{E_p^r}{E_s^i} \quad (4.88)$$

Using these reflections coefficients, we can define the Kerr rotation  $\Theta_{s,p}$  and ellipticity  $\varepsilon_{s,p}$  for  $s$  and  $p$  incident polarized light:

$$\begin{aligned} \Theta_s + i\varepsilon_s &= \frac{r_{sp}}{r_{ss}} \\ \Theta_p + i\varepsilon_p &= \frac{r_{ps}}{r_{pp}} \end{aligned} \quad (4.89)$$

## 4.2 Graphene under a static magnetic bias

In this section, we are going to investigate and exploit the gyrotropic and propagation properties of graphene in the presence of a magnetic bias. We start by describing the quantized Landau levels in magnetically biased graphene which are important to understand and explain the magneto-optical conductivity model presented in chapter 1. Next, the reflection and transmission coefficients through a single anisotropic monolayer graphene will be calculated. These calculations will be then used to derive the dispersion relation of surface magnetoplasmons polaritons propagating along a magnetized graphene sheet.

### 4.2.1 Landau Levels in monolayer graphene

Under the influence of a perpendicular magnetic field, the relativistic carriers in graphene are deflected by the Lorentz force and move in cyclotron orbits. At sufficiently high fields, the continuum Dirac quasiparticle spectrum becomes a discrete spectrum of degenerated Landau levels (LLs) (see Figure 4.6) with energies given by [11, 12]:

$$E_n = \text{sign}(n) \left( \frac{\hbar v_f}{l_B} \right) \sqrt{2|n|} = \text{sign}(n) v_f \sqrt{2e\hbar B |n|} \quad n = 0, \pm 1, \pm 2, \pm 3 \dots \quad (4.90)$$

Where  $l_B = \sqrt{\hbar/(eB)}$  denotes the magnetic length and  $n$  is the LL index. Note that this index can be positive or negative. The positive values correspond to electrons in conduction band. While the negative values correspond to the holes in valence band. From equation 4.90, one can see that the spectrum of quantized levels in graphene is different from the usual Landau quantization. In fact, in a conventional two dimensional electron gas, Landau quantization produces equidistant energy levels with energy difference  $\hbar\omega_c$  [13], where  $\omega_c$  being the cyclotron frequency. While, in graphene as shown in Figure 4.7, the quantized Landau energies are proportional to the square root of the

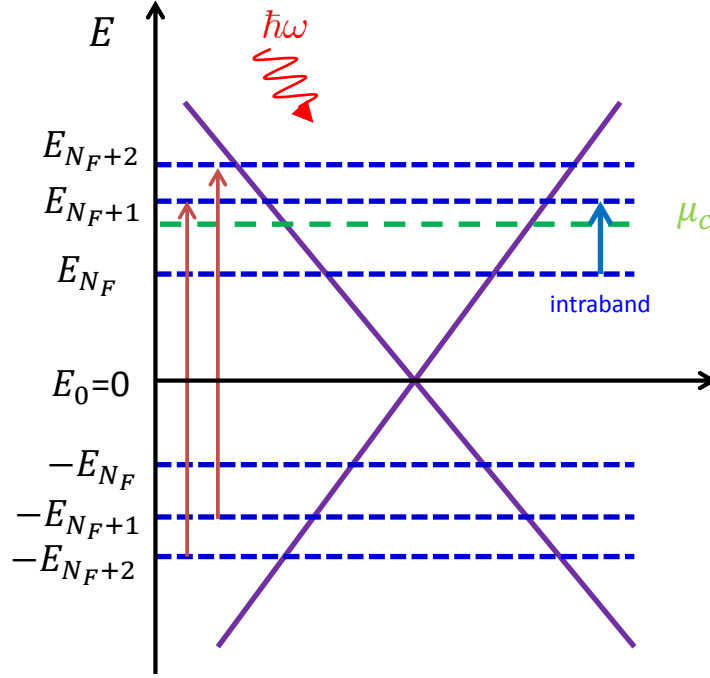


Figure 4.6: Schematic representation of the dispersion diagram of graphene when a static magnetic field is applied. Due to this field, the linear dispersion relation of graphene (purple curve) is quantized into Landau levels (blue dots lines) according to the Landau quantization. The red arrows represent the allowed interband transitions between energy levels and the blue arrow stands for the intraband transition.

magnetic field and are unequally spaced. Furthermore, the gap between two successive Landau levels is  $\Delta_n = E_{n+1} - E_n \propto 1/\sqrt{(n)}$  and it decreases as the energies increase. As a result, the largest energy separation in graphene  $\Delta_0$  is between the zeros and the first Landau level and is much higher than  $k_B T$ , ( $\Delta_0 \gg k_B T \simeq 26 \text{meV}$ ) which allows the observation of unusual quantum Hall effect (half-integer quantum Hall effect) in graphene at room temperature. This phenomenon was first observed in exfoliated graphene flakes [14, 15] and later in graphene epitaxially grown on silicon carbide (SiC) [16, 17]. For high energies, the Landau levels become very close to each other and therefore in this case the discrete energy spectrum can be treated as a continuum.

Another interesting fact of the Landau levels is the appearance of an anomalous Landau level ( $n = 0$ ) at zero energy (Dirac point) owing from the exceptional band structure of graphene. This level is independent of the magnetic field and is shared by electrons and holes. The transitions between Landau levels give rise to the cyclotron resonance. In graphene, the cyclotron resonance frequency corresponds to the difference between the Landau levels  $E_{N_F}$  and  $E_{N_F+1}$  and is given by:

$$\omega_c = \frac{E_{N_F+1} - E_{N_F}}{\hbar} = \text{sign}(N_F) \left( \frac{v_f \sqrt{2e\hbar B}}{\hbar \sqrt{|N_F + 1| + \sqrt{|N_F|}}} \right) \quad (4.91)$$

with  $N_F$  denotes the index of the last occupied LL and is defined as  $N_F = \text{int}[(\mu_c/E_1)^2]$  [11]. For high doped graphene where  $\mu_c \gg k_B T$  (semiclassical region where only intraband transitions can occur),  $N_F \gg 1$  and as a consequence since the Landau levels around  $\mu_c$  become very close to each other i.e  $N_F \simeq N_{F+1}$ , we get  $E_{N_F} \simeq E_{F+1} \simeq \mu_c$ . Therefore,

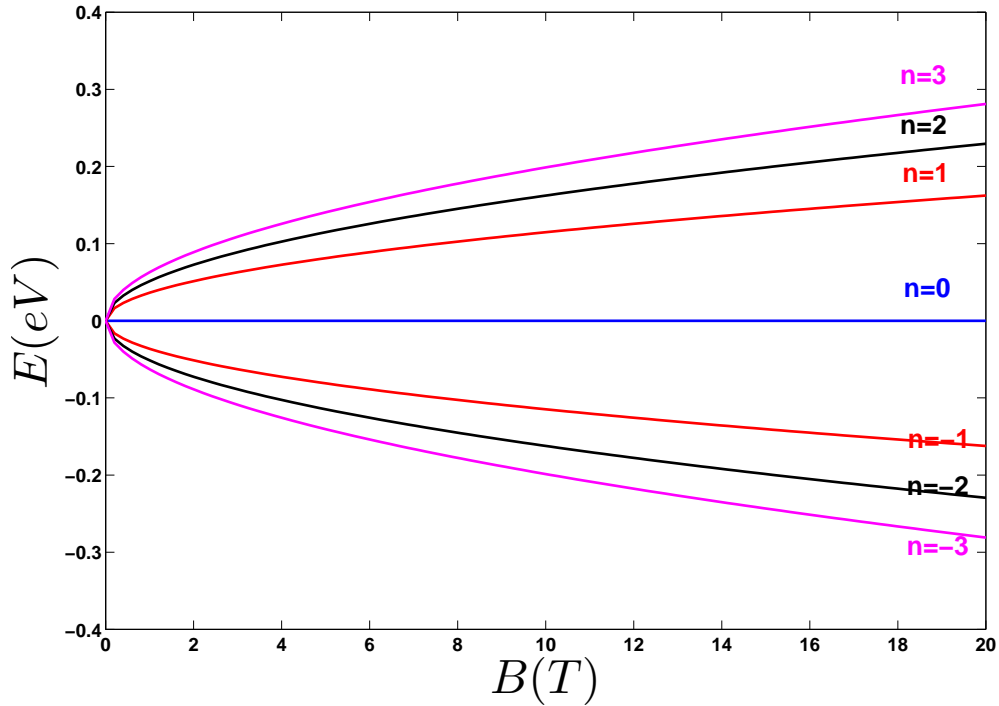


Figure 4.7: Energies calculated for the first four Landau levels of graphene as a function of magnetic field.

in this limiting case, the cyclotron frequency of graphene is given by: [18]

$$\omega_c = \frac{v_f^2 e B}{\mu_c} \quad (4.92)$$

Note that this  $\sqrt{B}$  dispersion of transitions between Landau levels has been experimentally observed in infrared transmission spectroscopy (see Figure 4.8) [19, 20, 21, 22]

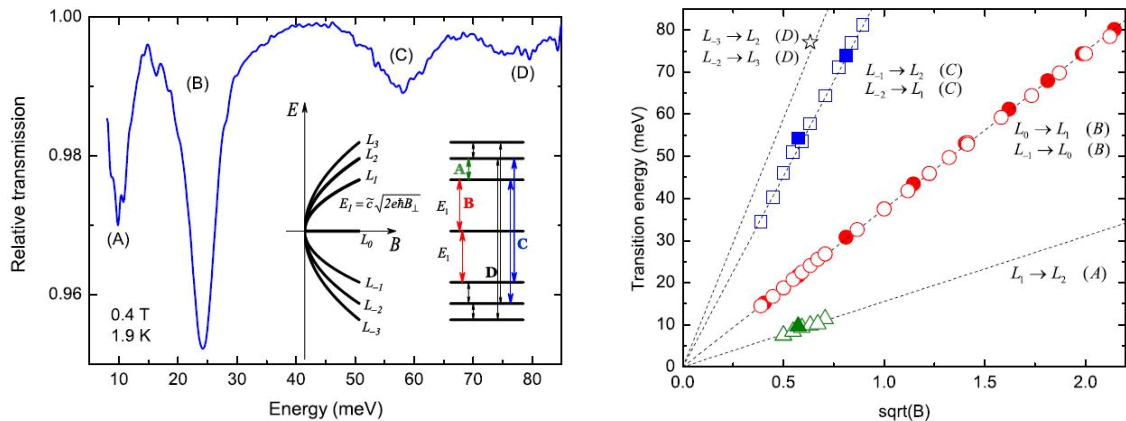


Figure 4.8: Landau Levels transitions in monolayer graphene. (a) relative transmission observed at  $B=0.4\text{ T}$  and  $T=1.9\text{ K}$ . This spectrum shows four transitions: A:  $L_1 \rightarrow L_2$ , B:  $L_0 \rightarrow L_1$  ( $L_{-1} \rightarrow L_0$ ), C:  $L_{-2} \rightarrow L_1$  ( $L_{-1} \rightarrow L_2$ ), D:  $L_{-3} \rightarrow L_2$  ( $L_{-2} \rightarrow L_3$ ). (b) The observed transitions as a function of magnetic field  $B$ . Adapted from ref [22]

### 4.2.2 Reflection and transmission properties of a magnetized graphene sheet

we shall now investigate the optical properties of a single anisotropic graphene sheet in the presence of an external static magnetic field, such as the reflectance and the transmittance. For this purpose, we consider the structure shown in Figure 4.9 where a graphene sheet is surrounded between two homogeneous and isotropic dielectric media with dielectric constants  $\varepsilon_1$  and  $\varepsilon_2$  and an external static magnetic field  $\vec{B}$  is applied perpendicular to the graphene (along  $z$  direction). A plane wave is impinging onto the graphene sheet under an angle  $\theta$  from the lower half space ( $z < 0$ ). In order to

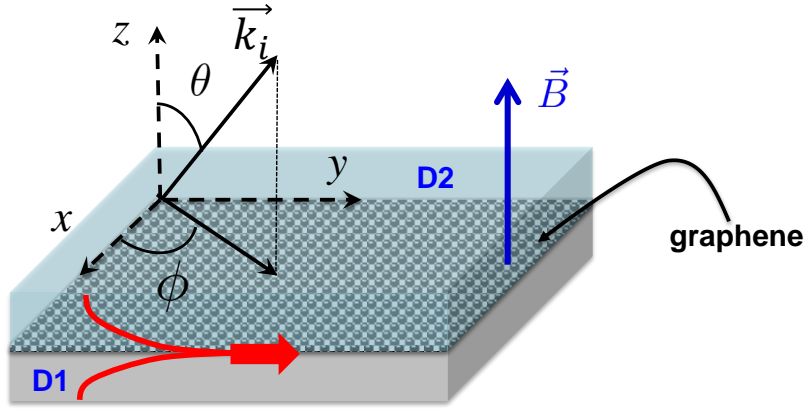


Figure 4.9: Schematic representation of the studied structure: a graphene sheet sandwiched between two homogeneous and isotropic dielectric media  $D_1$  and  $D_2$  and biased with a static magnetic field  $B_0$ . The external magnetic field is applied perpendicular to the graphene plane along  $z$  direction. A plane wave is obliquely impinging with angle  $\theta$  on graphene from medium  $D_1$  toward medium  $D_2$

calculate the reflectance and the transmission, we need to solve the Maxwell's equations in each medium and match subsequently the boundary conditions across the graphene interface. In cartesian coordinates, the components of the electromagnetic fields satisfy the following Maxwell's equations:

$$\begin{cases} \partial_y E_z - \partial_z E_y = i\omega\mu_0 H_x \\ \partial_z E_x - \partial_x E_z = i\omega\mu_0 H_y \\ \partial_x E_y - \partial_y E_x = i\omega\mu_0 H_z \end{cases} \quad \begin{cases} \partial_y H_z - \partial_z H_y = -i\omega\varepsilon_0\varepsilon_r E_x \\ \partial_z H_x - \partial_x H_z = -i\omega\varepsilon_0\varepsilon_r E_y \\ \partial_x H_y - \partial_y H_x = -i\omega\varepsilon_0\varepsilon_r E_z \end{cases} \quad (4.93)$$

$$\Rightarrow \begin{cases} \partial_z H_x = \partial_x H_z - i\omega\varepsilon_0\varepsilon_r E_y \\ \partial_z H_y = \partial_y H_z + i\omega\varepsilon_0\varepsilon_r E_x \\ H_z = \frac{1}{ik_0 Z_0} (\partial_x E_y - \partial_y E_x) \end{cases} \quad (4.94)$$

$$\begin{cases} \partial_z H_x = \frac{1}{ik_0 Z_0} (\partial_x^2 E_y - \partial_x \partial_y E_x) - \frac{ik_0}{Z_0} \varepsilon_r E_y \\ \partial_z H_y = \frac{1}{ik_0 Z_0} (\partial_y \partial_x E_y - \partial_y^2 E_x) + \frac{ik_0}{Z_0} \varepsilon_r E_x \end{cases} \quad (4.95)$$

The parallel components of the electric field in the medium 1 can be written as follows

$$\begin{cases} E_{x1} = (I_x e^{i\gamma_1 z} + R_x e^{-i\gamma_1 z}) e^{i\alpha x} e^{i\beta y} \\ E_{y1} = (I_y e^{i\gamma_1 z} + R_y e^{-i\gamma_1 z}) e^{i\alpha x} e^{i\beta y} \end{cases} \quad (4.96)$$

Similarly, in medium 2 the  $x$  and  $y$  components of  $E$  are given by:

$$\begin{cases} E_{x2} = T_x e^{i\gamma_2 z} e^{i\alpha x} e^{i\beta y} \\ E_{y2} = T_y e^{i\gamma_2 z} e^{i\alpha x} e^{i\beta y} \end{cases} \quad (4.97)$$

The  $x$  and  $y$  components of the magnetic field in each medium can be deduced from 4.95 and are expressed as:

$$\begin{cases} H_{x1} = -\frac{1}{k_0 Z_0 \gamma_1} ((\alpha\beta(I_x e^{i\gamma_1 z} - R_x e^{-i\gamma_1 z}) + (\beta^2 + \gamma_1^2)(I_y e^{i\gamma_1 z} - R_y e^{-i\gamma_1 z})) e^{i\alpha x} e^{i\beta y} \\ H_{y1} = \frac{1}{k_0 Z_0 \gamma_1} (\alpha\beta(I_y e^{i\gamma_1 z} - R_y e^{-i\gamma_1 z}) + (\alpha^2 + \gamma_1^2)(I_x e^{i\gamma_1 z} - R_x e^{-i\gamma_1 z})) e^{i\alpha x} e^{i\beta y} \end{cases} \quad (4.98)$$

$$\begin{cases} H_{x2} = -\frac{1}{k_0 Z_0 \gamma_2} (\alpha\beta T_x e^{i\gamma_2 z} + (\beta^2 + \gamma_2^2) T_y e^{i\gamma_2 z}) e^{i\alpha x} e^{i\beta y} \\ H_{y2} = \frac{1}{k_0 Z_0 \gamma_2} (\alpha\beta T_y e^{i\gamma_2 z} + (\alpha^2 + \gamma_2^2) T_x e^{i\gamma_2 z}) e^{i\alpha x} e^{i\beta y} \end{cases} \quad (4.99)$$

Let us now apply the boundary conditions at the interface which relate the electromagnetic fields in the two dielectric media. The first boundary condition imposes the continuity of the tangential electric field at the interface of graphene while the second condition relates the tangential components of the magnetic field at the interface to the surface current density over the graphene layer :

$$\begin{aligned} \vec{e}_z \wedge (\vec{E}_2 - \vec{E}_1) &= \vec{0} \\ \vec{e}_z \wedge (\vec{H}_2 - \vec{H}_1) &= \vec{J} \end{aligned} \quad (4.100)$$

Where  $\vec{J} = \bar{\sigma} \vec{E}$  with  $\bar{\sigma}$  is the conductivity tensor given in chapter 1. This leads us to find:

$$\begin{cases} E_{x1} = E_{x2} \\ E_{y1} = E_{y2} \\ H_{x2} - H_{x1} = J_y = \sigma_L E_y - \sigma_H E_x \\ H_{y2} - H_{y1} = -J_x = -(\sigma_L E_x + \sigma_H E_y) \end{cases} \quad (4.101)$$

Enforcing these conditions at  $z = 0$ , we obtain:

$$\begin{cases} I_x + R_x = T_x \\ I_y + R_y = T_y \\ \frac{1}{\gamma_2} (\alpha\beta T_x + (\beta^2 + \gamma_2^2) T_y) - \frac{1}{\gamma_1} ((\alpha\beta(I_x - R_x) + (\beta^2 + \gamma_1^2)(I_y - R_y)) = k_0 Z_0 (\sigma_H T_x - \sigma_L T_y) \\ \frac{\gamma_2}{\gamma_1} (\alpha\beta T_y + (\alpha^2 + \gamma_2^2) T_x) - \frac{1}{\gamma_1} ((\alpha\beta(I_y - R_y) + (\alpha^2 + \gamma_1^2)(I_x - R_x)) = k_0 Z_0 (-\sigma_L T_x - \sigma_H T_y) \end{cases} \quad (4.102)$$

This system of equations can be written in the following matrix form :

$$\begin{pmatrix} \frac{\alpha\beta}{\gamma_1} - \frac{\alpha\beta}{\gamma_2} + k_0 Z_0 \sigma_H & \gamma_1 + \frac{\beta^2}{\gamma_1} - \gamma_2 - \frac{\beta^2}{\gamma_2} - k_0 Z_0 \sigma_L \\ \gamma_1 + \frac{\alpha^2}{\gamma_1} - \gamma_2 - \frac{\alpha^2}{\gamma_2} - k_0 Z_0 \sigma_L & \frac{\alpha\beta}{\gamma_1} - \frac{\alpha\beta}{\gamma_2} - k_0 Z_0 \sigma_H \end{pmatrix} \begin{pmatrix} I_x \\ I_y \end{pmatrix} = \begin{pmatrix} \frac{\alpha\beta}{\gamma_1} + \frac{\alpha\beta}{\gamma_2} - k_0 Z_0 \sigma_H & \gamma_1 + \frac{\beta^2}{\gamma_1} + \gamma_2 + \frac{\beta^2}{\gamma_2} + k_0 Z_0 \sigma_L \\ \gamma_1 + \frac{\alpha^2}{\gamma_1} + \gamma_2 + \frac{\alpha^2}{\gamma_2} + k_0 Z_0 \sigma_L & \frac{\alpha\beta}{\gamma_1} + \frac{\alpha\beta}{\gamma_2} + k_0 Z_0 \sigma_H \end{pmatrix} \begin{pmatrix} R_x \\ R_y \end{pmatrix} \quad (4.103)$$

$$\begin{pmatrix} R_x \\ R_y \end{pmatrix} = \begin{pmatrix} \frac{\alpha\beta}{\gamma_1} + \frac{\alpha\beta}{\gamma_2} - k_0 Z_0 \sigma_H & \gamma_1 + \frac{\beta^2}{\gamma_1} + \gamma_2 + \frac{\beta^2}{\gamma_2} + k_0 Z_0 \sigma_L \\ \gamma_1 + \frac{\alpha^2}{\gamma_1} + \gamma_2 + \frac{\alpha^2}{\gamma_2} - k_0 Z_0 \sigma_L & \frac{\alpha\beta}{\gamma_1} + \frac{\alpha\beta}{\gamma_2} + k_0 Z_0 \sigma_H \end{pmatrix}^{-1} \\ \begin{pmatrix} \frac{\alpha\beta}{\gamma_1} - \frac{\alpha\beta}{\gamma_2} + k_0 Z_0 \sigma_H & \gamma_1 + \frac{\beta^2}{\gamma_1} - \gamma_2 - \frac{\beta^2}{\gamma_2} - k_0 Z_0 \sigma_L \\ \gamma_1 + \frac{\alpha^2}{\gamma_1} - \gamma_2 - \frac{\alpha^2}{\gamma_2} - k_0 Z_0 \sigma_L & \frac{\alpha\beta}{\gamma_1} - \frac{\alpha\beta}{\gamma_2} + k_0 Z_0 \sigma_H \end{pmatrix} \begin{pmatrix} I_x \\ I_y \end{pmatrix} \quad (4.104)$$

Therefore the reflected and incident fields can be connected by the Reflection Matrix  $M_R$  as follows:

$$\begin{pmatrix} R_x \\ R_y \end{pmatrix} = \begin{pmatrix} R_{xx} & R_{xy} \\ R_{yx} & R_{yy} \end{pmatrix} \begin{pmatrix} I_x \\ I_y \end{pmatrix} = M_R \begin{pmatrix} I_x \\ I_y \end{pmatrix} \quad (4.105)$$

where:

$$M_R = \begin{pmatrix} \frac{\alpha\beta}{\gamma_1} + \frac{\alpha\beta}{\gamma_2} - k_0 Z_0 \sigma_H & \gamma_1 + \frac{\beta^2}{\gamma_1} + \gamma_2 + \frac{\beta^2}{\gamma_2} + k_0 Z_0 \sigma_L \\ \gamma_1 + \frac{\alpha^2}{\gamma_1} + \gamma_2 + \frac{\alpha^2}{\gamma_2} - k_0 Z_0 \sigma_L & \frac{\alpha\beta}{\gamma_1} + \frac{\alpha\beta}{\gamma_2} + k_0 Z_0 \sigma_H \end{pmatrix}^{-1} \\ \begin{pmatrix} \frac{\alpha\beta}{\gamma_1} - \frac{\alpha\beta}{\gamma_2} + k_0 Z_0 \sigma_H & \gamma_1 + \frac{\beta^2}{\gamma_1} - \gamma_2 - \frac{\beta^2}{\gamma_2} - k_0 Z_0 \sigma_L \\ \gamma_1 + \frac{\alpha^2}{\gamma_1} - \gamma_2 - \frac{\alpha^2}{\gamma_2} - k_0 Z_0 \sigma_L & \frac{\alpha\beta}{\gamma_1} - \frac{\alpha\beta}{\gamma_2} + k_0 Z_0 \sigma_H \end{pmatrix} \quad (4.106)$$

In the simple case when  $\varepsilon_1 = \varepsilon_2$ , the reflection coefficients are expressed as:

$$R_{xx} = -\frac{2(\gamma^2 + \beta^2)\sigma_L + 2\alpha\beta\sigma_H + k_0 Z_0 \gamma(\sigma_L^2 + \sigma_H^2)}{2(\gamma^2 + k_0^2 \varepsilon)\sigma_L + 4\gamma \frac{k_0}{Z_0} \varepsilon + k_0 Z_0 \gamma(\sigma_L^2 + \sigma_H^2)} \quad (4.107)$$

$$R_{xy} = -\frac{2(\gamma^2 + \beta^2)\sigma_H - 2\alpha\beta\sigma_L}{2(\gamma^2 + k_0^2 \varepsilon)\sigma_L + 4\gamma \frac{k_0}{Z_0} \varepsilon + k_0 Z_0 \gamma(\sigma_L^2 + \sigma_H^2)} \quad (4.108)$$

$$R_{yx} = \frac{2(\gamma^2 + \alpha^2)\sigma_H + 2\alpha\beta\sigma_L}{2(\gamma^2 + k_0^2 \varepsilon)\sigma_L + 4\gamma \frac{k_0}{Z_0} \varepsilon + k_0 Z_0 \gamma(\sigma_L^2 + \sigma_H^2)} \quad (4.109)$$

$$R_{yy} = -\frac{2(\gamma^2 + \alpha^2)\sigma_L - 2\alpha\beta\sigma_H + k_0 Z_0 \gamma(\sigma_L^2 + \sigma_H^2)}{2(\gamma^2 + k_0^2 \varepsilon)\sigma_L + 4\gamma \frac{k_0}{Z_0} \varepsilon + k_0 Z_0 \gamma(\sigma_L^2 + \sigma_H^2)} \quad (4.110)$$

In addition, at normal incidence where  $\alpha = \beta = 0$ , these expressions are simplified to:

$$R_{xx} = -\frac{2k_0^2\varepsilon\sigma_L + k_0Z_0\gamma(\sigma_L^2 + \sigma_H^2)}{2(\gamma^2 + k_0^2\varepsilon)\sigma_L + 4\gamma\frac{k_0}{Z_0}\varepsilon + k_0Z_0\gamma(\sigma_L^2 + \sigma_H^2)} \quad (4.111)$$

$$R_{xy} = -R_{yx} = -\frac{2\gamma^2\sigma_H}{2(\gamma^2 + k_0^2\varepsilon)\sigma_L + 4\gamma\frac{k_0}{Z_0}\varepsilon + k_0Z_0\gamma(\sigma_L^2 + \sigma_H^2)} \quad (4.112)$$

$$R_{yy} = -\frac{2\gamma^2\sigma_L + k_0Z_0\gamma(\sigma_L^2 + \sigma_H^2)}{2(\gamma^2 + k_0^2\varepsilon)\sigma_L + 4\gamma\frac{k_0}{Z_0}\varepsilon + k_0Z_0\gamma(\sigma_L^2 + \sigma_H^2)} \quad (4.113)$$

Similarly, the transmission coefficients are given by:

$$\begin{pmatrix} T_x \\ T_y \end{pmatrix} = \begin{pmatrix} T_{xx} & T_{xy} \\ T_{yx} & T_{yy} \end{pmatrix} \begin{pmatrix} I_x \\ I_y \end{pmatrix} = M_T \begin{pmatrix} I_x \\ I_y \end{pmatrix} \quad (4.114)$$

Where  $M_T$  being the transmission matrix whose elements are deduced from those of reflection matrix  $M_R$  as:

$$\begin{cases} T_{xx} = 1 + R_{xx} \\ T_{yy} = 1 + R_{yy} \\ T_{xy} = R_{xy} \\ T_{yx} = R_{yx} \end{cases} \quad (4.115)$$

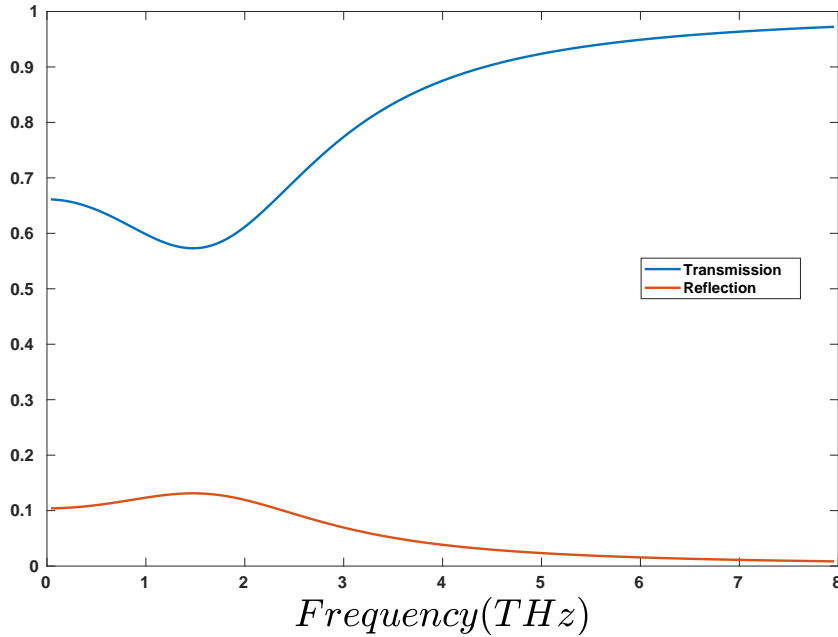


Figure 4.10: Transmission and Reflection spectra of a magnetized monolayer graphene surrounded by air under TM polarization at normal incidence. The parameters are:  $\mu_c = 0.2\text{eV}$ ,  $T = 300\text{K}$   $\tau = 0.2\text{ps}$  and  $B = 2T$

As an example, we plot in Figure 4.10, the transmittance and the reflectance spectra of a TM wave incident onto a monolayer graphene in free space magnetically biased with an external magnetic field  $B$  equal to  $2T$ . In our calculations, we consider the case of normal incidence and the parameters of the graphene layer are taken as:  $\mu_c = 0.2\text{eV}$ ,  $T = 300\text{K}$   $\tau = 0.2\text{ps}$ . The results are computed using equations (4.110) and (4.115).

One can see that there is a dip (peak) in the transmission (reflection) spectra around the frequency  $f = 1.49\text{THz}$ . This could be explained by the fact that at this frequency a worst impedance matching occurs between the graphene characteristic impedance and the air characteristic impedance.

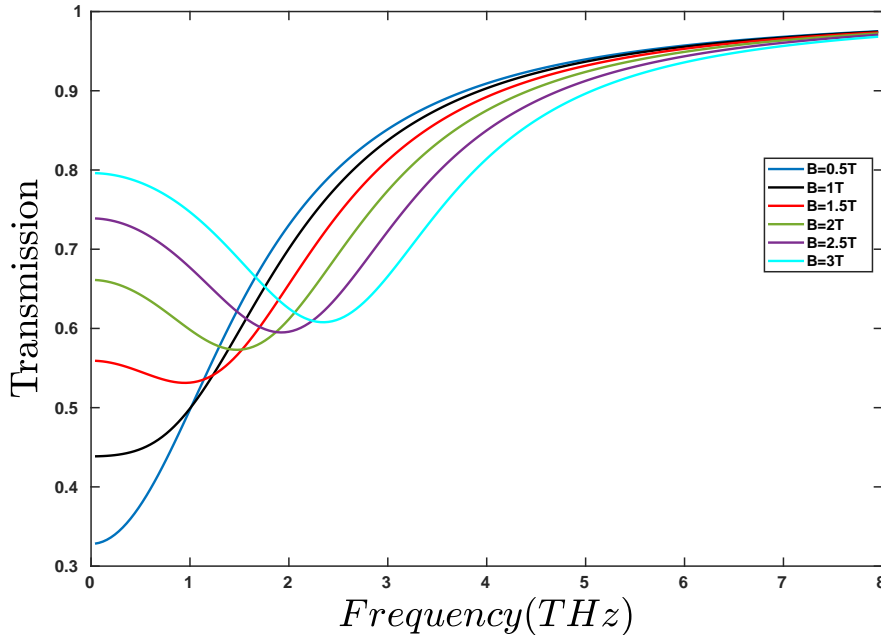


Figure 4.11: Transmission spectra of a monolayer graphene at normal incidence in the presence of different external magnetic fields:  $B = 0.5, 1, 1.5, 2, 2.5$  and  $3T$

In order to understand how the optical properties of the graphene monolayer are affected by the variation of an external magnetic field, we calculate the transmittance for a normally incident plane wave in TM polarization for different magnetic fields  $B = 0.5, 1, 1.5, 2, 2.5$  and  $3T$  as shown in Figure 4.11. We can see that when the external magnetic field increases from  $0.5$  to  $3T$ , the transmittance increases. In the same manner, we can find that for the TE polarization case, the transmittance increases with increasing  $B$ .

We pass now to analyse the influence of the incidence angle on the transmission spectra. Figure 4.12 shows the transmittance calculated under the TE and TM polarizations for different incident angles  $\theta = 0^\circ, 30^\circ$  and  $45^\circ$ . It is shown, that for the TE polarization case, the transmittance decreases with increasing the incident angle while it increases for the TM polarization. According to [23], this can be explained as follows: For the TE polarized wave, since the electric field is always parallel to the graphene surface for all incident angles, graphene always interacts with the wave. This interaction between the graphene and the incident wave enhances with increasing  $\theta$  which leads to decrease the transmission. While for the TM polarization, increasing  $\theta$ , leads to decrease the component of the electric field parallel to the graphene surface which attenuate the interaction between the graphene and the incident wave. As a consequence the transmission increases.

Having calculated the transmission and the reflection through a magnetically biased graphene sheet, we will use them in the next section to derive the dispersion relation of the surface magnetoplasmons polariton modes.

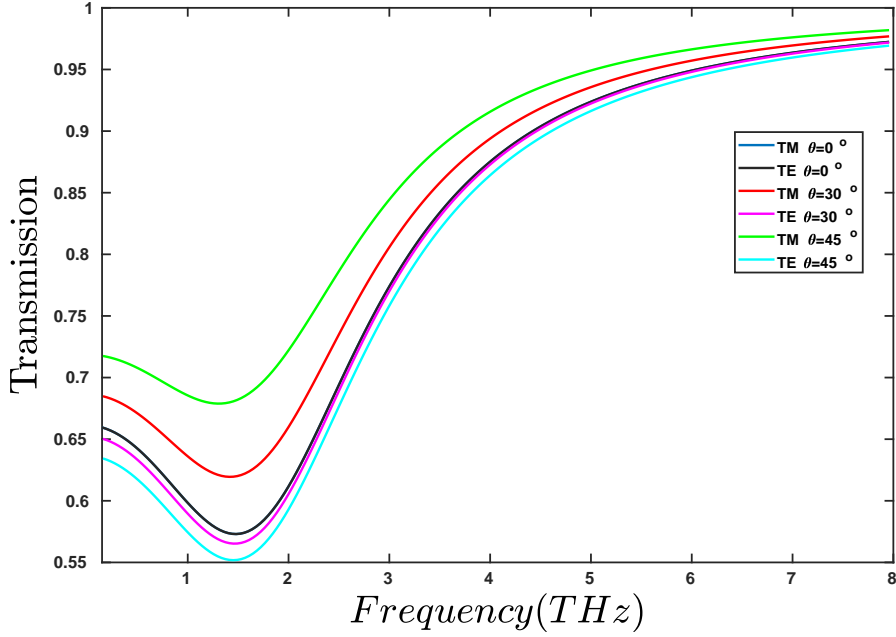


Figure 4.12: Transmission spectra of a monolayer graphene biased with a magnetic field  $B = 2T$  under the TE and TM polarized waves for different incident angles:  $\theta = 0^\circ, 30^\circ$  and  $45^\circ$

### 4.2.3 Surface magnetoplasmons polaritons on magnetically biased graphene sheet (GSMP)

When a magnetic field is applied perpendicular to the graphene sheet, plasmons and cyclotron excitations hybridize giving rise to surface magnetoplasmons polaritons modes (GSMPs) [24, 25]. In this section, we investigate the characteristics of these modes.

#### Graphene Surface magnetoplasmons polaritons Dispersion relation

In order to study the properties of the GSMPs modes, we need to derive their dispersion relation. Let us consider the structure described previously in Figure 4.9 where the GSMP is indicated in red. The reflection matrix  $M_R$  of this structure is introduced above in equation 4.106. The condition of existence of plasmons requires that there are outgoing waves without incoming waves. The modes are then given by the vanishing of the determinant of the inverse of the matrix  $M_R$ , that is:

$$(\gamma_1 + \gamma_2 + k_0 Z_0 \sigma_L) \left[ (\gamma_1 + \gamma_2 + k_0 Z_0 \sigma_L) + (k_1^2 - \gamma_1^2) \left( \frac{1}{\gamma_1} + \frac{1}{\gamma_2} \right) \right] = 2\alpha\beta k_0 Z_0 \sigma_H \left( \frac{1}{\gamma_1} + \frac{1}{\gamma_2} \right) + k_0^2 Z_0^2 \sigma_H^2 \quad (4.116)$$

Now, if we consider the case of electromagnetic modes propagating only along the  $x$  direction, we obtain:

$$(\gamma_1 + \gamma_2 + k_0 Z_0 \sigma_L) \left[ \left( \frac{1}{\gamma_1'} + \frac{1}{\gamma_2'} \right) + \frac{Z_0}{k_0} \sigma_L \right] = Z_0^2 \sigma_H^2 \quad (4.117)$$

This equation provides the dispersion relation of a SPP propagating along a magnetically biased graphene. It should be noted that unlike the GSPs supported by the

graphene sheet in the absence of a magnetic field which are pure TM or TE modes, surface magnetoplasmons polaritons in graphene are hybrid TM-TE modes. These hybrid modes result from the presence of the magnetic field that ensures the coupling between the TM and TE modes.

It should also be noted that in the absence of an external field  $B$ , we find the well-known dispersion relations of the decoupled TE and TM SPPs modes:

$$(\gamma_1 + \gamma_2 + k_0 Z_0 \sigma_L) \left[ \left( \frac{1}{\gamma'_1} + \frac{1}{\gamma'_2} \right) + \frac{Z_0}{k_0} \sigma_L \right] = 0 \quad (4.118)$$

$$\Rightarrow \begin{cases} (\gamma_1 + \gamma_2 + k_0 Z_0 \sigma_L) = 0 & \text{TE-GSP} \\ \left( \frac{1}{\gamma'_1} + \frac{1}{\gamma'_2} \right) + \frac{Z_0}{k_0} \sigma_L = 0 & \text{TM-GSP} \end{cases} \quad (4.119)$$

Figure 4.13 shows the dispersion relation of surface plasmons propagating on graphene

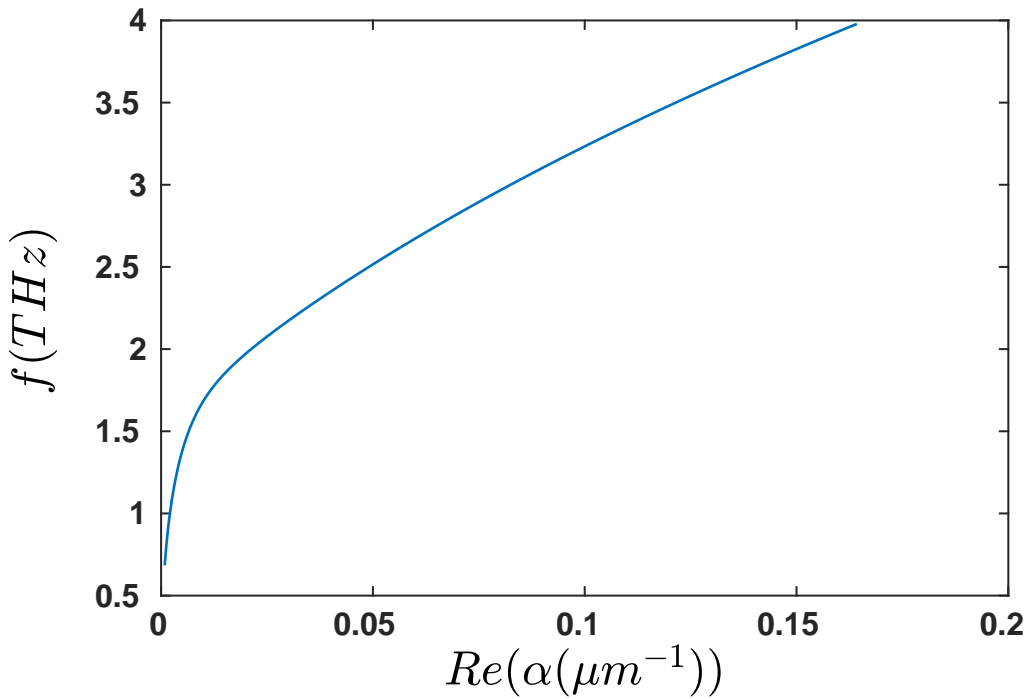


Figure 4.13: Dispersion relation of surface plasmons supported by a graphene sheet in free space in the presence of an external magnetic field  $B = 2T$ . The parameters are taken to be as:  $\mu_c = 0.5\text{eV}$ ,  $\tau =$

sheet surrounded by air when an external magnetic field  $B = 2T$  is applied. The curve is computed from equation 4.117. In order to show the effect of the variation of the magnetic field on the GSMP relation dispersion, we plot in Figure 4.14 the dispersion curve for different magnetic fields. It is shown that Increasing  $B$  pushes the dispersion curve upward. As a results, in addition to the chemical potential of graphene, applying an external magnetic field can be used to tune the surface plasmon polariton on graphene.

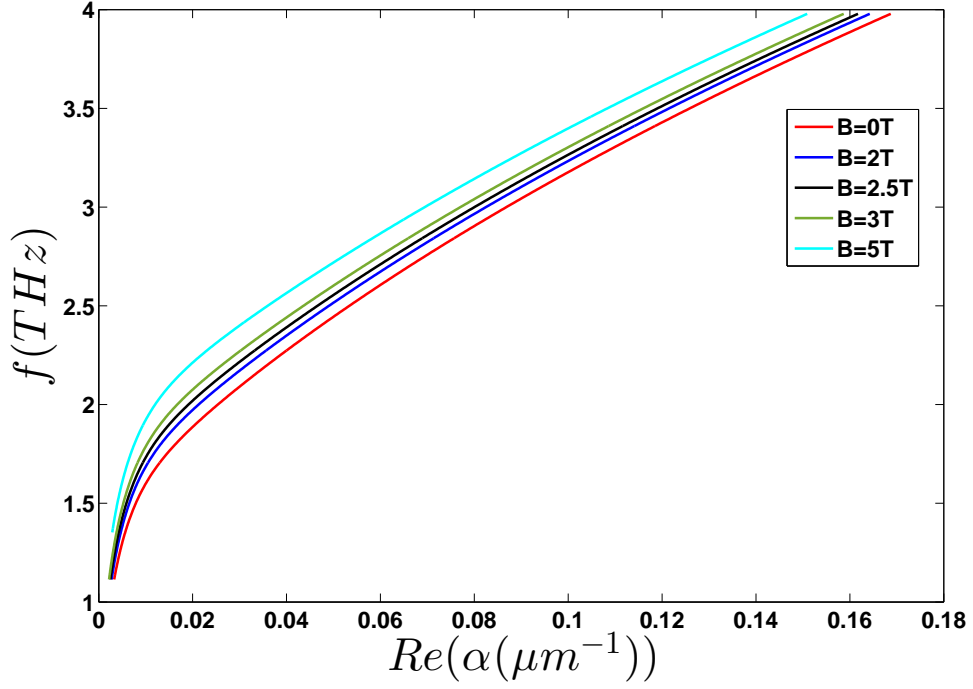


Figure 4.14: Dispersion relation of surface plasmons supported by a graphene sheet in free space for different external magnetic fields  $B = 0, 2, 2.5, 3, 4\text{T}$

#### 4.2.4 Nonreciprocity and gyrotropy of graphene

In this section we will exploit the transmission calculated above to explore the electromagnetic gyrotropic and non reciprocal properties of magnetically biased graphene. In particular, we will show how graphene affects the right-handed circularly polarized (RCP) and left-handed circularly polarized (LCP) and demonstrate that under certain conditions, this magnetic circular dichroism can lead to non reciprocal polarisation rotation phenomenon. Let us consider the structure of figure 4.9 where  $\varepsilon_1 = \varepsilon_2 = \varepsilon$ .

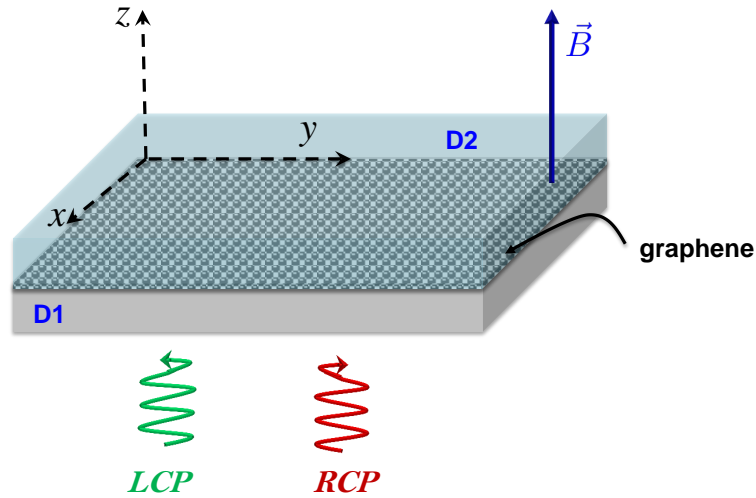


Figure 4.15: Same structure as 4.9 under circularly polarized waves.

Here we are interested to investigate the electromagnetic response of graphene under

normally incident right-handed circularly polarized (RCP) and left-handed circularly polarized (LCP) lights (see Figure 4.15). The electric fields corresponding to the right-handed and left handed circularly polarized incident waves are:

$$\vec{E}_i^\pm = I^\pm(\vec{e}_x \pm i\vec{e}_y) \quad (4.120)$$

where the (+) refers to the right-handed circularly polarized wave and (-) denotes the left handed circularly polarized wave. Substituting (4.120) in (4.114) and 4.115, we can deduce the transmitted waves which are also right-handed and left-handed circularly polarized waves :

$$\vec{E}_t^\pm = \frac{2}{2 + \frac{Z_0}{\sqrt{\epsilon}}\sigma^\pm}(\vec{e}_x + i\vec{e}_y) = t^\pm(\vec{e}_x + i\vec{e}_y) \quad (4.121)$$

where  $t^\pm$  are the transmission amplitudes and can be expressed as  $t^\pm = |t^\pm|e^{i\phi^\pm}$  and  $\sigma^\pm = \sigma_L \pm i\sigma_H$ . It is clearly seen from equation 4.121 that the amplitudes and the phases of  $\vec{E}_t^+$  and  $\vec{E}_t^-$  are not equal. Hence, we can deduce that when passing through a graphene sheet the (RCP) and (LCP) waves are affected differently both in amplitude and phase.

To investigate the gyrotropic properties of graphene, two main parameters will be used: (i) the amplitude ratio  $\frac{t^+}{t^-}$  and (ii) the phase difference  $\Delta_\phi = \phi^+ - \phi^-$ . Figure 4.16 illustrates  $R_a$  and  $\Delta_\phi$  as a function of frequency obtained for different magnetic fields and at fixed  $\mu_c = 0.2\text{eV}$ . One can see that by increasing  $B$ , both the amplitude ratio and the phase difference increase which leads to increase the gyrotropy of graphene. Consequently, applying a higher magnetic field results in larger gyrotropy. We pass

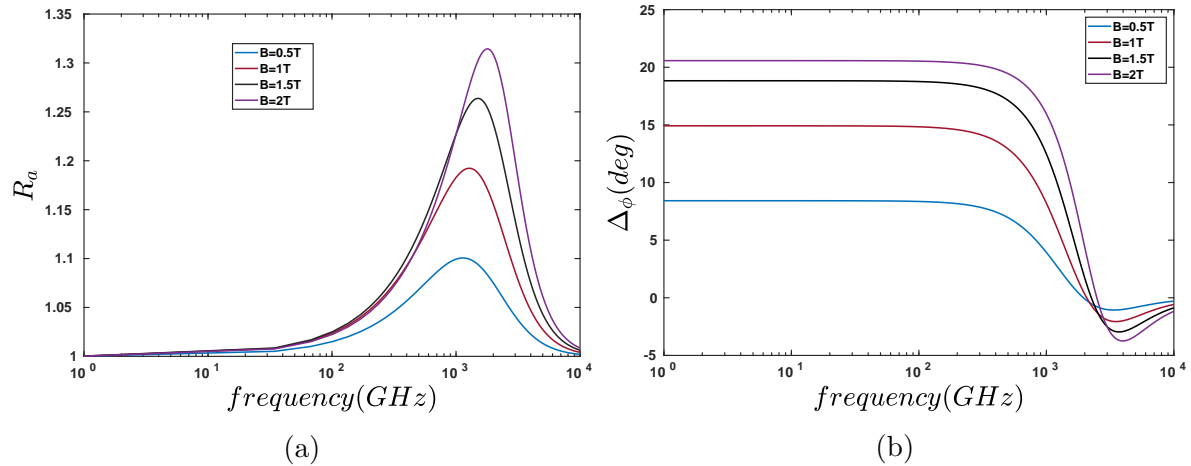


Figure 4.16: (a) Amplitude ratio  $R_a$  and (b)Phase difference  $\Delta_\phi$  between a right-handed and a left handed polarized wave transmitted through a free standing graphene sheet calculated for different external magnetic fields:  $B = 0.5, 1, 1.5, 2\text{T}$ . The graphene parameters are:  $T = 300\text{K}, \mu_c = 0.2\text{eV}, \tau = 0.1\text{ps}$

now to test the effect of the chemical potential on the gyrotropic characteristics of graphene. We set the magnetic field value to 1T and we plot in Figure 4.17 the amplitude ratio  $R_a$  and the phase difference  $\Delta_\phi$  as a function of frequency for different chemical potentials. It is clearly shown that as  $\mu_c$  increases,  $R_a$  and  $\Delta_\phi$  increase. This indicates that increasing  $\mu_c$  leads to increase gyrotropy in graphene. As a result, in

addition to the magnetic field the gyrotropy in graphene can be controlled and tuned by varying the chemical potential of graphene which presents an advantage for graphene over other gyrotropic materials.

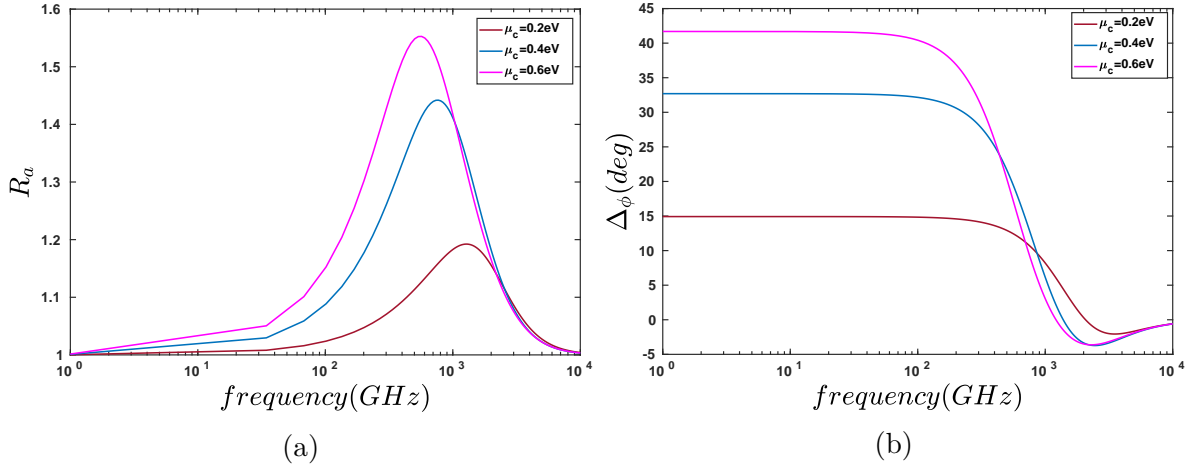


Figure 4.17: (a) Amplitude ratio  $R_a$  and (b) Phase difference  $\Delta_\phi$  between a right-handed and a left handed polarized wave transmitted through a free standing graphene sheet calculated for chemical potentials:  $\mu_c = 0.2, 0.4, 0.6\text{eV}$  and for  $B = 1\text{T}$ . The Other parameters are the same as Figure 4.16

From 4.16, we can also see that for all frequencies below to the cyclotron frequency  $\omega_c/2\pi$ ,  $R_a = 1$ ,  $\Delta_\phi > 0$ . In this range of frequencies and under these conditions for  $R_a$  and  $\Delta_\phi$  the polarization direction of a linearly polarized wave can be rotated by an angle when it transverses a graphene sheet. As mentioned above on previous sections, this phenomenon, known as Faraday rotation and the angle is called Faraday rotation angle (see Figure 4.18).

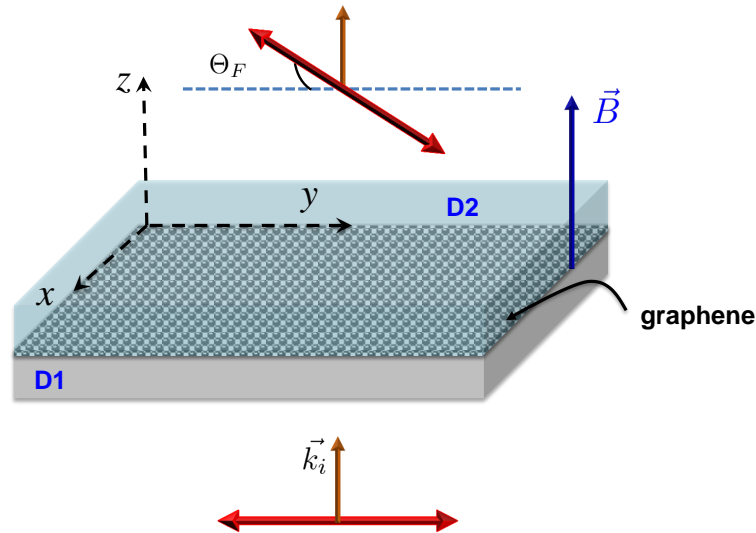


Figure 4.18: Schematic of the Faraday effect in graphene.

Let us consider a linearly  $x$ -polarized incident wave that can be written as a superposition of a right handed wave and left handed wave with the same amplitude:

$$\vec{E}_i = I((\vec{e}_x + i\vec{e}_y) + (\vec{e}_x - i\vec{e}_y)) = 2I\vec{e}_x \quad (4.122)$$

The transmitted wave is given by:

$$\vec{E}_t \propto e^{i\Delta_\phi}(\vec{e}_x + i\vec{e}_y) + (\vec{e}_x - i\vec{e}_y) = 2e^{i\Delta_\phi/2}(\cos(\Delta_\phi/2)\vec{e}_x - \sin(\Delta_\phi/2)\vec{e}_y) \quad (4.123)$$

From equations (4.123) and (4.121), we find the Faraday angle rotation as:

$$\Theta_F = \frac{1}{2}(\phi^+ - \phi^-) = -\arctan\left(\frac{Z_0\sigma_H}{2 + Z_0\sigma_L}\right) \quad (4.124)$$

As a consequence, the polarisation of the transmitted wave is rotated by an angle  $\Theta_F = \Delta_\phi/2$  in the clockwise sense with respect to the  $z$  axis. Figure 4.19 shows the Faraday angle rotation versus frequency for different magnetic fields and different potential chemicals. It is seen that  $\Theta_F$  increases when both  $B$  and  $\mu_c$  increase. It is worth noting that gyrotropy in graphene is observed in a very broadband frequency range ( $f < \omega_c/2\pi$ ) where the phase difference and then the Faraday angle rotation is almost a constant up to  $f = 200\text{GHz}$ . For  $f > 200\text{GHz}$ ,  $R_a$  increases and  $\Delta_\phi$  decreases which implies that the transmitted wave becomes elliptically polarized. Furthermore, the cyclotron frequency depends on both  $\mu_c$  and  $B$ . This allows to tune and control the working frequency of gyrotropy in graphene by varying the chemical potential and/or changing the magnetic field.

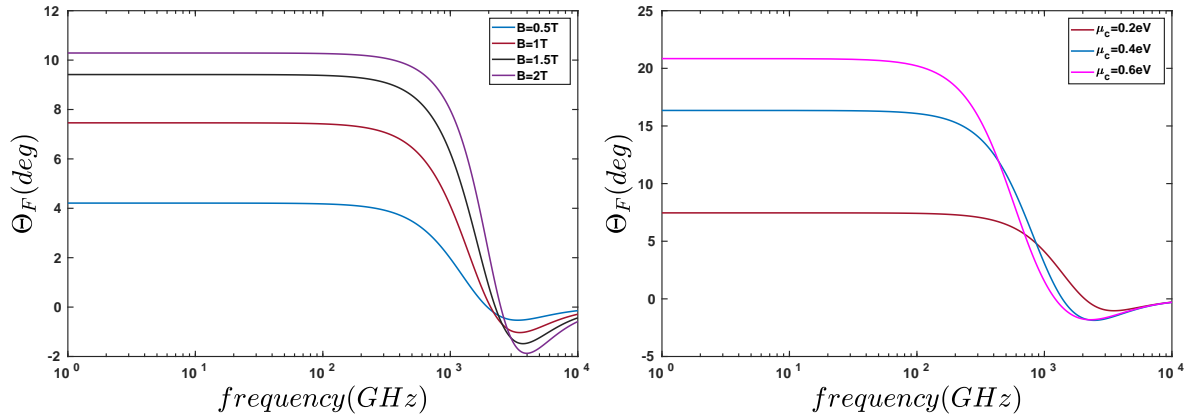


Figure 4.19: Faraday rotation angle (in degrees) for a light passes through a graphene sheet calculated (a) for different external magnetic fields:  $B = 0.5, 1, 1.5, 2\text{T}$  (b) for different chemical potentials:  $\mu_c = 0.2, 0.4, 0.6\text{eV}$

An additional important property of graphene is that this rotation of polarization is *nonreciprocal*. To prove this statement, we consider a plane wave impinges normally on graphene from medium 2 to medium 1 as depicted in figure 4.20. In this case the transmission can be deduced from the case of figure 4.9 by inverting the  $z$  axis. After some straightforward calculations, we find that  $M_{T12} = M_{T21}$ . This means that in the case of normal incidence the wave polarisation always rotates by an angle  $\Theta_F$  in the same direction (the clockwise sense) with respect to the  $z$  direction. So, if we assume that a transverse plane wave is impinging normally on graphene from medium 1 toward medium 2, after passing through the graphene sheet, the wave polarisation is rotated by angle  $\Theta_F$  in the clockwise sense with respect to the  $z$  direction. Now if we reverse the propagation direction (backward direction (from medium 2 to medium 1)), the polarisation is further rotated by an angle  $\Theta_F$  in the clockwise sense with respect to the  $z$  direction. Hence, the polarisation of a wave transmitted through graphene from medium 1 to medium 2 and then retransmitted from medium 2 to medium 1

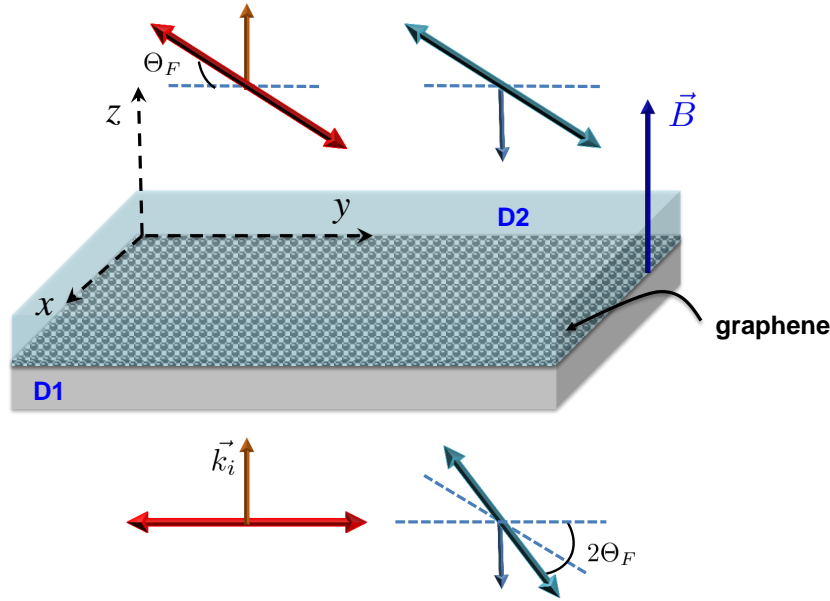


Figure 4.20: Non reciprocity in graphene: A transverse plane wave impinges normally on graphene from medium 1 toward medium 2 and transmitted back to medium 1

undergoes a total rotation of  $2\Theta_F$ . The nonreciprocal properties of graphene can be explored to develop and design novel non reciprocal ultrathin nanodevices operating at the microwave and terahertz frequency ranges such as optical isolators, which are of crucial importance in optical systems, Faraday rotators and circulators.

### 4.3 Conclusions

For a good understanding of this part of the thesis, we have chosen to start with this first chapter that summarizes the theory used in the following chapters. In the first part of this chapter, we have presented the notions of reciprocity and non reciprocity in general. This was followed by description of the non reciprocity caused by a static magnetic field. In particular, we have explained the optical hall effect which is responsible of the occurrence of an anisotropy in a material subjected to a magnetic field. We have given afterwards a detailed analysis of wave propagation and dispersion characteristics in gyrotropic media. Magneto-optical effects such as Faraday and Kerr effects were described subsequently. The second part of this chapter was dedicated to investigate magnetostatic biased graphene layer properties .



# Bibliography

- [1] L. Deák and T. Fülöp. Reciprocity in quantum, electromagnetic and other wave scattering. *Annals of Physics*, 327(4):1050 – 1077, 2012. [101](#)
- [2] George Gabriel Stokes. *On Attractions, and on Clairaut's Theorem*, volume 2 of *Cambridge Library Collection - Mathematics*, page 104–130. Cambridge University Press, 2009. [101](#)
- [3] H.Helmholtz. *Handbuch der physiologischen optik*. Impr.Bachelier, 1856. [101](#)
- [4] H.Lorentz. On the radiation of heat in a system of bodies having a uniform temperature. *Koninklijke Nederlandse Akademie van Wetenschappen Proceeding Series B physical Sciences*. [101](#)
- [5] V. S. Asadchy, M. S. Mirmoosa, A. Díaz-Rubio, S. Fan, and S. A. Tretyakov. Tutorial on electromagnetic nonreciprocity and its origins. *Proceedings of the IEEE*, pages 1–44, 2020. [103](#), [104](#)
- [6] Mathias Schubert, Tino Hofmann, and Craig M. Herzinger. Generalized far-infrared magneto-optic ellipsometry for semiconductor layer structures: determination of free-carrier effective-mass, mobility, and concentration parameters in n-type gaas. *J. Opt. Soc. Am. A*, 20(2):347–356, Feb 2003. [105](#)
- [7] Mathias Schubert, Philipp Kühne, Vanya Darakchieva, and Tino Hofmann. Optical hall effect—model description: tutorial. *J. Opt. Soc. Am. A*, 33(8):1553–1568, Aug 2016. [105](#)
- [8] E. H. Hall. On a new action of the magnet on electric currents. *American Journal of Mathematics*, 2(3):287–292, 1879. [105](#)
- [9] Michael Faraday. I. experimental researches in electricity.&#x2014;nineteenth series. *Philosophical Transactions of the Royal Society of London*, 136:1–20, 1846. [112](#)
- [10] John Kerr LL.D. Xliii. on rotation of the plane of polarization by reflection from the pole of a magnet. *The London, Edinburgh, and Dublin Philosophical Magazine and Journal of Science*, 3(19):321–343, 1877. [112](#)
- [11] Aires Ferreira, J. Viana-Gomes, Yu. V. Bludov, V. Pereira, N. M. R. Peres, and A. H. Castro Neto. Faraday effect in graphene enclosed in an optical cavity and the equation of motion method for the study of magneto-optical transport in solids. *Phys. Rev. B*, 84:235410, Dec 2011. [22](#), [24](#), [115](#)

- 
- [12] J. W. McClure. Diamagnetism of graphite. *Phys. Rev.*, 104:666–671, Nov 1956. [115](#)
- [13] L. D. Landau and E. M. Lifshitz. Quantum mechanics (non-relativistic theory). *Translated from the Russian*. [115](#)
- [14] S. V. Morozov D. Jiang M. I. Katsnelson I. V. Grigorieva S. V. Dubonos K. S. Novoselov, A. K. Geim and A. A. Firsov. Two-dimensional gas of massless dirac fermions in graphene. *Nature*. [115](#)
- [15] Stormer HL Kim P Zhang Y, Tan YW. Experimental observation of the quantum hall effect and berry’s phase in graphene. *Nature*. [115](#)
- [16] Johannes Jobst, Daniel Waldmann, Florian Speck, Roland Hirner, Duncan K. Maude, Thomas Seyller, and Heiko B. Weber. Quantum oscillations and quantum hall effect in epitaxial graphene. *Phys. Rev. B*, 81:195434, May 2010. [115](#)
- [17] Xiaosong Wu, Yike Hu, Ming Ruan, Nerasoa K Madiomanana, John Hankinson, Mike Sprinkle, Claire Berger, and Walt A. de Heer. Half integer quantum hall effect in high mobility single layer epitaxial graphene. *Applied Physics Letters*, 95(22):223108, 2009. [115](#)
- [18] A. M. Witowski, M. Orlita, R. Stępniewski, A. Wyszomolek, J. M. Baranowski, W. Strupiński, C. Faugeras, G. Martinez, and M. Potemski. Quasiclassical cyclotron resonance of dirac fermions in highly doped graphene. *Phys. Rev. B*, 82:165305, Oct 2010. [117](#), [133](#)
- [19] R. S. Deacon, K.-C. Chuang, R. J. Nicholas, K. S. Novoselov, and A. K. Geim. Cyclotron resonance study of the electron and hole velocity in graphene monolayers. *Phys. Rev. B*, 76:081406, Aug 2007. [117](#)
- [20] E. A. Henriksen, P. Cadden-Zimansky, Z. Jiang, Z. Q. Li, L.-C. Tung, M. E. Schwartz, M. Takita, Y.-J. Wang, P. Kim, and H. L. Stormer. Interaction-induced shift of the cyclotron resonance of graphene using infrared spectroscopy. *Phys. Rev. Lett.*, 104:067404, Feb 2010. [117](#)
- [21] Z. Jiang, E. A. Henriksen, L. C. Tung, Y.-J. Wang, M. E. Schwartz, M. Y. Han, P. Kim, and H. L. Stormer. Infrared spectroscopy of landau levels of graphene. *Phys. Rev. Lett.*, 98:197403, May 2007. [117](#)
- [22] M. L. Sadowski, G. Martinez, M. Potemski, C. Berger, and W. A. de Heer. Landau level spectroscopy of ultrathin graphite layers. *Phys. Rev. Lett.*, 97:266405, Dec 2006. [117](#)
- [23] Y. Ma, L. Shi, J. Wang, J. Li, Y. Liu, and Y. Ran. An analytical method to investigate propagation properties of magnetostatic biased graphene layers. *IEEE Access*, 8:107177–107184, 2020. [121](#)
- [24] Yu. A. Bychkov and G. Martinez. Magnetoplasmon excitations in graphene for filling factors  $\nu \leq 6$ . *Phys. Rev. B*, 77:125417, Mar 2008. [123](#)
- [25] Oleg L. Berman, Godfrey Gumbs, and Yurii E. Lozovik. Magnetoplasmons in layered graphene structures. *Phys. Rev. B*, 78:085401, Aug 2008. [123](#)

# Propagation properties of a magnetically biased array of graphene ribbons

*Following ancient customs and traditions does not mean that the dead are alive, but that the living are dead.*

Ibn Khaldun

## Contents

<b>5.1</b>	<b>Semi-analytical model for the analysis of a magnetically Biased subwavelength graphene-strip-grating . . . . .</b>	<b>134</b>
5.1.1	Physical system . . . . .	134
5.1.2	Theoretical Method . . . . .	135
5.1.3	Numerical Results and discussion . . . . .	140
<b>5.2</b>	<b>Conclusion . . . . .</b>	<b>145</b>

In chapter 1, we have shown that the conductivity of graphene and therefore its electromagnetic and plasmonic properties can be dynamically tuned by changing its chemical potential via electrostatic bias or chemical doping. We have also seen in chapter 4 that a magnetic bias can be applied to control the conductivity of graphene. In fact, when a perpendicular magnetic field is turned on, graphene becomes gyrotropic and exhibits non reciprocal properties [1]. This leads to many magneto-optical (MO) phenomena such as the half-integer quantum Hall effect[2], Giant Faraday rotation [3] and Kerr effects[4]. Furthermore, in the presence of the static magnetic field, plasmons and cyclotron excitations hybridize which leads to the appearance of graphene surface magnetoplasmons (GSMPs). One of the great advantages of graphene over others conventional plasmonic materials, is the high sensibility of magnetoplasmons to the application of an external magnetic field stemming from the comparable cyclotron frequency and plasmon frequency [5]. An additional advantage is that the cyclotron mass of the charge carriers is small and can be tuned by doping. Moreover while cryogenic temperatures are required to observe magneto-optical effect in 2DEGs, in graphene, they already arise at room temperature. All This makes graphene the most promising candidate for use in tunable plasmonic nonreciprocal devices in the microwave and terahertz frequencies such as optical isolation[6] and absorbers[7].

Recently, graphene surface magneto-plasmons have been widely studied in several theoretical and experimental studies under various forms and configurations including extended layers of graphene [8], nanoribbons [9, 10] and antidots[11]. It is shown that the excitation of GSMPs enhance significantly the MO effects of graphene structures and strong magnetoplasmonics resonances have been observed in a patterned array of graphene antidots. As a result, it is a great interest to analytically and numerically investigate the optical properties of patterned anisotropic graphene under magnetic bias. Among these structures, periodic magnetically biased graphene ribbons array has attracted a great deal of research interest and becomes one of the most studied graphene based structures.

Several and various numerical methods have been employed for modelling this structure such that the Fourier Modal Method [10], the finite difference time-domain method [12] and discontinuous Galerkin time domain (DGTD) [13]. However, it is shown that due to the ultrathin nature of graphene, these numerical methods suffer from slow convergence rate and require too much computational effort. In addition to these numerical methods, an analytical method has been proposed in [14] to study the electromagnetic behavior of strongly anisotropic metasurfaces implemented by a subwavelength array of graphene strips. It is based on the effective medium approach (EMA) which was applied to the conductivity tensor of graphene by the help of electrostatic approach. Nevertheless, this method provide an accurate results only for structures at the extreme subwavelength regime (with infinitesimally small periodicity). More recently, an analytical method has been performed in [15] to analyse magnetically-biased array of graphene ribbons by solving the integral equations governing the induced surface current on the graphene ribbons. The major drawback of this method is that it does not take into account the interaction between neighboring ribbons which make it less accurate when one is dealing with strip gratings with small gaps.

To the best of our knowledge, there is no analytical or semi analytical method has been presented to predict the electromagnetic response of a one dimensional graphene strip grating in the presence of an external magnetic field when the graphene is modeled as a bulk material using an effective medium approach. Accordingly, in the present work, we provide a simple and fast semi analytical model for investigation of the propagation properties of a 1D magnetically biased graphene-strip-grating. It is based on an effective medium approach and a cumulative phase technique. In our Model, graphene is regarded as extremely thin anisotropic layer with a finite thickness and unlike the approach proposed in [14] the effective medium approach will be applied to its permittivity tensor. Note that the present approach has two main advantages over the above reported methods: (i) although this method is developed to deal with the general case of a 1D magnetically biased graphene-strip-grating, it still valid even for a non magnetized structure where the magnetic bias is absent. (ii) this method can efficiently and accurately treat subwavelength graphene strip gratings with small gaps as well as large gaps. The chapter is organized as follows: In section 5.1.1, we introduce the physical system. The proposed semi analytical method will be explained and described in detail in the next section. Finally, some numerical results are given and discussed in the last section to illustrate the effectiveness of this approach. The accuracy of the proposed model will be validated by comparing it in the one hand with The PMM method and on the other hand with the effective medium approach proposed in [14].

## 5.1 Semi-analytical model for the analysis of a magnetically Biased subwavelength graphene-strip grating

### 5.1.1 Physical system

The structure under study is depicted in figure 5.1. It consists of a periodic 1D graphene ribbon array (along the  $x$  direction with width  $a$  and period  $d = a + s$ ) biased with magnetostatic field. The graphene ribbons array is suspended in free space and is placed on the  $xy$  plane. A plane wave is normally incident on the structure from the upper medium ( $z > 0$ ). Here we consider the Faraday geometry where the external static magnetic field  $B$  is applied perpendicular to the array along the propagation direction ( $z$  direction). As mentioned in the previous chapter, under the influence of a magnetostatic bias, graphene will exhibit an induced anisotropy and thus its surface magneto-optical conductivity will be described by an asymmetric tensor as: (see section 1.1.3 of chapter 1).

$$\sigma = \begin{pmatrix} \sigma_{xx} & \sigma_{xy} \\ \sigma_{yx} & \sigma_{yy} \end{pmatrix} = \begin{pmatrix} \sigma_L & \sigma_H \\ -\sigma_H & \sigma_L \end{pmatrix} \quad (5.1)$$

For highly doped graphene i.e  $\mu_c \gg \hbar\omega$  and  $\mu_c \gg k_B T$ , the conductivity of graphene

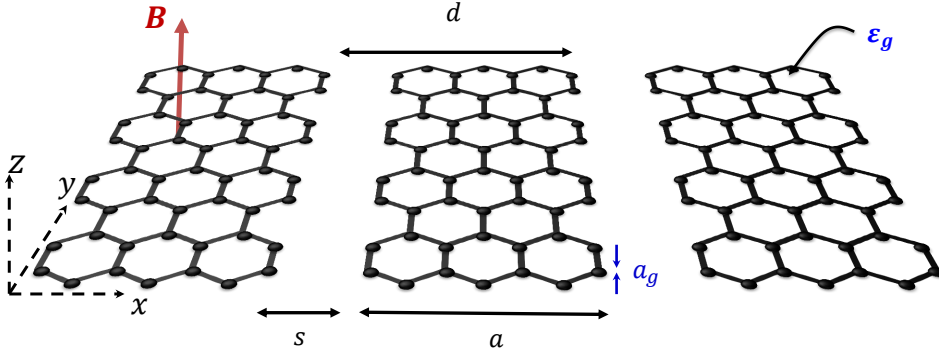


Figure 5.1: Sketch of the studied structure: a magnetically-biased subwavelength graphene strip grating with width  $a$  and period  $d = a + s$ . The grating is surrounded by air and the magnetic field is applied perpendicularly to the structure along the  $z$  direction ( $\vec{B} = B\vec{e}_z$ ).

is dominated by the intraband contribution and thus the general quantum mechanical conductivity reduces to the semiclassical Drude model form previously given in section 1.1.3 as:

$$\sigma_L = \frac{e^2 \tau \mu_c}{\hbar^2 \pi} \frac{1 - i\omega\tau}{(1 - i\omega\tau)^2 + (\tau\omega_c)^2} \quad (5.2)$$

$$\sigma_H = -\frac{e^2 \tau \mu_c}{\hbar^2 \pi} \frac{\tau\omega_c}{(1 - i\omega\tau)^2 + (\tau\omega_c)^2} \quad (5.3)$$

In our calculations, we model the graphene as an extremely thin anisotropic layer with a finite thickness  $a_g = 0.34$  nm and an effective dielectric permittivity tensor  $\varepsilon_g$  given by:

$$\varepsilon_g = \begin{pmatrix} \varepsilon_{xx} & \varepsilon_{xy} & 0 \\ -\varepsilon_{xy} & \varepsilon_{xx} & 0 \\ 0 & 0 & \varepsilon_{zz} \end{pmatrix} \quad (5.4)$$

Where  $\varepsilon_{xx} = 1 + i \frac{\sigma_L}{\omega \varepsilon_0 a_g}$ ,  $\varepsilon_{xy} = i \frac{\sigma_H}{\omega \varepsilon_0 a_g}$  and  $\varepsilon_{zz} = 1$ . Note that, the whole structure is invariant in the  $y$  direction and throughout this chapter, we assume a time harmonic dependence of the form  $e^{-i\omega t}$ . Having introduced the studied structure, we are now ready to explain and describe our approach

### 5.1.2 Theoretical Method

The First step to model the electromagnetic response of the studied structure and to understand its physical properties is to apply the effective medium approach which is an intuitive and effective technique allowing to obtain in a simple manner the macroscopic averaged response of an array of subwavelength resonators [16, 17, 18]. Since, the period  $d$  of the graphene-strip grating is small compared to the wavelength of the incident wave ( $d \ll \lambda$ ), it can be approximated by a homogeneous anisotropic effective layer with equivalent effective permittivity tensor  $\tilde{\varepsilon}$ . We seek in the following to calculate the components of the effective permittivity tensor  $\tilde{\varepsilon}$ . For this purpose, let us start by giving the constitutive relations that relate the displacement to the electric field components:

$$D^i(x) = \sum_j \varepsilon_{ij}(x) E_j(x) \quad \{i, j\} \in \{x, y\} \quad (5.5)$$

According to these relations, we can rewrite  $D^y$  and  $E_x$  with respect to  $D^x$  and  $E_y$  as:

$$\begin{bmatrix} E_x \\ D^y \end{bmatrix} = \begin{bmatrix} 1 & -\varepsilon_{xy} \\ \varepsilon_{xx} & \varepsilon_{xx} \varepsilon_{xy} \\ \varepsilon_{yx} & \varepsilon_{yy} - \varepsilon_{yx} \varepsilon_{xy} \\ \varepsilon_{xx} & \varepsilon_{xx} \end{bmatrix} \begin{bmatrix} D^x \\ E_y \end{bmatrix} \quad (5.6)$$

Averaging all quantities involving local fields and densities over the period  $d$ , and assuming that, electromagnetic fields and densities are continuous at any coordinate curve  $x = \text{constant}$ , we obtain:

$$\begin{bmatrix} \langle E_x \rangle \\ \langle D^y \rangle \end{bmatrix} = \begin{bmatrix} \langle \frac{1}{\varepsilon_{xx}} \rangle & -\langle \frac{\varepsilon_{xy}}{\varepsilon_{xx}} \rangle \\ \langle \frac{\varepsilon_{yx}}{\varepsilon_{xx}} \rangle & \langle \varepsilon_{yy} \rangle - \langle \frac{\varepsilon_{yx} \varepsilon_{xy}}{\varepsilon_{xx}} \rangle \end{bmatrix} \begin{bmatrix} \langle D^x \rangle \\ \langle E_y \rangle \end{bmatrix} \quad (5.7)$$

Treating the grating as effective medium require that these macroscopic fields satisfy the above constitutive relationships given by equation 5.5, such that:

$$\langle D^i \rangle = \sum_j \tilde{\varepsilon}_{ij} \langle E_j \rangle, \{i, j\} \in \{x, y\} \quad (5.8)$$

By comparing with equation 5.8, we can deduce the effective medium permittivity tensor components as:

$$\tilde{\varepsilon}_{xx} = \langle 1/\varepsilon_{xx} \rangle^{-1} \quad (5.9)$$

$$\tilde{\varepsilon}_{xy} = \langle 1/\varepsilon_{xx} \rangle^{-1} \langle \varepsilon_{xy}/\varepsilon_{xx} \rangle \quad (5.10)$$

$$\tilde{\varepsilon}_{yx} = \langle 1/\varepsilon_{xx} \rangle^{-1} \langle \varepsilon_{yx}/\varepsilon_{xx} \rangle \quad (5.11)$$

$$\tilde{\varepsilon}_{yy} = \langle \varepsilon_{yy} \rangle + \langle \tilde{\varepsilon}_{xy} \rangle \langle \varepsilon_{yx}/\varepsilon_{xx} \rangle - \langle \varepsilon_{yx} \varepsilon_{xy}/\varepsilon_{xx} \rangle \quad (5.12)$$

At this stage, it is important to emphasize that, close to a single strip, the wave see the latter as surrounded on both sides by an effective medium. Thus, the structure can be regarded as a strip grating inlayed into an effective medium. For that reason and in

order to take into account the resonance phenomena occurring in the grating, the departure periodic structure will be modeled by a subwavelength periodic graphene strip grating with the same dimensions but instead of vacuum the gaps between neighboring strips will be filled by the effective medium (see Fig 5.2). Let us now take a look at the different modes living in the new approximate structure. From Figure 5.2, one can distinguish two kinds of modes: the first is the most slowly decaying evanescent mode of the sub-wavelength periodic structure given by the couple  $(\tilde{\alpha}, \tilde{\gamma})$  and the second one correspond to the surface magnetoplasmons polaritons of graphene (GSMP) guided by the graphene strip  $(\alpha, \gamma)$ .

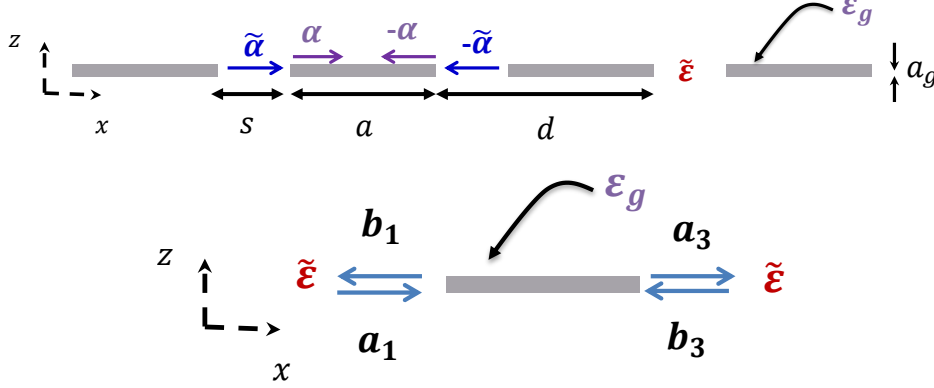


Figure 5.2: Schematic illustration of The mode coupling Model: (a) Coupling between the effective mode living in the gap and the GSMPs propagating on the graphene strip. (b) the Scattering matrix for one period.

The challenge now is to successfully introduce the coupling or the interaction between these modes. One powerful and insightful way to accomplish this is to adopt an analysis based on a scattering parameters of a two-port network. In the proposed analysis, we will use the scattering matrix formalism to describe the optical characteristics of the structure (see references [19, 20] for further details). The total scattering matrix associated to one period can be written as:

$$\begin{pmatrix} S_{11} & S_{12} \\ S_{21} & S_{22} \end{pmatrix} \begin{pmatrix} a_1 \\ b_3 \end{pmatrix} \begin{pmatrix} b_1 \\ a_3 \end{pmatrix} \quad (5.13)$$

Where:

$$S_{11} = S_{22} = r_1 \frac{1 - \phi^2}{1 - r_1^2 \phi^2}, S_{12} = S_{21} = \frac{t_1 t_2 \phi}{1 - r_1^2 \phi^2} \quad (5.14)$$

with

$$r_1 = \frac{1 - \nu_{eff}}{1 + \nu_{eff}}, t_1 = \frac{2}{1 + \nu_{eff}}, t_2 = \frac{2\nu_{eff}}{1 + \nu_{eff}}. \quad (5.15)$$

$$\nu_{eff} = \frac{\alpha \tilde{\epsilon}}{\epsilon \tilde{\alpha}} \quad (5.16)$$

As mentioned above, the  $\tilde{\alpha}$  denotes the in-plane effective index of the most slowly decaying evanescent mode of the sub-wavelength periodic structure and it can be approximated by:

$$\tilde{\alpha} \simeq \sqrt{\tilde{\epsilon}} \quad (5.17)$$

In the case of a periodic subwavelength strip grating with a small gap size ( $s \ll d$ ), we have  $\tilde{\epsilon} = \tilde{\epsilon}_{xx} \gg \epsilon_s$  this yields:

$$\tilde{\epsilon} = \tilde{\epsilon}_{xx} = \left\langle \frac{1}{\epsilon_{xx}} \right\rangle \simeq \frac{d}{s} \epsilon_s \quad (5.18)$$

Thus, in this particular case the effective index  $\nu_{eff}$  can be straightforwardly given by:

$$\nu_{eff} \simeq \frac{\alpha_\rho}{\epsilon} \sqrt{\tilde{\epsilon}} = \frac{\alpha_\rho}{\epsilon} \sqrt{\frac{d}{s} \epsilon_s} \quad (5.19)$$

In the proposed model, we assume that the phase  $\phi$  appearing in equation 5.14 can be given as the sum of two contributions:

$$\phi = e^{-ik_0 \alpha a} e^{i\theta_c(s/a)} = \phi_1 \phi_c \quad (5.20)$$

The first term  $\phi_1$  handles the propagation along the  $a$  – *width* graphene strip. While the second term  $\phi_c$  is related to the contribution of the periodicity of the strips array. In this term  $\theta_c$  is a corrective phase required to take into account the phase delay. To get an idea about the behavior of the phase of the electric field in the considered structure, we plot in Figure 5.3 its spatial distribution calculated at the resonance wavelength. One can clearly see that the phase of the electric field reveals a slot jump probably due to the interface metal/dielectric (graphene/dielectric) which confirm our initial assumption. Note that, unlike the phase  $\phi_1$ , the phase delay  $\theta_c$  cannot be provided

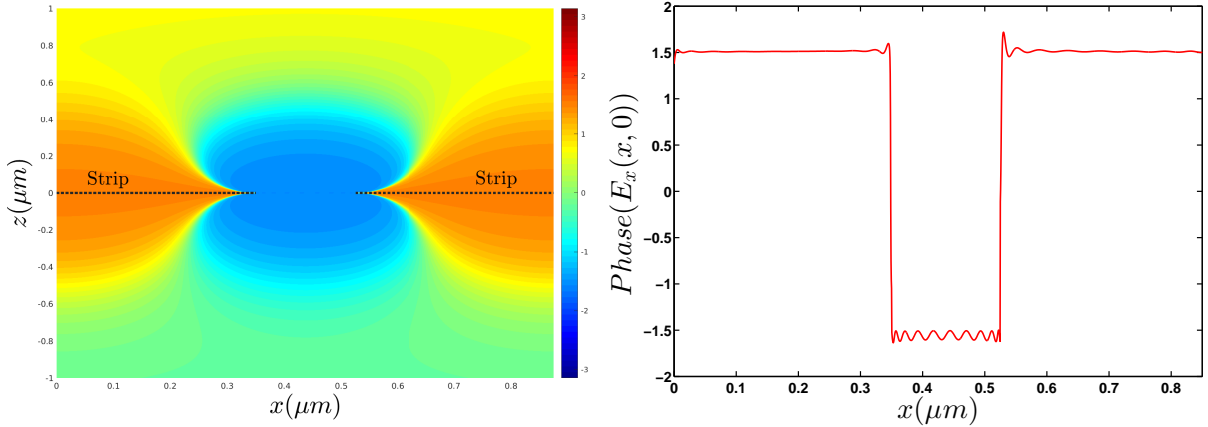


Figure 5.3: Spatial Distribution of the phase of the electric field calculated at the first resonance frequency. (a) Map of the phase of the  $x$  component of the electric field (b) Electric field phase  $E_x(x, 0)$  at the surface of the strip grating. The parameters are assumed:  $a = 0.7\mu\text{m}$ ,  $s = a/4$ ,  $\mu_c = 0.3eV$ ,  $\tau = 0.3ps$  and  $B = 1T$

analytically. However it may be estimated thanks to a rigorous simulation. In this context, several numerical simulations showed that this phase depends only on the geometric parameters, through the ratio  $a/s$ . For example, for  $s/a = 1/4$ , it is found that  $\theta_c(s/a) = \pi/2$  whatever the value of  $a$  and the magnitude of  $B$ . In the following, we search to provide a robust estimation of this phase using a cumulative technique. For this end, we suggest that  $\theta_c$  can be approximated by the following model

$$\theta_c(\zeta) = \begin{cases} \theta_c^{(1)}(\zeta) = \sum_{n=0}^{n=5} a_n^{(1)} \zeta^{1/n} & \text{if } \zeta \leq 0.5 \\ \theta_c^{(2)} = \sum_{n=0}^{n=6} a_n^{(2)} \zeta^{1/n} & \text{if } \zeta > 0.5 \end{cases} \quad (5.21)$$

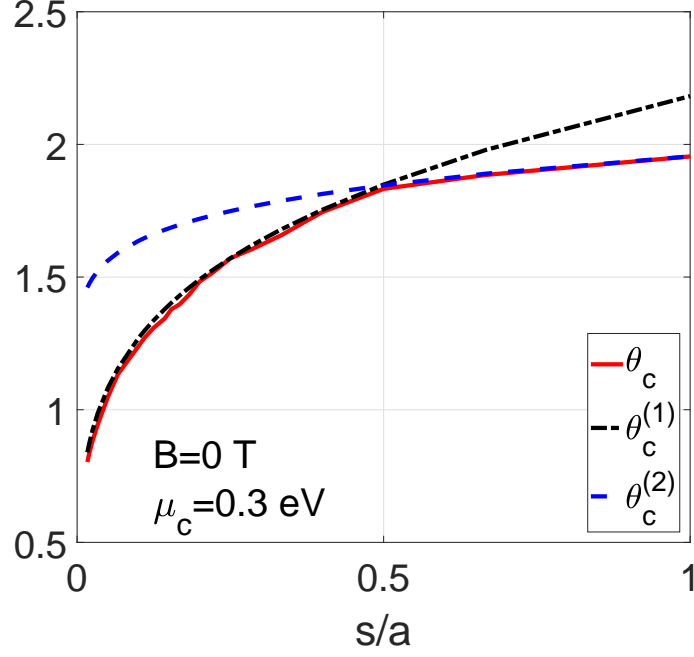


Figure 5.4: Comparison between the numerical results of the phase  $\theta_c$  (red line) and the results computed using the approximate model given by (5.21) and (5.22) (black dot line for  $\theta_c^{(1)}$  and blue dashed line for  $\theta_c^{(2)}$ ). The parameters are:  $\lambda = 30.35\mu m$ ,  $a = 0.735\mu m$ ,  $B = 0T$ ,  $\mu_c = 0.3eV$

where  $\zeta = s/a$ . Then, The coefficients of the above series are obtained numerically as:

$$\theta_c(\zeta) = \begin{cases} \theta_c^{(1)}(\zeta) = \zeta^{1/5} + 1.05\zeta^{1/4} + 0.2\zeta^{1/3} - 0.1\zeta^{1/2} + 0.05\zeta - 0.018 & \text{if } \zeta \leq 0.5 \\ \theta_c^{(2)}(\zeta) = \zeta^{1/6} + 0.955 & \text{if } \zeta > 0.5 \end{cases} \quad (5.22)$$

To show the reliability and the efficiency of the proposed approximate model, we plot in Figure 5.4 the behaviour of  $\theta_c$  as a function of the ratio  $s/a$  for the following numerical parameters:  $\lambda = 30.35\mu m$ ,  $a = 0.735\mu m$ ,  $B = 0T$ ,  $\mu_c = 0.3eV$ . The numerical results are compared to those computed by the approximate model. The red solid line shows the results obtained numerically and the results obtained using the approximate model are depicted by the blue dashed and the black dot lines. One can see that the blue line that corresponds to  $\theta_c^{(1)}$  fits perfectly the red line for  $(s/a) \geq 0.5$ . While the black one corresponding to  $\theta_c^{(2)}$  matches with the latter for  $(s/a) > 0.5$ . Hence, we conclude that in this case, the behavior of the phase delay  $\theta_c$  can be efficiently predicted by the above proposed approximate model. Note that, although we have presented here only the case of the structure without magnetic bias, the model has been also verified for  $B \neq 0$  and it is found that it remains valid and efficient for all values of  $B$  less than  $7T$ .

After having defined all the parameters required for determining the S-matrix. Let us now find the resonances modes of the system which are obtained by setting  $\det(S^{-1}) = 0$ , since the S matrix is calculated for symmetric structure (the input and the output medium are the same), it is found that the zeros of  $\det(S^{-1})$  are the same as those of  $\det(S)$ :

$$\det(S) = S_{12}(\omega)S_{21}(\omega) - S_{11}(\omega)S_{22}(\omega) = 0 \quad (5.23)$$

We get then two categories of solutions:

$$\Delta_+ = S_{11}(\omega) + S_{12}(\omega) = 0, \text{ or } \Delta_- = S_{11}(\omega) - S_{12}(\omega) = 0. \quad (5.24)$$

To find out which one corresponds to the resonance modes of the system, we compare each of them with the curves computed by the PMM method. As seen from Figure 5.5, the resonance frequency defined by the class of solutions satisfying to  $\Delta_+ = S_{11}(\omega) + S_{12}(\omega)$  matches with the resonant dip in the transmission spectrum of the structure. Thus, we can set:

$$t(\omega) = -(S_{11}(\omega) + S_{12}(\omega)) \quad (5.25)$$

$$r(\omega) = -(1 - t(\omega)) \quad (5.26)$$

where  $t$  and  $r$  denote the transmissions and reflection coefficients resulting from the resonance phenomena. In addition to this contribution, we should add a second term

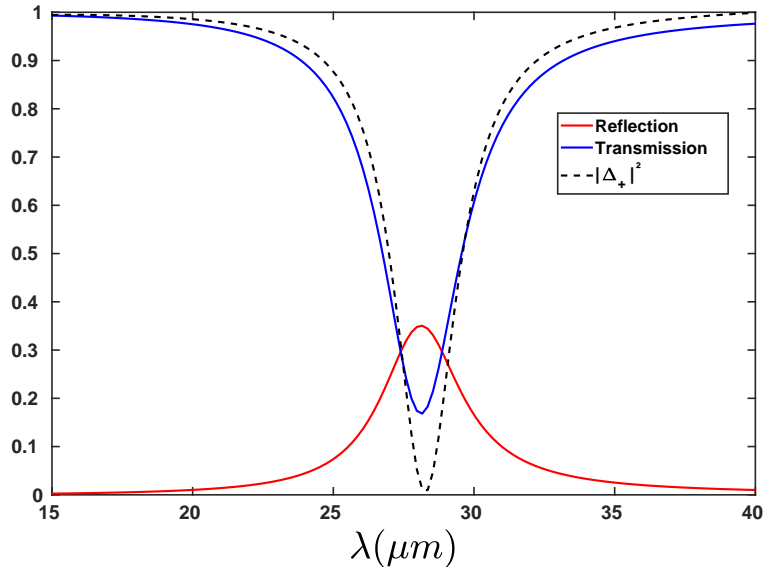


Figure 5.5: Comparison between the transmittance spectra of the structure computed using the PMM method and the one given by  $|\Delta_+|^2$ . The parameters are the same as Figure 5.3

that take into account the contribution of a single strip of graphene. Therefore the transmission and the reflection spectrums of the system can take the following form:

$$T = \frac{1}{2} (t + T_s) \quad (5.27)$$

$$R = \frac{1}{2} (r + R_s) \quad (5.28)$$

Where  $T_s$  and  $R_s$  are respectively the transmission and reflection coefficients through a graphene monolayer. These coefficients are those calculated in the previous chapter and given by equations (4.110) and (4.115). Now, our semi analytical model is completed and in the next section, we will attempt to validate and test it.

### 5.1.3 Numerical Results and discussion

In this section, some numerical examples are provided to validate the proposed semi analytical model and demonstrate its viability. For this purpose, we investigate the

transmission and reflection properties for two different cases: with an external magnetic field and without magnetic field. Firstly, let us consider a graphene strip grating with the following parameters:  $a = 0.9\mu\text{m}$ ,  $s = 0.45\mu\text{m}$ ,  $B = 3\text{T}$ ,  $\mu_c = 0.6\text{eV}$ ,  $\tau = 0.6\text{ps}$ . The reflection and transmission spectra are shown in Figure 5.6. Their real and imaginary parts are also plotted in Figure 5.7. These results are compared with the effective medium given in the ref [14] and the PMM method. We can see a good agreement between the PMM results and those obtained with our proposed model. By contrast, the comparison with the effective medium shows that the latter cannot reproduce the magneto-optical properties of the studied graphene grating.

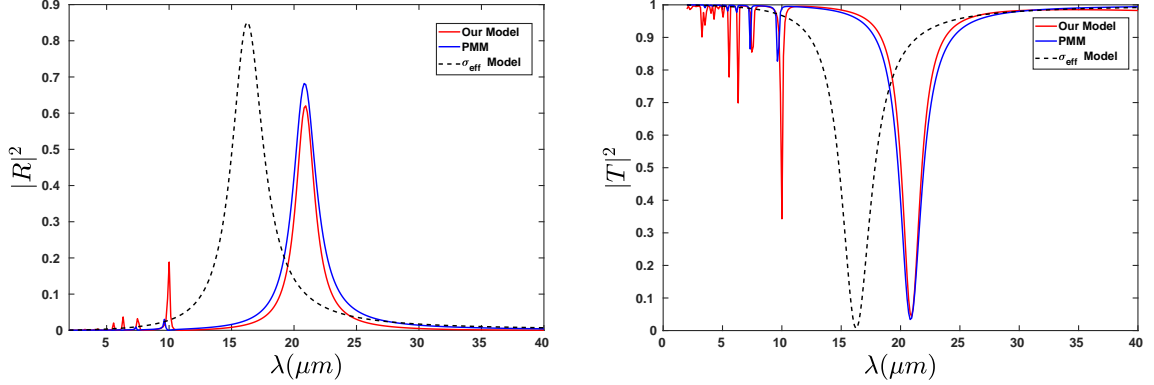


Figure 5.6: Comparison between the reflection and transmission spectra obtained from our Model (red solid lines) and those obtained from the PMM (blue solid lines) and from the effective medium approach [14] (dashed black lines). The results are calculated for a magnetically biased graphene strip grating with ribbon width  $a = 0.9\mu\text{m}$ , gap  $s = 0.45\mu\text{m}$  and  $B = 3\text{T}$ . Graphene parameters are  $\mu_c = 0.6\text{eV}$ ,  $T = 300\text{K}$  and  $\tau = 0.6\text{ps}$

As a second example, we consider the case of a graphene strip grating without magnetic field. The strip width is  $a = 0.25\mu\text{m}$  and the periodicity is assumed to be  $d = 0.35\mu\text{m}$ . The chemical potential of the graphene strips is set to  $\mu_c = 0.4\text{eV}$  and the relaxation time  $\tau$  is taken to be  $0.4\text{ps}$ . Figure 5.8 depicts the reflection and transmission spectra of this structure as a function of wavelength. The results are obtained using the proposed semi analytical model (red solid lines), the PMM model (blue solid lines) and the effective medium approach [14] (dashed black lines). Similarly to the first example, an excellent agreement is observed between our proposed model and the PMM results. While the effective medium proposed in [14] is not able to predict the magneto-optical response of this structure. From these results, we can conclude that the proposed semi analytical Model can efficiently and successfully treat the general case of a graphene strip grating biased with an external magnetic field as well as the particular case where no magnetic field is applied.

In the following, we are going to test and check the performance and the accuracy of our approach by examining it as a function of grating and graphene parameters including the geometric parameter  $a/d$ , the chemical potential and the magnetic bias. Let us begin by test it for different filling factor  $a/d$ . For doing so, we set  $d = 1.35\mu\text{m}$  and we plot in figure 5.9 the wavelength of the first resonance as a function of filling factor for two values of the magnetic field  $B = 0\text{T}$  and  $B = 3\text{T}$ . The results obtained with our approach (red plus) are compared with those performed by the help of the PMM method (blue asterisks). One can clearly see that the results correlate well with each other for all filling factors. In particular, an excellent agreement is observed for  $a/d$  smaller than 0.4 and for  $a/d$  greater than 0.7. For the remaining filling factors

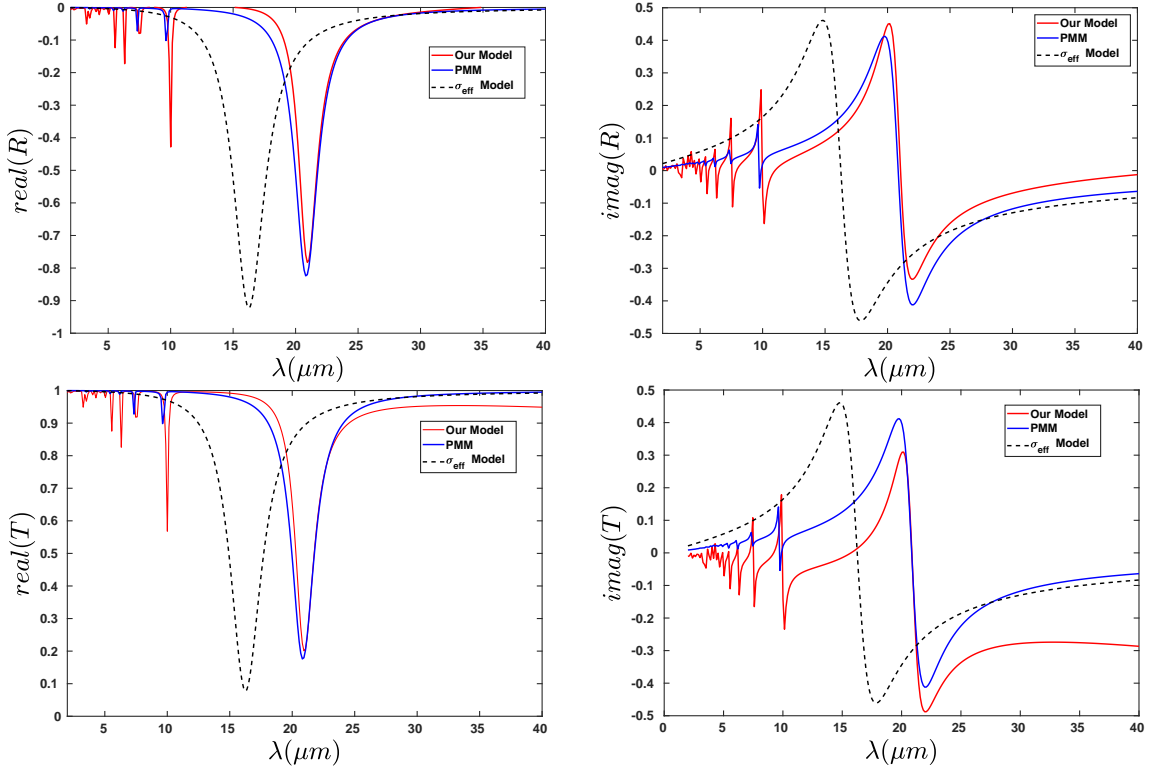


Figure 5.7: Real and imaginary parts of the reflection (the two upper panels) and transmission (the two lower panels). the red lines represent our model, the blue lines represent the PMM method and the black dashed lines represent those calculated using [14]. The parameters are the same as those in figure 5.6.

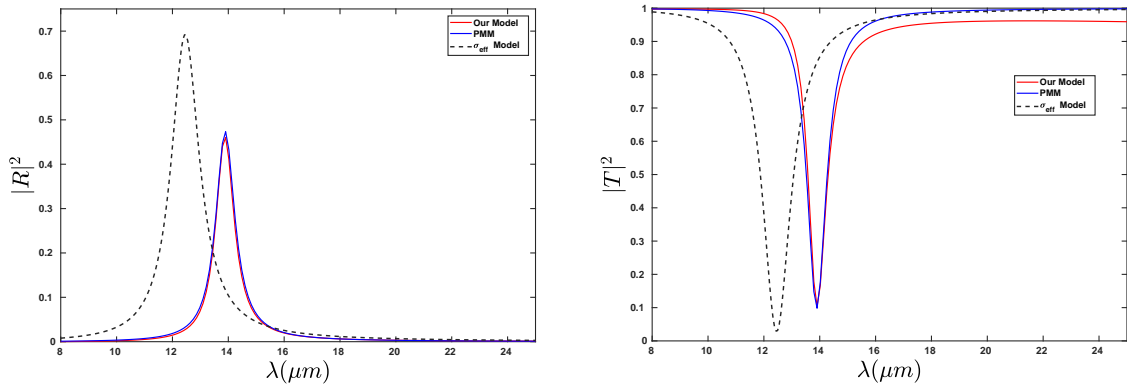


Figure 5.8: Comparison between the reflection and transmission spectra obtained from our proposed Model (red solid lines) and those obtained from the PMM (blue solid lines) and from the the effective medium approach [14] (dashed black lines). The results are calculated for a graphene strip grating with ribbon width  $a = 0.25\mu\text{m}$  and gap  $s = 0.1\mu\text{m}$ , when the magnetic bias is absent. Graphene parameters are  $\mu_c = 0.4\text{eV}$ ,  $T = 300\text{K}$  and  $\tau = 0.4\text{ps}$

$0.4 < a/d < 0.7$  the relative error does not exceed 4%. For example for  $a/d = 0.5736$ , the relative error is equal to 2.04% for  $B = 0\text{T}$  and 3.12% for  $B = 3\text{T}$ . Hence, the proposed model provides accurate results for all filling factors and can efficiently deals with the grating with a small gap as well as a large gap. It is important to note that the grating with a small gap constitute a critical case because in this case the interaction between neighboring strips becomes strong and thus to obtain accurate results, it is necessary to take into account this interaction.

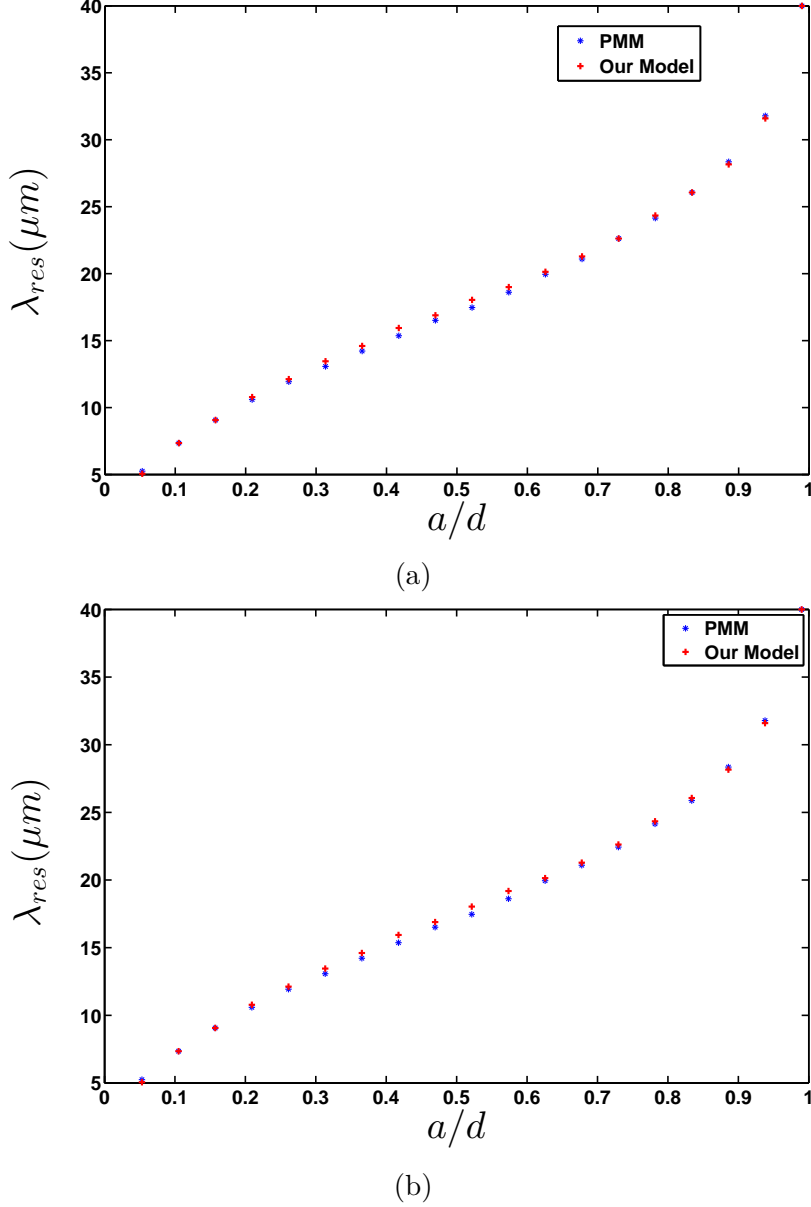


Figure 5.9: First resonance wavelength of the transmission spectrum as a function of filling factor  $a/d$  for (a)  $B = 0T$  and (b)  $B = 3T$ . Other parameters are  $d = 1.35\mu m$ ,  $\mu_c = 0.6eV$ ,  $\tau = 0.6ps$

We look now at the accuracy of the proposed approach as a function of the magnetic field. Figure 5.10 shows the wavelength of the first resonance as a function of the magnetic field for three values of the filling factor  $a/d = 0.2$ ,  $a/d = 0.5$  and  $a/d = 0.8$ . It is shown that for  $a/d = 0.2$  the results obtained from our model are well matched with those computed with the PMM method for all magnetic field between  $[0,10]T$ . While for  $a/d = 0.5$  and  $a/d = 0.8$  the results correlate well up to  $7T$ . For  $7 < B < 10$ , they shift away from those of the PMM method. This shift increases slightly with increasing  $B$ . For instance for  $B = 8.421T$ , the relative error is equal to  $2\%$  ( $a/d = 0.9$ ) and it increases for  $B = 10T$ , to reach  $3.41\%$ . This could be explained by the fact that the model proposed in (5.21) and (5.22) to approximate the phase decay  $\theta_c$  is only valid for  $B \leq 7T$ . So, to remove or minimize the difference between the two methods, we should numerically adjust the coefficients  $a_n^{(1)}$  and  $a_n^{(2)}$  to find the best fit model of the phase. Obviously this will affect the accuracy of our model which becomes less accurate for

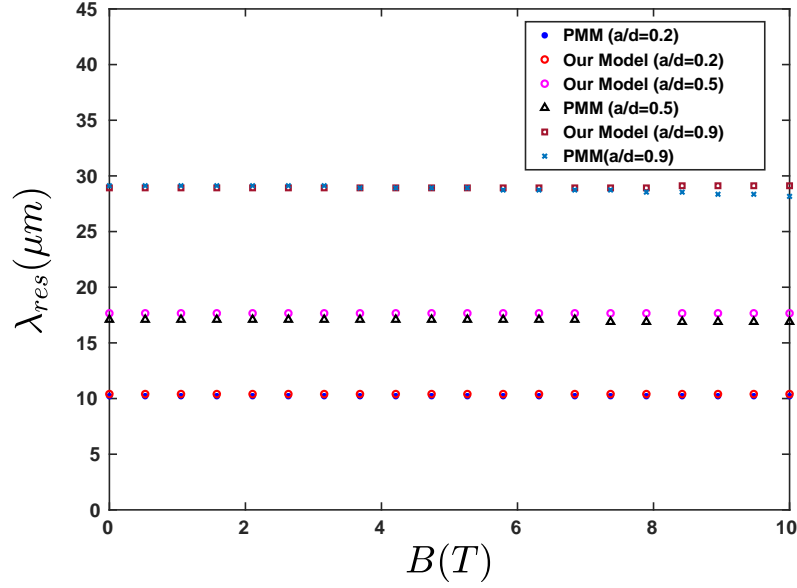


Figure 5.10: First resonance wavelength of the transmission spectrum as a function of magnetic field  $B$  for three different filling factors  $a/d = 0.2, 0.5$  and  $0.8$ . The Other parameters are  $d = 1.125\mu\text{m}$ ,  $\mu_c = 0.6\text{eV}$ ,  $\tau = 0.6\text{ps}$ .

$B > 7T$ . But, it does not pose a considerable and real problem since, from a practical point of view, the magnetic bias usually used to magnetize graphene does not exceed  $7T$  [21].

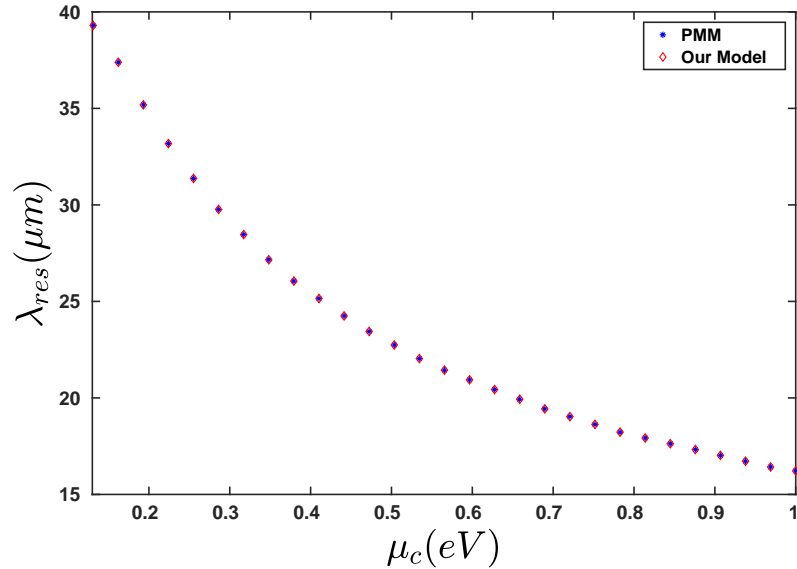


Figure 5.11: First resonance wavelength of the transmission spectrum as a function of the chemical potential of graphene  $\mu_c$ . The Other parameters are the same as those of Figure 5.6

We end this section by examining the stability of the proposed model with varying the chemical potential of the graphene strips. Figure 5.11 shows the wavelength of the first resonance as a function of the chemical potential. The reflection and transmission spectra for different chemical potential  $\mu_c$  namely for  $\mu_c = 0.4, 0.6$  and  $0.8\text{eV}$  are also plotted in figure 5.12. In these figures, we compare the results computed by our model

with those obtained from the PMM Method. We can see from figure 5.11 that for all chemical potentials the first resonance is successfully predicted by the proposed method. From figure 5.12, it is shown that the transmittance and the reflectance obtained with the PMM are well fitted by the proposed approach. One can also see that by decreasing  $\mu_c$ , the accuracy of the proposed method with respect to the amplitude of the transmittance and specifically of the reflectance is slightly decreased. This last behavior is expected. In fact as seen from equation 5.26, in our calculations, we do not take into account the absorption features within the structure. Therefore, when the chemical potential decreases, the losses in graphene increase and then the model becomes less accurate. However, it should be noted that the difference between the two curves is relatively small and thus this cannot be considered as a significant limitation of the proposed semi analytical approach.

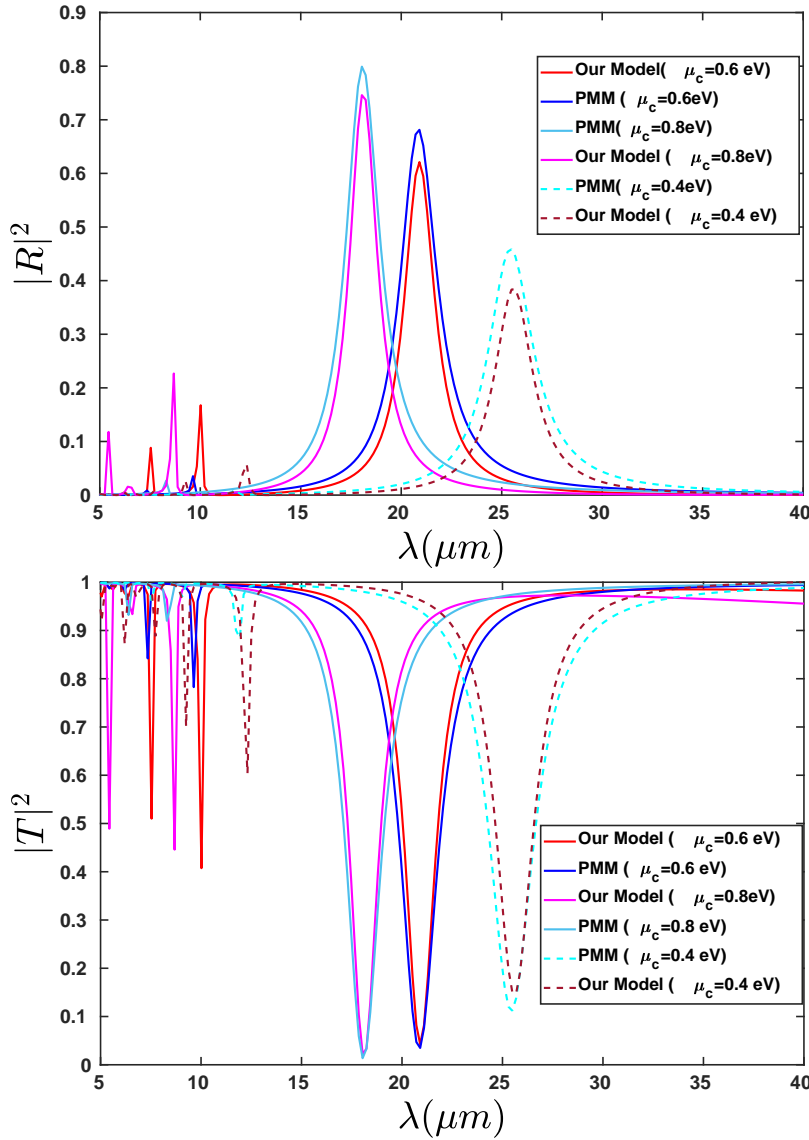


Figure 5.12: Reflection and transmission spectra calculated for different chemical potentials  $\mu_c = 0.4, 0.6$  and  $0.8\text{eV}$ . Other parameters are the same as those of Figure 5.6

## 5.2 Conclusion

In conclusion, in this chapter, we have presented a simple and fast semi analytical model to compute the transmittance and reflectance of a magnetically-biased subwavelength graphene strip grating. It is based on the effective medium approach when the graphene is modeled as an anisotropic layer with atomic thickness and a frequency-dependent and complex permittivity tensor. The proposed model is validated against the PMM method by numerical examples. The performance and the accuracy of this method has been also tested and checked as a function of the graphene and grating parameters. We have first showed that this proposed method is a general approach that can efficiently treat the structure when the magnetic field is applied and still valid even in the particular case of a structure without magnetic field which is not possible with the analytical methods already encountered in the literature. In addition to that, the study of the accuracy of the method as a function of the filling factor of the grating revealed that the proposed model can efficiently deal with the grating with a small gap as well as a large gap. Specifically, this method provides precise and reliable results in the case of gratings with small gaps which constitute a complicated case to deal with. Through this last structure it is possible to achieve a strong reflection ( near 90%) which could be of interest in devices that require high reflectivity such that reflectors in certain frequency ranges.

# Bibliography

- [1] D. L. Sounas, H. S. Skulason, H. V. Nguyen, A. Guermoune, M. Siaj, T. Szkopek, and C. Caloz. Faraday rotation in magnetically biased graphene at microwave frequencies. *Applied Physics Letters*, 102(19):191901, 2013. [133](#)
- [2] V. P. Gusynin and S. G. Sharapov. Unconventional integer quantum hall effect in graphene. *Phys. Rev. Lett.*, 95:146801, Sep 2005. [133](#)
- [3] Andrew L. Walter Markus Ostler Aaron Bostwick Eli Rotenberg Thomas Seyller Dirk van der Marel Alexey B. Kuzmenko Iris Crassee, Julien Levallois. Giant faraday rotation in single- and multilayer graphene. *Nature Phys*, (7):48–51, 2011. [6](#), [133](#)
- [4] Toshihiko Yoshino. Theory for oblique-incidence magneto-optical faraday and kerr effects in interfaced monolayer graphene and their characteristic features. *J. Opt. Soc. Am. B*, 30(5):1085–1091, May 2013. [6](#), [133](#)
- [5] A. M. Witowski, M. Orlita, R. Stępniewski, A. Wymolek, J. M. Baranowski, W. Strupiński, C. Faugeras, G. Martinez, and M. Potemski. Quasiclassical cyclotron resonance of dirac fermions in highly doped graphene. *Phys. Rev. B*, 82:165305, Oct 2010. [117](#), [133](#)
- [6] Fei Gao Baile Zhang Hongsheng Chen Xiao Lin, Zuoqia Wang. Atomically thin nonreciprocal optical isolation. *Sci Rep*, (4):4190, 2015. [133](#)
- [7] Min Wang, Yanqin Wang, Mingbo Pu, Chenggang Hu, Xiaoyu Wu, Zeyu Zhao, and Xiangang Luo. Circular dichroism of graphene-based absorber in static magnetic field. *Journal of Applied Physics*, 115(15):154312, 2014. [133](#)
- [8] Bin Hu, Jin Tao, Ying Zhang, and Qi Jie Wang. Magneto-plasmonics in graphene-dielectric sandwich. *Opt. Express*, 22(18):21727–21738, Sep 2004. [133](#)
- [9] J. M. Poumirol, W. Yu, X. Chen, C. Berger, W. A. de Heer, M. L. Smith, T. Ohta, W. Pan, M. O. Goerbig, D. Smirnov, and Z. Jiang. Magnetoplasmons in quasineutral epitaxial graphene nanoribbons. *Phys. Rev. Lett.*, 110:246803, Jun 2013. [133](#)
- [10] Mykhailo Tymchenko, Alexey Yu. Nikitin, and Luis Martín-Moreno. Faraday rotation due to excitation of magnetoplasmons in graphene microribbons. *ACS Nano*, 7(11):9780–9787, 2013. PMID: 24079266. [133](#), [134](#)

- [11] Tetiana M. Slipchenko Alexey Y. Nikitin Luis Martin-Moreno Jérôme Faist Alexey B. Kuzmenko Jean-Marie Pouirol, Peter Q. Liu. Electrically controlled terahertz magneto-optical phenomena in continuous and patterned graphene. *Nat Commun*, (8):14626, 2017. [133](#)
- [12] X. Wang, W. Yin, and Z. Chen. Matrix exponential fdtd modeling of magnetized graphene sheet. *IEEE Antennas and Wireless Propagation Letters*, 12:1129–1132, 2013. [134](#)
- [13] P. Li and L. J. Jiang. Modeling of magnetized graphene from microwave to thz range by dgtd with a scalar rbc and an ade. *IEEE Transactions on Antennas and Propagation*, 63(10):4458–4467, Oct 2015. [134](#)
- [14] J. S. Gomez-Diaz and A. Alù. Magnetically-biased graphene-based hyperbolic metasurfaces. In *2016 IEEE International Symposium on Antennas and Propagation (APSURSI)*, pages 359–360, June 2016. [8](#), [134](#), [140](#), [141](#), [142](#)
- [15] Mahdi Rahmanzadeh, Behzad Rejaei, Mohammad Memarian, and Amin Khavasi. Analytical and rigorous method for analysis of an array of magnetically-biased graphene ribbons. *Opt. Express*, 27(20):28395–28409, Sep 2019. [134](#)
- [16] J.M. Bell, G.H. Derrick, and R.C. McPhedran. Diffraction gratings in the quasi-static limit. *Optica Acta: International Journal of Optics*, 29(11):1475–1489, 1982. [136](#)
- [17] Philippe Lalanne and Dominique Lemerrier-lalanne. On the effective medium theory of subwavelength periodic structures. *Journal of Modern Optics*, 43(10):2063–2085, 1996. [136](#)
- [18] Philippe Lalanne and Dominique Lemerrier-Lalanne. Depth dependence of the effective properties of subwavelength gratings. *J. Opt. Soc. Am. A*, 14(2):450–459, Feb 1997. [136](#)
- [19] Kofi Edee. Understanding the plane wave excitation of the metal-insulator-metal gap plasmon mode of a nanoribbons periodic array: role of insulator-metal-insulator lattice mode. *OSA Continuum*, 2(2):389–399, Feb 2019. [137](#)
- [20] Kofi Edee, Maha Benrhouma, Mauro Antezza, Jonathan Albert Fan, and Brahim Guizal. Coupling between subwavelength nano-slit lattice modes and metal-insulator-graphene cavity modes: a semi-analytical model. *OSA Continuum*, 2(4):1296–1309, Apr 2019. [137](#)
- [21] I. Crassee, M. Orlita, M. Potemski, A. L. Walter, M. Ostler, Th. Seyller, I. Gaponenko, J. Chen, and A. B. Kuzmenko. Intrinsic terahertz plasmons and magneto-plasmons in large scale monolayer graphene. *Nano Letters*, 12(5):2470–2474, 2012. PMID: 22519967. [143](#)

# Theoretical analysis of Optical Hall effect in a 2D nano-cross-slits grating

*There is nothing more deceptive than an obvious fact.*

Arthur Conan Doyle, The  
Boscombe Valley Mystery

## Contents

<b>6.1 Statement</b> . . . . .	<b>150</b>
<b>6.2 Polarization independent EOT phenomenon through 2D cross-slits array</b> . . . . .	<b>151</b>
<b>6.3 Magneto-optical perturbation of the gap plasmon modes</b>	<b>158</b>
<b>6.4 Conclusion</b> . . . . .	<b>162</b>

As shown in chapter 5, the optical Hall effect can be considered as the physical phenomenon related to the appearance of magnetically induced anisotropy in a material's optical properties. This induced anisotropy leads to a non-reciprocal magneto-optical response of the anisotropic material. Significant efforts were made to create optical materials allowing to combine both extraordinary optical transmission (EOT) [1, 2, 3, 4, 5, 6] and magneto optical effects in order to enhance the magneto optical activity, namely the Faraday and/or Kerr rotation(s), chirality for photonics materials. In all these works, both 1D and 2D geometries combining non reciprocal surface plasmon modes and magnetic effect are studied. The 1D base structure is consisted of periodic array of nano-ribbons [7, 8, 9, 10, 11, 12] or sub-wavelength slits, while the 2D structures are generally based on nano-holes with different shapes [13, 14, 15, 16]. To the best of our knowledge, the EOT phenomenon involving a 2D structure consisting of a periodic array of cross-slits grating has never been reported. Firstly, we show in this chapter that, contrary to the case of periodic array of nano-holes, the 2D cross-slits grating can support fundamental guided cavity super-modes which are two-degree degenerate in the case of uniaxial slit-material and symmetrical geometry. Therefore, the EOT phenomenon through this structure does not depend on the incident field polarization. Secondly, we investigate the magneto optical activity in this structure when the slits are filled by an anisotropic gyrosopic material. The structure may support

non reciprocal cavity super-modes exhibiting one way behavior. To begin with, we provide analytical expressions of the reflection and transmission of the system allowing to fully describe and deepen the EOT mechanism occurring in the system. Later, these analytical expressions are extended the analytical model to explain the non reciprocal unidirectional light transmission in EOT-range.

## 6.1 Statement

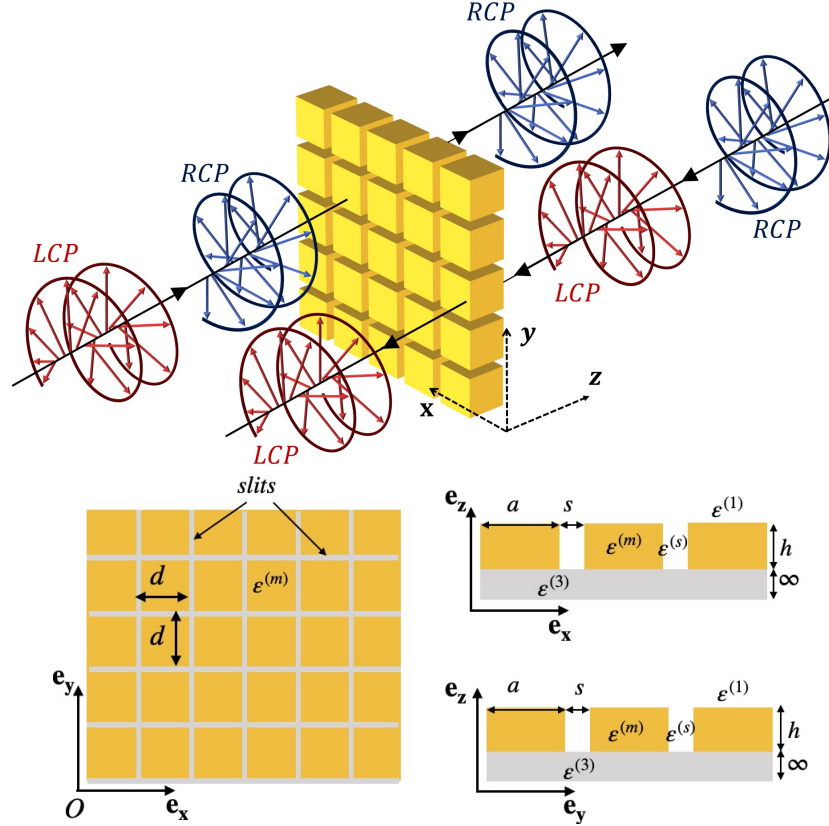


Figure 6.1: Sketch of 2D structure made of a dispersive gold metal film perforated with a 2D periodic subwavelength array of nano-slits.

The structure under study consists of a metal film perforated with a 2D periodic subwavelength array of nano-slits. See Fig. 6.1. The relative permittivity of the material in the slits is denoted by  $\epsilon^{(s)}$ . The relative permittivity of the dispersive metal (gold) is denoted by  $\epsilon^{(m)}$  and described by the Drude-Lorentz model [17, 18]. See reference [19] for the numerical parameters used to compute  $\epsilon^{(m)}$ . This structure is excited, from the upper medium (whose relative permittivity is  $\epsilon^{(1)} = \nu_1^2$ ) by a monochromatic plane wave with angular frequency  $\omega$  and wave vector  $\vec{K}_0 = k_0 (\alpha_0^{(1)} \vec{e}_x + \beta_0^{(1)} \vec{e}_y + \gamma_0^{(1)} \vec{e}_z)$ , where  $\alpha_0^{(1)} = \nu_1 \sin \theta_0 \cos \phi_0$ ,  $\beta_0^{(1)} = \nu_1 \sin \theta_0 \sin \phi_0$  and  $\gamma_0^{(1)} = \nu_1 \cos \theta_0$ .  $\theta_0$  and  $\phi_0$  are the polar and azimuth angles of incidence.  $k_0 = 2\pi/\lambda = \omega/c$  denotes the wavenumber,  $\lambda$  being the wavelength and  $c$  the speed of light in vacuum. The amplitudes of the transverse components of the electric field of the incident wave are:

$$\begin{cases} E_x^{inc} = \cos \phi_0 \cos \delta - \sin \phi_0 \sin \delta \\ E_y^{inc} = \cos \theta_0 \sin \phi_0 \cos \delta + \cos \phi_0 \sin \delta \end{cases} \quad (6.1)$$

The parameter  $\delta$  denotes the angle of polarization. In this work we use the following numerical parameters:  $\varepsilon^{(1)} = \varepsilon^{(3)} = \varepsilon^{(slit)} = 1$ ,  $\theta_0 = \phi_0 = 0^\circ$ ,  $h = 500 \text{ nm}$ ,  $d = 165 \text{ nm}$ ,  $a = 15 \text{ nm}$ . We will consider materials such that the permittivity and permeability have the following form

$$\varepsilon(x, y) = \begin{bmatrix} \varepsilon^{xx} & \varepsilon^{xy} & 0 \\ \varepsilon^{yx} & \varepsilon^{yy} & 0 \\ 0 & 0 & \varepsilon^{zz} \end{bmatrix}; \mu(x, y) = \begin{bmatrix} \mu^{xx} & \mu^{xy} & 0 \\ \mu^{yx} & \mu^{yy} & 0 \\ 0 & 0 & \mu^{zz} \end{bmatrix}. \quad (6.2)$$

It can be shown from Maxwell's equations that the transverse components of the electric field satisfy

$$-k_0^2 \gamma^2 \begin{bmatrix} E_x \\ E_y \end{bmatrix} = \mathcal{L}_{\mu, \varepsilon} \mathcal{L}_{\varepsilon, \mu} \begin{bmatrix} E_x \\ E_y \end{bmatrix}, \quad (6.3)$$

where the  $z$  dependence of the field is held by the  $e^{-ik_0 \gamma z}$  factor. The operators  $\mathcal{L}_{\kappa, \tau}$ ,  $\{\kappa, \tau\} \in \{\varepsilon, \mu\}$  are given by:  $\mathcal{L}_{\kappa, \tau} =$

$$\begin{bmatrix} -k_0 \kappa^{yx} + \frac{1}{k_0} \partial_x (\tau^{zz})^{-1} \partial_y & -k_0 \kappa^{yy} - \frac{1}{k_0} \partial_x (\tau^{zz})^{-1} \partial_x \\ +k_0 \kappa^{xx} + \frac{1}{k_0} \partial_y (\tau^{zz})^{-1} \partial_y & +k_0 \kappa^{xy} - \frac{1}{k_0} \partial_y (\tau^{zz})^{-1} \partial_x \end{bmatrix}.$$

In the current work we consider nonmagnetic materials ( $\mu^{xx} = \mu^{yy} = \mu^{zz} = 1$ , and  $\mu^{xy} = \mu^{yx} = 0$ ), and a gyrotropic medium which off-diagonal relative permittivity terms are of the form:  $\varepsilon^{xy} = -\varepsilon^{yx} = -i\Delta$ . In order to compute the spectral response of the structure, we use the polynomial modal method (PMM) to solve the eigenvalue Eq. (6.3) in the grating before writing the boundary conditions at the interfaces  $z = 0$  and  $z = -h$ . This leads to an algebraic system whose solution gives the reflected and transmitted amplitudes. It is important to stress that, in order to ensure the stability of the approach, we make use of the scattering matrix algorithm.

## 6.2 Polarization independent EOT phenomenon through 2D cross-slits array

Let us first discuss the EOT through the structure when the slits-dielectric is not magnetized and, therefore possesses only a diagonal dielectric tensor:

$$\begin{bmatrix} \varepsilon(x, y, \omega) & 0 & 0 \\ 0 & \varepsilon(x, y, \omega) & 0 \\ 0 & 0 & \varepsilon(x, y, \omega) \end{bmatrix}. \quad (6.4)$$

The structure is excited with a monochromatic plane wave with both right circular polarization (RCP:  $\vec{E}^{inc} = E_0(\vec{e}_x + i\vec{e}_y)$ ) and left circular polarization (LCP:  $\vec{E}^{inc} = E_0(\vec{e}_x - i\vec{e}_y)$ ),  $i^2 = -1$ . Fig. 6.2 shows the reflected and transmitted spectra. A Lorentz-like resonance corresponding to an EOT occurs around  $\lambda = 2.17 \mu\text{m}$ ; which, as pointed in reference [20] in the case of 1D slits-grating, is due to the excitation of a particular eigenmode (the most slowly decaying mode of the grating layer whose effective index is denoted by  $\gamma_0^{(2)}$ ) which ensures the energy transfer through the structure

But contrary to the 1D case, and because of the symmetry properties of the structure, this mode is two-degree degenerate in the current 2D case. In the following, we will first provide an extension of our simplified model for 1D structures (see chapter 3)

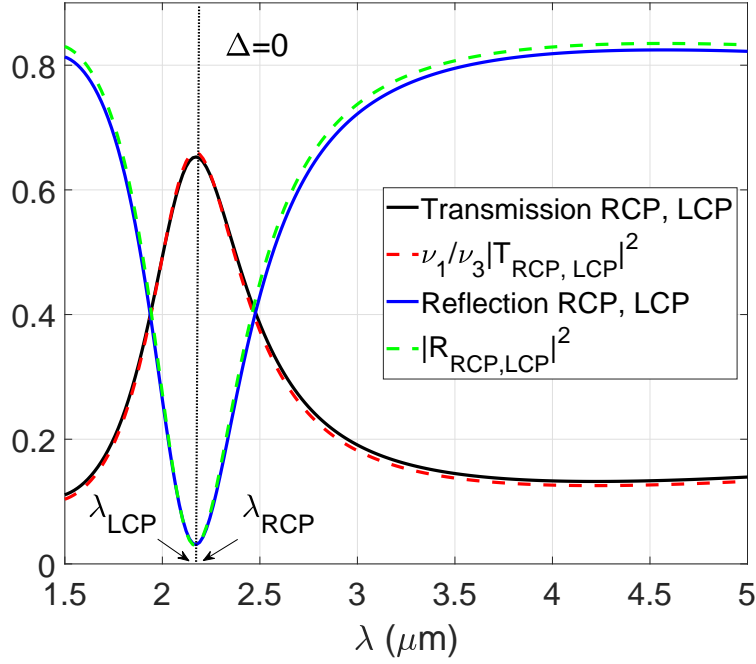


Figure 6.2: Reflection and transmission spectra of the array of the 2D subwavelength nano-slits in non magnetization configuration: illustration of EOT phenomenon. Comparison between rigorous computation with the PMM and the semi analytical model.

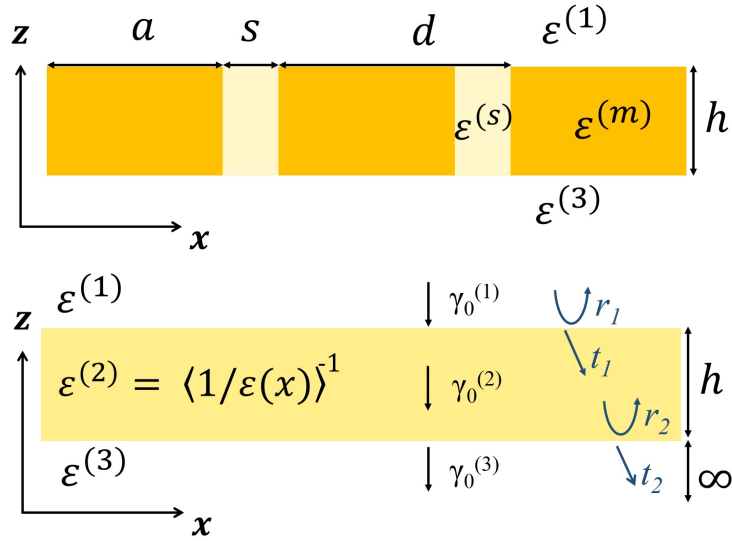


Figure 6.3: Sketch of 1D structure made of a dispersive gold metal film perforated with a 1D periodic subwavelength nano-slits. The structure is equivalent to an homogeneous layer of thickness  $h$  with effective permittivity  $\epsilon^{(2)}$  when  $\lambda \gg d$ .  $\gamma_0^{(i)}$  is the propagation constants in each medium and  $r_i$  and  $t_i$  the reflection and transmission coefficients of each interface.

[20] to the present 2D case. Then we will explain why this phenomenon is polarization-independent. A semi-analytic model describing the EOT phenomenon for a 1D periodic array of sub-wavelength nano-slits encapsulated between  $\epsilon^{(1)}$  and  $\epsilon^{(3)}$  media is already described in [19]. As pointed in that paper, the electromagnetic response of the 1D-system to a linearly polarized plane wave excitation, when the period  $d \ll \lambda$ , is equivalent to that of a slab with equivalent permittivity  $\epsilon^{(2)} = \langle 1/\epsilon^{(m,s)}(x) \rangle^{-1}$  and

height  $h$ . See Fig. 6.3. In chapter 3, phase correction terms are empirically introduced in order to take into account the phase matching between the lattice mode with effective index  $\gamma_0^{(2)}$  and the incident plane wave. The phase correction formulas were obtained from numerical experiments and no demonstration allowing to derive them were provided. However in recent works presented in references [21] and [22] we suggested another simplified and rigorous way to handle the influence of the surface plasmons polaritons (SPPs) in the EOT phenomenon. In this model, the coupling be-

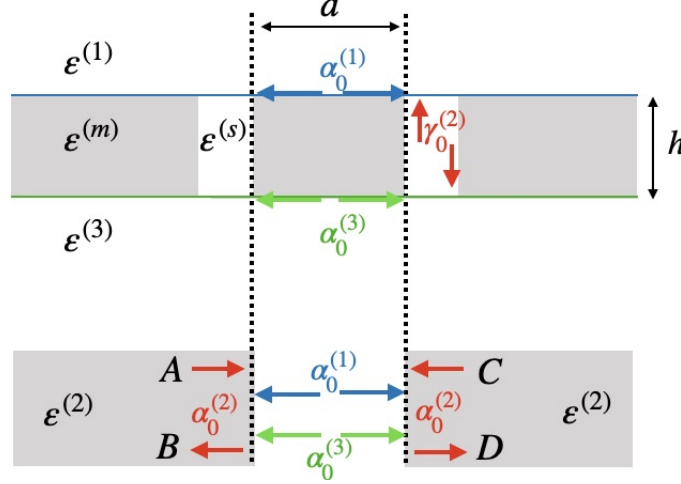


Figure 6.4: Sketch showing the coupling between the gap plasmon mode  $\gamma_0^{(2)}$  living in  $\epsilon^{(2)}$  homogeneous medium and  $\alpha^{(1)}$  and  $\alpha^{(3)}$  surface plasmons mode traveling in medium  $\epsilon^{(1)}$  and  $\epsilon^{(3)}$  respectively.

tween the SPPs and the gap plasmon cavity mode, schematized in Fig. 6.4 is analyzed through the scattering parameters:

$$\begin{bmatrix} B \\ D \end{bmatrix} = \begin{bmatrix} S_{11} & S_{12} \\ S_{21} & S_{22} \end{bmatrix} \begin{bmatrix} A \\ C \end{bmatrix} \quad (6.5)$$

where

$$\begin{cases} S_{11}^{(i)} = S_{22}^{(i)} = \frac{r_1^{(i)} + r_2^{(i)} e^{-i2k_0\alpha_0^{(i)}a}}{1 + r_1^{(i)}r_2^{(i)} e^{-i2k_0\alpha_0^{(i)}a}} \\ S_{12}^{(i)} = S_{21}^{(i)} = \frac{t_1^{(i)}t_2^{(i)} e^{-ik_0\alpha_0^{(i)}a}}{1 + r_1^{(i)}r_2^{(i)} e^{-i2k_0\alpha_0^{(i)}a}} \end{cases}, \quad (6.6)$$

with

$$\begin{cases} r_1^{(i)} = \frac{\alpha_0^{(2)}/\epsilon^{(2)} - \alpha_0^{(i)}/\epsilon^{(i)}}{\alpha_0^{(2)}/\epsilon^{(2)} + \alpha_0^{(i)}/\epsilon^{(i)}} = -r_2^{(i)} \\ t_1^{(i)} = \frac{2\alpha_0^{(2)}/\epsilon^{(2)}}{\alpha_0^{(2)}/\epsilon^{(2)} + \alpha_0^{(i)}/\epsilon^{(i)}}, t_2^{(i)} = \frac{2\alpha_0^{(i)}/\epsilon^{(i)}}{\alpha_0^{(2)}/\epsilon^{(2)} + \alpha_0^{(i)}/\epsilon^{(i)}} \end{cases}, \quad (6.7)$$

where  $\alpha_0^{(i=1,3)} = \sqrt{\frac{\epsilon^{(i)}\epsilon^{(m)}}{\epsilon^{(i)} + \epsilon^{(m)}}$  is the effective index of the SPP propagating along the interface  $\epsilon^{(m)}/\epsilon^{(i)}$  and  $\alpha_0^{(2)} = \sqrt{\epsilon^{(2)} - (\gamma_0^{(2)})^2}$ . The interaction between the cavity mode with effective index  $\gamma_0^{(2)}$  and the upper and lower SPPs are handled by the reflection coefficients  $s_1 = S_{12}^{(1)} - S_{11}^{(1)}$  and  $s_3 = S_{12}^{(3)} - S_{11}^{(3)}$  respectively. When  $d \ll \lambda$ , the

Homogeneous Slab method (HSM) leads to the following reflection  $R$  and transmission  $T$  coefficients:

$$\begin{cases} R = \frac{r_1 + e^{-ik_0\gamma_0^{(2)}h} s_1 r_2 s_3 e^{-ik_0\gamma_0^{(2)}h}}{1 + r_1 e^{-ik_0\gamma_0^{(2)}h} s_1 r_2 s_3 e^{-ik_0\gamma_0^{(2)}h}} \\ T = \frac{t_1 t_2 s_1 e^{-ik_0\gamma_0^{(2)}h}}{1 + r_1 e^{-ik_0\gamma_0^{(2)}h} s_1 r_2 s_3 e^{-ik_0\gamma_0^{(2)}h}} \end{cases}. \quad (6.8)$$

To extend this model to the current case of a 2D structure, we consider that the two-degree degenerate cavity mode, lives in an homogeneous medium with  $\varepsilon^{(2)} = \langle 1/\varepsilon^{(m,s)}(x) \rangle^{-1} = \langle 1/\varepsilon^{(m,s)}(y) \rangle^{-1}$ . We successfully compare in Fig. 6.2 the spectrum of the reflection and the transmission  $R_{RCP,LCP}$  and  $T_{RCP,LCP}$  respectively of the 2D structure, obtained from Eq. (6.8) to the rigorous results (Reflection and Transmission) obtained from the PMM. The structure is excited with both Right (RCP) and Left (LCP) circular polarized incident fields at normal incidence. This homogeneous equivalent slab model reproduces the extraordinary transmission mechanism and thus confirms that  $\gamma_0^{(2)}$  cavity mode is responsible for this enhancement. It should be emphasized that some numerical simulations, not reported here, show that the polarization of the incident field does not influence the current 2D EOT phenomenon. This is because the geometry and the physical properties of structure are symmetrical, and this property leads to the degeneracy of the fundamental mode with effective index  $\gamma_0^{(2)}$ , living in the 2D structure. Consequently any incident field with arbitrary polarization state should excite some linear combination of the eigenfunctions associated with the two-degree degenerate eigenvalue  $\gamma_0^{(2)}$ :

$$\vec{\Phi}^{(\eta,\chi)} = \eta \vec{\Phi}^{21} + \chi \vec{\Phi}^{22} \quad (6.9)$$

where  $\vec{\Phi}^{21}$  and  $\vec{\Phi}^{22}$  are vectors which components are

$$\left( \Phi_x^{(21)}, \Phi_y^{(21)} \right) \text{ and } \left( \Phi_x^{(22)}, \Phi_y^{(22)} \right), \quad (6.10)$$

respectively.  $\Phi$  stands for  $E$  and/or  $H$ . Because of the properties of symmetry of these linear combinations, they can be excited from both linear and circular polarized incident plane waves. The vectors

$$[E_x^{(21)}; E_y^{(21)}]^t, [E_x^{(22)}; E_y^{(22)}]^t \quad (6.11)$$

and

$$[H_x^{(21)}; H_y^{(21)}]^t, [H_x^{(22)}; H_y^{(22)}]^t \quad (6.12)$$

being the eigenvectors of the operators  $L_{EH}L_{HE}$  Eq. (6.3) and  $L_{HE}L_{EH}$ , respectively, associated with the two-degree degenerate eigenvalue  $\gamma_0^{(2)}$ .

As shown in Fig.(6.5), for  $(\eta, \chi) = (1, 1)$  and  $(\eta, \chi) = (1, -1)$  the linear combination of the degenerate eigenfunctions is polarized along  $(Ox)$  and  $(Oy)$  axis respectively. Consequently these modes combinations can be excited by a linearly polarized incident waves  $E^{inc}\vec{e}_x$  and  $E^{inc}\vec{e}_y$ . For  $(\eta, \chi) = (1, \pm i)$  modes combination may be excited by both RCP and LCP incident plane waves. The EOT phenomenon do not depend on the incident field polarization.

The dispersion curves of the effective index  $\gamma_0^{(2)}$  is plotted in Fig 6.6 for different values of  $s$  while  $d$  is kept equal to  $165nm$  and  $B = 0$ . It can be seen that increasing  $s$  leads to a decrease of the real part of  $\gamma_0^{(2)}$  and an increasing of its imaginary

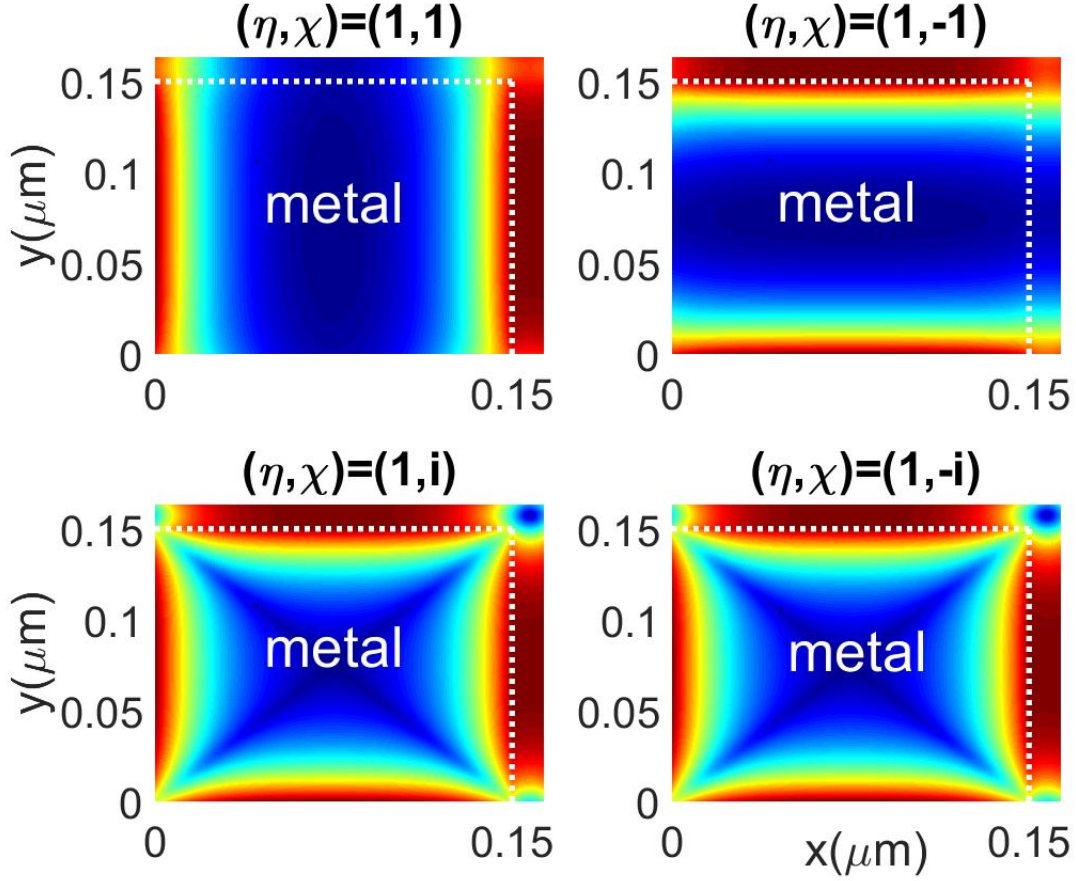


Figure 6.5: Modulus of  $\mathbf{H}^{(\eta,\chi)}(x,y)$  for different values of  $(\eta,\chi)$ . Because of the properties of symmetry of these linear combination, they can be excited from both linear and circular polarized incident plane waves. Linear  $E^{inc}(x,y)\mathbf{e}_x$  incident wave may excite  $(\eta,\chi) = (1,1)$  modes combination, while a  $E^{inc}(x,y)\mathbf{e}_y$  linear polarized wave may excite  $(\eta,\chi) = (1,-1)$  modes combination.  $(\eta,\chi) = (1,\pm i)$  modes combination may be excited by both RCP and LCP incident plane wave.

part. Since the  $z$  dependency of the electromagnetic field in the cavity may be approximated by  $\phi(z) = A^+ \exp(ik\gamma_0^{(2)}z) + A^- \exp(-ik\gamma_0^{(2)}z)$ , ( $k = 2\pi/\lambda$ ), for a given  $h$ -length cavity, the resonance wavelengths can be roughly approximately obtained through a phase condition on the term  $A^\pm \sin(2\pi h\gamma_0^{(2)}/\lambda_r)$ . When  $\gamma_0^{(2)}$  decreases, the resonance wavelength  $\lambda_r$  also decreases. See Fig. 6.7. Consequently increasing the slit-width  $s$  pushes the resonance wavelengths towards the visible wavelengths range, and simultaneously, the width of the resonance (FWHM) becomes narrower, because of the less losses (imaginary part of  $\gamma_0^{(2)}$ ).

In the same manner, when  $h$  decreases (but still large enough), the resonance wavelengths are pushing towards the visible wavelengths range, while the width of the resonance (FWHM) becomes narrower. See Fig. 6.8.

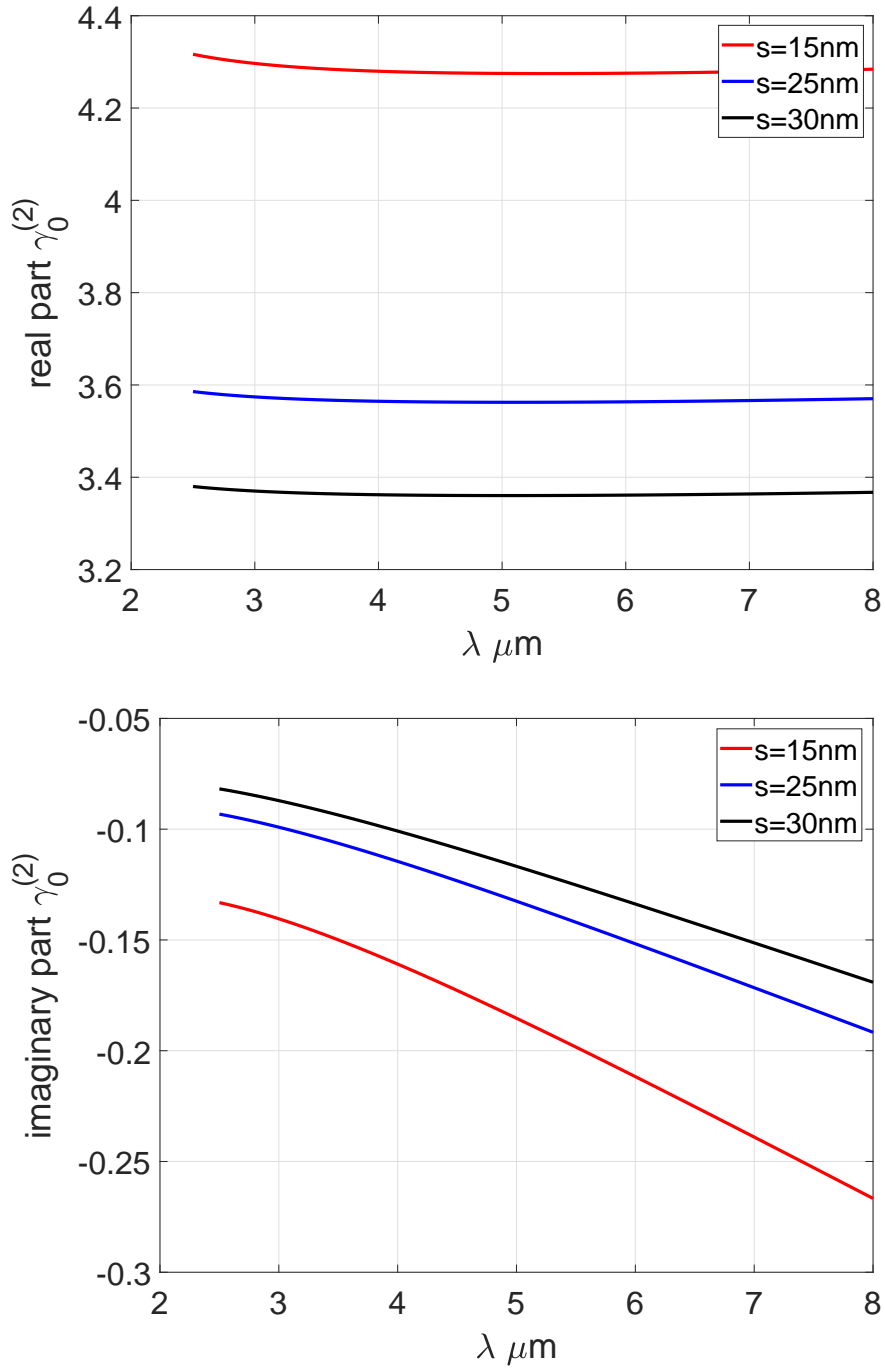


Figure 6.6: Spectrum of the effective index  $\gamma_0^{(2)}$  for different values of  $s$  and for  $d = 165\text{nm}$ . Increasing  $s$  leads to a decrease of the real part of  $\gamma_0^{(2)}$  and an increasing of its imaginary part.

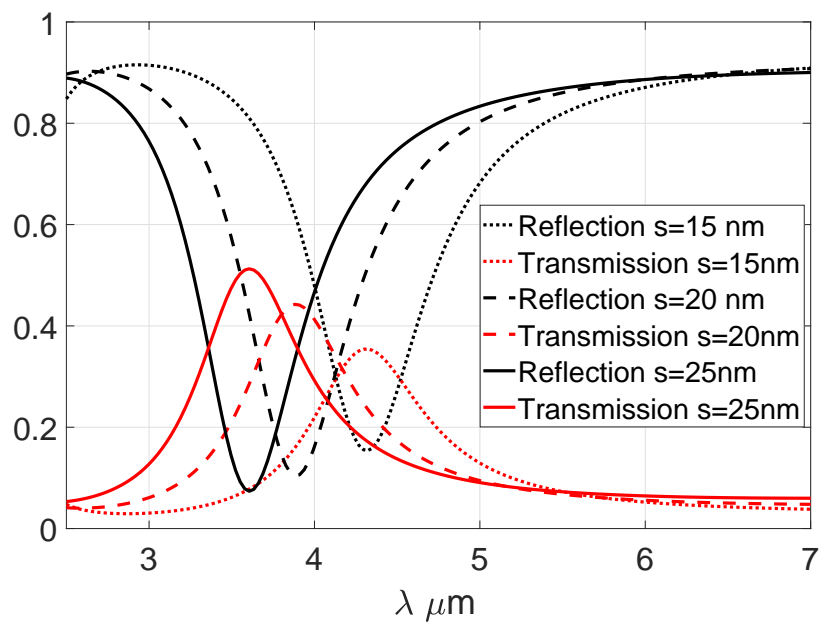


Figure 6.7: Spectrum of the reflection and transmission for different values of  $s$  and for  $d = 165 \text{ nm}$ .

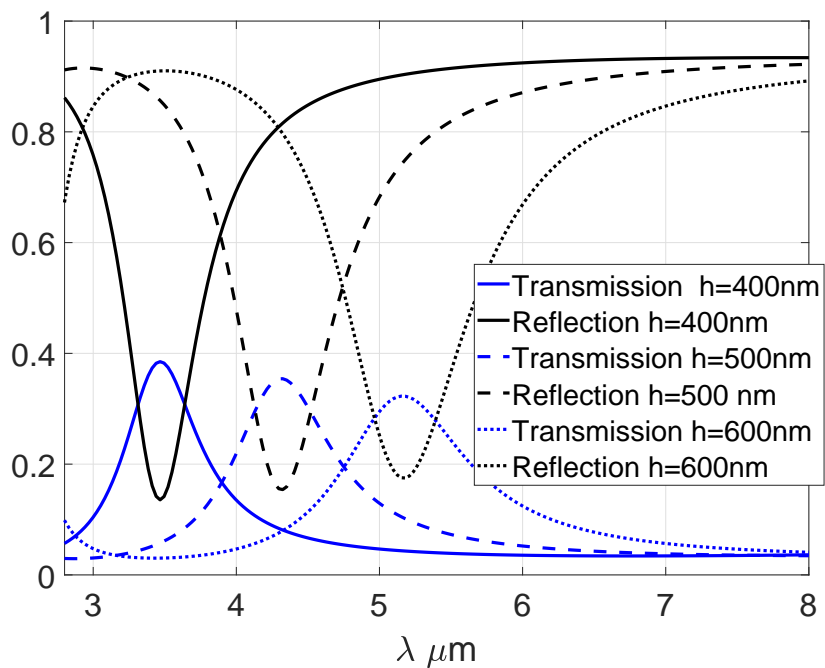


Figure 6.8: Spectrum of the reflection and transmission for different values of  $h$  and for  $s = 15 \text{ nm}$  and  $d = 165 \text{ nm}$ .

### 6.3 Magneto-optical perturbation of the gap plasmon modes

Now let us discuss the Magneto-optical side of the problem by considering the presence of magnetization in the dielectric-slits. We consider the EuS material uniformly magnetized in the polar configuration, i.e. the bias magnetic field is along  $(O, z)$  axis. In the presence of magnetization EuS possesses a permittivity of the form [23]

$$\begin{bmatrix} \varepsilon^{xx}(x, y, \omega) & \varepsilon^{xy}(x, y, \omega) & 0 \\ \varepsilon^{yx}(x, y, \omega) & \varepsilon^{xx}(x, y, \omega) & 0 \\ 0 & 0 & \varepsilon^{zz}(x, y, \omega) \end{bmatrix} \quad (6.13)$$

where

$$\begin{aligned} \varepsilon^{xx} = \varepsilon^{yy} &= \varepsilon_{\infty} + \frac{\omega_p^2}{\Omega^2 - \omega^2 - 2i\Gamma\omega} \\ \varepsilon^{xy} = -\varepsilon^{yx} &= \frac{i\beta\omega\omega_p^2}{(\Omega^2 - \omega^2 - 2i\Gamma\omega)^2} = -i\Delta, \end{aligned} \quad (6.14)$$

and modes conversion may take place in the grating array.  $\beta$  is a experimental parameter proportional to the magnetic field [23]. In our study we use the following numerical parameters  $\beta = 8.4 \times 10^{18} \text{rad s}^{-1}$ ,  $\varepsilon_{\infty} = 4.125$ ,  $\Omega = 2.77 \times 10^{15} \text{rad s}^{-1}$ ,  $\Gamma = 2 \times 10^{14} \text{s}^{-1}$ ,  $\omega_p = 4 \times 10^{14} \text{rad s}^{-1}$ . By solving the eigenvalue equation Eq. (6.3) in the case of uniformly magnetized slit-material, in the polar configuration, we observe numerically that the degeneracy of the eigenvalue  $\gamma_0^{(2)}$  is removed or lifted. As shown in Fig. 6.9, the polar bias magnetic field splits the fundamental mode into two non-degenerate eigenvalues denoted  $\gamma_{LCP}$  and  $\gamma_{RCP}$ . Since  $\gamma_{LCP} \neq \gamma_{RCP}$ , two resonance frequencies arise in the system. In Fig. (6.10) we present the reflection and the transmission spectra of the structure under a RCP and LCP polarized plane waves at normal incidence. A shift between the RCP and LCP spectra can be clearly observed. In this figure, Transmission RCP/LCP and Reflection RCP/LPC are rigorously computed with the PMM.

Since the presence of the uniform polar magnetization impacts directly the effective index of the 2D Gap plasmon of the sub-wavelength structure, we can explore the magneto-optical activity of the system by analyzing the EOT phenomenon of an electrical homogeneous slab with relative permittivity  $\varepsilon^{(2)}$  where live two modes  $\gamma_{RCP}$  and  $\gamma_{LCP}$ . Regarding Fig. 6.9, it is interesting to note that these non-degenerate modes can be derived from  $\gamma_0^{(2)}$  by the following analytical relation :

$$\gamma_+ \simeq \gamma_0^{(2)} + \frac{s}{2d}\Delta, \text{ and } \gamma_- \simeq \gamma_0^{(2)} - \frac{s}{2d}\Delta. \quad (6.15)$$

that only depend on the medium's gyration  $\Delta$  and the slit filing factor  $s/d$ . Now let's introduce

$$\alpha_{\pm} = \sqrt{\varepsilon^{(2)} - \gamma_{\pm}^2}, \quad (6.16)$$

and let us define the analytical reflection  $R_{RPC/LCP}$  and transmission  $T_{RPC/LCP}$  coefficients by introducing  $\gamma_{\pm}$  and  $\alpha_{\pm}$  in Eq. (6.8). We successfully compare in Fig. 6.10 the analytical model  $R_{RPC/LCP}$  and transmission  $T_{RPC/LCP}$  to the rigorous computation from PMM. Both EOT phenomenon and resonances shifting due to the MO activity in the MO plasmonic system are well held by the current semi-analytical model. Remark that the proposed structure is symmetric according to the  $(Oz)$  direction. By

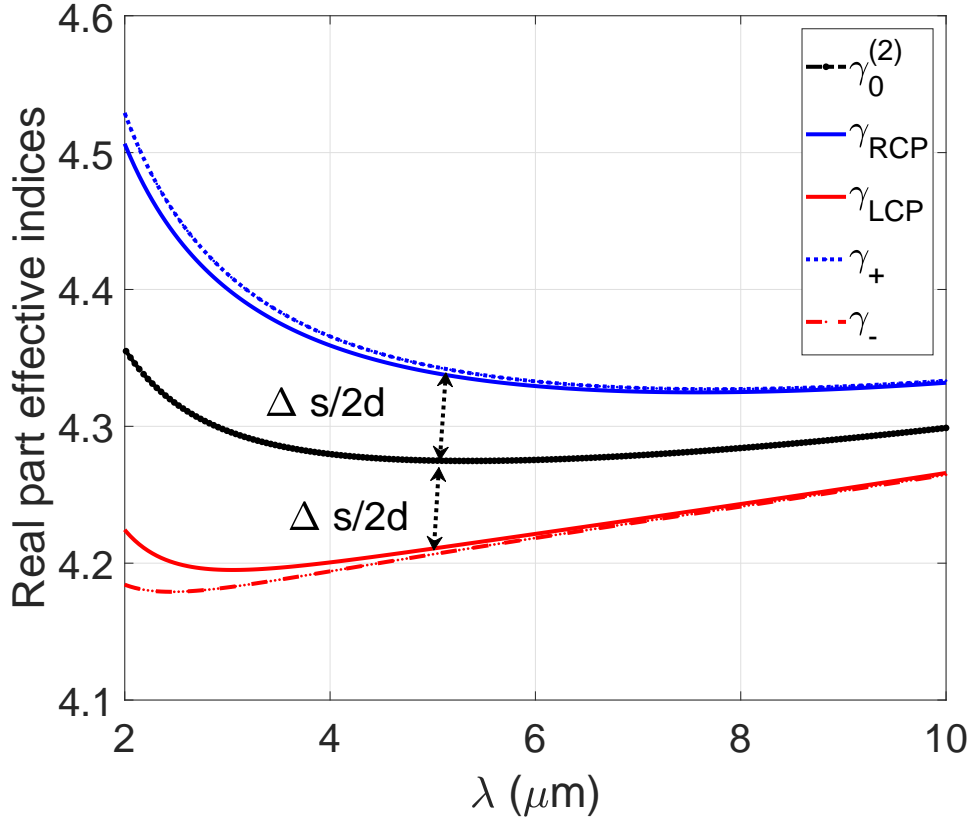


Figure 6.9: Dispersion curves of the degenerate effective index  $\gamma_0^{(2)}$  (dashed black line) and of  $\gamma_{RCP}$  and  $\gamma_{LCP}$ . The polar bias magnetic field removes the degeneracy in splitting the fundamental mode  $\gamma_0^{(2)}$  into two non degenerate eigenvalues  $\gamma_{LCP}$  and  $\gamma_{RCP}$ . The distance between these new sub-levels is approximately equal to  $\frac{s}{d}\Delta$ . Numerical parameters:  $\beta = 8.4 \times 10^{18} \text{rad s}^{-1}$ ,  $\epsilon_\infty = 4.125$ ,  $\Omega = 2.77 \times 10^{15} \text{rad s}^{-1}$ ,  $\Gamma = 2 \times 10^{14} \text{s}^{-1}$ ,  $\omega_p = 4 \times 10^{14} \text{rad s}^{-1}$ .

tuning the gyrotropic parameter  $\Delta$ , it is possible to shift the resonance wavelength of a given circular polarized RCP or LPC such that, the current plasmonic MO structure is transparent to the incoming forward wave whereas it is still reflective to the backward incoming wave. See Fig. 6.11. According to the results shown in this figure, the LCP and RCP EOT shift is even greater than  $\Delta$  is high. For  $\lambda = 3.409 \mu\text{m}$ , the structure is transparent to the LCP polarization while it reflects the RCP one. This structure acts as both a polarization-wavelength-filter and a polarization-isolator.

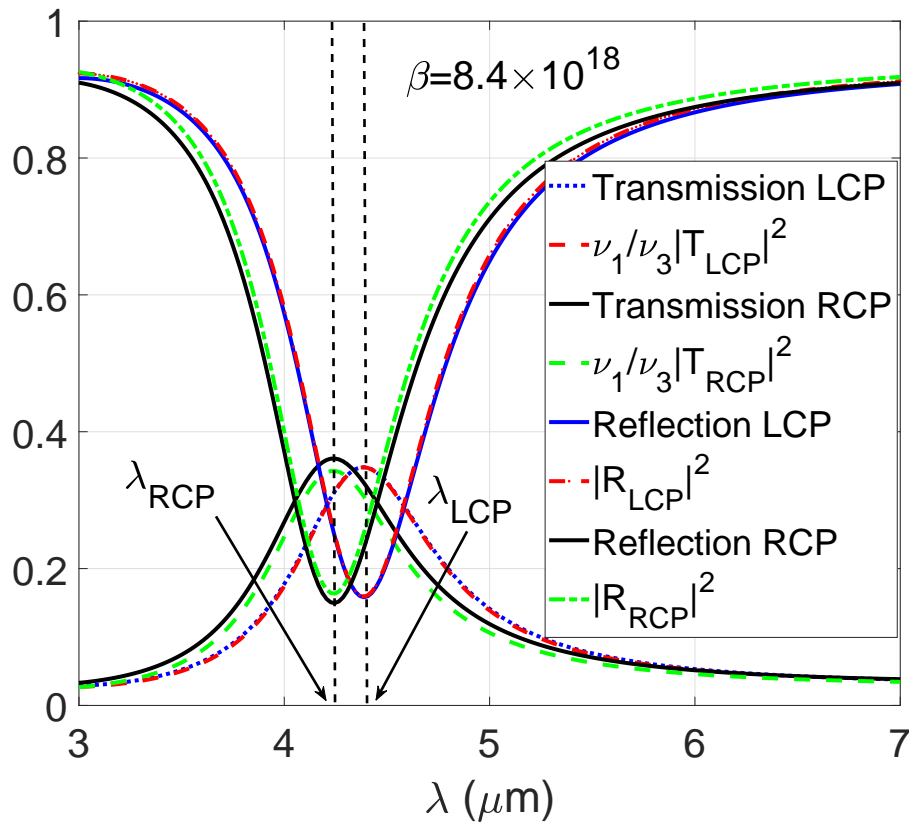


Figure 6.10: Reflection and transmission spectra of the array of the 2D subwavelength cross-slits grating in uniform polar magnetization configuration. Illustration of EOT-MO phenomenon. Comparison between rigorous computation with the PMM and the semi analytical model. Numerical parameters:  $\beta = 8.4 \times 10^{18} \text{rad s}^{-1}$ ,  $\epsilon_{\infty} = 4.125$ ,  $\Omega = 2.77 \times 10^{15} \text{rad s}^{-1}$ ,  $\Gamma = 2 \times 10^{14} \text{s}^{-1}$ ,  $\omega_p = 4 \times 10^{14} \text{rad s}^{-1}$ .

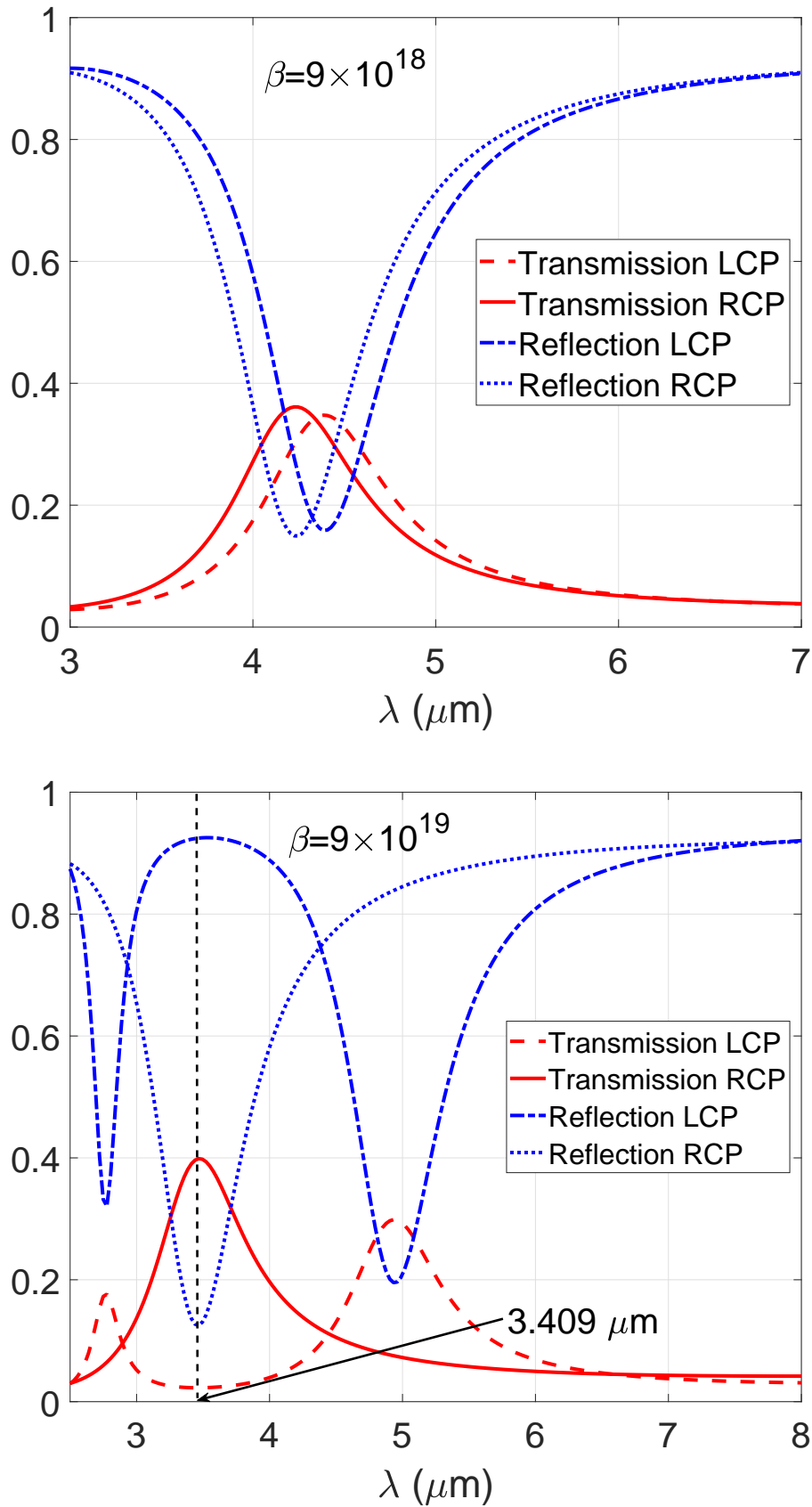


Figure 6.11: Illustration of EOT-MO phenomenon for  $\beta = 9 \times 10^{18} \text{rad s}^{-1}$  and  $\beta = 9 \times 10^{19}$ . Numerical parameters:  $\epsilon_{\infty} = 4.125$ ,  $\Omega = 2.77 \times 10^{15} \text{rad s}^{-1}$ ,  $\Gamma = 2 \times 10^{14} \text{s}^{-1}$ ,  $\omega_p = 4 \times 10^{14} \text{rad s}^{-1}$ .

## 6.4 Conclusion

In conclusion, we have proposed a theoretical analysis of a magneto optic plasmonic structure based on a magneto optical activity, namely the nonreciprocity around EOT frequency range. We provide a semi-analytical model based on a modal analysis of the system allowing efficient access to the full spectrum of the system. Our study revealed that when the proposed structure is symmetric, the fundamental mode is degenerate. That is why the EOT phenomenon through such a structure is independent of the incident wave polarization. On the other hand, under a polar bias magnetic field the degeneracy of the fundamental mode of the structure is removed. Two EOT phenomena, each one associated with LCP and RCP polarizations, are then observed. This results in the non-reciprocity behavior of the proposed structure.

# Bibliography

- [1] H.F. Ghaemi T. Thio T.W. Ebbesen, H.J. Lezec and P.A. Wolff. Extraordinary optical transmission through sub-wavelength hole arrays,”. *Nature*, (391):667–669, 1998. [77](#), [79](#), [149](#)
- [2] L. Martín-Moreno, F. J. García-Vidal, H. J. Lezec, K. M. Pellerin, T. Thio, J. B. Pendry, and T. W. Ebbesen. Theory of extraordinary optical transmission through subwavelength hole arrays. *Phys. Rev. Lett.*, 86:1114–1117, Feb 2001. [77](#), [149](#)
- [3] F. J. García de Abajo, R. Gómez-Medina, and J. J. Sáenz. Full transmission through perfect-conductor subwavelength hole arrays. *Phys. Rev. E*, 72:016608, Jul 2005. [149](#)
- [4] H. T. Liu and P. Lalanne. "microscopic theory of the extraordinary optical transmission. *Nature*, (452):728–731, 2008. [77](#), [149](#)
- [5] F.I. Baida, Y. Poujet, B. Guizal, and D. Van Labeke. New design for enhanced transmission and polarization control through near-field optical microscopy probes. *Optics Communications*, 256(1):190–195, 2005. [77](#), [149](#)
- [6] Fadi I. Baida, Yannick Poujet, Jérôme Salvi, Daniel Van Labeke, and Brahim Guizal. Extraordinary transmission beyond the cut-off through sub-annular aperture arrays. *Optics Communications*, 282(7):1463–1466, 2009. [77](#), [149](#)
- [7] Magneto-optical effects in the metal-dielectric gratings. *Optics Communications*, 278(1):104 – 109, 2007. [149](#)
- [8] Haibin Zhu and Chun Jiang. Nonreciprocal extraordinary optical transmission through subwavelength slits in metallic film. *Opt. Lett.*, 36(8):1308–1310, Apr 2011. [149](#)
- [9] Hua Xu and Byoung Seung Ham. Investigation of extraordinary optical transmission and faraday effect in one-dimensional metallic-magnetic gratings. *Opt. Express*, 16(26):21375–21382, Dec 2008. [149](#)
- [10] L. Halagačka, M. Vanwolleghem, F. Vaurette, J. Ben Youssef, K. Postava, J. Pištorá, and B. Dagens. Magnetoplasmonic nanograting geometry enables optical nonreciprocity sign control. *Opt. Express*, 26(24):31554–31566, Nov 2018. [149](#)
- [11] Zhichao Ruan and Min Qiu. Enhanced transmission through periodic arrays of subwavelength holes: The role of localized waveguide resonances. *Phys. Rev. Lett.*, 96:233901, Jun 2006. [149](#)

- [12] Yuehui Lu, Min Hyung Cho, YoungPak Lee, and Joo Yull Rhee. Polarization-independent extraordinary optical transmission in one-dimensional metallic gratings with broad slits. *Applied Physics Letters*, 93(6):061102, 2008. [149](#)
- [13] V. I. Belotelov, L. L. Doskolovich, and A. K. Zvezdin. Extraordinary magneto-optical effects and transmission through metal-dielectric plasmonic systems. *Phys. Rev. Lett.*, 98:077401, Feb 2007. [149](#)
- [14] Alexander B. Khanikaev, S. Hossein Mousavi, Gennady Shvets, and Yuri S. Kivshar. One-way extraordinary optical transmission and nonreciprocal spoof plasmons. *Phys. Rev. Lett.*, 105:126804, Sep 2010. [149](#)
- [15] Victor Dmitriev, Fernando Paix ao, and Marcelo Kawakatsu. Enhancement of faraday and kerr rotations in three-layer heterostructure with extraordinary optical transmission effect. *Opt. Lett.*, 38(7):1052–1054, Apr 2013. [149](#)
- [16] Daoyong Li, Chengxin Lei, Leyi Chen, Zhixiong Tang, Shaoyin Zhang, Shaolong Tang, and Youwei Du. Waveguide plasmon resonance induced enhancement of the magneto-optics in a ag/bi:yig bilayer structure. *J. Opt. Soc. Am. B*, 32(9):2003–2008, Sep 2015. [149](#)
- [17] R. Brendel and D. Bormann. An infrared dielectric function model for amorphous solids. *Journal of Applied Physics*, 71(1):1–6, 1992. [82](#), [150](#)
- [18] Aleksandar D. Rakić, Aleksandra B. Djurišić, Jovan M. Elazar, and Marian L. Majewski. Optical properties of metallic films for vertical-cavity optoelectronic devices. *Appl. Opt.*, 37(22):5271–5283, Aug 1998. [82](#), [150](#)
- [19] Kofi Edee. Single mode approach with versatile surface wave phase correction for the extraordinary optical transmission comprehension of 1d period nano-slits arrays. *OSA Continuum*, 1(2):613–624, Oct 2018. [78](#), [150](#), [151](#)
- [20] K. Edee and J. P. Plumey. Numerical scheme for the modal method based on subsectional gegenbauer polynomial expansion: application to biperiodic binary grating. *J. Opt. Soc. Am. A*, 32(3):402–410, Mar 2015. [151](#)
- [21] Kofi Edee. Understanding the plane wave excitation of the metal-insulator-metal gap plasmon mode of a nanoribbons periodic array: role of insulator-metal-insulator lattice mode. *OSA Continuum*, 2(2):389–399, Feb 2019. [152](#)
- [22] Kofi Edee, Maha Benrhouma, Mauro Antezza, Jonathan Albert Fan, and Brahim Guizal. Coupling between subwavelength nano-slit lattice modes and metal-insulator-graphene cavity modes: a semi-analytical model. *OSA Continuum*, 2(4):1296–1309, Apr 2019. [78](#), [152](#)
- [23] Dominik Floess and Harald Giessen. Nonreciprocal hybrid magnetoplasmonics. *Reports on Progress in Physics*, 81(11):116401, oct 2018. [158](#)

# Conclusion and outlook

*I am not always good and noble.  
I am the hero of this story, but I  
have my off moments.*

---

P. G. Wodehouse

In this thesis, we have exploited the extraordinary and unusual electromagnetic, optical and plasmonic properties of graphene for exploring and modelling graphene based plasmonic structures of academic and technological interests. The research carried out and presented in this work is articulated around two main parts. The first part is focused on the study of hybrid plasmonic structures based on graphene while the second part is aimed at investigating the magneto-optical properties of structures based on graphene and metals subjected to an external static magnetic field. Let us, in the following, summarize the main and important results obtained for these two parts.

After discussing and presenting the necessary basics and tools for this thesis in chapter 1, 2 and 4, we proposed in chapter 3 to investigate a hybrid plasmonic system consisting of a 1D array of periodic subwavelength metallic slits and a graphene sheet separated by a dielectric gap. This system puts in play two fundamental and important phenomena: an EOT phenomenon and a metal-insulator-graphene (M-I-G) cavity plasmon mode excitation. By the use of the PMM method, we have plotted the transmission and reflection spectra of the proposed structure. The obtained results revealed broadband and narrow band resonances. For a better understanding of the origin of these band resonances, we have proposed a semi analytical method that suggests to split the whole system into two coupled sub-systems. The first one is a weakly coupled sub-system made of a periodic array of subwavelength metallic nano-slits whose electromagnetic response can be merely predicted by replacing it by a homogeneous slab with an equivalent permittivity. This allows us to analytically obtain its corresponding reflection and transmission coefficients. By comparing the analytical results with the spectrum of the structure obtained by the PMM method, we showed that these approximated curves perfectly match the broadband resonances of the hybrid structure. Additionally, it was shown that the narrow-band nature of the hybrid system can be understood by studying the behaviour of a second strongly coupled sub-system. It was also demonstrated that these resonances modes are linked to the resonances of a metal/insulator/graphene horizontal Perot-Fabry cavity modes. Furthermore, we found that the effective index associated with these modes and then the resonance wavelengths of the system can be controlled and tuned by changing the chemical potential of graphene. By adjusting the chemical potential, we can achieve an

induced reflection phenomenon or perfect absorption within the structure. This finding may open up opportunities for various tunable applications such as reflectors and absorbers. Finally, we provided analytical expressions for the reflection and transmission coefficients of the global structure allowing to describe the resonance phenomena occurring in it. An interesting perspective is that our analysis can be extended to study more complex hybrid structures such as the coupling of the lattice modes with a substrate made of a non-reciprocal photonic topological material and hybrid configurations involving diffraction gratings coupled to hybrid graphene multilayered structures.

In the second part of this work concerning the study of the magneto-optical properties of structures based on graphene and metals, we have been interested in investigating two different structures. In chapter 5, we developed a simple and fast semi analytical method to accurately predict the optical response of a one dimensional graphene strip grating in the presence of an external static magnetic field, in which the graphene is modelled as an anisotropic layer with atomic thickness and a frequency dependent and complex permittivity tensor. The optical spectra are computed through an effective medium approach and a scattering formalism. This model is computationally efficient and can be readily applied to any graphene strip grating with different geometric parameters. In particular, we showed that the proposed model can efficiently deal with gratings with small gaps as well as with large gaps, specifically, it provides precise and reliable results in the case of gratings with small gaps which constitute a complicated case to deal with. Moreover, we found that, although the proposed model can efficiently treat structures with static magnetic fields, it is still valid even for structures where the static magnetic field is absent. We further analysed the proposed approach as a function of the static magnetic field and found that it can provide accurate results for all fields smaller than 7T. As a future work, we propose to employ this structure in the design of a spectrally and spatially tunable metasurface lens by exploiting the tunability of graphene magnetoplasmons.

Finally, chapter 6 has been dedicated to the study of magneto optical properties of a 2D plasmonic structure composed of a periodic array of metal crossed-slits grating when the slits are filled with an anisotropic gyrotropic material. Firstly, we have provided a semi-analytical model based on a modal analysis of the system that allows to reproduce the full spectrum of the system and describe the EOT mechanism occurring in it. Secondly, we have employed these analytical expressions to explore the non reciprocal unidirectional light transmission in the frequency ranges where EOT occurs.